SAPIENZA
UNIVERSITÀ DI ROMA

SCUOLA DI DOTTORATO "VITO VOLTERRA"
DOTTORATO DI RICERCA IN FISICA– XXIII CICLO

Monte Carlo simulations of high pressure hydrogen

THESIS SUBMITTED TO OBTAIN THE DEGREE OF
DOCTOR OF PHILOSOPHY ("DOTTORE DI RICERCA") IN PHYSICS
MAY 2011

BY

Elisa Liberatore

Program Coordinator
Prof. Enzo Marinari

Thesis Advisors
Prof. Giovanni Ciccotti
Prof. Carlo Pierleoni

Introduction

The application of extreme pressures on matter can change dramatically its physical properties. In particular, the prediction on the metallization transition in solids at pressures high enough was at the origin of the great interest on this subject: hydrogen, being the simplest element with a single electron per atom, was considered as prototypical system to understand the nature of this transition. Moreover, the knowledge of the physical properties of hydrogen at pressures of hundreds of GPa is fundamental in the fields of Astrophysics and Planetary Sciences, since hydrogen is the main constituent of giant planets (like Jupiter and Saturn), brown dwarfs and stars, systems in which those extreme conditions are easily reached. Theoretical models of the interior of such objects cannot prescind from the detailed knowledge of the hydrogen behavior at high pressure.

The present reconstruction of the hydrogen phase diagram by direct experimental inspection is quite limited, since also the most sophisticated experimental techniques do not allow to reach pressures higher than $\sim 300 - 350GPa$. The experimental methods led to the discover of unexpected solid molecular phases and of a peculiar reentrant behavior of the molecular melting curve in the (P, T) thermodynamic plane. However, the experiments are still not able to access the most interesting regions of the hydrogen phase diagram, as for instance those in which molecular dissociation and metallization of solid hydrogen occur.

The numerical *ab initio* methods are, as a consequence, fundamental tools to extend our knowledge to the high pressure hydrogen phases and get more insight on the nature of the low temperature metallization transition. In the framework of the Born-Oppenheimer approximation two different techniques have been developed. (i) Ab Initio Molecular Dynamics (AIMD), which uses Density Functional Theory (DFT) to determine the electronic structure at fixed nuclei and Classical Molecular Dynamics to evolve the protonic degrees of freedom on the resulting Born-Oppenheimer surface; (ii) Classical and Quantum Monte Carlo (QMC) techniques to treat both electronic and protonic degrees of freedom. AIMD simulations are generally accurate and faster than QMC simulations and allow to consider systems with a larger number of particles, of the order of hundreds or thousands. However, high pressure hydrogen is a system particularly hard to face for the AIMD technique. While the QMC methods are able to treat directly the many-electron problem, within DFT this problem is reformulated in terms of independent single-electron equations, with the introduction of approximations in the definition of the energy functional. As a consequence the DFT suffers of several limitations, as the well known problem of the underestimation of the valence-conduction band gap in semiconductors, which favors metallic states with respect to insulator ones. Due to inexact predictions of the DFT electronic state, the AIMD methods can lack of accuracy mainly in the regions to which we are most interested, i.e. near the transition from insulating to metallic phases. A second problem of the AIMD technique is that the inclusion of the zero point motion of protons is very expensive within AIMD and hence the most of the AIMD works on hydrogen assumes classical protons. Quantum nuclear effects, however, can be significant at high density and low temperature. Finally, AIMD can present convergence issues, both with respect to the number of particles and with the size of the basis set used to expand the electronic state, leading to incorrect results. As an example, early structure calculations of the solid phases of hydrogen predicted the existence of unusual planar and chain structures, a result that was later found to be only a spurious finite size effect. More recently different AIMD works on the metallization in the liquid phase arrived at different conclusions on the nature of the transition, some predicting a continuous dissociation leading to a final metallic state, others recognizing instead a sharp, first order transition. Again, the disagreement in the different predictions was determined by the use of systems with a number of particles too small.

From these examples it can be deduced that Quantum Monte Carlo techniques, despite their higher computational demand with respect to AIMD, are the unique methods capable to provide the necessary accuracy over the entire phase diagram.

The main technique adopted in my simulations is the Coupled Electron-Ion Monte Carlo (CEIMC) method, a first-principle technique entirely based on Monte Carlo and developed especially to address the hydrogen problem. Electrons are assumed to be in the ground state determined by the protonic instantaneous configuration. Protons, instead, are described either as classical or quantum particles in equilibrium with a heat bath at finite temperature T. Monte Carlo techniques are applied both to determine the electronic ground state energy and to sample the protonic configurational space. Two zero temperature QMC methods are implemented: the Variational Monte Carlo (VMC) and the Reptation QMC (RQMC). The protonic moves are accepted or rejected with a Metropolis MC - either the standard Metropolis for classical protons or Path Integral Monte Carlo for quantum protons - using the BO energy differences computed through a ground state QMC calculation, that must be repeated at each protonic step. Since more than 20000 protonic steps are necessary to estimate thermodynamic averages with an acceptable noise level and a complete QMC electronic calculation is needed for each one, the CEIMC simulation scheme is particularly expensive in terms of computational time resources. For this reason the systems which we can simulate in a reasonable amount of time are of as much as 100 atoms. In spite of this limit, the CEIMC technique has the merit of being fully *ab initio*, since it requires no a priori assumptions except on the form of the trial wave function used to represent the electronic states.

The method also implement several features to reduce systematic effects of different nature. A particular form of boundary conditions, known with the name of Twist Averaged Boundary Conditions (TABC), is used to reduce the finite size effects on the estimated energies and pressures. Biases on the sampling of the protonic configurational space due to the use of noisy energy differences (obtained from QMC simulations) are avoided by modifying the standard Metropolis sampling with the introduction into the acceptance formula of an additional contribution proportional to the noise on energy differences (penalty method).

In this work we focused our attention mainly on the monoatomic hydrogen phases, to determine the melting transition at pressures above the molecular dissociation, by means of free energy calculations. One of the main difficulties encountered is related to the absence of experimental data: while the structure of the molecular solid is well known, at least for pressures up to $\sim 250GPa$, the crystal structure of the atomic hydrogen is still undetermined, despite the various computational attempts.

At very high pressures, of the order of hundreds of TPa, hydrogen becomes a fully ionized plasma of electrons and protons, which can be well described as an effective system of pseudo-ions interacting via a screened Coulomb pair potential, which form can be derived assuming linear electronic response. This pair potential has a Yukawa decaying at small distances and is middle-ranged, going to zero as $cos(kr)/r^3$, at large distances. For this model system we first identified the most stable solid structures among a large set of lattices of different symmetries, by comparing their zero temperature energies and enthalpies, for classical protons. Then we considered the temperature behavior of the solids and we determined the melting curve by means of free energy calculations, both for classical and quantum protons (performing in the latter case Path Integral Monte Carlo simulations), and for all the hydrogen isotopes (hydrogen, deuterium and tritium).

At lower pressures, we performed a similar analysis on the *ab initio* system: we compared energies and enthalpies of several proton lattices at zero temperature, for classical protons. At finite temperature, we investigated the stability of different lattices and obtained a first point on the melting curve, assuming classical protons, by comparing the free energies of the fluid and of the solid phases.

Finally, we used the CEIMC technique to study the molecular dissociation in the fluid phase at low temperature, continuing a previous work at higher temperature. The first order liquid-liquid transition can be recognized by observing the behavior of the pressure P as a function of the density ρ along an isotherm: the presence of a plateau in the $P(\rho)$ curve is the index of a first order transition. We then performed CEIMC simulations, for classical protons, along the isotherm $T = 600K$ in a range of densities across the transition. In view of future calculations with quantum protons, applying the Path Integral Monte Carlo (PIMC) technique, we compared the results obtained by computing the Born-Oppenheimer electronic energies with the two different QMC methods implemented in our code: the Variational and the Reptation Quantum Monte Carlo. The first method indeed is several times faster than the second, but can be less accurate. In case of equivalence of the two electronic methods, a VMC+PIMC simulation would have nearly the same computational cost of a CEIMC simulation using RQMC electronic energies and classical protons.

This thesis is organized as follows. In Chapter 1 we introduce to the problem of the high pressure hydrogen, describing in detail the different regions of the phase diagram reconstructed so far through experiments and numerical simulations. In Chapter 2 we present the theoretical framework of this thesis. After a general discussion of the different Monte Carlo techniques applied in this work (Metropolis Monte Carlo for classical particles, Path Integral Monte Carlo for quantum particles at finite temperature, Variational and Reptation Quantum Monte Carlo for quantum ground state calculations), the Coupled Electron-Ion Monte Carlo method is presented. The the electronic wave functions adopted in the simulations and the wave function optimization procedure are described too. The remaining Chapters are devoted to the results of this work. Chapter 3 concerns the effective screened Coulomb system. It presents a short derivation of the screened Coulomb pair potential and the discussion of the results on the classical system and of the quantum correction to the classical melting line. In Chapter 4 we present the results of the CEIMC simulation on hydrogen in the atomic phase. The first part of this chapter deals with the study at $T = 0K$ of several crystal structures for the atomic hydrogen. The last part concerns the finite temperature study of the stability of the solid vs. the liquid phase. Finally, in Chapter 5 we discuss our results on the liquid-liquid transition.

Papers associated to the thesis work

- E. Liberatore, C. Pierleoni and D. M. Ceperley, "Liquid-solid transition in fully ionized hydrogen at ultra-high pressures", *J. Chem. Phys.* **134**, 184505 (2011)
- Within the Born-Oppenheimer approximations the Born-Oppenheimer electronic energies can be computed with different techniques providing different levels of accuracy. A paper on the application of the coupling constant integration method to relate the free energy of a system obtained with different QMC methods is in press on Molecular Physics.

List of Abbreviations & Symbols

AIMD	Ab Initio Molecular Dynamics
AIRSS	Ab Initio Random Structure Search
BO	Born-Oppenheimer
BOMD	Born-Oppenheimer Molecular Dynamics
BSP	Broken Symmetry Phase
CCI	Coupling Constant Integration
CEIMC	Coupled Electron-Ion Monte Carlo
CPMD	Car-Parrinello Molecular Dynamics
DAC	Diamond Anvil Cells
DFT	Density Functional Theory
FVT	Fluid Variational Theory
HNC	HyperNetted Chain (equation)
IR	InfraRed
MC	Monte Carlo
MD	Molecular Dynamics
OZ	Ornstein-Zernike (equation)
PBC	Periodic Boundary Conditions

PIMC	Path Integral Monte Carlo
PPT	Plasma Phase Transition
QMC	Quantum Monte Carlo
RPA	Random Phase Approximation
RQMC	Reptation Quantum Monte Carlo
r_s	ion sphere radius: $r_s = (3/4\pi\rho)^{1/3}$
TABC	Twist Averaged Boundary Conditions
VMC	Variational Monte Carlo

Contents

Chapter 1

High pressure hydrogen

1.1 Introduction

The study of matter under extreme conditions is a fascinating branch of Condensed Matter Physics. Hydrogen, in particular, being the simplest element, is a good prototypical system to understand the changes in the physics of materials at high pressures. Moreover, particular attention is focused on hydrogen also in the fields of Astrophysics and Planetary Sciences, since it is the main constituent of brown dwarfs [1], stars [2] and giant planets, in which pressures of hundreds GigaPascal ($1GPa = 10^{-2}Mbar$) and temperatures of thousands Kelvin are easily reached. The knowledge of the physical characteristics of the hydrogen at such high pressures is then crucial to build appropriate models to describe these systems [3, 4, 5].

In the 1935 E. Wigner and H. B. Huntington [6] first advanced the hypothesis of the metallization of solid elements at high enough pressures and applied a simple model to obtain a prediction of the metallization pressure of a Body Centered Cubic (BCC) hydrogen lattice. Even though the pressures that can be experimentally achieved at present time are more than 10 time higher than the Wigner-Huntington estimate for the hydrogen metallization pressure ($\approx 25GPa$), no evidence of a metallic transition has been found in the solid phase [7, 8] up to $P \approx 320GPa$ and $T \approx 300K$. On the contrary, high temperature experiments (up to 10^4K) proved the existence of a metallic fluid phase of partially dissociated hydrogen [9, 10, 11], even at not too high pressures ($P \approx 140GPa$).

Low temperature studies led to the discover of unexpected solid phases, others than the molecular Hexagonal Close Packed (HCP) characteristic of the solid hydrogen under ordinary pressures (also known as phase I): the so-called phase II and phase III. Another intriguing feature of the high pressure hydrogen phase diagram is the occurrence of a reentrant melting line in the (T, P) plane: the coexistence temperature between the molecular phase I solid and the liquid first increases with the pressure, reaches a maximum at about $80GPa$, then changes slope, decreasing with P. This behavior was first predicted by *ab initio* calculations of Bonev et al. [12] and then experimentally confirmed [13].

Well beyond the present experimental possibilities is the study of the atomic phases, appearing at very high pressure: only numerical techniques are up to now able to explore this region of the phase diagram.

In this chapter we will introduce the reader to the subject of the high pressure hydrogen, by describing our present knowledge of the phase diagram and stressing the main questions still remaining unanswered. The major experimental techniques to achieve pressures of hundreds of GPa (in hydrogen), i.e. the Diamond Anvil Cell technique and the shock wave method, will be briefly described in Appendix .1.

1.2 Hydrogen phase diagram

Figure 1.1 illustrates the hydrogen phase diagram, summarizing both experimental [9, 13, 14, 15, 16, 17] and computer simulation data [12, 18, 19].

Under normal conditions, hydrogen behaves in a quite standard way. At ambient pressure and temperature hydrogen is a molecular fluid. At low temperature it crystallizes as an HCP molecular solid with rotational freedom. The liquid-gas critical point is $T \approx 33K$ and $P \approx 1.3Pa$.

It is in the high pressure regime that the hydrogen phase diagram becomes more interesting, with the appearance of several different phases, that we will describe in detail in the following sections.

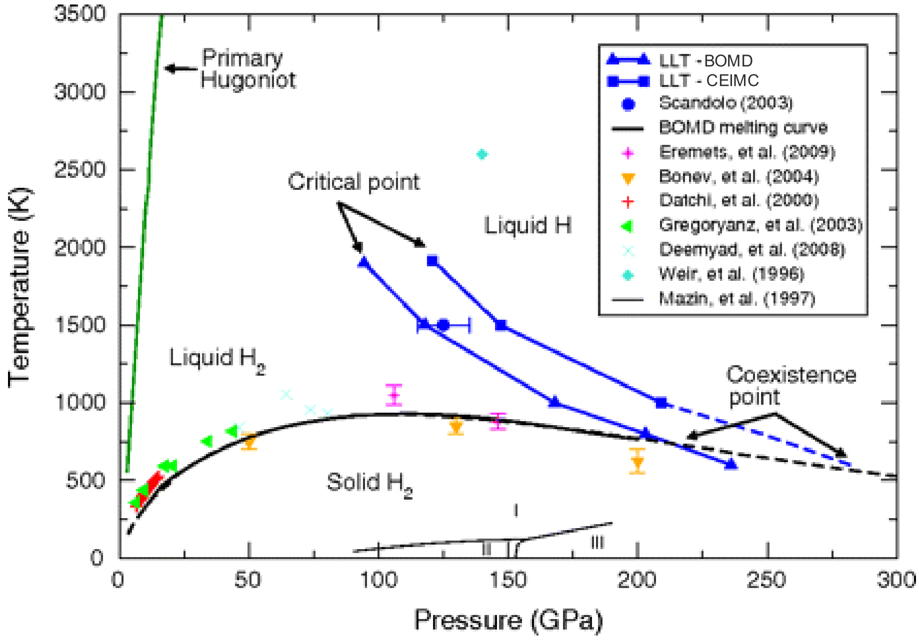

Figure 1.1. Hydrogen phase diagram, as obtained from high pressure experiments [9, 13, 14, 15, 16, 17] and numerical simulations [12, 18, 19], the latter represented as blue data in the picture. Figure from Ref. [19]. Dashed lines are high pressure extrapolations of data.

1.2.1 The molecular solid phases

In the low pressure/low temperature region of the phase diagram, hydrogen is a molecular solid. Three different phases, called phase I, II and III, have been experimentally identified through spectroscopic analysis of samples pressurized in Diamond Anvil Cells[1].

---

[1] see Appendix .1 for a description of this technique

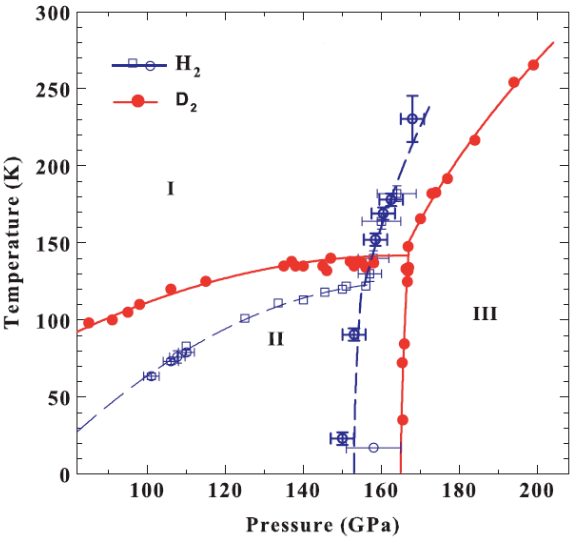

Figure 1.2. Detail of the solid-solid transitions in the molecular high pressure deuterium (D_2, red) and hydrogen (H_2, blue), from Ref. [22]. Points are from experimental measurements, while lines are fits of the data. The phases I-II-III triple point is located at $T \sim 142K$ and $P \sim 167GPa$ for deuterium and at $T \sim 122K$ and $P \sim 155GPa$. Experimental data to extend the transition lines are not available.

Figure 1.2, taken from Ref. [22], represents in detail the solid-solid coexistence lines experimentally observed in D_2 [21] and H_2 [17, 20] molecular crystals. Qualitatively the two isotopes present a similar behavior. The phase II is stable only in a restricted interval of pressures and for temperatures below $\approx 100K$. Phase I occupies the major part of the solid region of the phase diagram, being stable up to the melting in a wide range of pressures as showed in Figure 1.1. At pressures higher than $\approx 160GPa$ the phase III appears. Present at the beginning only at low temperatures, the phase III gradually gain stability also in temperature for increasing pressures. The three lines meet into a triple point ($T \sim 142K$ and $P \sim 167GPa$ for D_2 and $T \sim 122K$ and $P \sim 155GPa$ for H_2). Due to the quantitative differences in the D_2 and the H_2 transition lines, phase boundaries are very sensitive to isotopic effects.

In the phase I, the molecular centers occupy the lattice sites of an Hexagonal Close Packed crystal structure, as determined by X-ray diffraction measurements [21]. The main characteristic of this phase is the large zero point motion of protons: phase I is then a good example of quantum solid, characterized by a small localization of the H_2 on the lattice sites [23].

Another important feature of this phase, pointed out by experiments, is that the molecules, even if “fixed” in their lattice positions, behave as free rotors, being the angular distribution of the H_2 bonds almost isotropic [23]. This property reflects on the possibility of neglecting, as a first approximation, anisotropic interaction terms in the Hamiltonian $\hat{\mathcal{H}}$. In absence of anisotropy sources, it follows that $\hat{\mathcal{H}}$, the square of the angular momentum operator $\hat{\mathcal{L}}^2 = \sum_{i=1}^{N_{mol}} (\hat{\mathcal{L}}^2)_i$ and its projection along the azimuthal axis z $\hat{\mathcal{L}}_z = \sum_{i=1}^{N_{mol}} (\hat{\mathcal{L}}_z)_i$ commute and it is possible to find set of eigenstates common to the three operators, of the form $\left| \prod_{i=1}^{N_{mol}} \phi^i_{J_i,m_i} \right\rangle |\chi_{\mathbf{R}}\rangle$

where $|\chi_{\mathbf{R}}\rangle$ contains the **R** dependency of the wave function and the $|\phi^i_{J_i,m_i}\rangle$ are the simultaneous eigenstates of $(\hat{L}^2)_i$ with eigenvalue $J_i(J_i+1)\hbar^2$ and of $(\hat{L}_z)_i$ with eigenvalue $m_i\hbar$ (i.e. the spherical harmonics Y_J^m). It is then possible to distinguish into two species: the ortho and the para hydrogen, characterized by odd and even J, respectively [23]. Different techniques have been developed to prepare samples with the desired concentrations of orto and para hydrogen and it has been noticed experimentally that the relative abundance of the two species has a small but non negligible effect on the transitions temperature from phase I to phase II and phase III.

Phase II and III, instead, show molecular rotational ordering [21]. Obtaining accurate experimental indications of the crystal structure of hydrogen solids is not an easy matter: the electrons of hydrogen atoms are few so they are poor centers of scattering for X-rays and the obtained diffraction patterns are hence only low resolved. As a consequence the structures of those phases are not completely determined.

Phase II is obtained from the phase I by lowering the temperature: the lattice structure is still an HCP, but the molecular rotations are frozen and the molecular bonds are oriented. For that reason this phase is also called the Broken Symmetry Phase (BSP). The details of the molecular orientation in the HCP cell are still unknown, despite different suggestions from DFT calculations, trying to give explanation of the experimental X-ray data. The most probable candidate structures are summarized in Figure 1.3, from Ref. [24]. More recent X-ray and neutron diffraction studies [25, 26] advanced the possibility of the existence of distorted HCP structures for the phase II solid.

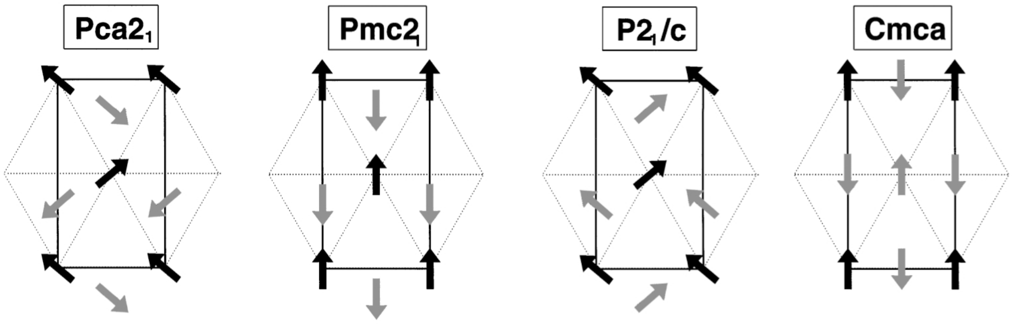

Figure 1.3. Candidates for the ground state structure of solid H_2 in phase II, indicated using the space group nomenclature (see Appendix .2). Lattices are projected on the horizontal (XY) plane. Molecules with centers belonging to the $z = nc$ planes are represented as black arrows, those having centers on the $z = (2n+1)c/2$ planes as gray arrows ($n = 0, 1, \cdots$). Arrows, which give the direction of the molecular bonds, lie out of the horizontal planes, pointing towards the positive z direction (i.e. for each molecule the head of the arrow represents the hydrogen over the plane, the tail the one under the plane). Image from Ref. [24].

The structural properties of the phase III are still under debate. The analysis of Raman and InfraRed (IR) spectra allows to discard a number of symmetries: in particular the phase III presents strong IR activity, probably arising from asymmetric distributions of the electronic charge responsible of an increased dipole moment with respect to the phases I and II [27].

Among the numerical simulation works aimed to determine a lattice structure able to account the experimental results, we can recall the one of Pickard and Needs [28]. They carried on an extensive zero temperature search of possible candidate structures for the phase III, using Density Functional Theory calculations to compute the electronic energies for fixed nuclei. To discard from the beginning the less favorable structures, they performed a random search of the more suitable lattices, starting from a number of random configurations and than relaxing them at constant pressure [29]. The initial configurations are obtained assuming some unit cells of suitable volume and then inserting inside them the desired number of atoms (or molecules) at random positions. The structures are then allowed to relax, under the effect of the DFT forces[2]. Pickard and Needs compared the enthalpies of the different equilibrium structures obtained after the relaxation, looking for those more favored energetically, having included the protonic zero point motion at an harmonic level (through the addition of the vibrational contribution $1/2h\nu_{vib}$ to the total energy). Vibrational spectra, to compare with the experimental, were also computed in Ref. [28] for the subset of solid structure having the lowest enthalpy. According to their analysis, the most plausible structures for the phase III might be a monoclinic structure belonging to the C2/c space group symmetry for pressures up to $250GPa$ and a structure with 12 atom per cell belonging to the Cmca space group symmetry (called Cmca-12), at higher pressures[3]. These structures are illustrated in Figure 1.4. However, no definitive experimental proof in favor of those suggested structures has been found yet.

Finally let us stress that, despite the pressures experimentally reached at present are one order of magnitude higher than the Wigner estimate [6] of the metallization pressure (of $25GPa$), no evidence of a metallic behavior has been found in the solid phases, up to $\approx 340GPa$ [7, 8].

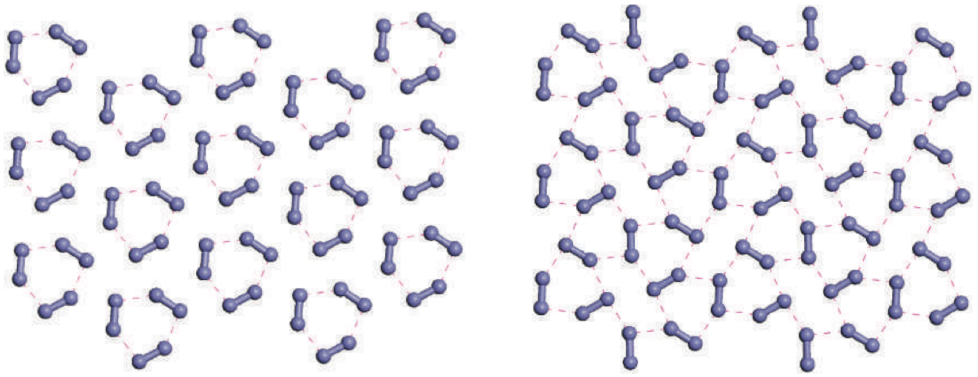

Figure 1.4. Left panel: A layer of the monoclinic C2/c structure. Three adjacent molecules form a distorted exagon: the distortion is responsible of intense IR activity. To obtain the 3d structure, many parallel layers identical to the one showed must be piled up along the vertical axis, each one at distance c from the adjacent layers and shifted with respect to the previous, following the sequence ABCDA. Right panel: A layer of the Cmca-12 structure. The sequence of parallel layers to obtain the 3d structure is ABA. Figures from Ref. [28].

---

[2] This technique is known with the name of Ab-Initio Random Structure Search (AIRSS).

[3] for a summary on the crystallographic nomenclatures see Appendix .2

1.2.2 The molecular melting

The transition from the low temperature molecular solid to an high temperature molecular fluid phase is well studied experimentally up to $\approx 150GPa$ with the aid of Diamond Anvil Cells [13, 14, 15, 16]. The peculiar feature of this transition is the reentrant shape of the melting temperature curve, that at first increases with the pressure, then reaches a maximum and finally starts to decrease, as showed in Figure 1.5

The presence of a reentrant melting in the molecular hydrogen was first pointed out by Bonev et al. [12] with *ab initio* Molecular Dynamics. They performed two-phases Car-Parrinello MD simulations, illustrated in Figure 1.6, with forces derived from DFT calculation of electronic structure and classical protons. With this technique they build the liquid-solid (phase I) coexistence line up to $200GPa$, observing a maximum in the melting curve at about $P = 90GPa$ and $T = 900K$. The presence of the maximum was interpreted as the consequence of an unbalanced softening of particles repulsion in the liquid and the solid phase, according to the following mechanism. A positive slope of the melting curve is due to the growth with the pressure of the repulsive forces among the molecules: as a consequence the displacement from the lattice sites becomes less energetically favorable and the melting temperature increases with P. On the other hand, as the particles become closer, the many body contributions to the interactions can soften the particle repulsions and balance this effect, leading to the reentrant shape of the liquid-solid coexistence curve [12]. More recently the stability of the molecular liquid versus the solid phase at high pressure and at low temperature has been confirmed by QMC-based *ab initio* Molecular Dynamics simulations [31].

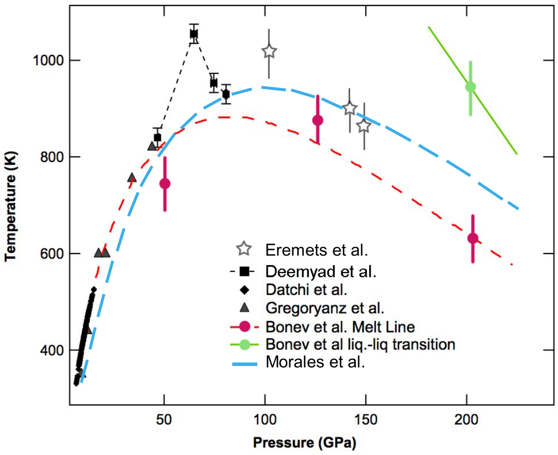

Figure 1.5. Melting transition in molecular hydrogen. Black points (stars, diamonds, triangles and squares, respectively): DAC experiments data [13, 14, 16, 15]; magenta circles: Bonev Molecular Dynamics data [12]. Red dashed line: fit of Bonev data according to an empirical formula based on the Lindemann melting criterion (the Kechin melting formula [30]). Green point: transition point to a metallic liquid phase [12]. Light-blue dashed line: Morales [19] prediction for the melting line. Figure from [15], modified to include Eremets, Bonev and Morales data points.

Earlier experimental data, reaching pressures up to $70GPa$ [15, 16], were

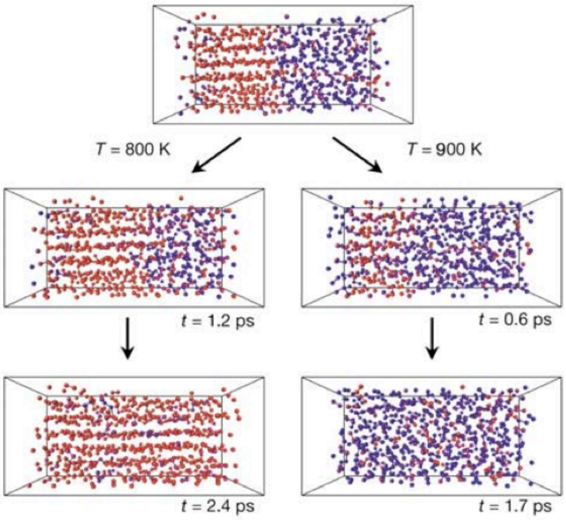

Figure 1.6. Illustration of the two phase simulation of Bonev et al. [12]. At the beginning of the simulation two supercells with particles arranged in a crystal (red points) and a disordered phase (blue points) are built and put in contact. During the evolution the solid-liquid interface will move towards the region of the less stable phase: the red particles will diffuse into the blue region or vice versa, and the two phase system will spontaneously rearrange into a single phase one. Figure from Ref. [12].

compatible with the presence of a maximum in the melting curve, but the definitive proof of the slope changing is due to the work of Eremets et al. [13]. They measured a melting temperature of about $1050K$ at $106GPa$ and of $880K$ at $145GPa$, confirming Bonev's results.

Indeed Bonev's results may be partially biased by finite size effects, particularly relevant in two-phase calculations. In this kind of simulations, in fact, the equilibrium phase reached depends on the evolution of the interface, but the large energy fluctuations typical of small systems can influence its "motion", favoring a phase rather than the other depending on the initial condition. Another source of bias can be due to the use of the Car-Parrinello method, since its level of accuracy in the liquid and the solid phase can be different: the two phases are simulated simultaneously, but particles in the liquid phase may move more than those in the solid. As a consequence in the two phases the updating of the electronic energy surface becomes necessary after a different number of protonic moves.

An independent indication of the reentrant shape of the molecular melting line is provided by the Born Oppenheimer MD (BOMD) calculations of Morales et al. [19]. They computed the transition line between the molecular liquid and the HCP phase I molecular solid, for classical protons, by comparing the Gibbs free energies of the solid and of the liquid phase. Qualitatively the two curves present similar behavior; Morales's curve, however, is closer to the experimental data at high pressure than the one determined by Bonev, as can be seen from Figure 1.5.

1.2.3 Metallization in the fluid phase

A large number of experiments were carried on using dynamic compression techniques in order to study the equation of state and the properties of high pressure fluid hydrogen and deuterium [32, 33, 34, 35, 36]. A liquid-liquid transition (LLT), from the insulating to the conducting fluid, was observed during shock wave experiments[4]: an increase of the conductivity up to $\approx 10^3 \Omega^{-1} cm^{-1}$ was first observed by Nellis et al. [9] in liquid hydrogen at $\approx 140 GPa$ and $\approx 2600 K$ and by Collins and collaborators [10] in liquid deuterium at $\approx 55 GPa$ and $\approx 8000 K$.

It is not clear if the metallization transition in the fluid phase is a continuous process, accompanied or driven by molecular dissociation, or if it occurs as a sharp, first-order phase transition, the so-called Plasma Phase Transition (PPT). Very recently the first experimental evidence of PPT has been found for deuterium by Fortov and collaborators [11]. During a shock wave compression experiment, they observed a sharp increase in the compressibility of the system, accompanied by a jump of 4 orders of magnitude of the deuterium conductivity.

However, during dynamic compression experiments to fine tuning both pressure and temperature it is not easy. As a consequence, the available experimental data are too dispersed to permit a deep understanding of this phenomenon and a robust theoretical support is hence needed.

Among the numerical works concerning the properties of dense hot hydrogen we can distinguish two different approaches: semi-empirical models based on a chemical picture and *ab initio* calculations.

To the first class it belongs a set of theoretical models and equations of state often used as a term of comparison for the interpretation of experimental data: the most commonly used are the equations of state of Chabrier-Saumon [38] and of Ross [39], and the SESAME tables [40] provided by the Los Alamos National Labs. Many other equations were derived by different authors, on the base of the Fluid Variational Theory (FVT) [41]. The basic assumption behind all those methodologies is that near the dissociation hydrogen is a mixture of different chemical species, such as H_2, H, H^+ and electrons. The free energy of the multi-component system is estimated as a linear combination of those of the single components, plus possibly polarization terms due to the interaction of the charged species with the neutral ones. Each term is determined independently, by introducing suitable effective potentials to model the interactions in the mono-component subsystems. All the thermodynamic properties can be derived from the free energy, using the standard thermodynamic relations. The relative abundance of the components into the mixture, for any given thermodynamic condition, is determined by imposing the equilibrium condition, i.e. equating the chemical potential, derived from the free energy, of the “reactants” and of the “products”. Despite those methods give results in good agreement with the experimental data and consistent with the existence of a metallic-insulator first order transition, the predictive power of those methods is minimal. The empirical effective potentials employed to determine the free energies are in fact based on experimental data available only in a small interval of pressures and temperatures and their applicability outside this range is limited. Moreover, the predictions of a discontinuous transition obtained with these methodologies may simply be an

---

[4] see Appendix.1 for more details on the shock wave experiments

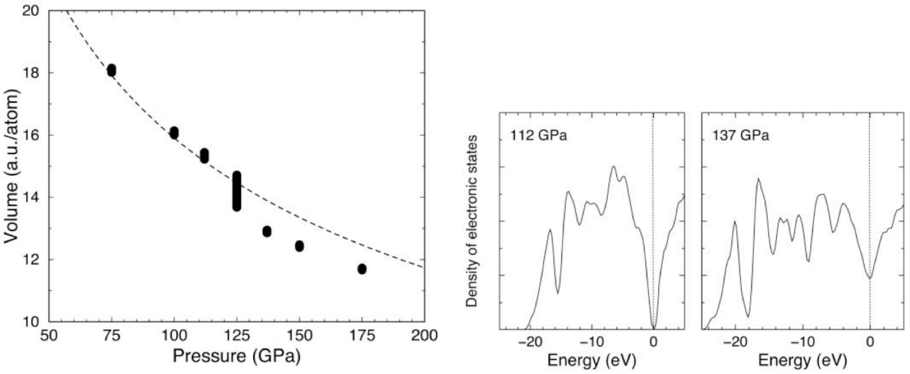

Figure 1.7. Evidence of first order liquid-liquid transition, from an insulator to a conducting fluid, from Ref. [18]. Left panel: specific volume behavior as a function of the pressure, along the isotherm $T = 1500K$. A phase transition can be recognized in correspondence of the discontinuity at $P = 125GPa$. Right panel: comparison between the electronic density of states above and below the transition. A nonzero density of states at the Fermi level (corresponding in the figure to energy zero) indicates a conducting phase.

intrinsic effect of the linear mixing model, which assumes that at the transition the system is made of two (or more) separate components in contact.

Conversely, first-principle simulations, based either on DFT or on Quantum Monte Carlo techniques, may be capable of clarifying essential aspects of the metal-insulator transition. However, the first-principle schemes can be very sensitive to the necessary approximations lying behind them and, as a consequence, there has been in the past no uniformity in the predictions obtained with different techniques about the nature of the metallic transition. Earlier Car-Parrinello simulations of S. Scandolo [18] indicate the presence of a first order transition, from an insulating liquid phase at low pressure to a conducting liquid phase at high pressure. In this work, a series of constant pressure simulations of systems of 448 classical protons and 448 electrons were carried on. A liquid-liquid transition was first recognized as a jump in the specific volume curve in pressure, along the isotherm at $T = 1500K$ at a pressure of about $125GPa$, as showed in the left panel of Figure 1.7. While at lower pressure the electronic density of states is zero in correspondence of the Fermi level, indicating an insulator phase, at higher pressure also states around the Fermi level are occupied and hence the system is conducting (see Figure 1.7). A first order transition point was also found by Bonev et al. [12] at $200GPa$ and $\approx 950K$, again with Car-Parrinello MD.

Later studies with Born Oppenheimer Molecular Dynamics (BOMD) [42, 43], however, seemed to disprove those results: instead of a sharp transition, a continuous passage from an insulating to a partially dissociated conducting phase was found. Similar results were also obtained in early Quantum Monte Carlo simulations [44], using the Coupled Electron Ion Monte Carlo (CEIMC) method. More recently, an accurate BOMD analysis of the transition [45], differing from the previous only for the use of larger simulation cells (256 atoms vs. the 64 and 128 employed in [43] and [42], respectively) leads to results compatible with a first order transition, showing that the previous BOMD results were essentially driven by finite size effects.

A very recent work [19] tried to explain those discrepancies by comparing both

CEIMC and BOMD simulation results in the density range in which the metallization occurs, finding a good qualitative agreement between the different methods. In both cases, analyzing the pressure behavior as a function of the density along different isotherms, a plateau (i.e. a discontinuity in the compressibility) has been detected. In correspondence of the transition, a sharp increase of the static electrical conductivity $\sigma(\omega = 0)$ has been noticed. Those results were hence interpreted as the index of a first-order insulator to metal transition.

As showed in Figure 1.1 (blue lines), the two methods are comparable only qualitatively. The blue curves represent the two different predictions for the metallic transition: BOMD data are represented with upper triangles, CEIMC data with squares. The curves are fairly parallel and both ends with a critical point at $T \approx 2000K$, but the pressure at the transition is noticeably lower for the BOMC data with respect to the CEIMC ones. This difference can be explained as an effect of the DFT underestimate of the electronic gap, which favors the delocalized electronic states, shifting to lower pressures the metallization transition.

Finally we can notice that, according to the CEIMC results illustrated in Figure 1.1, the metallization curve might cross the molecular melting line in a triple point at a pressure of about $290GPa$ and a temperature of $\sim 550K$, while the position of the triple point is at $P \sim 220GPa$ and $T \sim 700K$ for the BOMD data [19]. This predictions however do not account for quantum effects on protons that, at dissociation, may be relevant.

1.2.4 The atomic regime

The atomic region of the phase diagram is still unaccessible to experiments, in particular in the low temperature regime. As a consequence, our present knowledge of the hydrogen phase diagram in the atomic region is mainly limited to the computational data.

While at high temperature the liquid-liquid transition from the molecular and insulating to the atomic and conducting phase has been observed, together with a partial dissociation of molecules, in the solid phase the metallization and the dissociation lines are still not traced. Different estimates of the zero temperature metallization pressure have been proposed, moving the transition at always higher pressures as the accuracy of the calculations was improved. Moreover, it is still not clear whether in the solid phase the metallization is accompanied or not by the transition to the monoatomic phase. It follows that our knowledge on the behavior of atomic hydrogen is far from satisfactory.

The main problem encountered in the numerical studies of the atomic solid hydrogen relies on the individuation of stable crystal structures, since no experimental indications are available. Let us briefly review some of the most significant computational results on the zero temperature behavior. In an early ground state QMC study of different molecular and atomic crystals, including protonic zero point motion, Ceperley and Alder [47] locate a transition from a molecular FCC phase to a BCC atomic phase at $P \sim 300GPa$. A successive work of Barbee [48], based on DFT calculations, locates the metallization pressure in the solid phase at $P \sim 380GPa$, and for the atomic structure found the most stable crystal to be the HCP, not considered by Ceperley and Alder. In 1993, Natoli and Ceperley [49], found instead a lower molecular-to-atomic transition pressure, at $P \sim 230 GPa$, and a diamond-like atomic crystalline structure. A more recent and accurate work of Stadele and Martin [50], using Exact Exchange [5] DFT calculations and studying a set of molecular solid structures, moved the metallization pressures up to $\gtrsim 400 GPa$, suggesting that the molecular phase can be stable up to these pressures. However, it cannot be excluded that monoatomic structures not energetically favored at $T = 0K$ might gain stability at higher temperature.

Since the solid structure is still undetermined, it is not immediate to trace a melting line in the atomic region near the molecular dissociation. Only very recently the Ab Initio Random Structure Search (AIRSS) of Pickard and Needs [28, 29] has been applied to atomic hydrogen by McMahon and Ceperley [52]. They have found that in the range of pressures $P \in [500, 2500] GPa$ the most stable lattice for classical protons is a structure belonging to the $I4_1/amd$ symmetry group. With the addition of the zero point energies of protons, the $I4_1/amd$ structure remains the one of lowest enthalpy up to $\sim 650 GPa$, while at higher pressure a new structure, belonging to the $R3m$ space group, gains stability.

In the very high density regime, the hydrogen becomes a fully ionized plasma, that can be satisfactorily described introducing an equivalent effective model of pseudo-ions interacting through a Screened Coulomb potential [53]. In this limit BCC phase has been found to be the most stable among several simple structures by *ab initio* calculations and the atomic melting from the BCC crystal and the fluid phase has been studied both with Car-Parrinello MD [53, 54], assuming classical protons, and with Quantum Monte Carlo techniques and quantum protons[55].

1.2.5 Different scenarios

The available data on the high pressure hydrogen phases allow to depict a phase diagram of unexpected richness but are not sufficient to answer the most important questions related to the metallization transition. Different scenarios remain hence open.

The simplest situation is that, at high enough pressures, the molecular solids become atomic and, as a consequence of the molecular dissociation, also metallic, as suggested by Wigner and Hungtington [6]. Another possibility is that the transition to the atomic metallic solid occurs through the passage to an intermediate molecular conducting solid phase, due to band overlap [56].

The presence of a reentrant melting line and the slope of the PPT line (see again Figure 1.1) seem to support a third hypothesis, suggesting the existence of a low

---

[5] In the DFT, given the ground state density ρ, the electronic ground state energy is computed by solving self-consistently the Kohn-Sham equations for the single particle orbitals: $[-\nabla^2/2 + v_{\text{eff}}]\phi_i = \varepsilon_i \phi_i$ where the effective potential is given by $v_{\text{eff}} = v_{\text{ext}} + \int d\mathbf{r}' \rho(\mathbf{r}')/|\mathbf{r} - \mathbf{r}'| + \delta_\rho E_{xc}[\rho]$, being $E_{xc}[\rho]$ the unknown exchange-correlation functional. Usually, approximate expressions of the exchange and correlation energy are employed, the most common being the Local Density (LDA) and the Generalized Gradient (GGA) Approximations. In the Exact Exchange DFT (EXX) the exchange contributions $E_x[\rho]$ are computed exactly within the Hartree-Fock theory. The correlation energy $E_c[\rho]$ is then the only part that requires to be approximated. As a result EXX method reveals more accurate than LDA or GGA DFT, providing as an example very accurate band gap of various semiconductors. On the other hand, the calculation of $E_x[\rho]$ is quite demanding, as a consequence EXX calculations are noticeably slower than more standard DFT calculations. For a more detailed explanation of the method see for example Ref. [51]

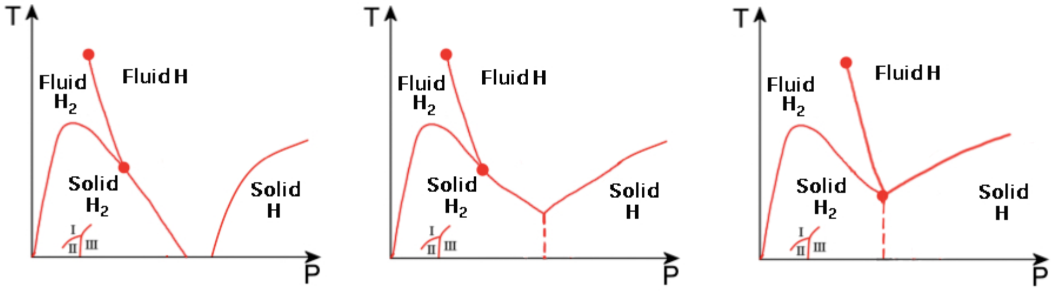

Figure 1.8. Sketch of three possible scenarios for the high pressure phase diagram near the metallization transition. The three possibilities are discussed in the text.

temperature metallic fluid separating the molecular insulating solid, at low pressures, from the atomic and conducting solids, at high pressure, possibility first proposed by N. W. Ashcroft [57, 58]. This phase can be stabilized with respect to the solid phases by the protonic zero point motion. A phase diagram accounting of this last possibility is sketched in the left panel of Figure 1.8. Moreover, according to the Aschroft predictions, this low temperature fluid may also present superconducting characteristics [59] or behave as a new kind of quantum liquid, both metallic and superfluid [60].

It is important to emphasize that the PPT and the molecular melting lines in Figure 1.1 do not take into account quantum effects on protons, that can have a significant effect on the transitions.

The middle panel of Figure 1.8 illustrated the phase diagram in the case in which the metallization transition at low temperature directly takes place in the solid. These two are not the only possible representation of the hydrogen phase diagram compatible with our present knowledge. A third possibility can be that the four transition lines (the molecular and the atomic melting, the metallization in the liquid phase and in the solid) mets in a quadruple point, represented in the right panel of Figure 1.8. This possibility is not in contrast with the Gibbs phases rule, because of the presence of two species in coexistence.

In this picture we have not yet considered the phase I-phase III coexisting line that could possibly reach the melting line at higher temperature, or the possibility of structural transitions also in the solid atomic region. Many possibilities are hence still open and, in absence of experimental data, the *ab initio* numerical simulation represents the unique tool to complete the reconstruction of the high pressure hydrogen phase diagram.

1.3 Present study

The work of this thesis is devoted to the extension of the present knowledge on the high pressure phase diagram, by means of Monte Carlo simulations.

Part of the work was focused on the determination of the melting line of atomic hydrogen at ultra high pressures ($P \gtrsim 20TPa$), where the interactions among protons can be well represented by an effective Screened Coulomb pair potential, obtained from the linear response theory. Adopting this form of pair potential it is possible to reduce the original system to a one-component system that mimic satisfactorily the hydrogen behavior [54]. For this model, we considered quantum protons and computed the melting line for all three hydrogen isotopes. Our results are presented in Chapter 3.

We employed the *ab initio* Coupled Electron-Ion Monte Carlo method to investigate the atomic region at pressures above $P \sim 350GPa$. This region of the phase diagram is slightly above the experimental accessibility. We then started by determining possible crystalline structures for the atomic hydrogen and then built the solid and liquid free energy to determine the melting transition. Results are discussed in Chapter 4.

Finally, in Chapter 5, we present our results on the liquid-liquid transition. To recognize the transition, we analyzed the behavior of the pressure with the density along the isotherm $T = 600K$. The fingerprint of a first order transition is the presence region of constant pressure along the isotherm. We also compare the results obtained computing the Born-Oppenheimer electronic energies with Quantum Monte Carlo methods at two levels of approximation.

Before discussing the results, in the next chapter we will illustrate the theoretical basis of the simulation methods we have employed.

Chapter 2

Theoretical and numerical approaches

2.1 Introduction

Ab initio simulation techniques are an essential tool to predict the properties of matter in the regions of the phase diagram unaccessible to experiments as well as to give an interpretation of experimental results when available. Different approaches have been developed in the years to simulate many-body systems, whose demand of computational resources increases with the complexity of the system and the accuracy achieved by the method.

In the framework of the Born-Oppenheimer approximation [61], we can distinguish between two different approaches used in first principles techniques to obtain the electronic energy surface, for fixed nuclei: electronic structure methods, as the Hartree Fock method or the Density Functional Theory (DFT), or Quantum Monte Carlo (QMC) techniques. Those methods for the electronic ground state can then be coupled to a Molecular Dynamics evolution of the nuclear coordinates or to a Monte Carlo sampling of the protonic configurational space.

The Coupled Electron Ion Monte Carlo (CEIMC) technique [62], that we adopted to perform most of the calculations presented in this thesis, uses Monte Carlo (MC) techniques both to obtain the (ground state) energy of electrons and to sample the protonic configurational space. The advantage of the CEIMC method with respect to first principle methods based on DFT is that the latter can suffer of the DFT limitations, such as the gap underestimation. This can lead to problems especially near the metallization transition. At variance, the CEIMC method is expected to be accurate over the entire phase diagram.

In this chapter we will provide the theoretical background necessary to understand this method.

In this chapter we will review the Born-Oppenheimer approximation, that lies behind the CEIMC - as well as behind other *ab initio* methods. Then we will introduce the Metropolis Monte Carlo technique [63], adopted in its classical version to sample the configurational space of classical protons, and the Path Integral Monte Carlo [64] method, applied in our case to quantum distinguishable protons. Two zero temperature Quantum Monte Carlo techniques are illustrated: the Variational

Monte Carlo [65], based on the variational principle, and the Reptation Quantum Monte Carlo [66], belonging to the cathegory of the Projection MC methods, in which a suitable evolution operator is applied to a trial wave function to suppress its excited state components. Together with the principal characteristics of those methods, the chapter will also present a description of the trial wave functions [67] used in Quantum Monte Carlo for hydrogen and of a strategy to take into account the fermion statistics [68]. Finally, in the last section of the chapter we will describe how those methodologies are merged together in the CEIMC technique.

2.2 The Born-Oppenheimer approximation

The non relativistic Hamiltonian of a system of N_p ions (protons, in the case of the hydrogen) and N_e electrons is given by

$$\hat{\mathcal{H}} = \hat{\mathcal{K}}_p + \hat{\mathcal{K}}_e + \hat{\mathcal{V}}_{pp} + \hat{\mathcal{V}}_{ep} + \hat{\mathcal{V}}_{ee} \tag{2.1}$$

where with $\hat{\mathcal{K}}$ we indicate the kinetic operators and with $\hat{\mathcal{V}}$ the potential terms. In the coordinates representation the previous expression becomes

$$\begin{aligned} \hat{\mathcal{H}}(\mathbf{R},\mathbf{r}) &= -\frac{\hbar^2}{2m_p}\sum_{I=1}^{N_p}\nabla^2_{\mathbf{R}_I} - \frac{\hbar^2}{2m_e}\sum_{i=1}^{N_e}\nabla^2_{\mathbf{r}_i} + z^2e^2\sum_{I=1}^{N_p}\sum_{J>i}^{N_p}\frac{1}{|R_I - R_J|} \\ &- ze^2\sum_{I=1}^{N_p}\sum_{i=1}^{N_e}\frac{1}{|R_I - r_i|} + e^2\sum_{i=1}^{N_e}\sum_{j>i}^{N_e}\frac{1}{|r_i - r_j|} \end{aligned} \tag{2.2}$$

where $\mathbf{R} = \{\mathbf{R}_1 \cdots \mathbf{R}_{N_p}\}$ and $\mathbf{r} = \{\mathbf{r}_1 \cdots \mathbf{r}_{N_e}\}$ are the ionic and the electronic coordinates, respectively; z is the ionic charge, in units of e (z=1 for protons); m_p and m_e are the ionic and the electronic masses, respectively.

The quantum state of the system can be obtained by solving the Scrödinger equation associated to the Hamiltonian (2.2)

$$\hat{\mathcal{H}}(\mathbf{R},\mathbf{r})\psi_l(\mathbf{R},\mathbf{r}) = E_l\psi_l(\mathbf{R},\mathbf{r}) \tag{2.3}$$

or, in the time dependent formulation,

$$i\hbar\frac{\partial}{\partial t}\psi_l(\mathbf{R},\mathbf{r}) = \hat{\mathcal{H}}(\mathbf{R},\mathbf{r})\psi_l(\mathbf{R},\mathbf{r}) \tag{2.4}$$

However, for a realistic system with many degrees of freedom and for a general form of the interaction potentials, this task is impossible to accomplish without introducing approximations.

The full problem starts simplifying thanks to the Born-Oppenheimer (BO) assumption [61], that allows to split the original problem in two parts: the determination of the electronic state for fixed protons and the evolution of the protonic degrees of freedom in the field due to the electrons. The underlying adiabatic hypothesis is that, since the electronic mass is nearly two thousand times smaller than the protonic one, the average kinetic energy of electrons is much higher than that of protons and thus we can assume that the relaxation of the electrons is almost instantaneous with respect to the proton motion. This implies, as we will see, that the coupling between different electronic states can be neglected.

Let us develop the total wave function in the basis set of electronic eigenfunctions $\Psi_n(\mathbf{r}|\mathbf{R})$ at fixed protonic positions

$$\psi_l(\mathbf{r},\mathbf{R}) = \sum_n \chi_{nl}(\mathbf{R})\Psi_n(\mathbf{r}|\mathbf{R}) \tag{2.5}$$

in which the coefficients $\chi_{nl} = \langle \Psi_n \, | \psi_l \rangle$ depend on the ionic coordinates alone and $\Psi_n(\mathbf{r}|\mathbf{R})$ satisfy, for any fixed protonic configuration $\mathbf{R}$, the electronic equation

$$\hat{\mathcal{H}}_e(\mathbf{r}|\mathbf{R})\Psi_n(\mathbf{r}|\mathbf{R}) = \left[\hat{\mathcal{K}}_e + \hat{\mathcal{V}}_{pp} + \hat{\mathcal{V}}_{ep} + \hat{\mathcal{V}}_{ee}\right] \Psi_n(\mathbf{r}|\mathbf{R}) = \mathcal{E}_n(\mathbf{R})\Psi_n(\mathbf{r}|\mathbf{R}) \tag{2.6}$$

where with the notation $f(\mathbf{r}|\mathbf{R})$ we indicate a dependency on the electronic coordinates $\mathbf{r}$ as variables and on the protonic coordinates $\mathbf{R}$ as parameters, and where we have introduced the electronic Hamiltonian $\hat{\mathcal{H}}_e = \hat{\mathcal{K}}_e + \hat{\mathcal{V}}_{pp} + \hat{\mathcal{V}}_{ep} + \hat{\mathcal{V}}_{ee}$, containing all the potential terms of the total Hamiltonian (2.1) and the electronic kinetic operator $\hat{\mathcal{K}}_e$ only.

Inserting into (2.3) the expression (2.5) for the total wave function $\psi_l(\mathbf{r},\mathbf{R})$, the time-independent Scrödinger equation becomes

$$\hat{\mathcal{K}}_p(\mathbf{R})\sum_n \chi_{ln}(\mathbf{R})\Psi_n(\mathbf{r}|\mathbf{R}) + \hat{\mathcal{H}}_e(\mathbf{r}|\mathbf{R})\sum_n \chi_{ln}(\mathbf{R})\Psi_n(\mathbf{r}|\mathbf{R}) = E_l\sum_n \chi_{ln}(\mathbf{R})\Psi_n(\mathbf{r}|\mathbf{R}) \tag{2.7}$$

The electronic Hamiltonian, being a purely multiplicative operator in the protonic coordinates, operates only on the electronic wave functions and not on the coefficients $\chi_{ln}(\mathbf{R})$. As a consequence, using (2.6), we can rewrite

$$\hat{\mathcal{H}}_e(\mathbf{r}|\mathbf{R})\sum_n \chi_{ln}(\mathbf{R})\Psi_n(\mathbf{r}|\mathbf{R}) = \sum_n \mathcal{E}_n(\mathbf{R})\chi_{ln}(\mathbf{R})\Psi_n(\mathbf{r}|\mathbf{R}) \tag{2.8}$$

The ionic kinetic operator, instead, acts on both $\chi_{ln}(\mathbf{R})$ and $\Psi_n(\mathbf{r}|\mathbf{R})$, leading to three contributions

$$\begin{aligned}\hat{\mathcal{K}}_p\sum_n \chi_{ln}(\mathbf{R})\Psi_n(\mathbf{r}|\mathbf{R}) = & - \frac{\hbar^2}{2m_p}\sum_n \left(\nabla^2_{\mathbf{R}}\chi_{ln}(\mathbf{R})\right)\Psi_n(\mathbf{r}|\mathbf{R}) \\ & - \frac{\hbar^2}{m_p}\sum_n \left(\nabla_{\mathbf{R}}\chi_{ln}(\mathbf{R})\right)\left(\nabla_{\mathbf{R}}\Psi_n(\mathbf{r}|\mathbf{R})\right) \\ & - \frac{\hbar^2}{2m_p}\sum_n \chi_{ln}(\mathbf{R})\left(\nabla^2_{\mathbf{R}}\Psi_n(\mathbf{R}|\mathbf{r})\right)\end{aligned} \tag{2.9}$$

being $\nabla^2_{\mathbf{R}} = \sum_{I=1}^{N_p}\nabla^2_{\mathbf{R}_I}$.

Substituting (2.8) and (2.9) into (2.7), multiplying on the left by $\Psi^*_m(\mathbf{r}|\mathbf{R})$ and integrating over the electronic degrees of freedom $\mathbf{r}$, we obtain

$$\begin{aligned}[\hat{\mathcal{K}}_p(\mathbf{R}) + \mathcal{E}_m(\mathbf{R}) - E_l]\chi_{lm}(\mathbf{R}) = & \frac{\hbar^2}{2m_p}\sum_n \langle\Psi_m(\mathbf{R})|\,\nabla_{\mathbf{R}}\,|\Psi_n(\mathbf{R})\rangle\,\nabla_{\mathbf{R}}\chi_{ln}(\mathbf{R}) \\ & + \frac{\hbar^2}{m_p}\sum_n \langle\Psi_m(\mathbf{R})|\,\nabla^2_{\mathbf{R}}\,|\Psi_n(\mathbf{R})\rangle\,\chi_{ln}(\mathbf{R})\end{aligned} \tag{2.10}$$

which represents a set of coupled equations for the nuclear coefficients $\chi_{ln}(\mathbf{R})$.

The Born-Oppenheimer approximation relies on neglecting the terms on the right hand side of the previous equation. This leads to decouple the equations relative to the different electronic states. In fact, we can first make the assumption that the ionic motion does not change the electronic eigenstate: the contribution of the off diagonal elements of the operators $\nabla_{\mathbf{R}}$ and $\nabla^2_{\mathbf{R}}$ may be then neglected. As for the diagonal contributions, we can consider negligible the effect of the operators $\nabla_{\mathbf{R}}$ and $\nabla^2_{\mathbf{R}}$ on the electronic wave functions. In particular, terms such as $\langle\Psi_m(\mathbf{R})|\,\nabla_{\mathbf{R}}\,|\Psi_m(\mathbf{R})\rangle$, are exactly zero being parametric derivatives of the norm of a normalized real function

$$\begin{aligned} 0 &= \nabla_{\mathbf{R}}\int d\mathbf{r}\Psi^*_m(\mathbf{r}|\mathbf{R})\Psi_m(\mathbf{r}|\mathbf{R}) = \int d\mathbf{r}\Psi^*_m(\mathbf{r}|\mathbf{R})\nabla_{\mathbf{R}}\Psi_m(\mathbf{r}|\mathbf{R}) \\ &+ \int d\mathbf{r}\Psi_m(\mathbf{r}|\mathbf{R})\nabla_{\mathbf{R}}\Psi^*_m(\mathbf{r}|\mathbf{R}) = 2\int d\mathbf{r}\Psi^*_m(\mathbf{r}|\mathbf{R})\nabla_{\mathbf{R}}\Psi_m(\mathbf{r}|\mathbf{R}) \end{aligned} \tag{2.11}$$

where the last equality holds since for real functions $\Psi_m(\mathbf{r}|\mathbf{R})\nabla_{\mathbf{R}}\Psi^*_m(\mathbf{r}|\mathbf{R}) = (\Psi_m(\mathbf{r}|\mathbf{R})\nabla_{\mathbf{R}}\Psi^*_m(\mathbf{r}|\mathbf{R}))^* = \Psi^*_m(\mathbf{r}|\mathbf{R})\nabla_{\mathbf{R}}\Psi_m(\mathbf{r}|\mathbf{R})$.

Neglecting the gradient and the Laplacian of the electronic wave functions with respect to the nuclear degrees of freedom leads to the following equation for the $\chi_{ln}(\mathbf{R})$

$$[\hat{\mathcal{K}}_p(\mathbf{R}) + \mathcal{E}_n(\mathbf{R})]\chi_{ln}(\mathbf{R}) = E_l\chi_{ln}(\mathbf{R}) \tag{2.12}$$

in which the electronic energy $\mathcal{E}_n(\mathbf{R})$ plays the role of an effective potential for the ions. Defining $\hat{\mathcal{H}}_p = \hat{\mathcal{K}}_p(\mathbf{R}) + \mathcal{E}_n(\mathbf{R})$, we can finally write two separate Schrödinger-like equations for the ionic and the electronic parts of the total wave function

$$\begin{aligned} \hat{\mathcal{H}}_e(\mathbf{r}|\mathbf{R})\Psi_n(\mathbf{r}|\mathbf{R}) &= \mathcal{E}_n(\mathbf{R})\Psi_n(\mathbf{r}|\mathbf{R}) & (2.13)\\ \hat{\mathcal{H}}_p(\mathbf{R})\chi_{ln}(\mathbf{R}) &= E_l\chi_{ln}(\mathbf{R}) & (2.14) \end{aligned}$$

To complete the description of Born-Oppenheimer approximation, we now write the partition function of the total system of electrons and protons. Assuming that the electrons can only be in a given electronic state (i.e. the ground state Ψ_0) and that protons are at thermal equilibrium with a reservoir at temperature $T = (K_B\beta)^{-1}$, working in the coordinate representation for the protons we have

$$\begin{aligned} \mathcal{Z} = Tr\{e^{-\beta\hat{\mathcal{H}}}\} &= \int d\mathbf{R}\,\langle\mathbf{R}|\,\langle\Psi_0|\,e^{-\beta\hat{\mathcal{H}}}\,|\Psi_0\rangle\,|\mathbf{R}\rangle \\ &= \sum_{m=0}^{\infty}\frac{(-\beta)^m}{m!}\int d\mathbf{R}\,\langle\mathbf{R}|\,\langle\Psi_0|\,(\hat{\mathcal{K}}_p + \hat{\mathcal{H}}_e)^m\,|\Psi_0\rangle\,|\mathbf{R}\rangle \\ &= 1 + \sum_{m=1}^{\infty}\frac{(-\beta)^m}{m!}\int d\mathbf{R}\,\langle\mathbf{R}|\,\langle\Psi_0|\,(\hat{\mathcal{K}}_p + \hat{\mathcal{H}}_e)^m\,|\Psi_0\rangle\,|\mathbf{R}\rangle \end{aligned} \tag{2.15}$$

where we have expanded in power series the exponential operator.

Let us write now the m-th term of the series, for a generic $m > 1$, as

$$\begin{aligned} \mathcal{Z}_m &= \int d\mathbf{R}\,\langle\mathbf{R}|\,\langle\Psi_0|\,(\hat{\mathcal{K}}_p + \hat{\mathcal{H}}_e)^m\,|\Psi_0\rangle\,|\mathbf{R}\rangle \\ &= \int d\mathbf{R}\sum_k\langle\mathbf{R}|\,\langle\Psi_0|\,(\hat{\mathcal{K}}_p + \hat{\mathcal{H}}_e)^{m-1}\,|\Psi_k\rangle\,\langle\Psi_k|\,(\hat{\mathcal{K}}_p + \hat{\mathcal{H}}_e)\,|\Psi_0\rangle\,|\mathbf{R}\rangle \end{aligned} \tag{2.16}$$

In the last line, we have introduced the identity in the electronic space, $\sum_k |\Psi_k\rangle \langle\Psi_k|$, to obtain two distinct matrix elements.

Introducing the operator $\mathcal{E}_0(\hat{\mathbf{R}})$, resulting from the application of the electronic Hamiltonian $\hat{\mathcal{H}}_e$ to the electronic ground state wave function, the matrix element $\langle\Psi_k| (\hat{\mathcal{K}}_p + \hat{\mathcal{H}}_e) |\Psi_n\rangle$ in the Born-Oppenheimer approximation becomes

$$\langle\Psi_k| (\hat{\mathcal{K}}_p + \hat{\mathcal{H}}_e) |\Psi_0\rangle = \langle\Psi_k|\ \Psi_0\rangle (\hat{\mathcal{K}}_p + \mathcal{E}_0(\hat{\mathbf{R}})) = \delta_{k0}(\hat{\mathcal{K}}_p + \mathcal{E}_0(\hat{\mathbf{R}})) \tag{2.17}$$

since in this approximation the electronic wave function is transparent to the protonic kinetic operator. Eliminating the k sum thanks to the presence of δ function, we obtain

$$\mathcal{Z}_m \quad = \quad \int d\mathbf{R}\, \langle\mathbf{R}|\, \langle\Psi_0| (\hat{\mathcal{K}}_p + \hat{\mathcal{H}}_e)^{m-1} |\Psi_0\rangle (\hat{\mathcal{K}}_p + \mathcal{E}_0(\hat{\mathbf{R}})) |\mathbf{R}\rangle \tag{2.18}$$

Repeating this procedure m times, each one lowering by one the exponent and inserting an electronic-space identity to obtain the matrix element (2.17) which we can compute straightforwardly within the BO approximation, we finally eliminate the electronic degrees of freedom, arriving at

$$\mathcal{Z}_m \quad = \quad \int d\mathbf{R}\, \langle\mathbf{R}| (\hat{\mathcal{K}}_p + \mathcal{E}_0(\hat{\mathbf{R}}))^m |\mathbf{R}\rangle \tag{2.19}$$

The substitution of (2.19) into (2.15) leads to the following expression for the total partition function

$$\mathcal{Z} = \sum_{m=0}^{\infty} \frac{(-\beta)^m}{m!} \int d\mathbf{R}\, \langle\mathbf{R}| (\hat{\mathcal{K}}_p + \mathcal{E}_0(\mathbf{R}))^m |\mathbf{R}\rangle = Tr\left\{e^{-\beta(\hat{\mathcal{K}}_p + \mathcal{E}_0(\hat{\mathbf{R}}))}\right\} \tag{2.20}$$

which is equivalent to the partition function of a system of protons interacting through a local many body potential $\mathcal{E}_0(\hat{\mathbf{R}})$.

In conclusion, within the BO approximation, the determination of the electronic state in the external potential provided by the nuclear arrangement and of the nuclear state given the Born-Oppenheimer electronic energy surface are two distinct, well defined problems, that we can handle using different techniques. The electronic ground state can be determined through computer simulations using, for example, the Density Functional Theory (DFT) or a Quantum Monte Carlo (QMC) scheme. Moreover, in many situations the nuclear coordinates can be considered as classical degrees of freedom: classical Molecular Dynamics (MD) or Monte Carlo (MC) simulations are used in this case. Otherwise, the Path Integral Monte Carlo (PIMC) scheme allows to determine the state of quantum particles at finite temperature T.

2.3 Generalities on the Monte Carlo method

Statistical mechanics relates thermodynamic properties of the system to statistical averages of microscopic observables over the equilibrium ensembles. For classical particles we have

$$\langle\mathcal{O}(\mathbf{\Gamma})\rangle = \frac{\int d\mathbf{\Gamma} f(\mathbf{\Gamma})\mathcal{O}(\mathbf{\Gamma})}{\int d\mathbf{\Gamma} f(\mathbf{\Gamma})} \tag{2.21}$$

where $\mathcal{O}(\mathbf{\Gamma})$ is a general phase space function depending on the particles coordinates $\mathbf{R}$ and momenta $\mathbf{P}$, $\mathbf{\Gamma} = (\mathbf{P}, \mathbf{R})$, $d\mathbf{\Gamma}$ is the volume element of the phase space and $f(\mathbf{\Gamma})$ is the equilibrium distribution corresponding to the external constraints under consideration. At equilibrium it is usually possible to separate the dependence on the momenta from the dependence on the spatial coordinates in the equilibrium distribution function: $f(\mathbf{\Gamma}) = g(\mathbf{P})\rho(\mathbf{R})$. Correspondently the total average $\langle \mathcal{O}(\mathbf{\Gamma}) \rangle$ can be split into an "ideal" contribution (due to the $\mathbf{P}$ dependence) and an "excess" part. The ideal contribution can be generally computed analytically, while the calculation of the excess part

$$\langle \mathcal{O}(\mathbf{R}) \rangle = \frac{\int_{\Omega^N} d\mathbf{R} \rho(\mathbf{R}) \mathcal{O}(\mathbf{R})}{\int_{\Omega^N} d\mathbf{R} \rho(\mathbf{R})} = I \tag{2.22}$$

(where Ω^N represents the volume in the configurational space) requires the use of numerical integration techniques. The conventional grid methods to estimate integrals have a computational cost increasing exponentially with the system dimension: just think that the number M_g of points on a uniform grid in a d dimensional space grows as a power of the phase space dimensionality dN, being N the number of particles.

A Monte Carlo method allows to evaluate multidimensional integrals by sampling stochastically points of the phase space, according to a given probability density $\pi(\mathbf{R})$, and then averaging $\mathcal{O}(\mathbf{R})$ over the sampled points. The advantage of this choice of the integration points is that in a Monte Carlo evaluation the error is independent of the space dimensionality and proportional to the inverse of the square root of the number M of sampled points [69]. The independence of the error from the dimension of the space makes the Monte Carlo techniques very powerful in computing multidimensional integrals.

In addition, the use of a probability $\pi(\mathbf{R})$ that reflects the distribution of points in the phase space allows to concentrate the computational efforts in the more significative regions, avoiding that large amounts of computer time are spent in evaluating insignificant contributions to the integral. The sampling of points according to the expected probability distribution $\pi(\mathbf{R})$ is called importance sampling and the $\pi(\mathbf{R})$ in this context is called the importance function [70].

To use a Monte Carlo scheme, let us rewrite the integral (2.22) in the more suitable form

$$I = \int_{\Omega^N} d\mathbf{R} \pi(\mathbf{R}) \mathcal{O}(\mathbf{R}) \tag{2.23}$$

where we have defined $\pi(\mathbf{R}) = \rho(\mathbf{R}) / \int_{\Omega^N} d\mathbf{R} \rho(\mathbf{R})$. Since $\pi(\mathbf{R})$ is normalized by definition, if it is also non negative everywhere in the configurational space,

$$\pi(\mathbf{R}) \geq 0 \ \forall \mathbf{R} \in \Omega^N \tag{2.24}$$

it can be interpreted as a probability density. Condition (2.24) is always satisfied by the equilibrium ensemble of classical systems or finite temperature systems of quantum distinguishable particles.

The Monte Carlo estimate of I is obtained by averaging over a finite number M of points distributed according to $\pi(\mathbf{R})$

$$I \approx \frac{1}{M} \sum_{i=1}^{M} \mathcal{O}(\mathbf{R}_i) = I_M \tag{2.25}$$

The error of this estimate, for statistically independent points $\mathbf{R}_i$, can be determined as $\varepsilon = \sigma/\sqrt{M}$, where σ is the variance of the observable $\mathcal{O}$ which can be estimated as

$$\sigma^2 \approx s^2 = \frac{1}{M-1}\sum_{i=1}^{M}\left[\mathcal{O}(\mathbf{R}_i) - I_M\right]^2 \tag{2.26}$$

As anticipated, the estimate of ε depends on the number of points M, but not on the space dimensionality.

The differences among the various Monte Carlo methods relies on the way to generate the points $\mathbf{R}_i$, as we will see in the following sections.

2.3.1 Markov chains and Metropolis MC

The main issue of the MC integral evaluation resides in the rules used to determine the points on which the properties are computed, in order to have them distributed according to the probability π; in other words, in the sampling of the space.

In the Metropolis scheme, starting from a suitable initial point $\mathbf{R}_0$ a sequence of configurations $\{\mathbf{R}_1, \mathbf{R}_2, \cdots, \mathbf{R}_n\}$, such that each point depends only on the previous one, is build. A chain of random events satisfying this property is called a Markov chain. Before we proceed in the description of the basic properties of the Markov chains needed to build a MC algorithm, let us assume the original configuration space to be divided in a number of identical small cells filling the entire volume Ω, each one labelled with the (discrete) index $\mathbf{R}$, in order to work with finite probabilities of occurrence of the state $\mathbf{R}$. Moreover, we can associate a fictitious time t_i to the each point i of the chain, such that $t_i = i\Delta t$. Since no physical time is connected to the t_i, we can assign to Δt an arbitrary positive value.

For a chain of uncorrelated events the probability $\Pi(\mathbf{R}_1, \mathbf{R}_2, \cdots, \mathbf{R}_n)$ of realizing a given ordered sequence $(\mathbf{R}_1, \mathbf{R}_2, \cdots, \mathbf{R}_n)$ is simply the product of the probabilities $\pi(\mathbf{R})$ of each individual state $\mathbf{R}$, $\Pi(\mathbf{R}_1, \mathbf{R}_2, \cdots, \mathbf{R}_n) = \Pi_{i=1}^{n}\pi(\mathbf{R}_i)$. In the opposite case of a fully correlated chain, each event is conditioned by all the previous and the probability $\Pi(\mathbf{R}_1, \mathbf{R}_2, \cdots, \mathbf{R}_n)$ has a more complicated expression. A Markov chain is the simplest example of a sequence of non independent events, in which each event is related only to the event that has come immediately before. In order to describe a Markov chain, it is necessary to introduce the conditional probability $A(\mathbf{R}'|\mathbf{R})$ for the system to be in the state $\mathbf{R}'$, given that it has been in the state $\mathbf{R}$ at the previous time. The probabilities $A(\mathbf{R}'|\mathbf{R})$ can be also interpreted as transition probabilities $A(\mathbf{R}'|\mathbf{R}) = A(\mathbf{R} \to \mathbf{R}')$ to go from the point $\mathbf{R}$ to $\mathbf{R}'$ in one step and, because of that, they must be normalized

$$\sum_{\mathbf{R}'} A(\mathbf{R} \to \mathbf{R}') = 1 \tag{2.27}$$

Since in a Markov process each event depends only on the previous, the transition probabilities are the only additional quantities we need to know in order to specify its stochastic evolution. The occurrence probability $\Pi(\mathbf{R}_1, \mathbf{R}_2, \cdots, \mathbf{R}_n)$ for a Markov chain of n ordered events $(\mathbf{R}_1, \mathbf{R}_2, \cdots, \mathbf{R}_n)$ is then

$$\Pi(\mathbf{R}_1, \mathbf{R}_2, \cdots, \mathbf{R}_n) = \pi(\mathbf{R}_1)A(\mathbf{R}_1 \to \mathbf{R}_2)A(\mathbf{R}_2 \to \mathbf{R}_3)\cdots A(\mathbf{R}_{n-1} \to \mathbf{R}_n) \tag{2.28}$$

The fundamental properties of the Markov chains exploited in the Monte Carlo methods are: a) the stationarity of the probability distribution of the points in the chain, reached after a large enough number of steps and b) the fact that the limiting distribution of the chain is independent of the initial distribution of events. We will see in this section under which conditions the Markov chain becomes stationary and how it is possible to build a Markov chain of the desired limiting probability distribution.

Let us start defining the time dependent probability density $\tilde{\pi}(\mathbf{R}, i)$, representing the probability of occurrence of the state $\mathbf{R}$ at the time i. It holds

$$\begin{aligned} \tilde{\pi}(\mathbf{R}, i+1) &= \sum_{\mathbf{R}'} A(\mathbf{R}' \to \mathbf{R}) \tilde{\pi}(\mathbf{R}', i) = \\ &= \sum_{\mathbf{R}' \neq \mathbf{R}} A(\mathbf{R}' \to \mathbf{R}) \tilde{\pi}(\mathbf{R}', i) + A(\mathbf{R} \to \mathbf{R}) \tilde{\pi}(\mathbf{R}, i) \end{aligned} \tag{2.29}$$

Using the normalization property (2.27) to substitute

$$A(\mathbf{R} \to \mathbf{R}) = 1 - \sum_{\mathbf{R}' \neq \mathbf{R}} A(\mathbf{R} \to \mathbf{R}') \tag{2.30}$$

equation (2.29) becomes

$$\tilde{\pi}(\mathbf{R}, i+1) - \tilde{\pi}(\mathbf{R}, i) = \sum_{\mathbf{R}' \neq \mathbf{R}} A(\mathbf{R}' \to \mathbf{R}) \tilde{\pi}(\mathbf{R}', i) - \sum_{\mathbf{R}' \neq \mathbf{R}} A(\mathbf{R} \to \mathbf{R}') \tilde{\pi}(\mathbf{R}, i) \tag{2.31}$$

This equation is known as *master equation* [71] and represents the rate of the variation of the occurrence probability $d\tilde{\pi}(\mathbf{R}, i)/dt$, due to the unbalancing between the transitions to $\mathbf{R}$ from any other state (first term on the right hand side (2.31)) and those from $\mathbf{R}$ to any other state (second term on the right hand side).

When the process has become stationary it holds

$$\begin{aligned} &\tilde{\pi}(\mathbf{R}, i+1) - \tilde{\pi}(\mathbf{R}, i) = 0 \\ \Rightarrow &\sum_{\mathbf{R}' \neq \mathbf{R}} A(\mathbf{R}' \to \mathbf{R}) \pi(\mathbf{R}') = \sum_{\mathbf{R}' \neq \mathbf{R}} A(\mathbf{R} \to \mathbf{R}') \pi(\mathbf{R}) \end{aligned} \tag{2.32}$$

where we have substituted to the time dependent $\tilde{\pi}(\mathbf{R}, i)$ the stationary - time-independent - distribution $\pi(\mathbf{R})$. The simplest solution of that equation is found making the equality (2.32) valid for each term of the sum

$$A(\mathbf{R} \to \mathbf{R}') \pi(\mathbf{R}) = A(\mathbf{R}' \to \mathbf{R}) \pi(\mathbf{R}') \tag{2.33}$$

This equation, known as *detailed balance* condition, expresses the equality between the number of states going from $\mathbf{R}$ to $\mathbf{R}'$ and those going from $\mathbf{R}'$ to $\mathbf{R}$ (i.e. the microscopic reversibility of the chain). Looking at (2.33) we can see that given the transition probabilities $A(\mathbf{R} \to \mathbf{R}')$ the probability distribution $\pi(\mathbf{R})$ of the stationary Markov chain is fixed. We can use this property on reverse and conclude that the desired limiting distribution $\pi(\mathbf{R})$ can be imposed to the Markov chain by building appropriately the transition probabilities $A(\mathbf{R} \to \mathbf{R}')$.

In order to express the conditions under which the stationarity of the Markov chain can be achieved, let us to introduce the $n-$steps probabilities $\Pi^{(n)}(\mathbf{R}'|\mathbf{R})$, expressing the probability that if the system is in the state $\mathbf{R}$ at the time t, it will arrive in the state $\mathbf{R}'$ at the time $t+n\Delta t$. $\Pi^{(1)}(\mathbf{R}'|\mathbf{R})$ coincides with the transition probability $A(\mathbf{R}\to\mathbf{R}')$; $\Pi^{(2)}$ is given by

$$\Pi^{(2)}(\mathbf{R}'|\mathbf{R}) = \sum_{\mathbf{R}''}\Pi^{(1)}(\mathbf{R}\to\mathbf{R}'')\Pi^{(1)}(\mathbf{R}''\to\mathbf{R}') = \sum_{\mathbf{R}''}A(\mathbf{R}\to\mathbf{R}'')A(\mathbf{R}''\to\mathbf{R}') \tag{2.34}$$

and, finally, $\Pi^{(n)}$ can be obtained from $\Pi^{(n-1)}$ as

$$\Pi^{(n)}(\mathbf{R}'|\mathbf{R}) = \sum_{\mathbf{R}''}\Pi^{(n-1)}(\mathbf{R}\to\mathbf{R}'')\Pi^{(1)}(\mathbf{R}''\to\mathbf{R}') \tag{2.35}$$

If the Markov chain satisfies the two following requirements

* the chain is *irreducible*: each point of the configuration space should be reachable from any other point during the sampling in a finite number of steps.

* the chain is *ergodic*: the chain can visit the entire space, returning back to any point (for a discrete configuration space; in a neighborhood of any point, for continuous space) in a finite time.

it is possible to prove the (Perron-Frobenius) theorem, stating that

a) $\lim_{n\to\infty}\Pi^{(n)}(\mathbf{R}'|\mathbf{R}) = \pi_{\text{lim}}(\mathbf{R}') \qquad \forall\mathbf{R}$
i.e. as the number of steps is increased the n-steps probabilities to go from $\mathbf{R}$ to $\mathbf{R}'$ converges to the limiting distribution $\pi_{\text{lim}}(\mathbf{R}')$, independent of the initial state $\mathbf{R}$.

b) $\pi_{\text{lim}}(\mathbf{R}) > 0 \qquad \forall\mathbf{R}$

c) $\sum_{\mathbf{R}}\pi_{\text{lim}}(\mathbf{R}) = 1$

d) $\pi_{\text{lim}}(\mathbf{R}) = \sum_{\mathbf{R}'}\pi_{\text{lim}}(\mathbf{R}')A(\mathbf{R}'\to\mathbf{R})$
This property is contained in the detailed balance condition already introduced for a stationary chain. In fact, if we sum the detailed balance equation (2.33) over $\mathbf{R}'$ we get $\sum_{\mathbf{R}'}A(\mathbf{R}\to\mathbf{R}')\pi_{\text{lim}}(\mathbf{R}) = \sum_{\mathbf{R}'}\pi_{\text{lim}}(\mathbf{R}')A(\mathbf{R}'\to\mathbf{R})$ where $\sum_{\mathbf{R}'}A(\mathbf{R}\to\mathbf{R}')$ is equal to 1 thanks to the normalization condition, i.e. we have recovered d)

Thanks to this theorem it is ensured that the chain has a finite memory of the initial state and admits a limiting distribution $\pi_{\text{lim}}(\mathbf{R})$, independent of time, achieved after a large enough number of steps.

This property of the Markov chains can be applied to build a Monte Carlo algorithm. To do that, the limiting distribution of the Markov chain must be equal to the desired ensemble distribution: from the detailed balance condition we can notice that the limiting distribution depends on the choice made for the transition probabilities $A(\mathbf{R}\to\mathbf{R}')$, and hence we need to obtain a suitable expression for them.

In the Metropolis Monte Carlo scheme, a Markov chain of the desired limiting distribution is generated through a two stage process: at any step, first a trial configuration is proposed according to a given rule, then the trial configuration is accepted or rejected. To this purpose, the total transition probability $A(\mathbf{R} \to \mathbf{R}')$ is factorized in two terms

$$A(\mathbf{R} \to \mathbf{R}') = t(\mathbf{R} \to \mathbf{R}')\alpha(\mathbf{R} \to \mathbf{R}') \tag{2.36}$$

$t(\mathbf{R} \to \mathbf{R}')$ is the a priori transition probability, used to generate a proposed configuration $\mathbf{R}'$ starting from the actual one $\mathbf{R}$; $\alpha(\mathbf{R} \to \mathbf{R}')$ is the acceptance probability, used to decide whether accept or reject the proposed configuration $\mathbf{R}'$ and to drive the limiting distribution towards the desired $\pi(\mathbf{R})$. In the original Metropolis implementation [63] the transition probability $t(\mathbf{R} \to \mathbf{R}')$ was chosen to be symmetric, $t(\mathbf{R} \to \mathbf{R}') = t(\mathbf{R}' \to \mathbf{R})$, but other choices are of course possible.

It remains now to determine an expression for the acceptance probability $\alpha(\mathbf{R} \to \mathbf{R}')$ allowing to reach the desired distribution $\pi(\mathbf{R})$. Introducing the factorization (2.36), the detailed balance equation (2.33) becomes

$$\frac{A(\mathbf{R} \to \mathbf{R}')}{A(\mathbf{R}' \to \mathbf{R})} = \frac{t(\mathbf{R} \to \mathbf{R}')}{t(\mathbf{R}' \to \mathbf{R})}\frac{\alpha(\mathbf{R} \to \mathbf{R}')}{\alpha(\mathbf{R}' \to \mathbf{R})} = \frac{\pi(\mathbf{R}')}{\pi(\mathbf{R})} \tag{2.37}$$

Looking at this expression, we can chose the acceptance probability such as

$$\alpha(\mathbf{R} \to \mathbf{R}') = min\left(1, \frac{\pi(\mathbf{R}')t(\mathbf{R}' \to \mathbf{R})}{\pi(\mathbf{R})t(\mathbf{R} \to \mathbf{R}')}\right) = min\left(1, F(\mathbf{R}, \mathbf{R}')\right) \tag{2.38}$$

Indeed with this choice

- if $F(\mathbf{R}, \mathbf{R}') < 1$:
  $\alpha(\mathbf{R} \to \mathbf{R}') = F(\mathbf{R}, \mathbf{R}')$ and $\alpha(\mathbf{R}' \to \mathbf{R}) = min\,(1, F(\mathbf{R}', \mathbf{R})) = 1$
- if $F(\mathbf{R}', \mathbf{R}) > 1$:
  $\alpha(\mathbf{R} \to \mathbf{R}') = 1$ and $\alpha(\mathbf{R}' \to \mathbf{R}) = F(\mathbf{R}', \mathbf{R})$.

By substituting these expressions for the acceptance probability $\alpha(\mathbf{R} \to \mathbf{R}')$ and the reverse probability $\alpha(\mathbf{R}' \to \mathbf{R})$ into (2.37) it is immediate to prove that the detailed balance holds.

Summarizing, the Metropolis algorithm is made of the following steps

1. Choose an initial configuration $\mathbf{R}_0 = \mathbf{R}$.
2. Sample a trial configuration $\mathbf{R}'$ according to the transition probability $t(\mathbf{R} \to \mathbf{R}')$.
3. Accept the trial configuration with probability

   $$\alpha(\mathbf{R} \to \mathbf{R}') = min\left(1, \frac{\pi(\mathbf{R})t(\mathbf{R} \to \mathbf{R}')}{\pi(\mathbf{R}')t(\mathbf{R}' \to \mathbf{R})}\right) \tag{2.39}$$

   If the move is accepted, $\mathbf{R}'$ will be the next point on the chain $\mathbf{R}_1 = \mathbf{R}'$, if not $\mathbf{R}_1 = \mathbf{R}$.
4. Compute properties at $\mathbf{R}_1$. From the behavior of these properties (such as the internal energy) it is possible to infer if the chain has reached the asintotic behavior. Only after a sufficient number of steps their values will become stationary and can be averaged to obtain the estimates of the thermodynamic quantities.
5. Return to point 2 and repeat n times to obtain a chain of the desired length.

2.4 Path Integral Monte Carlo

The Path Integral Monte Carlo technique [64] (PIMC) allows to simulate the behavior of a quantum system at finite temperature T, using the Feynman path integrals formalism [72]. In the following derivation of the PIMC technique the particle statistics (either bosonic or fermionic) is neglected. The statistics is unimportant as far as the thermal wavelength of the particles $\Lambda_T = \sqrt{\hbar^2/(2\pi m K_B T)}$ is smaller than the interparticle spacing d, that is roughly proportional to the inverse cube root of the density, $d \propto \rho^{-1/3}$. As a consequence, for temperatures well above the degeneracy temperature $T_d = \rho^{2/3}\hbar^2/(2\pi m K_B)$ particles can be safely considered distinguishable (Boltzmannions), otherwise bosonic or fermionic statistic must be introduced by symmetrizing or antisymmetrizing the correspondent density matrices for distinguishable particles.

2.4.1 Path integral formalism

In quantum mechanics, thermodynamic properties can be evaluated as the expectation values of suitable operators $\hat{\mathcal{O}}$ over the wave function Ψ representing the state of the systems. Actually, systems under consideration are not isolated but in contact with a reservoir: let us consider then an enlarged system, made by the original system plus the reservoir. This can be described through a wave function $\Psi_S = \Psi_S(\mathbf{R}, \mathbf{S})$ which depends on both the system ($\mathbf{R}$) and the environment coordinates ($\mathbf{S}$). If we introduce now two complete and orthonormal sets of functions, $\{\varphi_i\}$ and $\{\theta_J\}$ to represent the two portions of the global system, the wave function $\Psi_S(\mathbf{R}, \mathbf{S})$ in the coordinate representation becomes

$$\Psi_S(\mathbf{R}, \mathbf{S}) = \sum_i \sum_J \tilde{c}_{iJ} \varphi_i(\mathbf{R}) \theta_J(\mathbf{S}) = \sum_i \sum_J \tilde{c}_{iJ} \langle \mathbf{R} | \, \varphi_i \rangle \langle \mathbf{S} | \, \theta_J \rangle \tag{2.40}$$

We can also "hide" the coordinates of the reservoir by defining the functions $\bar{c}_i(\mathbf{S}) = \sum_J \tilde{c}_{iJ} \langle \mathbf{S} | \, \theta_J \rangle$ to get

$$\Psi_S(\mathbf{R}, \mathbf{S}) = \sum_i \bar{c}_i(\mathbf{S}) \langle \mathbf{R} | \, \varphi_i \rangle \tag{2.41}$$

Let us consider now an operator $\hat{\mathcal{O}}$ that acts only on the system coordinates and compute its expectation value over the wave function Ψ_S of the global system

$$\frac{\langle \Psi_S | \, \hat{\mathcal{O}} \, | \Psi_S \rangle}{\langle \Psi_S \, | \Psi_S \rangle} = \frac{\sum_{i,i'} \sum_{J,J'} \tilde{c}_{iJ} \tilde{c}^*_{i'J'} \langle \varphi_{i'} | \, \langle \theta_{J'} | \, \hat{\mathcal{O}} \, | \theta_J \rangle \, | \varphi_i \rangle}{\sum_i \sum_J \tilde{c}_{iJ} \tilde{c}^*_{iJ}} = \frac{\sum_{i,i'} \sum_J \tilde{c}_{iJ} \tilde{c}^*_{i'J} \langle \varphi_{i'} | \, \hat{\mathcal{O}} \, | \varphi_i \rangle}{\sum_i \sum_J \tilde{c}_{iJ} \tilde{c}^*_{iJ}} \tag{2.42}$$

This expression can be simplified by introducing the operator $\hat{\rho}$, acting only on the original system, of matrix elements $\rho_{ii'} = \langle \varphi_i | \, \hat{\rho} \, | \varphi_{i'} \rangle = \sum_J \tilde{c}_{iJ} \tilde{c}^*_{i'J}$. Indeed we have

$$\frac{\langle \Psi_S | \, \hat{\mathcal{O}} \, | \Psi_S \rangle}{\langle \Psi_S \, | \Psi_S \rangle} = \frac{\sum_{i,i'} \langle \varphi_i | \, \hat{\rho} \, | \varphi_{i'} \rangle \langle \varphi_{i'} | \, \hat{\mathcal{O}} \, | \varphi_i \rangle}{\sum_i \langle \varphi_i | \, \hat{\rho} \, | \varphi_i \rangle} = \frac{\sum_i \langle \varphi_i | \, \hat{\rho} \hat{\mathcal{O}} \, | \varphi_i \rangle}{\sum_i \langle \varphi_i | \, \hat{\rho} \, | \varphi_i \rangle} = \frac{\mathrm{Tr} \left\{ \hat{\rho} \hat{\mathcal{O}} \right\}}{\mathrm{Tr} \left\{ \hat{\rho} \right\}} \tag{2.43}$$

where we have simplified the identity in the form $\sum_i | \varphi_i \rangle \langle \varphi_i | = 1$ to arrive at the final expression. The operator $\hat{\rho}$ is called density matrix and can be used to derive quantum statistical mechanics. To proceed, let us then introduce the orthonormal and complete set of the eigenvectors of $\hat{\rho}$, $|\phi_n\rangle$, to rewrite the density matrix in the diagonal form

$$\hat{\rho} = \sum_n p_n |\phi_n\rangle \langle\phi_n| \tag{2.44}$$

The eigenstates of $\hat{\rho}$, p_n, are real, since the matrix is hermitian, and also positive.[1]

In this representation the expectation value (2.43) becomes

$$\frac{\langle\Psi_S| \hat{\mathcal{O}} |\Psi_S\rangle}{\langle\Psi_S |\Psi_S\rangle} = \frac{\sum_n p_n \langle\phi_n| \hat{\mathcal{O}} |\phi_n\rangle}{\sum_n p_n \langle\phi_n |\phi_n\rangle} \tag{2.45}$$

The average of the operator $\hat{\mathcal{O}}$ is then a weighted sum of contributions each one is equal to the expectation value of the operator $\hat{\mathcal{O}}$ over the state $|\phi_n\rangle$. We can then interpret the p_n as the probability for the system to be in the eigenstate $|\phi_n\rangle$ of the density matrix. One can at this point identify the $|\phi_n\rangle$ with the Hamiltonian eigenstates: this result allows to define the quantum statistical ensemble, described by the density matrix $\hat{\rho}$, as a mixture of pure Hamiltonian states, to each one is associated the probability p_n.

In a quantum system described by the Hamiltonian $\hat{\mathcal{H}}$ and in thermal equilibrium with a heat bath at the temperature T, the occupancy probabilities p_n associated to the Hamiltonian eigenstates ϕ_n are proportional to $\exp(-\beta\mathcal{E}_n)$, where β is the inverse of the temperature $\beta = 1/K_BT$ and $\mathcal{E}_n$ is the n^{th} energy eigenvalue of $\hat{\mathcal{H}}$. The density matrix - called thermal density matrix - of this system is then $\exp[-\beta\hat{\mathcal{H}}]$. In terms of $\hat{\rho}_\beta$, the expectation value of $\hat{\mathcal{O}}$ becomes

$$\left\langle \hat{\mathcal{O}} \right\rangle = \frac{\sum_n \langle\phi_n| e^{-\beta\hat{\mathcal{H}}}\hat{\mathcal{O}} |\phi_n\rangle}{\sum_n \langle\phi_n| e^{-\beta\hat{\mathcal{H}}} |\phi_n\rangle} = \frac{Tr\left\{\hat{\rho}_\beta\hat{\mathcal{O}}\right\}}{Tr\left\{\hat{\rho}_\beta\right\}} \tag{2.46}$$

An important property of the thermal density matrix is that it is a solution of the Bloch equation

$$-\frac{\partial\hat{\rho}_\beta}{\partial\beta} = \hat{\mathcal{H}}\hat{\rho}_\beta \tag{2.47}$$

with the initial condition $\rho(\mathbf{R}, \mathbf{R}'; 0) = \delta(\mathbf{R} - \mathbf{R}')$. The Bloch equation is formally analogous to a diffusion equation if we interpret the inverse temperature β as an imaginary time variable, $\beta = i\hbar t$. The thermal density matrix $\hat{\rho}_\beta$ is in fact formally equivalent to a time evolution operator, evaluated at the imaginary time β, which allows to evolve the system from the initial position $\mathbf{R}$, occupied at the imaginary time $t = 0$, to the final position $\mathbf{R}'$, reached after an imaginary time lapse of lenght β has passed. For this reason, in this section we will often use the word "time" referring to inverse temperatures.

From the equation (2.46), it is clear that the knowledge of the thermal density matrix is sufficient to determine all the equilibrium properties of a quantum system of Hamiltonian $\hat{\mathcal{H}}$ and at temperature T. Being the trace invariant under unitary transformations, we are in principle free to choose any complete set of states to evaluate the traces in (2.46). For our purposes it is convenient to use the

---

[1] To demonstrate that, let us notice that $Tr\{\hat{\rho}|\phi_m >< \phi_m|\} = p_n$ is also equal, using (2.43), to $< \Psi_S|\phi_m >< \phi_m|\Psi_S >= \sum_J |\tilde{c}_{mJ}|^2 \geq 0$.

coordinates representation in the $3N$ dimensional space of N distinguishable particles, $\{|\mathbf{R}\rangle\} = \{|\mathbf{R}_1\rangle \cdots |\mathbf{R}_N\rangle\}$, to rewrite

$$\begin{aligned} \rho(\mathbf{R},\mathbf{R}';\beta) &= \langle\mathbf{R}| e^{-\beta\hat{\mathcal{H}}} |\mathbf{R}'\rangle = \sum_n \langle\mathbf{R}|\phi_n\rangle \langle\phi_n| e^{-\beta\hat{\mathcal{H}}} |\phi_n\rangle \langle\phi_n|\mathbf{R}'\rangle \quad (2.48) \\ &= \sum_n \phi_n^*(\mathbf{R})\phi_n(\mathbf{R}')e^{-\beta\mathcal{E}_n} \quad (2.49) \end{aligned}$$

In the same representation the expectation value of the operator $\hat{\mathcal{O}}$ becomes

$$\left\langle\hat{\mathcal{O}}\right\rangle = \mathcal{Z}^{-1}\int d\mathbf{R}d\mathbf{R}' \langle\mathbf{R}| e^{-\beta\hat{\mathcal{H}}} |\mathbf{R}'\rangle \langle\mathbf{R}'|\hat{\mathcal{O}}|\mathbf{R}\rangle \quad (2.50)$$

having introduced the partition function of the system $\mathcal{Z}$

$$\mathcal{Z} = \int d\mathbf{R} \langle\mathbf{R}| e^{-\beta\hat{\mathcal{H}}} |\mathbf{R}\rangle \quad (2.51)$$

The evaluation of the density matrix elements in the coordinate basis is not straightforward: although we can obtain analytic expressions for the kinetic and the potential contributions separately, $\langle\mathbf{R}| e^{-\beta\hat{\mathcal{K}}} |\mathbf{R}'\rangle$ and $\langle\mathbf{R}| e^{-\beta\hat{\mathcal{V}}} |\mathbf{R}'\rangle$, it is not possible to factorize the exponential $e^{-\beta(\hat{\mathcal{K}}+\hat{\mathcal{V}})}$ into the product $e^{-\beta\hat{\mathcal{K}}}e^{-\beta\hat{\mathcal{V}}}$, since $\hat{\mathcal{K}}$ and $\hat{\mathcal{V}}$ do not commute. As a consequence, in order to arrive to an analytic form for $\rho(\mathbf{R},\mathbf{R}';\beta)$, some limit procedures must be introduced.

Within the path integral formalism the original density matrix is rewritten in terms of high T (low β) density matrices, exploiting the property

$$\begin{aligned} \rho(\mathbf{R},\mathbf{R}';\beta_1+\beta_2) &= \langle\mathbf{R}| e^{-(\beta_1+\beta_2)\hat{\mathcal{H}}} |\mathbf{R}'\rangle = \int d\mathbf{R}'' \langle\mathbf{R}| e^{-\beta_1\hat{\mathcal{H}}} |\mathbf{R}''\rangle \langle\mathbf{R}''| e^{-\beta_2\hat{\mathcal{H}}} |\mathbf{R}'\rangle \\ &= \int d\mathbf{R}''\rho(\mathbf{R},\mathbf{R}'';\beta_1)\rho(\mathbf{R}'',\mathbf{R}';\beta_2) \quad (2.52) \end{aligned}$$

useful for our purposes, since it is easier to find accurate approximations for high temperature density matrices, as we will see in the following. Let us hence rewrite the inverse temperature β as the product of M equal contributions $\tau = \beta/M$, in such a way that

$$e^{-\beta\hat{\mathcal{H}}} = (e^{-\tau\hat{\mathcal{H}}})^M = \underbrace{e^{-\tau\hat{\mathcal{H}}}\cdots e^{-\tau\hat{\mathcal{H}}}}_{\text{M times}} \quad (2.53)$$

Applying (2.52) $M-1$ times, we arrive at the discrete path integral representation for the thermal density matrix[2]

$$\begin{aligned} \rho(\mathbf{R},\mathbf{R}';\beta) &= \int d\mathbf{R}_1\int d\mathbf{R}_2\cdots\int d\mathbf{R}_{M-1}\rho(\mathbf{R},\mathbf{R}_1;\tau)\rho(\mathbf{R}_1,\mathbf{R}_2;\tau)\cdots \\ &\cdots\ \rho(\mathbf{R}_{M-1},\mathbf{R}';\tau) \quad (2.54) \end{aligned}$$

---

[2] In the PIMC sections, unlike stated at the beginning of this chapter and unless differently specified, the subscript attached to $\mathbf{R}$ identifies the point of the path from the initial to the final configuration. In other words $\mathbf{R}_i$ indicates the $3N-$dimensional vector of components given by the spatial coordinates of N particles, in the $i-$th point of the path. $\mathbf{R}_i = \{\mathbf{R}_1^i, \mathbf{R}_2^i, \cdots, \mathbf{R}_N^i\}$, where now $\mathbf{R}_j^i, j = 1, \cdots, N$ are the positions of the $j-$th particle.

or, adopting a compact notation

$$\rho(\mathbf{R},\mathbf{R}';\beta) = \int \left(\prod_{i=1}^{M-1} d\mathbf{R}_i\right) \prod_{i=0}^{M-1} \rho(\mathbf{R}_i,\mathbf{R}_{i+1};\tau) \tag{2.55}$$

with the conventions $\mathbf{R}_0 = \mathbf{R}$ and $\mathbf{R}_M = \mathbf{R}'$. The path integral notation (2.55) allows to determine accurate approximations for the thermal density matrix. On the other hand, the price to pay is the evaluation of multi-dimensional integrals, that however can be performed using Monte Carlo approaches.

The analogy between the thermal density matrix and a time evolution operator is useful to define a path integral notation. To join the initial point of the phase space $\mathbf{R}$, associated to the imaginary time 0, with the final point $\mathbf{R}'$, reached at time β, we can build many different paths, identified by a sequence of intermediate points $\mathbf{R}_1, \cdots, \mathbf{R}_{M-1}$, each distant a time τ from the previous and the following. The segment between two subsequent points $\mathbf{R}_i$ and $\mathbf{R}_{i+1}$ is called *time slice* and the time interval $\tau = \beta/M$ is the *time step.* The final value of the density matrix is given by the sum of all contributions from the possible paths (i.e. the possible sequences of $\mathbf{R}_i$).

The expression (2.55) is exact for any number of slices M, but the advantage of the factorization is that for M large enough (and hence a small enough time step τ) we are able to find good approximations for the short time (high temperature) density matrix $\rho(\mathbf{R}_i,\mathbf{R}_{i+1},\tau)$. Indeed, for non commuting operators, the following relation (Zassenhaus formula) is valid [73]

$$e^{-\tau(\hat{\mathcal{K}}+\hat{\mathcal{V}})} = e^{-\tau\hat{\mathcal{K}}} e^{-\tau\hat{\mathcal{V}}} \prod_{n=2}^{\infty} e^{C_n(\hat{\mathcal{K}},\hat{\mathcal{V}})} \tag{2.56}$$

where the C_n are functions of the operators $\hat{\mathcal{K}}$ and $\hat{\mathcal{V}}$ of order n in τ. As an example, we give here the first two C_n functions [73]: $C_2 = -\tau^2[\hat{\mathcal{K}},\hat{\mathcal{V}}]/2$ and $C_3 = \tau^3[\hat{\mathcal{K}},[\hat{\mathcal{K}},\hat{\mathcal{V}}]]/6 + \tau^3[\hat{\mathcal{V}},[\hat{\mathcal{K}},\hat{\mathcal{V}}]]/3$.

If the lowest eigenvalues of the operators $\hat{\mathcal{K}}$ and $\hat{\mathcal{V}}$ are finite[3] , as $\tau \rightarrow 0$ the $n-th$ terms decay more rapidly than the terms linear in τ and thus can be neglected, leading to the lower order approximation of (2.56)

$$e^{-\tau(\hat{\mathcal{K}}+\hat{\mathcal{V}})} = e^{-\tau\hat{\mathcal{K}}} e^{-\tau\hat{\mathcal{V}}} + o(\tau^2) \tag{2.57}$$

called *primitive approximation.* Using (2.57) the thermal density matrix $\rho(\mathbf{R}_i,\mathbf{R}_{i+1};\tau)$ becomes

$$\rho(\mathbf{R}_i,\mathbf{R}_{i+1};\tau) = \langle\mathbf{R}_i|\, e^{-\tau\hat{\mathcal{K}}} e^{-\tau\hat{\mathcal{V}}}\, |\mathbf{R}_{i+1}\rangle = \langle\mathbf{R}_i|\, e^{-\tau\hat{\mathcal{K}}}\, |\mathbf{R}_{i+1}\rangle\, e^{-\tau\mathcal{V}(\mathbf{R_{i+1}})} \tag{2.58}$$

since the potential operator is diagonal in the position representation. This approximated expression for the density matrix, however, does not share a fundamental property with the exact density matrix that, being Hermitian and real, is a symmetric matrix, i.e. $\rho(\mathbf{R},\mathbf{R}';\tau) = \rho(\mathbf{R}',\mathbf{R};\tau)$. To introduce a symmetric approximation for the density matrix we can notice that

$$e^{-\tau(\hat{\mathcal{K}}+\hat{\mathcal{V}})} = e^{-\tau(\hat{\mathcal{V}}/2+\hat{\mathcal{K}}+\hat{\mathcal{V}}/2)} = e^{-\tau\hat{\mathcal{V}}/2} e^{-\tau\hat{\mathcal{K}}} e^{-\tau\hat{\mathcal{V}}/2} + o(\tau^3) \tag{2.59}$$

---

[3] i.e. the spectrum of each operator is lower bounded

Applying this factorization of the original operator, we can reproduce an exact property of the density matrix and also lower of one order in τ (with respect to (2.57)) the error due to the factorization.

One may think that as the number of slices is increased the neglected contributions will sum, leading to a huge error in the density matrix estimate. However the Trotter theorem [74]

$$e^{-\beta(\hat{\mathcal{K}}+\hat{\mathcal{V}})} = \lim_{M\to\infty}\left[e^{-\tau\hat{\mathcal{V}}/2}e^{-\tau\hat{\mathcal{K}}}e^{-\tau\hat{\mathcal{V}}/2}\right]^M \tag{2.60}$$

holding for each pair of self-adjoint operators $\hat{\mathcal{K}}$ and $\hat{\mathcal{V}}$ that are lower bounded, guarantees that, in the limit of an infinite number of slices, the use of the primitive approximation on the single slice gives the exact overall result.

In practical applications we are always dealing with a finite number of slices, and higher order approximations are generally required, to speed the convergence in τ. For the moment however we can proceed by making explicit the expression of the density matrix in the primitive (symmetrized) approximation

$$\begin{aligned}\rho(\mathbf{R}_i,\mathbf{R}_{i+1};\tau) &= \langle\mathbf{R}_i|\, e^{-\tau\hat{\mathcal{V}}/2}e^{-\tau\hat{\mathcal{K}}}e^{-\tau\hat{\mathcal{V}}/2}\,|\mathbf{R}_{i+1}\rangle \\ &= \langle\mathbf{R}_i|\, e^{-\tau\hat{\mathcal{K}}}\,|\mathbf{R}_{i+1}\rangle\, e^{-\frac{\tau}{2}(\mathcal{V}(\mathbf{R}_i)+\mathcal{V}(\mathbf{R}_{i+1}))}\end{aligned} \tag{2.61}$$

useful to make several comments about path integrals. The kinetic contribution can be obtained by introducing the eigenstates $|\mathbf{K}_n\rangle$ of the kinetic operator $\hat{\mathcal{K}} = -\lambda\sum_{j=1}^N \nabla_j^2$, assuming distinguishable particles in a cubic box of side lenght L. In the coordinate representation the eigenstates become

$$\langle\mathbf{R}\,|\mathbf{K}_n\rangle = L^{-3N/2}exp\left[-i\mathbf{K}_n\cdot\mathbf{R}\right] \tag{2.62}$$

where the wave vectors are given by $\mathbf{K}_n = 2\pi\mathbf{n}/L$, with $\mathbf{n}$ a $3N-$dimensional vector of integers. We then have

$$\begin{aligned}\langle\mathbf{R}_i|\, e^{-\tau\hat{\mathcal{K}}}\,|\mathbf{R}_{i+1}\rangle &= \sum_n \langle\mathbf{R}_i|\,\mathbf{K}_n\rangle\,\langle\mathbf{K}_n|\, e^{-\tau\hat{\mathcal{K}}}\,|\mathbf{K}_n\rangle\,\langle\mathbf{K}_n\,|\mathbf{R}_{i+1}\rangle \\ &= \sum_n L^{-3N}e^{-\tau\lambda\mathbf{K}_\mathbf{n}^2-i\mathbf{K}_\mathbf{n}\cdot(\mathbf{R}_i-\mathbf{R}_{i+1})}\end{aligned} \tag{2.63}$$

where $\lambda = \hbar^2/2m$. The sum over $\mathbf{n}$ can be performed analytically for $L\to\infty$ by going to the continuous limit, making the transformation $L^{-3N}\sum_n \to \int(2\pi)^{-3N}d\mathbf{K}$. The integral in the $\mathbf{K}$ variables can be reduced to a Gaussian integral by completing the square

$$-(\tau\lambda\mathbf{K}^2+i\mathbf{K}\cdot(\mathbf{R}_i-\mathbf{R}_{i+1})) = -(\sqrt{\tau\lambda}\mathbf{K}+i(\mathbf{R}_i-\mathbf{R}_{i+1})/\sqrt{4\tau\lambda})^2-(\mathbf{R}_i-\mathbf{R}_{i+1})^2/4\tau\lambda \tag{2.64}$$

We then have

$$\begin{aligned}\langle\mathbf{R}_i|\, e^{-\tau\hat{\mathcal{K}}}\,|\mathbf{R}_{i+1}\rangle &= e^{-\frac{(\mathbf{R}_i-\mathbf{R}_{i+1})^2}{4\tau\lambda}}\int\frac{d\mathbf{K}}{(2\pi)^{3N}}e^{-(\sqrt{\tau\lambda}\mathbf{K}+i\frac{(\mathbf{R}_i-\mathbf{R}_{i+1})}{\sqrt{4\tau\lambda}})^2} \\ &= (4\pi\lambda\tau)^{-\frac{3N}{2}}e^{-\frac{(\mathbf{R}_i-\mathbf{R}_{i+1})^2}{4\lambda\tau}}\end{aligned} \tag{2.65}$$

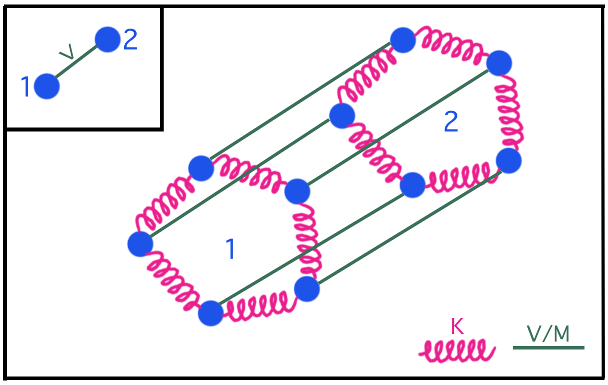

Figure 2.1. Schematic representation of the classical isomorphism. In inset, we represented two quantum particles 1 and 2 interacting via the potential $V(\mathbf{R}_{12})$. Using the path integral formalism, the two particle system becomes equivalent to a system of two classical ring polymers in which the kinetic energy K represents the harmonic bonding between two adjacent beads belonging to the same polymer. The two polymers interact via the original potential (divided by the number of beads M) that however relates only pairs of beads occupying the same position in the polymer.

Substituting (2.65) in (2.61) we find, for a single slice

$$\rho(\mathbf{R}_i, \mathbf{R}_{i+1}; \tau) = (4\pi\lambda\tau)^{-\frac{3N}{2}} e^{-\frac{(\mathbf{R}_i - \mathbf{R}_{i+1})^2}{4\lambda\tau}} e^{-\frac{\tau(\mathcal{V}(\mathbf{R}_i)+\mathcal{V}(\mathbf{R}_{i+1}))}{2}} \tag{2.66}$$

In the primitive approximation, the total density matrix is then given by

$$\rho(\mathbf{R}, \mathbf{R}'; \beta) = \int \prod_{i=1}^{M-1} d\mathbf{R}_i \left(\frac{1}{4\pi\lambda\tau}\right)^{\frac{3}{2}NM} e^{-\sum_{i=0}^{M-1}\left[\frac{(\mathbf{R}_i - \mathbf{R}_{i+1})^2}{4\lambda\tau} + \frac{\tau(\mathcal{V}(\mathbf{R}_i)+\mathcal{V}(\mathbf{R}_{i+1}))}{2}\right]} \tag{2.67}$$

and the partition function of the system is

$$\mathcal{Z} = \int \prod_{i=0}^{M-1} d\mathbf{R}_i \left(\frac{1}{4\pi\lambda\tau}\right)^{\frac{3}{2}NM} e^{-\sum_{i=0}^{M-1}\left[\frac{(\mathbf{R}_i - \mathbf{R}_{i+1})^2}{4\lambda\tau} + \frac{\tau(\mathcal{V}(\mathbf{R}_i)+\mathcal{V}(\mathbf{R}_{i+1}))}{2}\right]} \tag{2.68}$$

where $\mathbf{R}_0 = \mathbf{R}_M$. This expression is identical to the the partition function of a classical system of N ring polymers, each one made of M beads and subjected to a very specific interaction. The kinetic contribution in the exponential in (2.68) has the form of a spring potential connecting two adjacent beads in the same chain. The potential term $\tau\mathcal{V}(\mathbf{R}_i)$ represents instead an inter-polymer interaction, that has however a peculiarity: at variance with a real system of classical polymers, in which each bead of a given polymer interact in principle with all other beads, in our system the interactions among different polymers are only restricted to same-time beads. Moreover, in the equation (2.68), as well as in the formulas for the expectation values of operators $\hat{\mathcal{O}}$ diagonal in the $\mathbf{R}$ representation, the first and the last bead of the polymers are coincident: $\mathbf{R}_0 = \mathbf{R}_M$. The polymer folds on itself and is hence a ring polymer. A pictorial representation of the classical isomorphism is sketched in Figure 2.1.

The classical isomorphism is useful also to understand the limiting behavior in temperature. Consider a ring polymer of a given time slice $\tau = \beta/M$, describing a quantum particle within the path integral formalism. At low temperature, corresponding to large β, the ring polymer is represented by a polymer with a large number of beads $M + 1$ and occupies a defined portion of space. The particle is delocalized and its quantum nature is well evident. As the temperature increases, β decreases and the number of slices M decreases as well. As $\beta \to 0$ also $M \to 0$: the polymer collapse into a point. In this limit we can say that the particle has become localized and behaves as a classical particle.

In the formalism introduced so far we have considered discrete paths, made of a finite number M of intermediate points. While the discrete path integral representation (2.55) is formally exact for any M, the Trotter theorem states that the primitive factorization (2.67) which we adopted to write an explicit expression for the thermal density matrix becomes exact only in the limit of an infinite number of slices. We want now go to this limit, corresponding to $M \to \infty$ and $\tau \to 0$, providing that $M\tau = \beta =$ constant.

As the number of slices goes to infinity, a path, defined for finite M by a sequence of discrete points $\mathbf{R}_0, \cdots, \mathbf{R}_M$, becomes described by a continuous function of the imaginary time $\mathbf{R}(t)$, being $t \in [0, \beta]$. It follows that in (2.54) the integrals over the variables $\mathbf{R}_i$ can be substituted with a functional integral in $\mathbf{R}(t)$, with the boundary conditions $\mathbf{R}(0) = \mathbf{R}$ and $\mathbf{R}(\beta) = \mathbf{R}'$

$$\int \prod_{i=0}^{M-1} \frac{d\mathbf{R}_i}{(4\pi\lambda\tau)^{3/2M}} \to \int_{\substack{\mathbf{R}(0)=\mathbf{R} \\ \mathbf{R}(\beta)=\mathbf{R}'}} \mathcal{D}\mathbf{R} \tag{2.69}$$

Let us consider now the exponential term in the path integral expression (2.67) for the primitive density matrix,

$$-\tau \sum_{i=0}^{M-1} \left[\frac{(\mathbf{R}_{i+1} - \mathbf{R}_i)^2}{4\lambda\tau^2} + \frac{\mathcal{V}(\mathbf{R}_{i+1}) + \mathcal{V}(\mathbf{R}_i)}{2} \right] \tag{2.70}$$

We can notice that in the limit $\tau \to 0$ the ratio $(\mathbf{R}_{i+1} - \mathbf{R}_i)/\tau$ becomes the (imaginary) time derivative of the path coordinate $\mathbf{R}$, that is, the velocity $\dot{\mathbf{R}}$

$$\lim_{\tau\to 0} \frac{\mathbf{R}_{i+1} - \mathbf{R}_i}{\tau} = \frac{d\mathbf{R}}{d\tau} = \dot{\mathbf{R}} \tag{2.71}$$

Moreover, in the same limit, the sum in (2.70) corresponds to the Riemann definition of integral, and hence we have

$$\lim_{\substack{\tau\to 0 \\ M\to\infty}} \sum_{i=0}^{M-1} \left[\frac{(\mathbf{R}_{i+1} - \mathbf{R}_i)^2}{4\lambda\tau^2} + \frac{\mathcal{V}(\mathbf{R}_{i+1}) + \mathcal{V}(\mathbf{R}_i)}{2} \right] \tau = \int_0^\beta \left[\frac{|\dot{\mathbf{R}}(\tau)|^2}{4\lambda} + \mathcal{V}(\mathbf{R}(\tau)) \right] d\tau \tag{2.72}$$

The continuous representation of the thermal density matrix hence becomes

$$\rho(\mathbf{R}, \mathbf{R}'; \beta) = \int_{\substack{\mathbf{R}(0)=\mathbf{R} \\ \mathbf{R}(\beta)=\mathbf{R}'}} \mathcal{D}\mathbf{R} \, \exp\left[-\int_0^\beta \left[\frac{|\dot{\mathbf{R}}|^2}{4\lambda} + \mathcal{V}(\mathbf{R}) \right] d\tau \right] \tag{2.73}$$

2.4.2 Beyond the primitive approximation: the pair density matrix

The previous expression for the thermal density matrix cannot be evaluated analytically for a generic form of the potential and, in practical applications, it is necessary to go back to the discretized form (2.55). However, in this case the error due to the primitive factorization remains finite and the number M of slices must be large enough in order to obtain an accurate representation of the density matrix. It is however possible to go beyond the primitive approximation and obtain an expression for the density matrix that converges more rapidly with M. In this section we will introduce a possible choice of approximated expression for the discretized density matrix.

Let us first introduce a notation that will be useful to this aim. In absence of interactions among the particles the continuous path density matrix (2.73) reduces to

$$\rho_0(\mathbf{R},\mathbf{R}';\beta) = \int_{\substack{\mathbf{R}(0)=\mathbf{R}\\ \mathbf{R}(\beta)=\mathbf{R}'}} \mathcal{D}\mathbf{R}\ \exp\left[-\int_0^\beta \left[\frac{|\dot{\mathbf{R}}|^2}{4\lambda}\right] d\tau\right] \tag{2.74}$$

that represents the thermal density matrix of an ideal gas. For classical systems, it is common to distinguish into ideal and excess contributions to the thermodynamic quantities: in quantum systems this distinction is no more valid. However, we can still introduce an "excess" density matrix $\rho_{\mathrm{ex}}(\mathbf{R},\mathbf{R}';\beta)$, by factorizing the total density matrix as follows

$$\rho(\mathbf{R},\mathbf{R}';\beta) = \frac{\rho_0(\mathbf{R},\mathbf{R}';\beta)}{\rho_0(\mathbf{R},\mathbf{R}';\beta)}\rho(\mathbf{R},\mathbf{R}';\beta) = \rho_0(\mathbf{R},\mathbf{R}';\beta)\rho_{\mathrm{ex}}(\mathbf{R},\mathbf{R}';\beta) \tag{2.75}$$

where

$$\rho_{\mathrm{ex}}(\mathbf{R},\mathbf{R}';\beta) = \frac{\rho(\mathbf{R},\mathbf{R}';\beta)}{\rho_0(\mathbf{R},\mathbf{R}';\beta)} = \frac{\int_{\substack{\mathbf{R}(0)=\mathbf{R}\\ \mathbf{R}(\beta)=\mathbf{R}'}} \mathcal{D}\mathbf{R}\ e^{-\int_0^\beta \left[\frac{|\dot{\mathbf{R}}|^2}{4\lambda}+\mathcal{V}(\mathbf{R})\right]d\tau}}{\int_{\substack{\mathbf{R}(0)=\mathbf{R}\\ \mathbf{R}(\beta)=\mathbf{R}'}} \mathcal{D}\mathbf{R}\ e^{-\int_0^\beta \frac{|\dot{\mathbf{R}}|^2}{4\lambda}d\tau}} \tag{2.76}$$

Unlike the classical case, our definition of the excess density matrix contains terms arising from the kinetic energy. However, it is possible to factorize the integrand in the numerator of (2.76) into the product $\exp[-\int_0^\beta |\dot{\mathbf{R}}|^2/(4\lambda)d\tau]\exp[-\int_0^\beta \mathcal{V}(\mathbf{R})d\tau]$ and to obtain

$$\rho_{\mathrm{ex}}(\mathbf{R},\mathbf{R}';\beta) = \int_{\substack{\mathbf{R}(0)=\mathbf{R}\\ \mathbf{R}(\beta)=\mathbf{R}'}} \mathcal{D}\mathbf{R}\ w(\mathbf{R},\mathbf{R}';\beta)e^{-\int_0^\beta \mathcal{V}(\mathbf{R})d\tau} = \left\langle e^{-\int_0^\beta \mathcal{V}(\mathbf{R})d\tau}\right\rangle_{\mathrm{FP}} \tag{2.77}$$

where the ratio $w(\mathbf{R},\mathbf{R}';\beta) = \exp[-\int_0^\beta |\dot{\mathbf{R}}|^2/(4\lambda)d\tau]/\rho_0(\mathbf{R},\mathbf{R}';\beta)$ can be interpreted as the probability associated to a free particle path starting in $\mathbf{R}$ and ending in $\mathbf{R}'$, and we introduced the symbol $\langle\cdots\rangle_{\mathrm{FP}}$, meaning an average over the free particle paths with fixed end points. Expression (2.77) is still exact, since we have simply recast in a different way terms arising from the continuous representation of the density matrix.

However, we can use (2.77) to derive for the density matrix of systems with pair interactions (described through the potential $v(r)$) an approximation accurate and fast to compute: the *pair density matrix* approximation [64, 75].

Suppose that the total potential energy of the system under consideration can be written as the sum of pairwise terms

$$\mathcal{V}(\mathbf{R}) = \sum_{i<j} v(\mathbf{R}_{ij}) \tag{2.78}$$

where $\mathbf{R}_{ij} = \mathbf{R}_i - \mathbf{R}_j$ are here three dimensional vectors, representing the vectorial distance between the particle i and the particle j. Formula (2.77) in this case becomes

$$\begin{aligned} \rho_{ex}(\mathbf{R}, \mathbf{R}'; \beta) &= \left\langle e^{-\int_0^\beta d\tau \mathcal{V}(\mathbf{R}(\tau))} \right\rangle_{\mathrm{FP}} = \left\langle \prod_{i<j} \exp\left[-\int_0^\beta d\tau \; v(\mathbf{R}_{ij}(\tau)) \right] \right\rangle_{\mathrm{FP}} \\ &= \left\langle \prod_{i<j} e_{ij} \right\rangle_{\mathrm{FP}} \end{aligned} \tag{2.79}$$

having defined $e_{ij} = \exp\left[-\int_0^\beta d\tau \; v(\mathbf{R}_{ij}(\tau)) \right]$. At low temperature, since the paths are spread in the configuration space, many body contributions cannot be neglected and the factors e_{ij} cannot be considered independent from each other. However as the temperature is increased the paths shrink and we can assume that the e_{ij} becomes less correlated[4]. Under this assumption we can invert the product and the average in (2.79), obtaining

$$\rho_{ex}(\mathbf{R}, \mathbf{R}'; \beta) \approx \prod_{i<j} \left\langle \exp\left[-\int_0^\beta d\tau \; v(\mathbf{R}_{ij}(\tau)) \right] \right\rangle_{\mathrm{FP}_{ij}} \tag{2.80}$$

in which each factor represents the excess density matrix of a pair of particles, exact since it is just the continuous representation of the density matrix written for a system of two particles. The two body density matrix can be computed without introducing further approximations, apart to solve numerical issues. A technique used to obtain the pair density matrix for a pair of particles, is the squaring method, developed by Storer [76] and described in detail in Ref. [64].

To conclude, let us compare now the pair density matrix with the primitive expression. At very high temperature, as $\beta \to 0$, we can approximate the τ integral in (2.80) as the product of β times the average of the potential: $-\beta(v(\mathbf{R}_{ij}(0)) + v(\mathbf{R}_{ij}(\beta)))/2$, recovering the primitive approximation (2.67). At finite temperature, this form of the density matrix is instead more accurate than the primitive approximation, since it contains, on average, informations about the interactions along the entire path and not only at the extremes.

2.4.3 Path sampling

Once obtained an explicit expression for the thermal density matrix, we need to define an algorithm to sample the path configuration space. A simple approach to

---

[4] being the value of τ determined by convergence issues, as the temperature increases, β decreases and so the number of slices of which the paths are made. As a consequence the average distance among paths of different particles increases and the correlations among different beads are reduced.

generate new paths is the Lévy reconstruction method [77], a recursive procedure to build a Brownian path of the desired number of slices between two fixed end points. Let us assume that $\mathbf{R}(t=0)=\mathbf{R}_0$ and $\mathbf{R}(t=\beta)=\mathbf{R}_M$ are fixed and that M is an *even* integer, $M=2^n$. Let us call τ the time length of each slice, such that $\beta = M\tau = 2^n\tau$.

The first step of the Lévy algorithm reside in the random sampling of the mid point $\mathbf{R}_{M/2}$ as

$$\mathbf{R}_{M/2} = \frac{\mathbf{R}^0 + \mathbf{R}^\beta}{2} + \eta_\beta \tag{2.81}$$

where η_β is a gaussian random number of zero mean and variance $\sigma_\beta = \sqrt{\lambda\beta}$. Together with the fixed end points, $\mathbf{R}_{M/2}$ will define two intervals, $[\mathbf{R}_0, \mathbf{R}_{M/2}]$ and $[\mathbf{R}_{M/2}, \mathbf{R}_M]$, of time lenght $\beta/2$. The next step of the Lévy algorithm consist in the application of (2.81) to each one of these new intervals, adjusting the variance of the random number to the new interval time length $\beta/2$, to obtain their middle points. The resulting two new points are given by

$$\mathbf{R}_{M/4} = \frac{\mathbf{R}_0 + \mathbf{R}_{M/2}}{2} + \eta_{\beta/2} \qquad \text{and} \qquad \mathbf{R}_{3M/4} = \frac{\mathbf{R}_{M/2} + \mathbf{R}_M}{2} + \eta_{\beta/2}$$

Generalizing, at the l^{th} step, 2^{l-1} new points are sampled from a gaussian of suitable variance. The procedure must be repeated n times, until the desired number of slices is reached, as illustrated in Figure 2.2.

For free particles the Lévy construction gives the exact sampling, since it samples the coordinates from a gaussian distribution of right variance. To prove that, we can apply the Lévy construction to a chain of $M=3$ beads. In this case, two edges $\mathbf{R}_0$ and $\mathbf{R}_2$ are fixed and one must sample only the central point $\mathbf{R}_1$. For non interacting particles the correct path probability associated to the point $\mathbf{R}_1$ is given by the product of two gaussians

$$\Pi(\mathbf{R}_1|\mathbf{R}_0,\mathbf{R}_2) \propto e^{-\frac{(\mathbf{R}_1-\mathbf{R}_0)^2}{4\lambda\tau}} e^{-\frac{(\mathbf{R}_2-\mathbf{R}_1)^2}{4\lambda\tau}} \tag{2.82}$$

that we can expand separating the part that depends on $\mathbf{R}_1$

$$\begin{aligned}\Pi(\mathbf{R}_1|\mathbf{R}_0,\mathbf{R}_2) &\propto e^{-\frac{(2\mathbf{R}_1^2-2\mathbf{R}_0\mathbf{R}_1-2\mathbf{R}_2\mathbf{R}_1)}{4\lambda\tau}} e^{-\frac{(\mathbf{R}_2^2+\mathbf{R}_1^2)}{4\lambda\tau}} = e^{-\frac{(\mathbf{R}_2^2+\mathbf{R}_0^2-2\bar{\mathbf{R}}^2)}{4\lambda\tau}} e^{-\frac{(\mathbf{R}_1-\bar{\mathbf{R}})^2}{2\lambda\tau}} \\ &= A e^{-\frac{(\mathbf{R}_1-\bar{\mathbf{R}})^2}{2\lambda\tau}}\end{aligned} \tag{2.83}$$

where $A = \exp[-(\mathbf{R}_2^2 + \mathbf{R}_0^2 - 2\bar{\mathbf{R}}^2)/(4\lambda\tau)]$ and we have introduced the symbol $\bar{\mathbf{R}}$ to indicate the midpoint of the path: $\bar{\mathbf{R}} = (\mathbf{R}_1 + \mathbf{R}_2)/2$. The distribution of the point $\mathbf{R}_1$ is then a gaussian centered in $\bar{\mathbf{R}}$ with variance $\eta = \sqrt{\lambda\tau}$, as assumed in the Lévy construction.

In the presence of interaction this is no longer true and, in order to correct the sampling accounting of the particle interactions, it is necessary to add an acceptance test at the end of the path construction. However, if the path displacements are too large, frequent rejections of the attempted moves can occur and needlessly waste computational resources. The sampling can be performed more efficiently by adopting other algorithms. We choose the bisection algorithm [78], which can be viewed as a minor modification of the Lévy method. The difference consists in applying the acceptance test at each step of the path reconstruction (i.e. each time that new points of the path are added) rather than at the end of the procedure. Only if the new positions are accepted the path reconstruction proceed to the next step, otherwise the procedure is repeated from the beginning, discarding also the steps previously accepted.

The advantage of the bisection method with respect to the Lévy reconstruction relies on the fact that the application at each step of the acceptance test can help in discarding in advance the less favorable move, without waiting that the building procedure has arrived at the end, saving in this way large amounts of computer time. The reason may be better understood looking at Figure 2.2. At the l^{th} step of the Lévy reconstruction 2^{l-1} beads sampled together and than 2^{l-1} density matrices must be computed at once. The major part of the computational effort required by the algorithm is then spent in the more advanced steps of the algorithm. However, for those steps the intervals on which one applies the Lévy rule (2.81) have small time length and the new points cannot be too far from the midpoints of the respective intervals: the new positions have then high probability to be accepted. On the other hand, in the first step of the algorithm a single coordinate must be sampled. The trial move has the largest variance, $\eta_\tau = \sqrt{\lambda\tau}$, and is hence more likely to be source of rejection of the proposed path; on the other hand, it is also the cheapest from the point of view of the computational resources required, since it involves the calculation of only one density matrix. As a consequence if this move is discarded since the beginning the waste of computer time is quite limited, while if it is accepted, a noticeable jump forward in the path sampling is achieved. In order to guarantee that the detailed balance condition is overall satisfied, a modification of the acceptance test, accounting for the previous rejections, is required [78].

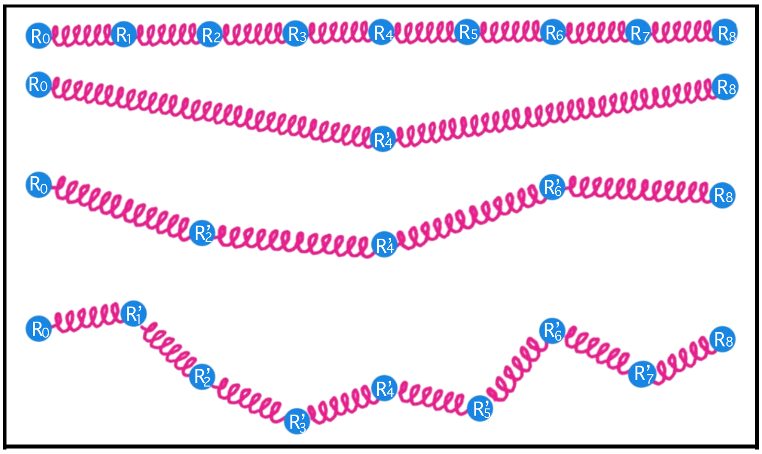

Figure 2.2. Illustration of the Lévy construction of the path, for $M = 8$ slices. The three construction steps are showed from top to bottom. To begin, all the links of the old path are deleted, leaving only the endpoints $\mathbf{R}_0$ and $\mathbf{R}_8$ unchanged. Then the construction starts: first, the point $\mathbf{R}_4$ is sampled according to (2.81), then other two points, $\mathbf{R}_2$ and $\mathbf{R}_6$, are obtained. Finally, with the sampling of the last four points ($\mathbf{R}_1$, $\mathbf{R}_3$, $\mathbf{R}_5$ and $\mathbf{R}_7$) the path construction is completed. In the bisection method the path building follows the same steps, apart for the fact that an acceptance test is applied each time a new set of points is sampled, rather than only at the end of the construction.

2.4.4 Estimators

In the previous section we have described the Path Integral Monte Carlo scheme that allows to compute the density matrix of a quantum system and to obtain the averages of observables related to thermodynamic quantities, for which, however, we still need to define suitable estimators. This section is devoted to the description of different estimators for the most common quantities of interest, namely the total energy, the kinetic energy and the pressure.

Before proceeding, let us recall the expressions of the partition function in the discretized path integral representation (2.67), which we will use to derive the estimators and which we can rewrite as

$$\mathcal{Z} = \int \prod_{i=0}^{M-1} d\mathbf{R}_i e^{-\sum_{i=0}^{M-1} \mathcal{S}(\mathbf{R}_i,\mathbf{R}_{i+1};\tau)} \tag{2.84}$$

where the functions S_i are given by

$$\mathcal{S}_i = \mathcal{S}(\mathbf{R}_i, \mathbf{R}_{i+1}; \tau) = \frac{3N}{2}\ln(4\pi\lambda\tau) + \frac{(\mathbf{R}_i - \mathbf{R}_{i+1})^2}{4\lambda\tau} + \mathcal{U}(\mathbf{R}_i, \mathbf{R}_{i+1}; \tau, \lambda) \tag{2.85}$$

In the primitive approximation $\mathcal{U}_i = \mathcal{U}(\mathbf{R}_i, \mathbf{R}_{i+1}; \tau, \lambda) = -\tau[\mathcal{V}(\mathbf{R}_i) + \mathcal{V}(\mathbf{R}_{i+1})]/2$. We have introduced this quantity to obtain more general expressions for the estimator of interest.

Thermodynamic estimators

The most straightforward way to obtain an energy estimator may seem to apply the definition of operator average to the Hamiltonian $\hat{\mathcal{H}}$: $\langle\hat{\mathcal{H}}\rangle = \mathrm{Tr}\{\hat{\rho}_\beta\hat{\mathcal{H}}\}/\mathrm{Tr}\{\hat{\rho}_\beta\}$. However, the application of the Hamiltonian operator $\hat{\mathcal{H}} = -\lambda\nabla^2 + \hat{\mathcal{V}}$ to the density matrix will produce terms that contains the gradient and the Laplacian of the functions $\mathcal{U}_i(\mathbf{R}_i, \mathbf{R}_{i+1}, \tau)$, whose determination requires a noticeable additional computational cost. For this reason, it is commonly preferred to employ different estimators.

Thermodynamic estimators of energy and pressure can be derived starting from the relationships of those quantities with the thermodynamic derivatives of the free energy $\mathcal{F}$

$$\mathcal{F} = -\frac{1}{\beta}\ln\mathcal{Z} \tag{2.86}$$

Let us start with the total energy. The average total energy can be obtained from the first derivative of the free energy with respect to the inverse of the temperature, as

$$E_T = \frac{\partial(\beta\mathcal{F})}{\partial\beta} = -\frac{\partial\ln\mathcal{Z}}{\partial\beta} = -\frac{1}{\mathcal{Z}}\frac{\partial\mathcal{Z}}{M\partial\tau} \tag{2.87}$$

where in the last equality we have substituted the β derivative with the derivative with respect to the time step $\tau = \beta/M$.

Using the expression (2.84) for the partition function and performing the τ derivative we easily obtain

$$E_T = \left\langle \sum_{i=0}^{M-1} \frac{1}{M}\frac{\partial S_i}{\partial\tau} \right\rangle = \left\langle \frac{\partial S_i}{\partial\tau} \right\rangle = \left\langle \frac{3N}{2\tau} - \frac{(\mathbf{R}_i - \mathbf{R}_{i+1})^2}{4\lambda\tau^2} + \frac{\partial\mathcal{U}_i}{\partial\tau} \right\rangle \tag{2.88}$$

where $\langle \cdots \rangle$ indicates a path average. In the final expression, we have considered only the contribution of a single slice i, being the contribution of each slice equal on average because of the time translational symmetry of the density matrices.

This estimator will converge to the exact energy of the system for sufficiently small values of τ. However, it may seem that the first and the second term on the right hand side of the previous expression will diverge for $\tau \to 0$. It can be proven that the kinetic contribution remains finite also at small τ, converging in this limit to the classical kinetic energy

$$\lim_{\tau \to 0} \left\langle \frac{3N}{2\tau} - \frac{(\mathbf{R}_i - \mathbf{R}_{i+1})^2}{4\lambda\tau^2} \right\rangle = \frac{3N}{2\beta} \tag{2.89}$$

Separate thermodynamic estimators of the kinetic and the potential energy contributions can be also be obtained. In order to derive an estimator for the kinetic energy, let us start from computing the derivative of the free energy with respect to $\lambda = \hbar^2/2m$, $\partial\mathcal{F}/\partial\lambda = -(\beta\mathcal{Z})^{-1}\partial\mathcal{Z}/\partial\lambda$. For sake of simplicity to obtain this derivative we do not use the path integral representation for the partition function and we write

$$\frac{\partial\mathcal{F}}{\partial\lambda} = -\frac{1}{\beta\mathcal{Z}}\frac{\partial}{\partial\lambda}\int d\mathbf{R}\,\langle\mathbf{R}|\,e^{-\beta(-\lambda\nabla^2+\hat{\mathcal{V}})}\,|\mathbf{R}\rangle \tag{2.90}$$

where $\mathbf{R}$ are now $3N-$dimensional vectors representing the particle coordinates. Starting from the general formula[5] for the derivative of an exponential operator

$$\frac{\partial}{\partial\lambda}\left[e^{\beta\hat{X}(\lambda)}\right] = \int_0^\beta e^{t\hat{X}(\lambda)}\frac{\partial\hat{X}(\lambda)}{\partial\lambda}e^{(\beta-t)\hat{X}(\lambda)}dt \tag{2.91}$$

and inverting the order of the integrals in t and in $\mathbf{R}$, equation (2.90) becomes

$$\frac{\partial\mathcal{F}}{\partial\lambda} = -\frac{1}{\beta\mathcal{Z}}\int_0^\beta dt\int d\mathbf{R}\,\langle\mathbf{R}|\,e^{t(\lambda\nabla^2-\hat{\mathcal{V}})}\nabla^2 e^{(\beta-t)(\lambda\nabla^2-\hat{\mathcal{V}})}\,|\mathbf{R}\rangle \tag{2.92}$$

We can now make a ciclic permutation of the operators into the trace, to reconstruct the operator $\exp[\beta(\lambda\nabla^2 - \hat{\mathcal{V}})]$ and eliminate the dependence on the variable t. In this way the integral over t can be performed trivially and we obtain

$$\frac{\partial\mathcal{F}}{\partial\lambda} = -\frac{1}{\beta\mathcal{Z}}\int_0^\beta dt\int d\mathbf{R}\,\langle\mathbf{R}|\,e^{\beta(\lambda\nabla^2-\hat{\mathcal{V}})}\nabla^2\,|\mathbf{R}\rangle = -\left\langle\nabla^2\right\rangle = \frac{1}{\lambda}\left\langle\hat{\mathcal{K}}\right\rangle \tag{2.93}$$

showing that the average kinetic energy is proportional to the partial derivative of the free energy $\mathcal{F}$ with respect to λ.

The thermodynamic estimator of the kinetic energy can be then obtained from the derivative $\partial\mathcal{F}/\partial\lambda$, proceeding in analogy with the derivation of the total energy estimator in order to arrive at an explicit formula.

We now use the path integral representation (2.84) of the partition function and equation (2.85) to get

$$\begin{aligned} K_T &= -\frac{1}{\beta\mathcal{Z}}\frac{\partial\mathcal{Z}}{\partial\lambda} = \frac{\lambda}{\tau}\left\langle\frac{\partial S_i}{\partial\lambda}\right\rangle = \frac{\lambda}{\tau}\left\langle\frac{3N}{2\lambda} - \frac{(\mathbf{R}_i - \mathbf{R}_{i+1})^2}{4\lambda^2\tau} + \frac{\partial\mathcal{U}_i}{\partial\lambda}\right\rangle \\ &= \left\langle\frac{3N}{2\tau} - \frac{(\mathbf{R}_i - \mathbf{R}_{i+1})^2}{4\lambda\tau^2} + \frac{\lambda}{\tau}\frac{\partial\mathcal{U}_i}{\partial\lambda}\right\rangle \end{aligned} \tag{2.94}$$

---

[5] see Appendix .3 for the derivation of this identity.

that represents the thermodynamic estimator for the kinetic energy.

Finally, we can obtain the potential energy thermodynamic estimator, as the difference between (2.88) and (2.94)

$$E_T - K_T = \left\langle \frac{\partial \mathcal{U}_i}{\partial \tau} - \frac{\lambda}{\tau}\frac{\partial \mathcal{U}_i}{\partial \lambda} \right\rangle = V_T \tag{2.95}$$

A thermodynamic estimator can be derived also for the pressure, as the first derivative of the free energy with respect to the volume Ω

$$P_T = \frac{1}{\beta \mathcal{Z}}\frac{\partial \mathcal{Z}}{\partial \Omega} = \frac{1}{M\tau\mathcal{Z}}\frac{\partial \mathcal{Z}}{\partial \Omega} \tag{2.96}$$

To compute the volume derivative let us introduce the dimensionless variables $\mathbf{S}_i = \mathbf{R}_i/\Omega^{1/3}$, allowing to rewrite

$$\begin{aligned} P_T &= \frac{1}{M\tau\mathcal{Z}}\frac{\partial}{\partial \Omega}\left[\Omega^{NM}\int \prod_{i=0}^{M-1} d\mathbf{S}_i e^{-\sum_{i=1}^{M}\mathcal{S}(\mathbf{S}_i,\mathbf{S}_{i+1}|\Omega)}\right] \\ &= \frac{1}{M\tau}\left[\frac{NM}{\Omega} - \left\langle \sum_{i=1}^{M} \frac{\partial \mathcal{S}(\mathbf{S}_i,\mathbf{S}_{i+1}|\Omega)}{\partial \Omega} \right\rangle\right] \end{aligned} \tag{2.97}$$

If we now use the fact that $\partial/\partial\Omega = \sum_k (\partial_\Omega \mathbf{R}_k)\nabla_{\mathbf{R}_k} = \sum_k \mathbf{R}_k \nabla_{\mathbf{R}_k}/(3\Omega)$, we can rewrite

$$\begin{aligned} \frac{\partial \mathcal{S}_i}{\partial \Omega} &= \frac{1}{3\Omega}\left(\mathbf{R}_i\nabla_{\mathbf{R}_i} + \mathbf{R}_{i+1}\nabla_{\mathbf{R}_{i+1}}\right)\mathcal{S}_i \\ &= \frac{2}{3\Omega}\frac{(\mathbf{R}_i - \mathbf{R}_{i+1})\cdot(\mathbf{R}_i - \mathbf{R}_{i+1})}{4\lambda\tau} - \frac{1}{3\Omega}\left[\mathbf{R}_i\nabla_{\mathbf{R}_i}\mathcal{U}_i + \mathbf{R}_{i+1}\nabla_{\mathbf{R}_{i+1}}\mathcal{U}_i\right] \end{aligned} \tag{2.98}$$

and we finally get, by averaging

$$P_T = \frac{1}{3\tau\Omega}\left\langle 3N - \frac{(\mathbf{R}_i - \mathbf{R}_{i+1})^2}{2\lambda\tau} + 2\mathbf{R}_i\nabla_{\mathbf{R}_i}\mathcal{U}_i \right\rangle \tag{2.99}$$

where, in the last term we have used the fact that $\mathcal{U}_i$ is symmetric with respect to $\mathbf{R}_i$ and $\mathbf{R}_{i+1}$ and then $\left\langle \mathbf{R}_i\nabla_{\mathbf{R}_i}\mathcal{U}_i + \mathbf{R}_{i+1}\nabla_{\mathbf{R}_{i+1}}\mathcal{U}_i \right\rangle = 2\left\langle \mathbf{R}_i\nabla_{\mathbf{R}_i}\mathcal{U}_i \right\rangle$.

Virial estimators

The main issue concerning the use of thermodynamic estimators is the huge variance of the estimated quantities, that increases with the number of slices. It has been observed that the most of the variance arises from the kinetic contribution to the energy. In fact, while the difference in (2.89) goes to the classical kinetic energy at low τ and then remains finite, the variance of this term diverges. To overcome this problem, Herman et al. [79] proposed a new estimator for the energy, the *virial estimator*, that, as the name suggest, can be derived in the primitive approximation by applying the virial theorem[6]. This estimator, recasting in a different form

---

[6] The virial theorem states that the average kinetic energy of a system can be obtained as $\langle K_V \rangle = -\left\langle \sum_{i=1}^{N} \mathbf{R}_i \cdot \mathbf{F}_i \right\rangle /2$, where $\mathbf{F}_i = -\nabla_i V$ is the total force on the $i-th$ particle.

the kinetic contributions to the total energy is able to noticeably reduce energy fluctuations.

Again, we will present here the expressions for the virial estimators obtained for a generic approximation of the density matrix. The general expression for the virial estimator of the total energy is given by (see Appendix .4 or Ref. [64] for the derivation)

$$E_V = \left\langle \frac{3N}{2M\tau} - \frac{1}{4M\tau^2\lambda}(\mathbf{R}_{M+i} - \mathbf{R}_i)\cdot(\mathbf{R}_{i+1} - \mathbf{R}_i) - \frac{1}{2}F_i\Delta_i + \frac{\partial \mathcal{U}_i}{\partial \tau} \right\rangle \tag{2.100}$$

where $F_i = -(\nabla_i \mathcal{U}_{i-1} + \nabla_i \mathcal{U}_i)/\tau$ and $\Delta_i = \sum_{j=-M+1}^{M-1}(\mathbf{R}_i - \mathbf{R}_{i+j})/2M$. The kinetic energy can be simply obtained by subtracting the potential energy contribution from (2.100)

$$K_V = E_V - \langle V \rangle \tag{2.101}$$

and the pressure, in Coulombian systems, can be computed as

$$P_V = \frac{1}{3\Omega}\left(2\left\langle K_V \right\rangle - \left\langle V \right\rangle\right) \tag{2.102}$$

To obtain the expression of the pressure estimator for a generic form of the interactions, we can notice, comparing (2.88) and (2.100), that

$$\left\langle \frac{3N}{2\tau} - \frac{(\mathbf{R}_i - \mathbf{R}_{i+1})^2}{4\lambda\tau} \right\rangle = \left\langle \frac{3N}{2M\tau} - \frac{1}{4M\tau^2\lambda}(\mathbf{R}_{M+i} - \mathbf{R}_i)\cdot(\mathbf{R}_{i+1} - \mathbf{R}_i) - \frac{1}{2}F_i\Delta_i \right\rangle \tag{2.103}$$

Substituting the average appearing in the expression for the pressure (2.99) with the right hand side of the previous equation we arrive at

$$P_V = \frac{2}{3\tau\Omega}\left\langle \frac{3N}{2M\tau} - \frac{1}{4M\tau^2\lambda}(\mathbf{R}_{M+i} - \mathbf{R}_i)\cdot(\mathbf{R}_{i+1} - \mathbf{R}_i) - \frac{1}{2}F_i\Delta_i - \mathbf{R}_i\nabla_{\mathbf{R}_i}\mathcal{U}_i \right\rangle \tag{2.104}$$

2.5 Quantum Monte Carlo methods for electrons

In the previous sections we have introduced the basic notions on Monte Carlo simulations for classical systems and described the path integral technique that allows to simulate the behavior of a quantum system at finite temperature. In this section we will describe two Quantum Monte Carlo techniques used to compute ground state properties of quantum systems, that we will apply in our calculations to obtain the Born-Oppenheimer energy for a given protonic configuration.

2.5.1 Trial wave functions

Before proceeding in the description of the QMC techniques let us introduce the wave function we adopt in our calculation to describe the electronic ground state.

The choice of a good trial wave function to represent the system is crucial in Quantum Monte Carlo methods since the overlap between ψ_T and the (a priori unknown) true ground state ψ_0 determines both the efficiency and the accuracy of the simulation. While in principle the final state reached in the QMC calculation is independent of the ψ_T, in practice we have to deal with finite human and computing time resources and hence a good starting guess for the wave function is important for speeding up the convergence. Moreover, there are features of the ψ_T that remains unchanged during the QMC simulation, as the nodal surface $\psi_T(\mathbf{r}) = 0$, biasing the final result.

The most general requirements that a trial wavefuncion ψ_T must satisfy are the following [67]

- To be an acceptable solution of a Schrödinger equation, ψ_T must be continuous and have a continuous and differentiable gradient $\nabla\psi_T$ wherever the potential is finite, in order for the kinetic energy to be well-defined.

- The integrals $\langle\psi_T|\,\psi_T\rangle$ and $\langle\psi_T|\,\hat{\mathcal{H}}\,|\psi_T\rangle$ must exist: the wave function must be normalizable and give a definite value of the expectation value of the energy.

- The integral $\langle\psi_T|\,\hat{\mathcal{H}}^2\,|\psi_T\rangle$ must exist too, in order to keep finite the energy variance σ ($\sigma^2 = \langle\hat{\mathcal{H}}^2\rangle - \langle\hat{\mathcal{H}}\rangle$).

- Last but not least, a good trial function must have the same simmetry of the problem.

A typical wave function, which can fulfill the previous conditions and is frequently used in QMC simulations to describe the electronic state, is the Slater-Jastrow wave function [80]

$$\psi_T(\mathbf{r},\mathbf{s}|\mathbf{R}) = e^{-\mathcal{J}(\mathbf{r}|\mathbf{R})}\mathcal{D}_N(\mathbf{r},\mathbf{s}|\mathbf{R}) \tag{2.105}$$

in which $\mathbf{r} = (\mathbf{r}_1, \cdots, \mathbf{r}_N)$ and $\mathbf{R} = (\mathbf{R}_1, \cdots, \mathbf{R}_N)$ are, respectively, the electronic and the protonic spatial coordinates and $\mathbf{s} = (s_1, \cdots, s_N)$ the electronic spins; $\mathcal{J}(\mathbf{r}|\mathbf{R})$ is the Jastrow term [81], containing correlations between pairs (or triplets) of particles; $\mathcal{D}(\mathbf{r},\mathbf{s}|\mathbf{R})$ is the $N \times N$ Slater determinant of single particle spin-orbitals $\psi(\mathbf{r}_i, s_i) = \phi_n(\mathbf{r}_i)\chi_\sigma(s_i)$, being $\phi_n(\mathbf{r}_i)$ the spatial part of the orbital and $\chi_\sigma(s_i)$ the spin functions $\chi_\sigma = \{\chi_\uparrow, \chi_\downarrow\}$

$$\mathcal{D}_N(\mathbf{r},\mathbf{s}) = \begin{vmatrix} \phi_1(\mathbf{r}_1)\chi_\uparrow(s_1) & \phi_1(\mathbf{r}_2)\chi_\uparrow(s_2) & \phi_1(\mathbf{r}_3)\chi_\uparrow(s_3) & \cdots & \phi_1(\mathbf{r}_N)\chi_\uparrow(s_N) \\ \phi_2(\mathbf{r}_1)\chi_\uparrow(s_1) & \phi_2(\mathbf{r}_2)\chi_\uparrow(s_2) & \phi_1(\mathbf{r}_3)\chi_\uparrow(s_3) & \cdots & \phi_2(\mathbf{r}_N)\chi_\uparrow(s_N) \\ \vdots & \vdots & \vdots & \vdots & \vdots \\ \phi_{N_\uparrow}(\mathbf{r}_1)\chi_\uparrow(s_1) & \phi_{N_\uparrow}(\mathbf{r}_2)\chi_\uparrow(s_2) & \phi_{N_\uparrow}(\mathbf{r}_3)\chi_\uparrow(s_3) & \cdots & \phi_{N_\uparrow}(\mathbf{r}_N)\chi_\uparrow(s_N) \\ \vdots & \vdots & \vdots & \vdots & \vdots \\ \phi_N(\mathbf{r}_1)\chi_\downarrow(s_1) & \phi_N(\mathbf{r}_2)\chi_\downarrow(s_2) & \phi_1(\mathbf{r}_3)\chi_\downarrow(s_3) & \cdots & \phi_N(\mathbf{r}_N)\chi_\downarrow(s_N) \end{vmatrix} \tag{2.106}$$

To simplify the notation, in this expression we omitted the parametric dependency on the nuclear coordinates $\mathbf{R}$. We also assumed that our system has a constant spin projection along the $z-$axis, i.e. that there are $N_\uparrow$ and $N_\downarrow$ electrons with spin up and spin down, respectively.

The presence of the determinant ensures the fermionic ψ_T to be totally antisymmetric under particle exchange. However, the evaluation of a Slater determinant is highly time consuming: for this reason we will use a modified form of the trial wave function in (2.105). Since we are interested in evaluating properties that do not depend on the spin, we can remove the spin dependency from the Slater determinant, imagining to assign to each electron a spin state that will be conserved during the simulation - let us say the spin up to particles from 1 to $N_\uparrow$ and the spin down to the others, from $N_\uparrow + 1$ to N. Under this hypothesis, the spin-down orbitals of the first $N_\uparrow$ electrons are empty as well as the spin-up orbitals of remanent $N_\downarrow$ electrons; the total $N \times N$ matrix of the spin orbitals becomes a block matrix, made of two blocks of dimension $N_\uparrow \times N_\uparrow$ and $N_\downarrow \times N_\downarrow$, and the total Slater determinant can be replaced with the product of the determinants of the two blocks. The Slater-Jastrow trial wave function (2.105) is then

$$\psi_T(\mathbf{r},\mathbf{s}|\mathbf{R}) = e^{-\mathcal{J}(\mathbf{r}|\mathbf{R})}\mathcal{D}_{N_\uparrow}(\mathbf{r}_\uparrow|\mathbf{R})\mathcal{D}_{N_\downarrow}(\mathbf{r}_\downarrow|\mathbf{R}) \tag{2.107}$$

where $\mathcal{D}_{N_\sigma}(\mathbf{r}_\sigma|\mathbf{R})$ are the reduced Slater determinants of electron orbitals of same spin $\sigma =\uparrow,\downarrow$ [67]

$$\mathcal{D}_{N_\uparrow}(\mathbf{r}_\uparrow) = \begin{vmatrix} \phi_1(\mathbf{r}_1) & \phi_1(\mathbf{r}_2) & \cdots & \phi_1(\mathbf{r}_{N_\uparrow}) \\ \phi_2(\mathbf{r}_1) & \phi_2(\mathbf{r}_2) & \cdots & \phi_2(\mathbf{r}_{N_\uparrow}) \\ \vdots & \vdots & \vdots & \vdots \\ \phi_{N_\uparrow}(\mathbf{r}_1) & \phi_{N_\uparrow}(\mathbf{r}_2) & \cdots & \phi_{N_\uparrow}(\mathbf{r}_{N_\uparrow}) \end{vmatrix} \tag{2.108}$$

and similarly from the spin down determinant. Usually we are treating spin unpolarized systems, with an equal number of electrons with spin up and with spin down, $N_\uparrow = N_\downarrow = N/2$, this assumption is particularly advantageous since the computational cost of the determinant evaluation is noticeably reduced.

Although this form of the wave function is not antisymmetric under exchange of two electrons of different spin, we can prove that it gives the right expectation values for spin-independent observables. To demonstrate that [80], we can start noticing that our choice to assign a spin up state to electrons from 1 to $N_\uparrow$ and a spin down state to the remanent $N_\downarrow$ is just one of the possible ways to describe a system with a fixed number of spin up and down: our choice was only most convenient, since it allowed to reduce the size of the original determinant. Let us indicate with S a generic sequence $S = \chi(\mathbf{s}_1), \cdots, \chi_\sigma(\mathbf{s}_N)$ that can be obtained considering $N_\uparrow$ spin up and $N_\downarrow$ spin down particles. For a given realization of the spins S, we can introduce the correspondent Slater-Jastrow wave function $\psi_S(\mathbf{r}, \mathbf{s}) = e^{-J(\mathbf{r})}\mathcal{D}_S(\mathbf{r}, \mathbf{s})$, where $\mathcal{D}_S(\mathbf{r}, \mathbf{s})$ is the $N \times N$ Slater determinant corresponding to the sequence of assigned spins S. A complete antisymmetric state is given by the sum of all the contributions arising from all the possible spin permutations, i.e. for all the possible sequences S given $N_\uparrow$ and $N_\downarrow$: $\psi_T = \sum_S \psi_S(\mathbf{r}, \mathbf{s})$. The expectation value of a given observable $\hat{\mathcal{O}}$ over this state is

$$\left\langle \hat{\mathcal{O}} \right\rangle = \frac{\sum_S \int \psi_S^*(\mathbf{r}, \mathbf{s})\mathcal{O}(\mathbf{r})\psi_S^*(\mathbf{r}, \mathbf{s})d\mathbf{r}}{\sum_S \int \psi_S^*(\mathbf{r}, \mathbf{s})\psi_S(\mathbf{r}, \mathbf{s})d\mathbf{r}} \tag{2.109}$$

In principle then, to compute correctly the averages we need to sum over all the spin sequences S. However, if the operator $\hat{\mathcal{O}}$ is not dependent on the spin, since the wave function ψ_T is by construction totally antisymmetric under particle exchange, we can substitute to each ψ_S its permutation corresponding to a given spin realization S_0 (in our case, we want to choose an S_0 in which the first $N_\uparrow$ electrons have spin up and the last $N_\downarrow$ have spin down). Each term of the sum over S will give the same contribution and hence (2.109) can be reduced to

$$\left\langle \hat{\mathcal{O}} \right\rangle = \frac{\int \psi_{S_0}^*(\mathbf{r}, \mathbf{s})\mathcal{O}(\mathbf{r})\psi_{S_0}(\mathbf{r}, \mathbf{s})d\mathbf{r}}{\int \psi_{S_0}^*(\mathbf{r}, \mathbf{s})\psi_{S_0}(\mathbf{r}, \mathbf{s})d\mathbf{r}} \tag{2.110}$$

which proves our statement.

The choice of the single particle orbitals $\phi_n(\mathbf{r})$ for the Slater determinants should be driven by the characteristics of the problem. It is possible to assume an analytic form for the $\phi_n(\mathbf{r})$, as in the case of the delocalized electrons in a metal which can be satisfactorily described by plane waves. However, in a general case it is preferable to adopt another approach. In order to obtain orbitals that can provide a more accurate description of the system, the ϕ_n can be obtained from Hartree-Fock or DFT calculations, by solving self-consistently the eigenvalue equations

$$\hat{h}_{\text{eff}}(\mathbf{r}|\mathbf{R})\phi_n(\mathbf{r}|\mathbf{R}) = \left[-\frac{1}{2}\nabla_{\mathbf{r}}^2 + V_{\text{eff}}(\mathbf{r}|\mathbf{R})\right]\phi_n(\mathbf{r}) = \epsilon_n(\mathbf{R})\phi_n(\mathbf{r}|\mathbf{R}) \tag{2.111}$$

in which the dependency on the nuclear coordinates $\mathbf{R}$ is only parametric.

Let us now describe the Jastrow part of the trial function, reporting, without demonstration, a number of exact results about its properties. Although a single Slater determinant can be by itself a valid approximation of the electronic eigenstate, it can miss of essential features possessed by the true wave function. One of the requirements about the trial wave function is that it must be continuous and with continuous and differentiable gradient wherever the potential is finite, to guarantee the kinetic energy to be well defined. However, when the distance between two particles reduces to zero, the potential energy diverges and the kinetic energy must diverge as well, in order to cancel the potential singularity and keep the total energy finite. This reflects in a cusp shape assumed by the wave function in the proximity of the potential divergences. The balancing among the potential and the kinetic energy divergences is ensured if the behavior of the wave function near $\mathbf{r}_i = \mathbf{r}_j$ (electron-electron cusp) or $\mathbf{r}_i = \mathbf{R}_J$ (electron-proton cusp) obeys to the so-called *Kato conditions* [82, 83]

$$\left.\frac{\partial \langle \psi_T(\mathbf{l}_{ij}) \rangle}{\partial l_{ij}}\right|_{\mathbf{l}_{ij}=0} = \mu_{ij} q_i q_j \psi_T(\mathbf{l}_{ij} = 0) \tag{2.112}$$

where, to simplify the notation, we have omitted in the argument of ψ_T the coordinates of all the particles but the pair i, j (or iJ); $\mathbf{l}_{ij}$ is the vectorial distance between the two particles i and j (which can be either two electrons or an electron and a proton), $l_{ij} = |\mathbf{l}_{ij}|$, $\mu_{ij} = m_i m_j/(m_i + m_j)$ is the reduced mass of the two particles, $q_i and q_j$ their charges and $\langle \psi_T \rangle$ the spherical average (over the angles defining the vector $\mathbf{l}_{ij}$) of the wave function around the singularity. Otherwise, the local energy will not be a well defined quantity.

Since the single particle orbitals used to build the determinants are not able to reproduce the correct behavior near the singularities, the introduction of an exponential "weighting" term $e^{-\mathcal{J}(\mathbf{r}|\mathbf{R})}$, the so-called Jastrow factor, can be used to impose the constraint (2.112) to the trial wave function so avoiding energy divergences. Moreover, the Jastrow term introduces in the wave function correlations not present in the determinants and can correct existing correlations.

The exponent in the Jastrow term can be represented as a sum of single and two body functions, of a suitable form

$$\mathcal{J}(\mathbf{r}|\mathbf{R}) = \sum_{i,j>i} u_{ee}(|\mathbf{r}_i - \mathbf{r}_j|) + \sum_{i,J} u_{ep}(|\mathbf{r}_i - \mathbf{R}_J|) \tag{2.113}$$

in which we separated electron-electron terms (the two body functions u_{ee}) and electron-proton contributions (the one body functions u_{ep}). Three body terms can eventually be added, to try to further improve the wave function.

The short range behavior of the u's must be such that the correct cusp (2.112) is reproduced. Moreover it was proven [84] that as $r \to \infty$ the Jastrow functions for Coulomb interactions must decay as r^{-1}. Analytic forms for the Jastrow functions with the correct limiting behaviors were computed by Gaskell [85] within the Random Phase Approximation (RPA)[7]. The Fourier components of the RPA Jastrow function are [86]

$$\begin{aligned} 2\rho u_{ee}^{RPA}(\mathbf{k}) &= -1 + \left(1 + \frac{2\rho v_k}{\epsilon_k}\right)^{1/2} && (2.114) \\ 2\rho u_{ep}^{RPA}(\mathbf{k}) &= -\frac{2\rho v_k/\epsilon_k}{(1 + 2\rho v_k/\epsilon_k)^{1/2}} && (2.115) \end{aligned}$$

---

[7] The Random Phase Approximation (RPA) is a theory developed by Bohm and Pines [84] to address the electron gas problem. They assumed, in the linear response regime, that the electrons respond to a total potential obtained as the sum of an external field (i.e. electron-nucleous) plus a screened potential (i.e. electron-electron potential). With the assumption that the density fluctuation in the reciprocal space are related only to same $\mathbf{k}$ component of the potential, they arrive at a particular form for the electronic response and for the dielectric functions. For more details see also [104]

being ρ the electronic density, $v_k = 4\pi/k^2$ and $\epsilon_k = \hbar^2 k^2/2m$.

The RPA Jastrow functions have by construction the correct behavior at long and short distances. At intermediate distances, however, the form of the Jastrow term can be improved with respect to the RPA by adding a parameter dependent correction of suitable functional form. The final expression for the Jastrow functions that we adopted for hydrogen is

$$u(\mathbf{l}_{ij}) = u^{RPA}(\mathbf{l}_{ij}) + a_{\mathcal{J}} e^{-b_{\mathcal{J}} l_{ij}^2} \tag{2.116}$$

where $\mathbf{l}_{ij}$ can represent an electron-electron distance $\mathbf{l}_{ij} = \mathbf{r}_i - \mathbf{r}_j$ (in the case of the two body function u_{ee}) or an electron-proton distance $\mathbf{l}_{ij} = \mathbf{r}_i - \mathbf{R}_J$ (for the one body function u_{ep}) and $a_{\mathcal{J}}$ and $b_{\mathcal{J}}$ are two parameters whose values can be numerically optimized [67]. [8]

The Slater-Jastrow wave function can be improved with the addition of a transformation of the coordinates $\mathbf{r}_i$ inside the determinants $\mathcal{D}_s(\mathbf{r})$, the so-called backflow transformation [86, 87]. First introduced by Feynman [88] - on the base of current-conservation arguments - to describe the excitation wave-functions of superfluid helium, this transformation inserts a supplementary correlation between the particles by mixing the electronic coordinates

$$\mathbf{r}_i \rightarrow \mathbf{q}_i = \mathbf{r}_i + \sum_{ij} \eta_{ij}(\mathbf{r}_{ij})\mathbf{r}_j \tag{2.117}$$

The form of the $\eta_{ij}(\mathbf{r}_{ij})$ describing the backflow transformation can be derived following different procedures [86]. As for the Jastrow functions, the expression for the backflow functions $\eta_{ij}(\mathbf{r}_{ij})$ can be computed for the electron gas within the RPA approximation [86] and then a mid range, parameter-dependent correction $\tilde{\eta}$ can be added, leading to the final formula

$$\eta_{ij}(\mathbf{r}_{ij}) = \eta_{ij}^{RPA}(\mathbf{r}_{ij}) + \tilde{\eta}_{ij}(\mathbf{r}_{ij}) \tag{2.118}$$

where

$$\tilde{\eta}_{ij}(\mathbf{r}_{ij}) = \gamma_1 e^{-(r_{ij}-\gamma_2)^2/\gamma_3^2} \tag{2.119}$$

and γ_1, γ_2 and γ_3 are additional variational parameters whose numerical value is determined by optimizing the wave function with respect to them [67]. The use of backflow transformations into the determinants can help in better approaching the true ground state. We will speak about the importance of the nodal surface in Section 2.5.5 regarding the fermion sign problem. For the moment let us just say that it has been observed [86] that the introduction of backflow transformations, allowing to modify the nodal surface of the trial wave function, can be useful to obtain lower energy states.

2.5.2 Variational Monte Carlo

The Variational Monte Carlo (VMC) is the simplest approach among the Quantum Monte Carlo methods [65]. It allows to optimize the electronic wave function starting

---

[8] Details on our optimization procedure will be presented at the end of this Chapter, in Section 2.6.4, once completed the discussion of our simulation technique, necessary background to understand the contents of the Section.

from an initial guess $\psi_T(\mathbf{r})$ and using the variational principle.

If the ground state is not degenerate, from the variational principle we know that the expectation value E_T of the Hamiltonian $\hat{\mathcal{H}}$ over the trial wave function ψ_T is an upper bound for the exact ground state energy E_0

$$E_T = \frac{\int \psi_T^* \mathcal{H} \psi_T d\mathbf{r}}{\int \psi_T^* \psi_T d\mathbf{r}} \geqslant E_0 \tag{2.120}$$

the equality holding only if ψ_T is the ground state of $\hat{\mathcal{H}}$.

In order to use the Monte Carlo techniques to compute the integral appearing in (2.120) we rewrite the energy as [89]

$$E_T = \frac{\int \psi_T^* \mathcal{H} \psi_T d\mathbf{r}}{\int \psi_T^* \psi_T d\mathbf{r}} = \frac{\int (\psi_T^* \psi_T)(\psi_T^{-1} \mathcal{H} \psi_T) d\mathbf{r}}{\int \psi_T^* \psi_T d\mathbf{r}} = \int \pi(\mathbf{r}) E_L(\mathbf{r}) d\mathbf{r} = \langle E_L \rangle_\pi \tag{2.121}$$

where we have defined the local energy $E_L = \psi_T^{-1} \mathcal{H} \psi_T$ and we are interpreting the square modulus of the normalized wave function as a probability density $\pi(\mathbf{r}) = |\psi_T(\mathbf{r})|^2 / \int |\psi_T(\mathbf{r})|^2 d\mathbf{r}$.

We then estimate the trial energy as the average of the local energy over a set of points in the electronic configuration space, $\mathbf{r}_i (i = 1, \cdots, M)$, sampled according to the probability $\pi(\mathbf{r})$

$$E_T = \langle E_L \rangle \approx \frac{1}{M} \sum_{i=1}^{M} E_L(\mathbf{r}_i) \tag{2.122}$$

An important quantity to monitor is the variance of the local energy, $\sigma_L^2 = \langle E_L^2 \rangle - \langle E_L \rangle^2$. Indeed, looking at (2.121) we can notice that when ψ_T is an eigenfunction of the Hamiltonian, the local energy does not depend on the electronic coordinates and therefore its variance vanishes. It follows that, for a generic trial wave function, the value of σ_L^2 is a measure of its quality: the more ψ_T approaches the ground state, the lower will be not only the energy but also the variance. Since we do not know the minimum of the energy (i.e. the ground state energy of the system) but we know that for a true eigenfunction its variance must be zero, it is easier to check the quality of the wave function by looking also at σ_L^2 instead of E_L alone.

Usually in the VMC implementations wave function optimization steps are alternated to the electronic space sampling. Indeed in the previous section we saw that the trial wave function depends on a set of parameters $\{\alpha_i\}$. Those parameters can be varied according to some minimization algorithm to achieve low energy/variance states, that, as stated by the variational principle, are much closer to the ground state.

In our simulation technique, the Coupled Electron-Ion Monte Carlo method, the calculation of the electronic ground state energy, at fixed protons, must be performed each time the proton arrangement is changed. In the first CEIMC implementation, M. Dewing et al. [90] in considering fluid molecular hydrogen assumed as trial function a Slater determinant of gaussian molecular orbitals centered on the bond center of each molecule. Each gaussian was represented by an independent set of 3 parameters (the weight, the center and the variance of the gaussian). In those calculations the optimization of the variational parameters of the electronic wave function, in number proportional to the number of electrons, was carried on after each protonic step. Because of the large number of variational parameters in the wave function, the optimization was however the major bottleneck of the method. In our present CEIMC implementation, we use self-consistent single electron orbitals, obtained from DFT, to build the ψ_T: the starting form of the wave function is then closer to the ground state function and we can safely adopt a wave function with few variational parameters, as described in the previous section. Details about the wave function optimization applied in our simulations are presented in Section 2.6.4, where we also show that the energy gain in the optimization is of a limited amount only ($\sim 1mHa$/particle). For this reason, instead of repeating the wave function optimization at each protonic move, the values of the variational parameters can be fixed after a preliminary optimization.

2.5.3 Reptation Quantum Monte Carlo

A further improvement of the QMC results can be achieved using a different type of Quantum Monte Carlo algorithms, usually indicated with the generic name of Projection MC. The idea beyond these techniques is that, if there exist a finite energy gap among the ground state and the first excited state, the components of the trial wave function orthogonal to the ground state can be zeroed by applying the operator $\hat{\rho}_t = e^{-t\hat{\mathcal{H}}}$, where t is a positive real number. This is evident if we decompose the trial wave function into a linear combination of the Hamiltonian eigenstates $|\phi_n\rangle$

$$|\psi_T\rangle = \sum_n c_n |\phi_n\rangle \tag{2.123}$$

and then compute the expectation value of the energy over the state $|\psi_T(t/2)\rangle = e^{-t\hat{\mathcal{H}}/2}|\psi_T\rangle$

$$\left\langle \hat{\mathcal{H}} \right\rangle_{t/2} = \frac{\langle\psi_T(t/2)|\,\hat{\mathcal{H}}\,|\psi_T(t/2)\rangle}{\langle\psi_T(t/2)\,|\psi_T(t/2)\rangle} = \frac{\sum_n |c_n|^2 e^{-t\mathcal{E}_n}\mathcal{E}_n}{\sum_n |c_n|^2 e^{-t\mathcal{E}_n}} = \frac{\sum_n |c_n|^2 e^{-t(\mathcal{E}_n-\mathcal{E}_0)}\mathcal{E}_n}{\sum_n |c_n|^2 e^{-t(\mathcal{E}_n-\mathcal{E}_0)}} \tag{2.124}$$

where in the last equality we multiplied both numerator and denominator by $\exp(t\mathcal{E}_0)$. Thinking of the parameter t as the analogous of imaginary time , $\bar{t} = -it\hbar$, the operator $\hat{\rho}_t$ assume the meaning of an imaginary-time evolution operator. The symbol $\langle\cdots\rangle_{t/2}$ indicates the expectation value over the state $\psi_T(t/2)$, i.e. over the trial wave function evolved for a "time" $t/2$.

In the limit $t \to \infty$ we get

$$\lim_{t\to\infty}\left\langle \hat{\mathcal{H}} \right\rangle_{t/2} = \mathcal{E}_0 \tag{2.125}$$

since the excited state components ($n > 0$ terms) decay exponentially as $t \to \infty$, being the difference $\mathcal{E}_n - \mathcal{E}_0$ between the n^{th} exited state and the ground state energies always positive. This prove that the state $|\psi_T(t)\rangle$ tends to the ground state as the value of t increases.

Despite different projection schemes have been developed, we will limit here to the description of the method adopted in our CEIMC code: the Reptation Quantum Monte Carlo (RQMC) [66]. Formally, the RQMC has many similarities with the Path Integral MC tecnhique: indeed, the operator $\hat{\rho}_\beta = \exp[-\beta\hat{\mathcal{H}}]$, density matrix of a quantum system at temperature $T = (k_B\beta)^{-1}$, is formally equal to the operator $\hat{\rho}_t$ we want to use to zero the excited state components of the trial wave function. It follows that some ideas exposed in the PIMC section 2.4 can be used to derive the basic equations of the RQMC method. In particular, we will exploit the path integral formalism.

In order to derive the equations that defines the Reptation Monte Carlo algorithm, let us start introducing the function $\mathcal{Z}_T(t)$, normalization of the averages carried on over the trial wave function propagated for a time $t/2$

$$\mathcal{Z}_T(t) = \langle \psi_T(t/2) | \, \psi_T(t/2) \rangle = \langle \psi_T | \, e^{-t\hat{\mathcal{H}}} \, | \psi_T \rangle \tag{2.126}$$

$\mathcal{Z}_T(t)$ is the generating function of the moments of $\hat{\mathcal{H}}$, from which it is possible to obtain the energy $E(t)$ and its variance $\sigma_E^2(t)$ as

$$\begin{aligned} E(t) &= \left\langle \hat{\mathcal{H}} \right\rangle_{t/2} = -\frac{\partial}{\partial t} \ln \mathcal{Z}(t) && (2.127) \\ \sigma_E^2(t) &= \left\langle \left(\hat{\mathcal{H}} - E(t) \right)^2 \right\rangle_{t/2} = \frac{\partial^2}{\partial t^2} \ln \mathcal{Z}(t) = -\frac{\partial}{\partial t} E(t) \geq 0 && (2.128) \end{aligned}$$

From the variational principle we know that $E(t)$ is an upper bound for the ground state energy E_0; since the variance is a definite positive quantity, from the last two terms of (2.128) it follows that the energy $E(t)$ decreases monotonically with the time t, until the ground state, corresponding to the state of minimum energy and zero variance, is reached.

Given a generic observable $\hat{\mathcal{O}}$, its expectation value over the state achieved at time $t/2$ can be determined as

$$\begin{aligned} \left\langle \hat{\mathcal{O}} \right\rangle_{t/2} &= \frac{\langle \psi_T(t/2) | \, \hat{\mathcal{O}} \, | \psi_T(t/2) \rangle}{\langle \psi_T(t/2) | \, \psi_T(t/2) \rangle} = \frac{\langle \psi_T | \, e^{-t\hat{\mathcal{H}}/2} \hat{\mathcal{O}} e^{-t\hat{\mathcal{H}}/2} \, | \psi_T \rangle}{\langle \psi_T | \, e^{-t\hat{\mathcal{H}}} \, | \psi_T \rangle} \\ &= \frac{1}{\mathcal{Z}(t)} \int d\mathbf{r} d\mathbf{r}' d\mathbf{r}'' d\mathbf{r}''' \psi_T^*(\mathbf{r}) \rho(\mathbf{r}, \mathbf{r}'; t/2) \mathcal{O}(\mathbf{r}', \mathbf{r}'') \rho(\mathbf{r}'', \mathbf{r}'''; t/2) \psi_T(\mathbf{r}''') \end{aligned} \tag{2.129}$$

where, in the last line we have introduced the coordinate representation of the operator $\hat{\rho}_t$, formally analogous to a thermal density matrix

$$\rho(\mathbf{r}, \mathbf{r}'; t) = \langle \mathbf{r} | \, e^{-t\hat{\mathcal{H}}} \, | \mathbf{r}' \rangle \tag{2.130}$$

$\hat{\rho}_t$ is related to the generating function $\mathcal{Z}(t)$ by

$$\mathcal{Z}(t) = \int d\mathbf{r} d\mathbf{r}' \, \langle \psi_T | \, \mathbf{r} \rangle \, \langle \mathbf{r} | \, e^{-t\hat{\mathcal{H}}} \, | \mathbf{r}' \rangle \, \langle \mathbf{r}' \, | \psi_T \rangle = \int d\mathbf{r} d\mathbf{r}' \psi_T^*(\mathbf{r}) \rho(\mathbf{r}, \mathbf{r}'; t) \psi_T(\mathbf{r}') \tag{2.131}$$

If the time t is large enough, the initial trial wave function evolved with the operator $\hat{\rho}_{t/2}$ will converge to the true electronic ground state Ψ_0 and the average (2.129) will represent the expectation value of the observable $\hat{\mathcal{O}}$ over the ground state. Hence, in order to be able to compute the ground state averages we first need to obtain an explicit expression for the matrix elements of the operator $\hat{\rho}_t$. In the PIMC section

2.4, we discussed the analogous problem of the thermal density matrix calculation for a system of generic Hamiltonian $\hat{\mathcal{H}}$ and its solution using the path integral formalism; to determine the matrix elements (2.130) we proceed in a similar way, showing here only the main points of the derivation of the explicit expression of the $\rho(\mathbf{r},\mathbf{r}';t)$ and referring to Section 2.4 for additional details.

First we factorize the time interval $[0,t]$ into the product of M sub intervals of equal length $\tau = t/M$, to rewrite

$$\rho(\mathbf{r},\mathbf{r}';t) = \int \prod_{i=1}^{M-1} d\mathbf{r}_i \left(\prod_{i=1}^{M} \langle \mathbf{r}_{i-1} | \, e^{-\tau\hat{\mathcal{H}}} \, | \mathbf{r}_i \rangle \right) = \int \prod_{i=1}^{M-1} d\mathbf{r}_i \left(\prod_{i=1}^{M} \rho(\mathbf{r}_{i-1},\mathbf{r}_i;\tau) \right) \tag{2.132}$$

with the conditions $\mathbf{r}_0 = \mathbf{r}$ and $\mathbf{r}_M = \mathbf{r}'$.

In the PIMC section 2.4, we have seen that for τ small enough it is possible to find accurate approximations for the density matrix. We discussed the primitive approximation and the pair density matrix approximation. Analogous forms can be in principle used in the RQMC for the $\rho(\mathbf{r}_{i-1},\mathbf{r}_i;\tau)$. However, mainly for historical reasons, in the context of ground state Quantum Monte Carlo methods, a different approach has been developed, known as “importance sampling”. The underlying idea is based on the observation that while the potential energy is a wildely varing function in the configurational space of electrons, the local energy $E_L(\mathbf{r}) = \psi_T^{-1}(\mathbf{r})\hat{\mathcal{H}}\psi_T(\mathbf{r})$ has a smoother behavior and becomes a constant[9] for an exact hamiltonian eigenfunction. Rather than separating the Hamiltonian operator $\hat{\mathcal{H}}$ as $\hat{\mathcal{H}} = \hat{\mathcal{K}} + \hat{\mathcal{V}}$, as done to derive the primitive approximation, it is more convenient then to rewrite

$$\hat{\mathcal{H}} = \hat{\mathcal{H}}' + \hat{E}_L \tag{2.133}$$

where

$$\hat{\mathcal{H}}' = -\lambda\nabla^2 + \lambda\psi_T^{-1}\nabla^2\psi_T, \qquad \hat{E}_L = V - \lambda\psi_T^{-1}\nabla^2\psi_T \tag{2.134}$$

being $\lambda = \hbar^2/2m_e$.

For τ small enough, we can factorize the operator $\exp[-\tau(\hat{\mathcal{H}} = \hat{\mathcal{H}}' + \hat{E}_L)]$ applying the symmetric formula (2.59) and obtaining

$$\begin{aligned} \rho(\mathbf{r}_{i-1},\mathbf{r}_i;\tau) &\approx \langle \mathbf{r}_{i-1} | \, e^{-\tau\hat{\mathcal{H}}'} \, | \mathbf{r}_i \rangle \, e^{-\frac{\tau}{2}[E_L(\mathbf{r}_i)+E_L(\mathbf{r_{i-1}})]} & (2.135) \\ &= \rho'(\mathbf{r}_{i-1},\mathbf{r}_i;\tau) e^{-\frac{\tau}{2}[E_L(\mathbf{r}_i)+E_L(\mathbf{r_{i-1}})]} & (2.136) \end{aligned}$$

The factor $\rho'(\mathbf{r}_{i-1},\mathbf{r}_i;\tau)$ can be determined by requiring that $\tilde{\rho}$ satisfies the Bloch equation for $\hat{\mathcal{H}}'$

$$-\partial_\tau \rho'(\mathbf{r}_{i-1},\mathbf{r}_i;\tau) = \hat{\mathcal{H}}'\rho'(\mathbf{r}_{i-1},\mathbf{r}_i;\tau) \tag{2.137}$$

with the initial condition $\tilde{\rho}(\mathbf{r}_{i-1},\mathbf{r}_i;0) = \delta(\mathbf{r}_{i-1} - \mathbf{r}_i)$. In the limit of small τ, defining $\mathbf{F} = 2\nabla\mathrm{ln}\psi_T$ and assuming that for small enough τ we can approximate $1 + \tau(\nabla\mathbf{F} + \mathbf{F}^{-1}\nabla^2\mathbf{F}) \approx 1$, it can be proven by substitution into (2.137) that the desired solution is

$$\tilde{\rho}(\mathbf{r}_{i-1},\mathbf{r}_i;\tau) = \frac{\psi_T(\mathbf{r}_{i-1})}{\psi_T(\mathbf{r}_i)} \left(\frac{1}{4\pi\lambda\tau}\right)^{3N/2} \exp\left[-\frac{|\mathbf{r}_i - \mathbf{r}_{i-1} - 2\lambda\tau\mathbf{F}_{i-1}|^2}{4\lambda\tau}\right] \tag{2.138}$$

---

[9] for a given protonic configuration: in fact the local energy remains a function of the protonic coordinates **R**.

where $\mathbf{F}_{i-1} = \mathbf{F}(\mathbf{r}_{i-1})$.

The new factorization of the $\rho(\mathbf{r}_{i-1}, \mathbf{r}_i; \tau)$ is advantageous with respect to the standard primitive approximation because of the presence of the smooth local energy instead of the fluctuating potential. Notwithstanding the use of a symmetric factorization, the obtained $\rho(\mathbf{r}_{i-1}, \mathbf{r}_i; \tau)$ is not symmetric under exchange of $\mathbf{r}_i$ and $\mathbf{r}_{i-1}$. In order to restore this important property of the exact propagator we can define a symmetrized form as $\ln(\rho_s(\mathbf{r}_{i-1}, \mathbf{r}_i; \tau)) = [\ln(\rho(\mathbf{r}_{i-1}, \mathbf{r}_i; \tau)) + \ln(\rho(\mathbf{r}_i, \mathbf{r}_{i-1}; \tau))]/2$. We get

$$\rho_s(\mathbf{r}, \mathbf{r}'; t) = \int \prod_{i=0}^{M} d\mathbf{r}_i (4\pi\lambda\tau)^{-\frac{3NM}{2}} e^{-\tau \sum_{i=1}^{M} L(\mathbf{r}_i, \mathbf{r}_{i-1}; \tau)} e^{-\tau \left[\sum_{i=1}^{M-1} E_L(\mathbf{r}_i) + \frac{E_L(\mathbf{r}_0) + E_L(\mathbf{r}_M)}{2}\right]} \tag{2.139}$$

where

$$L(\mathbf{r}_i, \mathbf{r}_{i-1}; \tau) = \frac{|\mathbf{r}_i - \mathbf{r}_{i-1}|^2}{4\lambda\tau^2} + \frac{\lambda}{2}\left(\mathbf{F}_{i-1}^2 + \mathbf{F}_i^2\right) - \frac{(\mathbf{r}_i - \mathbf{r}_{i-1}) \cdot (\mathbf{F}_{i-1} - \mathbf{F}_i)}{2\tau} \tag{2.140}$$

Before to proceed, let us compare now (2.139) and (2.140) with the corresponding primitive expression (2.67). In the present expression the role of the potential is played by the local energy, that, as anticipated, is a more regular function of the electronic coordinates. Moreover the gaussian term, representing in the primitive approximation the free particle contribution, is different because of the presence of the functions $\mathbf{F}(\mathbf{r})$, which have the effect of moving the center of the gaussians to the regions of higher $|\psi_T|^2$. The quantity $\mathbf{F}(\mathbf{r})$ is for this reason called drift force.

In the continuous limit ($t = M\tau$, $\tau \to 0$ and $M \to \infty$) the multidimensional integration over the discrete variables $\mathbf{r}_i$ is substituted by a functional integration over the continuous variable $\mathbf{r}(t)$. We obtain

$$\begin{aligned} \rho(\mathbf{r}, \mathbf{r}'; t) &= \int_{\substack{\mathbf{r}(0)=\mathbf{r} \\ \mathbf{r}(t)=\mathbf{r}'}} \mathcal{D}\mathbf{r} \exp\left[-\int_0^t d\tau \left(L(\mathbf{r}(\tau)) + E_L(\mathbf{r}(\tau))\right)\right] && (2.141) \\ &\propto \left\langle \exp\left[-\int_0^t d\tau E_L(\mathbf{r}(\tau))\right] \right\rangle_{DP_{\mathbf{r}\to\mathbf{r}'}} && (2.142) \end{aligned}$$

where the symbol $\langle \cdots \rangle_{DP_{\mathbf{r}\to\mathbf{r}'}}$ indicates the average over the "drifted" paths (DP) starting at $\mathbf{r}(0) = \mathbf{r}$ and ending at $\mathbf{r}(t) = \mathbf{r}'$, of distribution proportional to $\exp(-\int_0^t L(\mathbf{r}(\tau))d\tau)$. In Section 2.4 we derived a similar expression for the thermal density matrix in the primitive approximation.

Using this form for the $\hat{\rho}_t$ in (2.131), the generating function becomes

$$\mathcal{Z}_T(t) = \int d\mathbf{r}d\mathbf{r}' \psi_T(\mathbf{r}) \left\langle \exp\left[-\int_0^t d\tau E_L(\mathbf{r}(\tau))\right] \right\rangle_{DP_{\mathbf{r}\to\mathbf{r}'}} \psi_T(\mathbf{r}') \tag{2.143}$$

and the average of a generic operator $\hat{\mathcal{O}}$ is

$$\begin{aligned} \left\langle \hat{\mathcal{O}} \right\rangle_{t/2} = &\int d\mathbf{r}d\mathbf{r}'d\mathbf{r}''d\mathbf{r}''' \psi_T(\mathbf{r}) \left\langle \exp\left[-\int_0^{t/2} d\tau E_L(\mathbf{r}(\tau))\right] \right\rangle_{DP_{\mathbf{r}\to\mathbf{r}'}} \mathcal{O}(\mathbf{r}', \mathbf{r}'') \\ &\left\langle \exp\left[-\int_0^{t/2} d\tau E_L(\mathbf{r}(\tau))\right] \right\rangle_{DP_{\mathbf{r}''\to\mathbf{r}'''}} \psi_T(\mathbf{r}''') \end{aligned} \tag{2.144}$$

For the energy estimator, however, a more efficient form can be found, in which the local energy appears. Using the fact that $\hat{\rho}_t$ and $\hat{\mathcal{H}}$ are commuting operators we can permute the operator $\hat{\mathcal{H}}$ with one of the two exponentials $\exp[-t\hat{\mathcal{H}}/2]$ appearing in brackets and rewrite

$$E_T = \left\langle \hat{\mathcal{H}} \right\rangle_{t/2} = \frac{\langle \psi_T | \, e^{-t\hat{\mathcal{H}}} \hat{\mathcal{H}} \, | \psi_T \rangle}{\langle \psi_T | \, e^{-t\hat{\mathcal{H}}} \, | \psi_T \rangle} = \frac{\langle \psi_T | \, \hat{\mathcal{H}} e^{-t\hat{\mathcal{H}}} \, | \psi_T \rangle}{\langle \psi_T | \, e^{-t\hat{\mathcal{H}}} \, | \psi_T \rangle} \tag{2.145}$$

Introducing the local energy, the previous expression becomes

$$\begin{aligned} E_T &= \frac{1}{\mathcal{Z}(t)} \int d\mathbf{r} d\mathbf{r}' \psi_T(\mathbf{r}) \rho(\mathbf{r}, \mathbf{r}'; t) \hat{\mathcal{H}} \psi_T(\mathbf{r}') \\ &= \frac{1}{\mathcal{Z}(t)} \int d\mathbf{r} d\mathbf{r}' \psi_T(\mathbf{r}) \rho(\mathbf{r}, \mathbf{r}'; t) \psi_T(\mathbf{r}') \psi_T^{-1}(\mathbf{r}') \hat{\mathcal{H}} \psi_T(\mathbf{r}') \\ &= \frac{1}{\mathcal{Z}(t)} \int d\mathbf{r} d\mathbf{r}' \psi_T(\mathbf{r}) \rho(\mathbf{r}, \mathbf{r}'; t) \psi_T(\mathbf{r}') E_L(\mathbf{r}') \end{aligned} \tag{2.146}$$

or, equivalently, by permuting $\hat{\rho}$ and $\hat{\mathcal{H}}$ in the first line of the previous formula

$$E_T = \frac{1}{\mathcal{Z}(t)} \int d\mathbf{r} d\mathbf{r}' E_L(\mathbf{r}) \psi_T(\mathbf{r}) \rho(\mathbf{r}, \mathbf{r}'; t) \psi_T(\mathbf{r}') \tag{2.147}$$

It is then possible (and convenient) to estimate the energy as

$$\left\langle \hat{\mathcal{H}} \right\rangle = E_T = \frac{1}{2} \left\langle E_L(\mathbf{r}) + E_L(\mathbf{r}') \right\rangle \tag{2.148}$$

being $\langle \cdots \rangle$ the electronic average (represented by an average over the path distribution $\propto \psi_T(\mathbf{r}) \rho(\mathbf{r}, \mathbf{r}'; t) \psi_T(\mathbf{r}')$).

Analogously the variance of the energy is

$$\begin{aligned} \sigma_E^2 &= \left\langle \hat{\mathcal{H}}^2 \right\rangle - \left\langle \hat{\mathcal{H}} \right\rangle^2 = \frac{1}{\mathcal{Z}(t)} \int d\mathbf{r} d\mathbf{r}' \psi_T(\mathbf{r}) \hat{\mathcal{H}} \rho(\mathbf{r}, \mathbf{r}'; t) \hat{\mathcal{H}} \psi_T(\mathbf{r}') - E_T^2 \\ &= \frac{1}{\mathcal{Z}(t)} \int d\mathbf{r} d\mathbf{r}' \psi_T(\mathbf{r}) \hat{\mathcal{H}} \psi_T^{-1}(\mathbf{r}) \psi_T(\mathbf{r}) \rho(\mathbf{r}, \mathbf{r}'; t) \psi_T(\mathbf{r}') \psi_T^{-1}(\mathbf{r}') \hat{\mathcal{H}} \psi_T(\mathbf{r}') - E_T^2 \\ &= \frac{1}{\mathcal{Z}(t)} \int d\mathbf{r} d\mathbf{r}' E_L(\mathbf{r}) \psi_T(\mathbf{r}) \rho(\mathbf{r}, \mathbf{r}'; t) \psi_T(\mathbf{r}') E_L(\mathbf{r}') - E_T^2 \end{aligned} \tag{2.149}$$

The energy variance σ_E^2 will vanish if the time t is long enough for the two ends of the path to be uncorrelated.

2.5.4 Path sampling: the bounce algorithm

To sample the paths in the PIMC method we adopted the bisection construction, that allows to efficiently reconstruct portions of the single particle paths among two fixed extremes. Conventionally this construction is not used in the RQMC, in part for historical reasons, since the PIMC and the RQMC methods have been developed independently. Moreover in the RQMC scheme we are dealing with open paths, then the "reptile" motion we will describe in this section is in some sense more natural to apply. Finally, in the CEIMC scheme it is more efficient to move all electrons at once[10] and in this case a reptation algorithm allows to keep a good acceptance rate of moves compared to a global bisection algorithm.

Let $\mathbf{P}$ be a sequence of $M+1$ points in the electronic configuration space, i.e. a set of $3N(M+1)$ coordinates representing a path of total lenght $M\tau$: $\mathbf{P} = \{\mathbf{r}_0, \cdots, \mathbf{r}_M\}$. The probability distribution of the paths $\pi(\mathbf{P})$ can be obtained from the expression (2.131) of the generating function, using the form (2.139) for the matrix elements $\rho(\mathbf{r}, \mathbf{r}'; t)$

$$\pi(\mathbf{P}) = |\psi_T(\mathbf{r}_0)\psi_T(\mathbf{r}_M)|\, e^{-\sum_{i=1}^{M} L(\mathbf{r}_i,\mathbf{r}_{i-1};\tau)} e^{-\tau\left[\sum_{i=1}^{M-1} E_L(\mathbf{r}_i)+\frac{E_L(\mathbf{r}_0)+E_L(\mathbf{r}_M)}{2}\right]} \tag{2.150}$$

with L given by (2.140).

In the original RQMC implementation the path sampling is performed as follows. Starting from a given many body path a new path can be obtained by adding a segment of time length τ to one of the two ends of the original path and, consequently, by deleting the opposite end of the path in order to keep constant the number of beads in the chain. First of all it is then necessary to decide which one of the two ends will be the growing end and this is done by choosing at random between the two, with probability 1/2: let us indicate with $\mathbf{r}_h$ the growing end and with $\mathbf{r}_t$ the opposite extreme of the path. Then, a new point of the path is sampled from a gaussian distribution centered at a distance $2\lambda\tau F(\mathbf{r}_h)$ from $\mathbf{r}_h$, which comes from the term $e^{-\sum_{i=1}^{M} L(\mathbf{r}_i,\mathbf{r}_{i-1};\tau)}$ in (2.150). Let us also introduce a variable d representing the growth direction. Since there exist only two possible growth directions, d can assume only two values: by convention, let us choose $d = +1$ when $\mathbf{r}_h = \mathbf{r}_M$ and $d = -1$ when $\mathbf{r}_h = \mathbf{r}_0$. The proposed configuration is accepted or rejected according to a standard Metropolis rule

$$\alpha_d(\mathbf{P} \to \mathbf{P}') = min\left[1, \frac{\pi(\mathbf{P}')t_{-d}(\mathbf{P}' \to \mathbf{P})}{\pi(\mathbf{P})t_d(\mathbf{P} \to \mathbf{P}')}\right] \tag{2.151}$$

where the acceptance probability α_d and the transition probability t_d both depends on the growth direction, while the path probability $\pi(\mathbf{P})$ is independent of d.

The resulting evolution of the path is something similar to a snake motion, and for that reason the algorithm is called reptation; chosen the motion direction, the ends of the path, $\mathbf{r}_h$ and $\mathbf{r}_t$, are also called the head and the tail of the reptile, respectively. After the acceptance step, the procedure is repeated, starting by the sampling of the moving end.

Proceeding as described however, the electronic configurational space may be sampled inefficiently. This algorithm is in fact characterized by a large autocorrelation time - defined as the number of MC steps required to obtain two uncorrelated configurations - which scales as the square of the beads number M divided by the acceptance rate[11]. Moreover persistent configurations may occasionally appear: since

---

[10] The reason of this choice is related to the form of the trial wave function, used to represent the electronic state, which contains a Slater determinant of single particle orbitals. Inside the determinants the electronic coordinates are not mutually independent, due to the application of a coordinate transformation, the backflow transformation, used to improve the wave function. As a consequence, also in the case of a single electronic move an entire determinant must be recomputed: since this operation has a computational cost that scales with the cube of the number of particles, it is preferable to adopt global electronic moves.

[11] Intuitively, we can estimate the autocorrelation time of the reptation algorithm by noticing that, if the motion direction would always remain unchanged and all the moves were accepted, a

the moving direction of the polymer can change frequently, the polymer can simply oscillate back and forth without really explore the space. In CEIMC, in which the electronic ground state calculation must be repeated at each protonic move, these features make the standard reptation algorithm undesirable.

The reptation algorithm can be improved using a slightly different approach. Instead of sampling at random the head of the reptile each time we perform a move, the motion direction d is chosen only at the beginning of the simulation and retained until the move is rejected. After any rejection the motion direction of the reptile is inverted. This algorithm to sample the path configurational space is known as *bounce algorithm* [91]. Although this scheme does not satisfy the detailed balance, it is possible to prove that it samples the right limiting distribution. To demonstrate that, following [91], let us add to the $3N(M+1)$ dimensional path space the additional variable d, representing the direction of motion of the path, which can assume only two values, $+1$ and -1. We can also define in this extended space the path transition probability $A(\mathbf{r}, d \to \mathbf{r}', d') = \alpha_d(\mathbf{r} \to \mathbf{r}') t_d(\mathbf{r}' \to \mathbf{r})$. Since the algorithm represents a Markov process in the extended space, under the assumptions of ergodicity and irreducibility, it admits a unique stationary distribution $\Pi(\mathbf{P}, d)$ that satisfies

$$\Pi(\mathbf{P}', d') = \sum_{\mathbf{P}} \sum_{d} \Pi(\mathbf{P}, d) A(\mathbf{P}, d \to \mathbf{P}', d') \tag{2.152}$$

We need to show that, with the transition probability of the bounce algorithm, our path distribution $\pi(\mathbf{P})$ independent of the coordinate d is a solution of this equation. Let us first notice that in the bounce algorithm if the move is discarded the moving direction is inverted and hence $A(\mathbf{P}', d' \to \mathbf{P}', d') = 0$ and $A(\mathbf{P}', d' \to \mathbf{P}', -d') = 1$. On the other hand, if the move is accepted, the growth direction remain unchanged and hence $A(\mathbf{P}', d' \to \mathbf{P}, -d') = 0$ for any $\mathbf{P}' \neq \mathbf{P}$. With these observations we are able to eliminate the sum over d in the previous equation, that becomes

$$\Pi(\mathbf{P}', d') = \Pi(\mathbf{P}', -d') A(\mathbf{P}', -d' \to \mathbf{P}', d') + \sum_{\mathbf{P} \neq \mathbf{P}'} \Pi(\mathbf{P}, d') A(\mathbf{P}, d' \to \mathbf{P}', d') \tag{2.153}$$

By substituting our distribution $\pi(\mathbf{P})$, independent of the direction d, to the generic probability distribution in the extended space $\Pi(\mathbf{P}, d)$ the (2.153) can be rewritten as

$$\begin{aligned} \pi(\mathbf{P}') &= \pi(\mathbf{P}') A(\mathbf{P}', -d' \to \mathbf{P}', d') + \sum_{\mathbf{P} \neq \mathbf{P}'} \pi(\mathbf{P}) A(\mathbf{P}, d' \to \mathbf{P}', d') \\ &= \pi(\mathbf{P}') \left[A(\mathbf{P}', -d' \to \mathbf{P}', d') + \sum_{\mathbf{P}} A(\mathbf{P}', -d' \to \mathbf{P}, -d') \right] \end{aligned} \tag{2.154}$$

where in the last line we used the detailed balance condition $\pi(\mathbf{P}) A(\mathbf{P}, d' \to \mathbf{P}', d') = \pi(\mathbf{P}') A(\mathbf{P}', -d' \to \mathbf{P}, -d')$. The transition probabilities are normalized, hence terms in square bracket sum to 1: this proves that equation (2.152) is identically satisfied by the path distribution $\pi(\mathbf{P}')$ for each $\mathbf{P}'$, and, as a consequence, that the bounce algorithm samples correctly the paths.

---

completely new polymer, of zero overlap with the original, is sampled after a number of steps equal to the lenght M of the polymer. Due to the rejections the correlation time is increased of a factor equal to the acceptance rate N_{tot}/N_{acc}. The sampling of the growth direction after each move gives an additional factor proportional to M.

2.5.5 The fermion sign problem

In the previous section we have implicitly neglected that the electrons are fermions and treated them as distinguishable particles. If the Hamiltonian does not depend explicitly on the spin, we can use the results derived in the previous sections, provided we introduce the particle statistics by considering states totally antisymmetric under particle exchange. Since the Hamiltonian $\hat{\mathcal{H}}$ and the particle permutation operator $\hat{P}$ commute, the symmetry is preserved during the evolution in the imaginary time and then it is sufficient to define an antisymmetric initial condition for the Bloch equation (2.137)

$$\rho_F(\mathbf{r},\mathbf{r}';0) = \mathcal{A}\delta(\mathbf{r}-\mathbf{r}') = \frac{1}{N!}\sum_P (-1)^P \delta(\mathbf{r}-\hat{P}\mathbf{r}') \tag{2.155}$$

to ensure the right symmetry of the matrix ρ_F at any time t. The matrices $\hat{\rho}_F$ for a system of Fermions can be then rewritten in terms of density matrices $\hat{\rho}_D$ of a system of distinguishable particles as

$$\rho_F(\mathbf{r},\mathbf{r}';t) = \frac{1}{N!}\sum_P (-1)^P \rho_D(\mathbf{r},\hat{P}\mathbf{r}';t) \tag{2.156}$$

Namely, the matrix elements between $\mathbf{r}$ and $\mathbf{r}'$ of the fermionic matrix $\hat{\rho}_F$ are obtained by summing the matrix elements corresponding to the state $\mathbf{r}$ and all the permutations $\hat{P}\mathbf{r}'$ of $\mathbf{r}'$ of the matrix $\hat{\rho}_D$ of a system of distinguishable particles. Each contribution $\rho_D(\mathbf{r},\hat{P}\mathbf{r}';t)$, arising from all the paths going from $\mathbf{r}$ to $\hat{P}\mathbf{r}'$ in the time t, is weighted with a positive or negative sign, due to the parity of the specific permutation. We can also speak of positive and negative paths referring to the sign carried by the permutation.

While the $\rho_D(\mathbf{r},\hat{P}\mathbf{r}';t)$ are always positive, the fermionic matrix elements can be either positive or negative and this leads to the so-called *fermion sign problem* [68]. Since the fermionic matrix elements (2.156) have not a definite sign, they cannot be thought as conditional probabilities and it is not possible to use then in a Monte Carlo scheme to perform the integrals and compute averages. It has been shown [68] that the absolute value of $\rho_F(\mathbf{r},\mathbf{r}';t)$, $f(\mathbf{r},\mathbf{r}';t) = |\rho_F(\mathbf{r},\mathbf{r}';t)| = |\sum_P(-1)^P\rho_D(\mathbf{r},\hat{P}\mathbf{r}';t)|/N!$ positive by definition, represents the optimal probability to sample the electronic paths. Unfortunately, the use of a bosonic probability instead of the fermionic $\rho_F(\mathbf{r},\mathbf{r}';t)$ simply move the problem related to the negative signs from the sampling to the calculations of averages. Let us rewrite the average of an operator $\hat{\mathcal{O}}$ - for simplicity diagonal in the coordinate representation and that commutes with the Hamiltonian - as

$$\left\langle \hat{\mathcal{O}} \right\rangle = \frac{\int d\mathbf{r}d\mathbf{r}'\psi(\mathbf{r})\rho_F(\mathbf{r},P\mathbf{r}')\mathcal{O}(P\mathbf{r}')\psi(P\mathbf{r}')}{\int d\mathbf{r}d\mathbf{r}'\psi(\mathbf{r})\rho_F(\mathbf{r},P\mathbf{r}')\psi(P\mathbf{r}')} \tag{2.157}$$

The distribution $f(\mathbf{r},\mathbf{r}';t)$ can be introduced by multiplying and dividing by $f(\mathbf{r},\mathbf{r}';t)$ the integrands in both the numerator and the denominator, arriving at

$$\left\langle \hat{\mathcal{O}} \right\rangle = \frac{\langle \mathrm{sign}(\rho_F(\mathbf{r},\mathbf{r}';t))\mathcal{O}(\mathbf{r}')\rangle_f}{\langle \mathrm{sign}(\rho_F(\mathbf{r},\mathbf{r}';t))\rangle_f} \tag{2.158}$$

where in the last equality sign(ρ_F) is the sign of the function $\rho_F(\mathbf{r},\mathbf{r}';t)$ and $\langle\cdots\rangle_f$ indicates the MC average over a sample distributed according to the function $f(\mathbf{r},\mathbf{r}';t)$. Since the sampling does not discriminate among negative and positive paths $\mathbf{r}\to P\mathbf{r}'$, on average the number of positive and negative contributions to the numerator and the denominator of (2.158) will be equal, leading to a diverging noise-to-signal ratio.

The impossibility of sampling correctly the fermionic configuration space with a bosonic probability density is just a consequence of the existence, in the Hilbert space, of states with different symmetry (antisymmetric, symmetric and mixed) which form mutually orthogonal sets [92]: as a consequence it is not possible to obtain informations on a fermionic state starting from a bosonic sampling. Despite that, different schemes allowing to overcome in an approximate fashion this issue exist.

In this section we will describe the fixed node scheme [80], that is used to obtain a positive expression for the $\hat{\rho}_F$ and for the generating function $\mathcal{Z}(t)$.

The nodes of the density matrix, implicitely defined as the set of points $\mathbf{r}'$ such that, for a given $\mathbf{r}$ and t, satisfy $\rho_F(\mathbf{r},\mathbf{r}',t)=0$, divide the total configuration space in regions of positive and negative ρ_F. Since the matrix $\hat{\rho_F}$ at any t satisfies the property [72]

$$\rho_F(\mathbf{r},\mathbf{r}';t)=\int d\mathbf{r}''\rho_F(\mathbf{r},\mathbf{r}'';\tau)\rho_F(\mathbf{r}'',\mathbf{r}';t-\tau)\qquad\forall\tau\in(0,t)\tag{2.159}$$

if, for any time τ, the configuration $\mathbf{r}''(\tau)$ evoluted from the initial condition $\mathbf{r}(0)$ lies on the nodal surface $\rho_F(\mathbf{r},\mathbf{r}'';\tau)=0$, it will not contribute to the matrix elements at any future time t. That means that paths reaching the nodal surface at a given t can be safely discarded from sampling, or, in other words that the sampling can be restricted only to paths that do not change sign.

In order to consider only those paths which gives a non zero contribution to the matrix elements, we can introduce the *reach* of $\mathbf{r}$ at the time t, $\Upsilon(\mathbf{r},t)$, representing the set of configurations that can be reached from $\mathbf{r}$ in a time t without crossing the nodal surface at previous time. In terms of the reach we can rewrite the fermionic matrix - using the expression (2.141) for the distinguishable matrix elements $\rho_D(\mathbf{r},\mathbf{r}';t)$ - as

$$\begin{aligned}\rho_F(\mathbf{r},\mathbf{r}';t) &= \frac{1}{N!}\sum_P(-1)^P\left[\int_{\substack{\mathbf{X}(0)=\mathbf{r}\\ \mathbf{X}(t)=P\mathbf{r}'}}\mathcal{D}\mathbf{X}e^{-\int_0^t\left[\frac{L(\mathbf{X}(\tau))}{\tau}+E_L(\mathbf{X}(\tau))\right]}\right]_{\Upsilon(\mathbf{r},t)}\\ &= \frac{1}{N!}\sum_P(-1)^P\left[\int_{\substack{\mathbf{X}(0)=\mathbf{r}\\ \mathbf{X}(t)=P\mathbf{r}'}}\mathcal{D}\mathbf{X}e^{-S[\mathbf{X}]}\right]_{\Upsilon(\mathbf{r},t)}\end{aligned}\tag{2.160}$$

with $L(\mathbf{X}(\tau))$ given by (2.140).

The generating function $\mathcal{Z}(t)$ hence becomes

$$\begin{aligned}
\mathcal{Z}(t) &= \int d\mathbf{r}d\mathbf{r}'\psi_T(\mathbf{r})\frac{1}{N!}\sum_P(-1)^P\left[\int_{\substack{\mathbf{r}(0)=\mathbf{r}\\ \mathbf{r}(t)=P\mathbf{r}'}}\mathcal{D}Xe^{-\mathcal{S}(X)}\right]_{\Upsilon(\mathbf{r},t)}\psi_T(\mathbf{r}') \\
&= \int d\mathbf{r}d\mathbf{r}''\psi_T(\mathbf{r})\left[\int_{\substack{\mathbf{r}(0)=\mathbf{r}\\ \mathbf{r}(t)=\mathbf{r}''}}\mathcal{D}Xe^{-\mathcal{S}(X)}\right]_{\Upsilon(\mathbf{r},t)}\frac{1}{N!}\sum_P(-1)^P\psi_T(P^{-1}\mathbf{r}'') \\
&= \int d\mathbf{r}d\mathbf{r}''\psi_T(\mathbf{r})\left[\int_{\substack{\mathbf{r}(0)=\mathbf{r}\\ \mathbf{r}(t)=\mathbf{r}''}}\mathcal{D}Xe^{-\mathcal{S}(X)}\right]_{\Upsilon(\mathbf{r},t)}\psi_T(\mathbf{r}'') \qquad (2.161)
\end{aligned}$$

where, in the last line, we used the antisymmetry of ψ_T to eliminate the permutation operator $\hat{P}$. The restriction of the integral to paths of positive sign only ensures that the generating function $\mathcal{Z}(t)$, normalization of the averages, remains always positive.

The problem is only apparently solved: in fact in order to know the nodal surface of the fermionic matrix, a complicated function of $6N-1$ variables, one must know $\hat{\rho}_F$ itself, so we are back at the original problem of the density matrix determination. A possible approach to overcome this difficulty consists in the *fixed node approximation*, that relies in the substitution of the exact (and unknown) nodal surface with the nodal surface of a trial density matrix $\hat{\rho}_T$. This surface is maintained unchanged during the simulation. The usual choice in QMC methods is to approximate the nodal surface of the fermion density matrix with the nodes of the trial wave function $\Psi_T(r)=0$. In this approximation a time dependent function is replaced with a time independent function. In the implementation of the fixed node algorithm, to ensure the path restriction it is sufficient to verify the condition $\psi_T(\mathbf{r}_i)\psi_T(\mathbf{r}_{i+1})>0$ for each link of the discrete path, including the extremes.

It can be demonstrated [80] that the variational principle on the energy can also be applied within the fixed node approximation, i.e. that the energy computed assuming the nodal surface S_T is always greater than or equal to the ground state energy, $E_{S_T}\geq E_0$, the equality holding only if the trial nodal surface S_T coincides with the nodal surface of the exact ground state function.

As we will see in Section 2.6.3, in our calculations the trial wave function carries a phase introduced to minimize the finite size effects. In this case a slight modification of the fixed node approach must be introduced, called *fixed phase* method [93, 94]. Let us rewrite the total wave function as

$$\psi_T(\mathbf{r})=|\psi_T(\mathbf{r})|e^{i\theta_T(\mathbf{r})} \qquad (2.162)$$

where $|\psi_T(\mathbf{r})|$ and $\theta_T(\mathbf{r})$ are two real functions of the electronic coordinates.

In the VMC scheme, nothing changes if the wave function is a complex function, since the sampling is performed according to its square modulus. The only difference is in the estimators, in which an imaginary part can appear. As an example, using the form (2.162) for the ψ_T, the local energy becomes

$$E_L=V(\mathbf{r})-\lambda\frac{\nabla^2|\psi_T|}{|\psi_T|}+\lambda(\nabla\theta_T)^2-i\lambda\left(2\nabla\theta_T\frac{\nabla|\psi_T|}{\psi_T}+\nabla^2\theta_T\right) \qquad (2.163)$$

However, as the trial wave function approaches the ground state the local energy will converge to the ground state energy of the system, which is a real number. It follows that in this limit the imaginary part of the local energy will tend to zero: the energy estimator is then chosen to be equal to the real part of E_L.

Let us now describe how to modify the Reptation Monte Carlo scheme for complex trial wave functions. For general complex function $\Phi(\mathbf{r})$ we can split the time independent Schrödinger equation in two equations, one for the modulus and one for the phase of the wave function

$$\begin{aligned} \left[-\lambda\nabla^2 + \left(V(\mathbf{r}) + \lambda(\nabla\theta_T)^2\right)\right]|\psi_T| &= E|\psi_T| \qquad (2.164)\\ \nabla^2\theta_T + 2\nabla\theta_T \cdot \frac{\nabla|\psi_T|}{|\psi_T|} &= 0 \qquad (2.165) \end{aligned}$$

The two equations must be solved together; adopting the fixed phase approximation, one choose an analytic form for the function $\theta_T(\mathbf{r})$ and disregarding the equation for the phase, try to solve the equation for the modulus. This is equivalent to a Schrödinger equation for an Hamiltonian $-\lambda\nabla^2 + V(\mathbf{r}) - \lambda(\nabla\theta_T)^2$. Moreover, since we solve the equation for $|\psi_T|$ the solution is bosonic, i.e. symmetric under particle exchange. The fixed node approximation for real trial functions can be recast in the fixed phase form by defining $\theta_T = \pi[1 - \Theta(\psi_T/|\psi_T|)]$, where $\Theta(x)$ is the step function: in this case indeed the phase factor of the wave function changes of $e^{i\pi} = -1$ across the nodal surface.

2.6 The Coupled Electron-Ion Monte Carlo

The Coupled Electron-Ion Monte Carlo [62] is a first principle technique that relies on the Born-Oppenheimer approximation. The CEIMC scheme is entirely based on the Monte Carlo methods, for determining both the electronic and the protonic state: given a fixed proton configuration, the correspondent electronic ground state energy is determined through a zero temperature Quantum Monte Carlo method, either VMC or RQMC. The computed Born-Oppenheimer energy is then used to sample the proton configurational space. Protons can be considered, as a first approximation, classical particles and the Metropolis algorithm is applied in this case. To study quantum protons at finite temperature, the Path Integral Monte Carlo can be used.

2.6.1 Penalty method

In a standard Metropolis MC, the configuration space for a system of classical protons at temperature T is sampled according to the Boltzmann distribution $e^{-\beta E}$, by proposing a trial configuration with a given probability $t(\mathbf{R} \to \mathbf{R}')$ and then by applying the acceptance/rejection filter, driven by the probability

$$A(\mathbf{R} \to \mathbf{R}') = \min\left[1, \frac{t(\mathbf{R}' \to \mathbf{R})e^{-\beta E(\mathbf{R}')}}{t(\mathbf{R} \to \mathbf{R}')e^{-\beta E(\mathbf{R})}}\right] = \min\left[1, e^{-\beta\Delta E(\mathbf{R},\mathbf{R}')}\right] \qquad (2.166)$$

where the last equation holds in case of symmetric transition probability $t(\mathbf{R} \to \mathbf{R}') = t(\mathbf{R}' \to \mathbf{R})$.

However, in a CEIMC simulation this basic scheme is not directly applicable, since the energies of the protonic configurations are computed during QMC runs and are hence affected by statistical noise; being the energy differences ΔE_{BO} usually quite small, the effect of the noise can be very relevant and can lead to a biased sampling, unless very long electronic calculations are carried on to reduce the noise level. However, this strategy is not very efficient: since the noise scales as $1/\sqrt{N_s}$, being N_s the number of independent sampled electronic configurations per proton move, the simulation time required to make the noise level negligible can be prohibitively long.

An alternative and more efficient approach is to take the noise into account during the sampling, introducing an additional contribution into the acceptance formula. If this contribution is properly chosen, the acceptance of configurations with high noise level will be reduced. This is the idea beyond the so called penalty method [95], which we explain in detail in this section.

Given two protonic configurations, $\mathbf{R}$ and $\mathbf{R}'$, let us indicate with $\delta(\mathbf{R},\mathbf{R}')$ the running value of the BO energy difference computed during the QMC simulation (i.e. the difference between the BO energies of the two protonic configuration for a given electronic configuration), multiplied by the inverse temperature β. Since the BO energies are computed by a stochastic integration method, given $\mathbf{R}$ and $\mathbf{R}'$ $\delta(\mathbf{R},\mathbf{R}')$ will be a stochastic variable distributed according some unknown probability density $P(\delta|\mathbf{R},\mathbf{R}')$. Let us call $\Delta(\mathbf{R},\mathbf{R}')$ and $\sigma(\mathbf{R},\mathbf{R}')$ the average value and the variance of $\delta(\mathbf{R},\mathbf{R}')$, over $P(\delta|\mathbf{R},\mathbf{R}')$

$$\begin{aligned}\Delta(\mathbf{R},\mathbf{R}') &= \left\langle\beta(E_{BO}(\mathbf{R}) - E_{BO}(\mathbf{R}'))\right\rangle = \left\langle\delta(\mathbf{R},\mathbf{R}')\right\rangle && (2.167)\\ \sigma^2(\mathbf{R},\mathbf{R}') &= \left\langle\left(\Delta(\mathbf{R},\mathbf{R}') - \delta(\mathbf{R},\mathbf{R}')\right)^2\right\rangle && (2.168)\end{aligned}$$

We can also indicate with $a(\delta|\mathbf{R}\rightarrow\mathbf{R}')$ the acceptance relative to the running energy difference $\delta(\mathbf{R},\mathbf{R}')$ and with $A(\mathbf{R}\rightarrow\mathbf{R}')$ the average of $a(\delta|\mathbf{R}\rightarrow\mathbf{R}')$ over the noise distribution $P(\delta|\mathbf{R}\rightarrow\mathbf{R}')$

$$A(\mathbf{R}\rightarrow\mathbf{R}') = \int_{-\infty}^{\infty} d\delta P(\delta|\mathbf{R}\rightarrow\mathbf{R}')a(\delta|\mathbf{R}\rightarrow\mathbf{R}') \qquad (2.169)$$

In order to sample the right distribution, proportional to the Boltzmann factor $e^{-\mathcal{E}_{BO}}$, the acceptance probability must satisfy the detailed balance condition. Let us suppose instead, in this case, to impose that the detailed balance condition holds only on average, over the noise distribution. This can be done by requiring that $A(\mathbf{R}\rightarrow\mathbf{R}')$ satisfies[12]

$$A(\mathbf{R}\rightarrow\mathbf{R}') = \exp(-\Delta(\mathbf{R}',\mathbf{R}))A(\mathbf{R}'\rightarrow\mathbf{R}) \qquad (2.170)$$

Assuming that the instantaneous acceptance is independent of the protonic configurations ($a(\delta|\mathbf{R}\rightarrow\mathbf{R}') = a(\delta)$) and that the noise distribution is symmetric ($P(\delta|\mathbf{R}\rightarrow\mathbf{R}') = P(-\delta|\mathbf{R}'\rightarrow\mathbf{R})$), it is possible to rewrite (2.170) as

$$\int_{-\infty}^{\infty} d\delta P(\delta|\mathbf{R}\rightarrow\mathbf{R}')\left[a(\delta) - a(-\delta)\exp(-\Delta(\mathbf{R}',\mathbf{R}))\right] = 0 \qquad (2.171)$$

---

[12] we are assuming that the transition probability $t(\mathbf{R}\rightarrow\mathbf{R}')$ is symmetric, only to simplify the notation

that we has to be solved for $a(\delta)$. To do that, a further assumption is needed, since in principle also the noise distribution is unknown. However, we can make the hypothesis that, for well behaved energy differences, the noise has a gaussian distribution, with variance σ and so that

$$P(\delta|\mathbf{R} \to \mathbf{R}') = \frac{1}{\sqrt{2\pi\sigma^2}} \exp(-(\delta - \Delta)^2/(2\sigma^2)) \tag{2.172}$$

In this case we can prove that

$$a(\delta|\sigma) = min\left[1, e^{-\delta-\frac{\sigma^2}{2}}\right] \tag{2.173}$$

satisfies (2.171). In fact, this expression is equivalent to

$$a(\delta|\sigma) = e^{-\delta-\frac{\sigma^2}{2}}\theta\left(\delta + \frac{\sigma^2}{2}\right) + \theta\left(-\delta - \frac{\sigma^2}{2}\right) \tag{2.174}$$

where $\theta(x)$ is the Heaviside step function, $\theta(x) = 0$ for $x < 0$ and $\theta(x) = 1$ for $x \geq 0$. Substituting (2.172) and (2.174) into the definition of the average acceptance $A(\mathbf{R} \to \mathbf{R}')$ (2.169) we get

$$A(\mathbf{R} \to \mathbf{R}') = \frac{1}{\sqrt{2\pi\sigma^2}} \int_{-\infty}^{-\frac{\sigma^2}{2}} e^{-\frac{(\delta-\Delta)^2}{2\sigma^2}} d\delta + \frac{1}{\sqrt{2\pi\sigma^2}} \int_{-\frac{\sigma^2}{2}}^{\infty} e^{-\frac{(\delta-\Delta)^2}{2\sigma^2}} e^{-\delta-\frac{\sigma^2}{2}} d\delta = A_1 + A_2 \tag{2.175}$$

The first integral on the right hand side, A_1, can be computed making the variable substitution $t = (\Delta - \delta)/\sqrt{2\sigma^2}$

$$A_1 = \frac{1}{\sqrt{2\pi\sigma^2}} \int_{-\infty}^{-\frac{\sigma^2}{2}} e^{-\frac{(\delta-\Delta)^2}{2\sigma^2}} d\delta = \frac{1}{\sqrt{\pi}} \int_{t_0}^{\infty} e^{-t^2} dt = \frac{1}{2}\mathrm{erfc}(t_0) \tag{2.176}$$

being $t_0 = (\Delta + \sigma^2/2)/\sqrt{2\sigma^2}$.

In the second integral, A_2, the exponent can be rearranged as

$$-\frac{1}{2\sigma^2}\left[\delta^2 - 2\delta(\Delta - \sigma^2) + \Delta^2 + \sigma^4 - 2\sigma^2\Delta + 2\sigma^2\Delta\right] = -\frac{(\delta - \Delta + \sigma^2)^2}{2\sigma^2} - \Delta \tag{2.177}$$

and then,

$$A_2 = e^{-\Delta} \frac{1}{\sqrt{2\pi\sigma^2}} \int_{-\frac{\sigma^2}{2}}^{\infty} e^{-\frac{(\delta-(\Delta-\sigma^2))^2}{2\sigma^2}} d\delta \tag{2.178}$$

Introducing the variable $t' = -(\delta - \Delta + \sigma^2)/\sqrt{2\sigma^2}$ and defining $t'_0 = (\Delta - \sigma^2/2)/\sqrt{2\sigma^2}$, we get

$$A_2 = e^{-\Delta} \frac{1}{\sqrt{\pi}} \int_{t'_0}^{\infty} dt' e^{-t'^2} = e^{-\Delta}\frac{1}{2}\mathrm{erfc}(t'_0) \tag{2.179}$$

Summing the two contributions we obtain the explicit expression for $A(\mathbf{R} \to \mathbf{R}')$

$$A(\mathbf{R} \to \mathbf{R}') = \frac{1}{2}\left[\mathrm{erfc}\left(\frac{\Delta(\mathbf{R}, \mathbf{R}') + \frac{\sigma^2}{2}}{\sqrt{2\sigma^2}}\right) + e^{-\Delta(\mathbf{R},\mathbf{R}')}\mathrm{erfc}\left(\frac{\frac{\sigma^2}{2} - \Delta(\mathbf{R}, \mathbf{R}')}{\sqrt{2\sigma^2}}\right)\right] \tag{2.180}$$

for which it is not difficult to prove that a detailed balance condition in the form $A(\mathbf{R} \to \mathbf{R}') = e^{-\Delta(\mathbf{R},\mathbf{R}')} A(\mathbf{R}' \to \mathbf{R})$ is satisfied, reminding that $\Delta(\mathbf{R}',\mathbf{R}) = -\Delta(\mathbf{R},\mathbf{R}')$.

We may think that Eq. (2.180) is the expression for the acceptance we were looking for. However, we have derived this formula by assuming that the variance of the energy differences was known. In the CEIMC scheme also the variance σ, not only the BO energy difference Δ, is unknown a priori, and must be estimated during the simulation. Moreover, the variance fluctuates more than the energy difference. It follows that the previous expression cannot be applied in general and must be substituted by an expression accounting for the variance fluctuations.

The steps necessary to derive an expression for the acceptance in this more general case are the same we have illustrated above for the penalty with known variance, however the derivation is more complex and several approximations must be made. In order to make understandable the final result and define a notation, we summarize here, without in fact derive the final formula, the main points of the derivation given in [95]. Suppose to run different QMC simulations to obtain N_s statistically independent estimates of the Born-Oppenheimer energy difference δ_i for a given pair of protonic configurations $\mathbf{R}$ and $\mathbf{R}'$ and let us call Δ and σ^2 the mean and the variance of the energy difference and D and χ^2 their estimates

$$D = \frac{1}{N_s}\sum_{m=1}^{N_s} \delta_i \qquad (2.181)$$

$$\chi^2 = \frac{1}{N_s(N_s-1)}\sum_{m=1}^{N_s} (D-\delta_i)^2 \qquad (2.182)$$

Then we can introduce the acceptance $a(D,\chi^2)$, that depends on the estimates of the energy difference D and of its variance χ^2, and its average, $A(\Delta,\sigma^2)$, that depends instead on the mean Δ and the variance σ^2

$$A(\Delta,\sigma^2) = \int_{-\infty}^{\infty} dD \int_{0}^{\infty} d\chi^2 P(D,\chi^2;\Delta,\sigma^2)a(D,\chi^2) \qquad (2.183)$$

where $P(D,\chi^2;\Delta,\sigma^2)$ is a joint probability of realizing an energy and a variance estimate. Assuming the independence of Δ and σ^2, the joint probability can be factorized into the product of a gaussian probability distribution for the energy difference $P_G(D-\Delta;\sigma^2)$ times a chi-square distribution for the variance $P_{\text{chi}}(\chi^2;\sigma^2)$. As in the case with fixed variance, we want to find an $a(D,\chi^2)$ such that $A(\Delta,\sigma^2)$ satisfies the detailed balance condition $A(\Delta,\sigma^2) = e^{-\Delta}A(-\Delta,\sigma^2)$. One can look for a solution that reduces to the expression (2.180) in the limit of small variance fluctuations. Following these guidelines it has been found [95] that

$$a(D,\chi) = min\left[1, e^{-D-u_\chi}\right] \qquad (2.184)$$

where the term u_χ in (2.184) is a power series of χ^2 which first terms are given by

$$u_\chi = \frac{\chi^2}{2} + \frac{\chi^4}{4}\frac{1}{N_s+1} + \frac{\chi^6}{3}\frac{1}{(N_s+1)(N_s+3)} + \cdots \qquad (2.185)$$

The additional condition $\chi^2/N_s \leq 4$ is needed to ensure the convergence of the series. As N_s goes to ∞, the formula (2.184) reduces to the one for known variance (2.173), otherwise we have additional rejections. If the variance goes to zero, we go back to the standard Metropolis acceptance (2.166).

2.6.2 Pre-rejection

The calculation of the Born-Oppenheimer energies is the most expensive part of a CEIMC calculation since it requires a converged QMC electronic calculation. For that reason, an high level of rejection of the protonic moves will imply an unacceptable waste of resources. In order to improve the efficiency of the protonic space sampling, a classical filter is applied to the proposed configurations, useful to discard the less unfavorable, as for example those containing pair of particles that are too close to each other. This is the essence of the pre-rejection method. To build the classical filter, one first assumes a classical pair potential V_{cl} of some analitic form, used to model the proton-proton interactions; then, when a protonic displacement is attempted the classical energy difference ΔV_{cl} between the initial and the trial proton configurations is determined; finally the acceptance test with the classical energies is applied to decide if the trial displacement must be accepted or rejected

$$A_{cl}(\mathbf{R} \to \mathbf{R}') = \min\left\{1, e^{-\beta \Delta V_{\mathrm{cl}}}\right\} \tag{2.186}$$

Only if the proposed configuration passes the classical filter, the BO energy difference is computed and a new acceptance test is performed

$$A(\mathbf{R} \to \mathbf{R}') = \min\left[1, e^{\beta \Delta V_{\mathrm{cl}} - \beta \Delta E_{BO} - u_\chi}\right] \tag{2.187}$$

where $\exp(-u_\chi)$ represents the penalty contribution and the classical bias, already taken into account, is removed.

The computer resources used in the evaluation of the classical energies are negligible in comparison with a QMC run. On the other hand, the screening of the less probable moves allow to save a noticeable amount of simulation time. The more accurate the effective pseudo-ion system is in representing the true electron-ion system, the higher is the computational gain achieved with the prerejection.

2.6.3 Finite size effects

The high level of accuracy that can be reached using QMC techniques to obtain the electronic ground state pays a price in terms of computer time, that scales as the number of particles to the third power. Since in a CEIMC simulation the electronic state must be recomputed each time a protonic move is attempted, to have results in a reasonable amount of time, the systems simulated are usually of no more than a hundred of particles. This number cannot be enough if we are interested in bulk properties of a material, and it is necessary to take care of the finite size effects on the wanted results.

In the following paragraph we will present two techniques used in our simulations to reduce the finite size error.

Twist averaged boundary conditions [96]

In simulation of bulk-like properties, periodic boundary conditions (PBC) are usually assumed to avoid surface effects in finite size systems: when a particle exits the simulation box it re-enters from the the opposite side, and the electronic wave function is assumed to remain unchanged. However, the use of PBC in the case of the delocalized electronic wave functions gives a slow convergence to the thermodynamic limit, because of the filling shell effects. To illustrate this problem let us consider a system of N not interacting fermions (electrons) enclosed in a cubic box of side L, such that the density of the system is $\rho = N/L$. The state of any electron is represented by a plane wave $\propto e^{i\mathbf{k}_n}$ and has an energy $E_n = \hbar^2\mathbf{k}_n^2/2m$, being $\mathbf{k}_n = \mathbf{n}2\pi/L$. The occupied states lie in a sphere of radius equal to the Fermi wave lenght ($k_F = (3\pi\rho)^{1/3}$ for $3-$dimensional systems and $k_F = 2(\pi\rho)^{1/2}$ for $2-$dimensional systems). For finite N the wave vector distribution is given by a square lattice of discrete points $\{\mathbf{k}_i\}$, as showed - for a $2-$dimensional system - in the left panel of Figure 2.3. As a consequence the number of occupied states (in black in the figure) increases discontinuously with N: a large number of states passes from unoccupied to occupied each time that the modulus of the Fermi wave lenght equals that of a vector of the $\{\mathbf{k}_i\}$ lattice. This causes a discontinuous behavior of the estimated energy with the the number of particles N (see Figure 2.4) and makes particularly difficult to attempt an extrapolation to the infinite size limit.

To try to reduce the finite size error a general way to proceed has been developed.

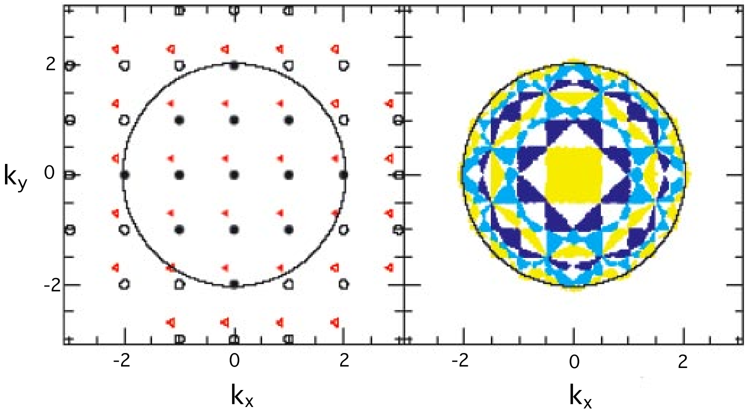

Figure 2.3. Momentum distribution for a 2-dimensional system of 13 not interacting fermions in a square box of side $L = 2\pi$. The occupied states are represented by the closed symbols inside the black circle of radius equal to the Fermi wave lenght. The left panel illustrates the occupation in the case of Periodic Boundary Conditions (black circles) and in the case of a single twist angle $\bar{\theta} = 2\pi(0.3, 0.15)$ (red triangles). In the right panel the occupation using Twist Averaged Boundary Conditions is shown. Figure from Ref. [96].

It consist in allowing the wave function to pickup a phase while an electron crosses the edges of the simulation box

$$\psi_{\bar{\theta}}(\mathbf{r}_1, \cdots, \mathbf{r}_i + \mathbf{L}, \cdots, \mathbf{r}_N) = e^{i\bar{\theta}}\psi_{\bar{\theta}}(\mathbf{r}_1, \cdots, \mathbf{r}_i, \cdots, \mathbf{r}_N) \tag{2.188}$$

where $\mathbf{L}$ is the box sides vector and $\bar{\theta}$ is a 3-dimensional vector called the twist angle, whose components can vary independently in the range $-\pi < \theta_i < \pi$ $(i = 1, \cdots, 3)$.

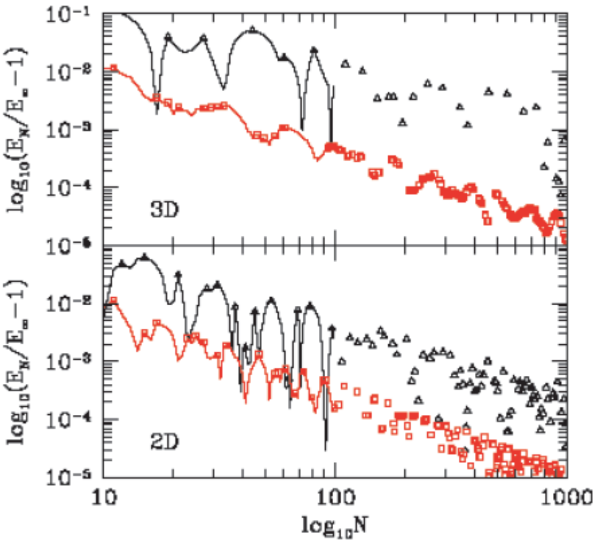

Figure 2.4. Relative finite size error of the energy $(E_N - E_\infty)/E_N$ as a function of the number of particles N, using PBC (black curves) and TABC (red curves) in 2D and 3D. With the use of TBC both the finite size error and the fluctuations of the energy with the N are reduced. Figure from Ref. [96].

This kind of periodic conditions are called Twist Boundary Conditions (TBC) [96]; the standard PBC are recovered by setting $\bar{\theta} = 0$. In our example of the fermionic system to impose the TBC corresponds to change the wave vectors $\mathbf{k}_n$ from $\mathbf{k}_n = \mathbf{n}2\pi/L$ to $\mathbf{k}_{n,\bar{\theta}} = \mathbf{n}2\pi/L + \bar{\theta}/L$. This shift breaks the symmetry of the momentum distribution with respect to the origin and can reduce the energy jumps observed when the Fermi wave lenght is equal to the modulus of some $\mathbf{k}_{n,\bar{\theta}}$. The effect of the TBC on the momentum distribution can be better understood by looking at the left panel of Figure 2.3. If we imagine to shift all the wave vectors of a (vectorial) angle $\bar{\theta}$, we pass from the momentum distribution given by the black circles to those corresponding to the red triangles: in the latter case the number of k points which enters simultaneously the Fermi sphere as the number of particles increases is reduced and one can expect that then the energy behavior with N is more regular.

To reduce the finite size errors, values of the thermodynamic quantities are averaged over the twist angles. Given the observable $\hat{\mathcal{O}}$, a twist average is defined as

$$\left\langle \hat{\mathcal{O}} \right\rangle_{\bar{\theta}} = \int_{-\pi}^{\pi} \frac{d\bar{\theta}}{(2\pi)^3} \left\langle \psi_{\bar{\theta}} \right| \hat{\mathcal{O}} \left| \psi_{\bar{\theta}} \right\rangle \tag{2.189}$$

The straightforward way to evaluate the integral in (2.189) is to run a number of independent simulations for each angle on a fixed grid in the 3-dimensional space of the twists, compute the expectation values $\left\langle \psi_{\bar{\theta}} \right| \hat{\mathcal{O}} \left| \psi_{\bar{\theta}} \right\rangle$ and then sum up the contributions. Another possibility is to sample the twist angles during the simulation.

The justification of TBC comes directly from the many-body generalization of the Bloch theorem; moreover, a correspondence between a twist angle and a vector of the reciprocal space lattice can be established: summing over twist angles is then equivalent to a sum in the (first) Brillouin zone.

Finite size corrections

In spite of the use of TABC, a residual error on the estimated quantities remains, due to the limited size of the simulated system and coming from its artificial periodicity. The high computational demand of a CEIMC simulation makes impossible to increase the number of particles until the thermodynamic convergence is achieved. A valid alternative to reduce finite size errors is to add suitable corrections to the estimated thermodynamic quantities - such as energy and pressure. In this section we will derive the expressions used to correct the potential and the kinetic contributions to the energy, following Refs. [97] and [98].

Let us start considering the potential energy. In a system of N electrons and N protons enclosed in a finite volume Ω and interacting via Coulomb potential, the average potential energy, in atomic units, is given by

$$\begin{aligned} \langle \mathcal{V}(\mathbf{r},\mathbf{R}|\Omega)\rangle &= \left\langle \frac{1}{2}\sum_{i,j\neq} \frac{1}{|\mathbf{r}_i-\mathbf{r}_j|} + \frac{1}{2}\sum_{I,J\neq} \frac{1}{|\mathbf{R}_I-\mathbf{R}_J|} - \sum_{i,J} \frac{1}{|\mathbf{r}_i-\mathbf{R}_J|} \right\rangle \\ &= \left\langle \frac{1}{2}\sum_{\mathbf{k}} \hat{v}_k \left[\rho^e_{\mathbf{k}}\rho^e_{-\mathbf{k}} - N + \rho^p_{\mathbf{k}}\rho^p_{-\mathbf{k}} - N - \rho^p_{\mathbf{k}}\rho^e_{-\mathbf{k}} - \rho^e_{\mathbf{k}}\rho^p_{-\mathbf{k}}\right] \right\rangle \end{aligned} \tag{2.190}$$

where the uppercase symbols are referred to the protons and the lowercase symbols to the electrons. We introduced in the last line the Fourier transform of the potential $\hat{v}_k = 4\pi/k^2$ and the Fourier components of the microscopic charge density $\rho^\alpha_{\mathbf{k}} = z_\alpha \sum_{i=1}^N e^{i\mathbf{k}\cdot\mathbf{r}_i}$ $(\alpha = e, p)$, being z_α the electrical charge: $z_p = +1$ and $z_e = -1$, in our units. A more compact form can be obtained by rewriting the average potential in terms of the charge-charge structure factor

$$\begin{aligned} S_C(k) &= \frac{1}{2N}\left\langle \Big(z_p\sum_I e^{i\mathbf{k}\mathbf{R}_I} + z_e\sum_i e^{i\mathbf{k}\mathbf{r}_i}\Big)\Big(z_p\sum_J e^{-i\mathbf{k}\mathbf{R}_J} + z_e\sum_j e^{-i\mathbf{k}\mathbf{r}_j}\Big)\right\rangle = \\ &= \frac{1}{2N}\left\langle \rho^e_{\mathbf{k}}\rho^e_{-\mathbf{k}} + \rho^p_{\mathbf{k}}\rho^p_{-\mathbf{k}} - \rho^p_{\mathbf{k}}\rho^e_{-\mathbf{k}} - \rho^e_{\mathbf{k}}\rho^p_{-\mathbf{k}}\right\rangle = S^{ee}_N(\mathbf{k}) + S^{pp}_N(\mathbf{k}) - 2S^{ep}_N(\mathbf{k}) \end{aligned} \tag{2.191}$$

In the last equality the relationship with the partial number structure factors $S^{\alpha\beta}_N(\mathbf{k}) = \langle \rho^\alpha_{\mathbf{k}}\rho^\beta_{-\mathbf{k}} + \rho^\beta_{\mathbf{k}}\rho^\alpha_{-\mathbf{k}}\rangle/2/2N$ has been stressed.

Introducing the charge structure factor S_C, the (2.190) becomes

$$\langle \mathcal{V}(\mathbf{r},\mathbf{R}|\Omega)\rangle = \frac{2N}{2\Omega}\sum_{\mathbf{k}\neq 0} \hat{v}_k \left(S_C(\mathbf{k}) - 1\right) \tag{2.192}$$

To treat long range potentials it is however convenient to rewrite the previous expression applying the Ewald decomposition to separate the original potential into a long range and a short range part, that will be treated differently. The contribution to the total energy due to the short range part of the potential, $v^s(\mathbf{r})$, will be computed in the real space, while the remaining contribution will be obtained as a truncated sum in the reciprocal space, since the Fourier transform $\hat{v}^l_k$ of the long range potential $v^l(\mathbf{r})$ is a rapidly decaying function of k. Applying the standard Ewald decomposition, described in detail Appendix .5, the average potential energy is

$$\langle \mathcal{V}(\mathbf{r},\mathbf{R}|\Omega)\rangle = \left\langle \frac{1}{2}\sum_{i,j\neq i} v^s(|\mathbf{r_{ij}}|)\right\rangle + \frac{N}{\Omega}\sum_{\mathbf{k}\neq 0}\hat{v}^l_k S_C(\mathbf{k}) + C_E \tag{2.193}$$

where $v^s(r) = \mathrm{erfc}(\alpha r)/r$, $\hat{v}^l_k = 4\pi\mathrm{exp}[-k^2/4\alpha^2]/k^2$ and $C_E = 2N\alpha/\sqrt{\pi}$, for a charge neutral system.

Choosing a value of α small enough, the short range potential will decay very rapidly and will not contribute to the finite size error. Let us focus therefore on the term

$$\left\langle \mathcal{V}^l(\mathbf{r},\mathbf{R}|\Omega)\right\rangle = \frac{N}{\Omega}\sum_{\mathbf{k}\neq 0}\hat{v}^l_k S_C(\mathbf{k}) \tag{2.194}$$

Equation (2.194) contains two sources of finite size errors: (a) the use of the charge structure factor $S_C(\mathbf{k})$ computed for a system of small size instead of its thermodynamic limit $S_\infty(\mathbf{k}) = \lim_{N\to\infty} S_C(\mathbf{k})$ and (b) the presence of the discrete sum, that in the limit of an infinite system would be a three-dimensional integral over the continuous variable $\mathbf{k}$.

However, since the structure factor converges rapidly with the system size [98, 97], we can neglect the N dependency of the $S_C(\mathbf{k})$ also for the number of particles used in a typical CEIMC run (≈ 50).

We are hence interested in obtaining an estimate of the finite size error due to the integral discretization, given by the difference

$$\langle \delta\mathcal{V}\rangle = N\int \frac{d\mathbf{k}}{(2\pi)^3}\hat{v}_k\left(S_C(\mathbf{k})-1\right) - \frac{N}{\Omega}\sum_{\mathbf{k}\neq 0}\hat{v}_k\left(S_C(\mathbf{k})-1\right) \tag{2.195}$$

In order to determine a computable expression for the finite size error $\langle\delta\mathcal{V}\rangle$, let us first rewrite (2.195) in a more general form

$$\Delta = \int \frac{d\mathbf{k}}{(2\pi)^3}\hat{f}_{\mathbf{k}} - \frac{1}{\Omega}\sum_{\mathbf{k}\neq 0}\hat{f}_{\mathbf{k}} \tag{2.196}$$

being $\hat{f}_{\mathbf{k}}$ a generic function of the reciprocal space.

At this point we can introduce the Poisson summation formula, holding for a generic periodic function $f(\mathbf{r})$ and its Fourier transform $\hat{f}_{\mathbf{k}}$

$$\sum_{\mathbf{n}} f(\mathbf{n}L) = \frac{1}{\Omega}\sum_{\mathbf{k}}\hat{f}_{\mathbf{k}} \tag{2.197}$$

where $\mathbf{n}L$ are the periodicity vectors in the direct space - in our case the box image vectors; L is the lenght of the box side (let us assume for simplicity that the simulation box is cubic).

Since in the expression (2.196) the discrete sum over the $\mathbf{k}$ vectors does not contain the $\mathbf{k} = 0$ term, let us rewrite the Poisson formula 2.197 in the more suitable form

$$\frac{1}{\Omega}\sum_{\mathbf{k}\neq 0}\hat{f}_{\mathbf{k}} = \frac{1}{\Omega}\sum_{\mathbf{k}}\hat{f}_{\mathbf{k}} - \frac{1}{\Omega}\hat{f}_{\mathbf{k}=0} = \left(\sum_{\mathbf{n}\neq 0} f(\mathbf{n}L) + f(\mathbf{n}=0)\right) - \frac{1}{\Omega}\hat{f}_{\mathbf{k}=0} \tag{2.198}$$

We can notice that the term $f(\mathbf{n}=0)$ is

$$f(\mathbf{n}=0)=f(\mathbf{r}=0)=\int\frac{d\mathbf{k}}{(2\pi)^3}\hat{f}_{\mathbf{k}} \tag{2.199}$$

because $f(\mathbf{r})$ and $\hat{f}_{\mathbf{k}}$ are - by definition - Fourier transform pairs. The finite size error Δ then becomes

$$\begin{aligned}\Delta &= \int\frac{d\mathbf{k}}{(2\pi)^3}\hat{f}_{\mathbf{k}}-\frac{1}{\Omega}\sum_{\mathbf{k}\neq 0}\hat{f}_{\mathbf{k}}=\int\frac{d\mathbf{k}}{(2\pi)^3}\hat{f}_{\mathbf{k}}-\sum_{\mathbf{n}\neq 0}f(\mathbf{n}L)-f(\mathbf{n}=0)+\frac{1}{\Omega}\hat{f}_{\mathbf{k}=0}\\ &= \frac{1}{\Omega}\hat{f}_{\mathbf{k}=0}-\sum_{\mathbf{n}\neq 0}f(\mathbf{n}L)\end{aligned} \tag{2.200}$$

Comparing (2.200) with (2.195), by substituting $\hat{f}_{\mathbf{k}}=\hat{v}^l_{\mathbf{k}}S_C(k)$ and neglecting, to the lower order, the real space contribution (the sum over $\mathbf{n}$), we arrive at the lower order correction formula for the potential energy

$$\langle\delta V\rangle=\frac{N}{\Omega}\lim_{k\to 0}\left[\frac{4\pi}{k^2}e^{-\frac{k^2}{2\alpha^2}}S_C(k)\right]=4\pi\frac{N}{\Omega}\lim_{k\to 0}\frac{S_C(k)}{k^2}=\frac{3}{r_s^3}\lim_{k\to 0}\frac{S_C(k)}{k^2} \tag{2.201}$$

that can be computed by extrapolating at $k=0$ the behavior of the static structure factor obtained from simulations.

The correction to the average kinetic energy $\langle\hat{\mathcal{K}}\rangle$ can be derived following a similar procedure. To start, it is convenient to consider the VMC estimator of the kinetic energy and rewrite it as [99]

$$\left\langle\hat{\mathcal{K}}\right\rangle=-\frac{1}{2}\frac{\int d\mathbf{r}\psi(\mathbf{r})\nabla^2\psi(\mathbf{r})}{\int d\mathbf{r}|\psi(\mathbf{r})|^2}=-\frac{1}{4}\frac{\int d\mathbf{r}|\psi(\mathbf{r})|^2\nabla^2\ln\psi(\mathbf{r})}{\int d\mathbf{r}|\psi(\mathbf{r})|^2}=-\frac{1}{4}\left\langle\nabla^2\ln\psi(\mathbf{r})\right\rangle \tag{2.202}$$

being $\langle\cdots\rangle$ the average over the distribution $|\psi(\mathbf{r})|^2$.

This expression can be derived by noticing that, since $\nabla\psi(\mathbf{r})=\psi(\mathbf{r})\nabla\ln\psi(\mathbf{r})$, $\nabla^2\psi(\mathbf{r})=\nabla\psi(\mathbf{r})\nabla\ln\psi(\mathbf{r})+\psi(\mathbf{r})\nabla^2\ln\psi(\mathbf{r})$ and then

$$-\frac{1}{2}\int d\mathbf{r}\psi(\mathbf{r})\nabla^2\psi(\mathbf{r})=-\frac{1}{2}\int d\mathbf{r}\psi(\mathbf{r})\nabla\psi(\mathbf{r})\nabla\ln\psi(\mathbf{r})-\frac{1}{2}\int d\mathbf{r}|\psi(\mathbf{r})|^2\nabla^2\ln\psi(\mathbf{r}) \tag{2.203}$$

The first integral on the right hand side can be rewritten by using $\psi(\mathbf{r})\nabla\psi(\mathbf{r})=\nabla\psi(\mathbf{r})^2/2$ and then computed by parts, obtaining

$$-\frac{1}{2}\int d\mathbf{r}\psi(\mathbf{r})\nabla\psi(\mathbf{r})\nabla\ln\psi(\mathbf{r})=-\frac{1}{4}\int d\mathbf{r}\nabla|\psi(\mathbf{r})|^2\nabla\ln\psi(\mathbf{r})=\frac{1}{4}\int d\mathbf{r}|\psi(\mathbf{r})|^2\nabla^2\ln\psi(\mathbf{r}) \tag{2.204}$$

By substituting this result into (2.203) we get

$$-\frac{1}{2}\int d\mathbf{r}\psi(\mathbf{r})\nabla^2\psi(\mathbf{r})=-\frac{1}{4}\int d\mathbf{r}|\psi(\mathbf{r})|^2\nabla^2\ln\psi(\mathbf{r}) \tag{2.205}$$

and then arrive at the form (2.202) for the average kinetic energy.

In our calculation the trial wave function ψ_T representing the electronic ground state is of the the Slater-Jastrow wave form

$$\psi_T=\mathcal{D}_\uparrow\mathcal{D}_\downarrow e^{-\frac{1}{2\Omega}\sum_{\mathbf{k}\neq 0}u_k\rho_{\mathbf{k}}\rho_{-\mathbf{k}}}=\psi_{\mathcal{D}}e^{-\frac{1}{2\Omega}\sum_{\mathbf{k}\neq 0}u_k\rho_{\mathbf{k}}\rho_{-\mathbf{k}}} \tag{2.206}$$

where u_k is the Fourier transform of the Jastrow functions and $\psi_D = \mathcal{D}_\uparrow \mathcal{D}_\downarrow$.

With this form for the ψ_T the average kinetic energy (2.202) can be written as a sum of two terms

$$\left\langle \hat{\mathcal{K}} \right\rangle = \left\langle \hat{\mathcal{K}}_{\mathcal{D}} \right\rangle - \frac{2N}{8\Omega} \sum_{k \neq 0} u(k) k^2 \left[S_C(k) - 1 \right] \tag{2.207}$$

being $\left\langle \hat{\mathcal{K}}_{\mathcal{D}} \right\rangle$ the contribution arising from the Slater determinants $\psi_{\mathcal{D}}$.

In order to determine an expression for the correction, we will neglect, to the lower order, the N dependency of the term $\left\langle \hat{\mathcal{K}}_{\mathcal{D}} \right\rangle$ and assume, as a first approximation, that most of the finite size error on the kinetic energy comes from the long range correlations due to the Jastrow functions, that, at large distances, decays as r^{-1}. Moreover, we will consider the integration error (2.196) as the main responsible of finite size effects, and apply the formula (2.200) that, substituting $\hat{f}_k = u(k) k^2 \left[S_C(k) - 1 \right]$ and neglecting the real space contribution, becomes

$$\langle \delta \mathcal{K} \rangle = -\frac{N}{4\Omega} \lim_{k \to 0} u(k) k^2 \left[S_C(k) - 1 \right] \tag{2.208}$$

Since the static structure factor goes to zero quadratically with k, it can be neglected to the lower order of the correction. The amount of the correction can be analytically computed using the RPA form for the Jastrow (2.114); we finally obtain

$$\langle \delta \mathcal{K} \rangle = \frac{N}{4\Omega} \lim_{k \to 0} u(k) k^2 = \frac{1}{4} \sqrt{\frac{3}{r_s^3}} \tag{2.209}$$

This correction remains the same also if an improved Jastrow factor of the form (2.116) is used: in fact the additional term to the RPA gives no contribution to the $k = 0$ limit of the $u(k)$. An higher order correction, adding to the previous the supplementary contribution $\langle \delta \mathcal{K} \rangle = -5.083/(4\pi r_s^2 (2N)^{1/3})$ has been derived in [98].

Pressure correction can be derived from formulas (2.201) and (2.209) recalling that the pressure is obtained as

$$\langle p \rangle = \frac{2 \langle \mathcal{K} \rangle + \langle V \rangle}{3\Omega} \tag{2.210}$$

$$\Rightarrow \quad \langle \delta p \rangle = \frac{2 \langle \delta \mathcal{K} \rangle + \langle \delta V \rangle}{3\Omega} \tag{2.211}$$

2.6.4 Electronic wave function optimization in CEIMC simulations

To conclude this Chapter, we want now to go back to the form of the trial wave functions used to represent the electronic ground state and describe the procedure we follow to assign the values to the numerical parameters contained into them.

Before proceeding let us briefly recall the notation adopted in Section 2.5.1 to represent the various terms of the trial wave functions. In our simulations the electronic state is described by a Slater-Jastrow trial wave function of the form

$$\Psi_T(\mathbf{r}, \mathbf{s} | \mathbf{R}) = e^{-\mathcal{J}(\mathbf{r}|\mathbf{R})} \mathcal{D}_{N_\uparrow}(\mathbf{r}_\uparrow | \mathbf{R}) \mathcal{D}_{N_\downarrow}(\mathbf{r}_\downarrow | \mathbf{R}) \tag{2.212}$$

in which $\mathbf{r} = (\mathbf{r}_1, \cdots, \mathbf{r}_N)$ and $\mathbf{R} = (\mathbf{R}_1, \cdots, \mathbf{R}_N)$ are, respectively, the electronic and the protonic spatial coordinates and $\mathbf{s} = (\mathbf{s}_1, \cdots, \mathbf{s}_N)$ the electronic spins;

$\mathcal{D}_{N_\sigma}(\mathbf{r}_\sigma|\mathbf{R})$ are reduced Slater determinants of single particle electron orbitals of same spin $\sigma =\uparrow, \downarrow$ and $\mathcal{J}(\mathbf{r}|\mathbf{R})$ is the Jastrow term which in our implementation is represented as

$$\mathcal{J}(\mathbf{r}|\mathbf{R}) = \sum_{i,j>i} u_{ee}(|\mathbf{r}_i - \mathbf{r}_j|) + \sum_i \sum_J u_{ep}(|\mathbf{r}_i - \mathbf{R}_J|) \tag{2.213}$$

where the single and two particle functions u_{ep} and u_{ee} are given by

$$u(\mathbf{l}_{ij}) = u^{RPA}(\mathbf{l}_{ij}) + a_{\mathcal{J}} e^{-l_{ij}^2 b_{\mathcal{J}}^2} \tag{2.214}$$

where $\mathbf{l}_{ij} = \mathbf{r}_i - \mathbf{r}_j$ for the electron-electron Jastrow function and $\mathbf{l}_{ij} = \mathbf{r}_i - \mathbf{R}_J$ for the electron-proton function.

The Slater-Jastrow wavefunction contains a backflow transformation of the coordinates inside the determinants, that can be described as the sum of an RPA contribution, η^{RPA}, plus a parameter-dependent expression, represented by gaussians

$$\eta(\mathbf{l}_{ij}) = \gamma_1 e^{-(|\mathbf{l}_{ij}|-\gamma_2)^2/\gamma_3^2} \tag{2.215}$$

where $\mathbf{l}_{ij}$ can represent an electron-electron distance for the electron-electron backflow or electron-proton distance for the electron-proton backflow and γ_1, γ_2 and γ_3 are the variational parameters.

Optimization procedure

The parameters $\{\alpha\} = \{a_{\mathcal{J}}^{ee}, b_{\mathcal{J}}^{ee}, a_{\mathcal{J}}^{ep}, b_{\mathcal{J}}^{ep}, \gamma_1^{ee}, \gamma_2^{ee}, \gamma_3^{ee}, \gamma_1^{ep}, \gamma_2^{ep}, \gamma_3^{ep}\}$ appearing into the electronic trial wave function Ψ_T can be varied according to a suitable optimization procedure to achieve low energy and low variance states. In the VMC simulations, optimization steps are usually alternated to the sampling of the electronic configurational space. Since the electronic ground state depends on the protonic configuration, during a CEIMC simulation a VMC runs must be performed after each protonic displacement to compute the Born-Oppenheimer energy of the proposed protonic configuration. Because of that, it may be prohibitively expensive in terms of computer time to repeat the wave function optimization during each electronic state calculation and it is necessary to develop a more feasible procedure to determine the values of the wave function parameters $\{\alpha\}$.

In our approach, at any given density we determine through a preliminary optimization the best values of the parameters $\{\alpha\}$. Those values will be used in any CEIMC calculation that is performed at the same density[13].

The optimization of the trial wave functions is carried on following the scheme summarized below:

(i) For a given density and a selected temperature, we perform a CEIMC simulation using unoptimized electronic wave functions, until the equilibrium is achieved. The electronic calculation method is the VMC.

(ii) Along the equilibrium trajectory, we choose a number N of uncorrelated protonic configurations, $n_c = 1, ..., N$; typically a number N around 20 is used.

---

[13] Implicitly we are assuming that the dependency of the parameters on the (protonic) temperature is weak and can be neglected

(iii) For each protonic configuration n_c in the selected set we optimize independently the electronic wave function, by requiring the minimization of a linear combination of the energy and of the variance , $f(\{\alpha\})$, with respect to the N_p parameters α_{i_p}, $i_p = 1, ..., N_p$. To find the minimum, an iterative Newtonian method is applied.

(iv) Finally we average over the final values obtained in the optimizations for different protonic configurations, to estimate the best value of the variational parameters: $\alpha_{i_p}^{best} = \sum_{n_c=1}^{N} \alpha_{i_p}(n_c)/N$.

Let us now describe in more detail the point (iii) of this procedure.

To determine the optimal values of the electronic wave function parameters, for a fixed protonic configuration, it is possible to require the minimization of the electronic energy E with respect to the $\{\alpha\}$. Generally, exploiting the zero variance principle, it is preferred to minimize a linear combination of the energy and the variance σ_E

$$f(\{\{\alpha\}) = E(\{\alpha\}) + \lambda\sigma_E(\{\alpha\}) \tag{2.216}$$

where λ is a parameter that can be tuned to adjust the weight of the variance with respect to the energy.[14]

For a given set $\{\alpha^0\}$ of values of the variational parameters a VMC run with fixed protons allows to sample the electronic coordinate space according to the distribution $\pi(\mathbf{r}|\{\alpha^0\}) = \left|\Psi_T(\mathbf{r}|\mathbf{R}, \{\alpha^0\})\right|^2$ and to generate a number of uncorrelated configurations $\mathbf{r}_m^0$, $m = 1, \cdots, M$, with M of the order of a few thousands, on which the energy and its variance are estimated as

$$E(\{\alpha^0\}) = \frac{1}{M}\sum_{m=1}^{M} E_L(\mathbf{r}_m|\{\alpha^0\}) \tag{2.217}$$

$$\sigma_E^2(\{\alpha^0\}) = \frac{1}{M}\sum_{m=1}^{M} \left(E_L(\mathbf{r}_m|\{\alpha^0\}) - E(\{\alpha^0\})\right)^2 \tag{2.218}$$

During the optimization procedure, each time the values of the parameters are changed, according to the desired minimization scheme, the wave function and hence the distribution $\pi(\mathbf{r}|\{\alpha\})$ also changes. To obtain a new estimate of E and σ^2 one could resample the space, according to the new distribution $\pi(\mathbf{r}|\{\alpha\})$. However, energy and variance are affected by noise which, in particular near a local minimum, would make very difficult to do the optimization. A way out of this problem is the so called "correlated sampling" in which the M electronic configurations initially generated with $\{\alpha^0\}$ are retained and the energy an the for a new set of parameters $\{\alpha^1\}$ are estimated by a reweighting procedure[62]

$$E(\{\alpha^1\}) = \frac{\sum_{m=1}^{M} w_m E_L(\mathbf{r}_m|\{\alpha^1\})}{\sum_{m=1}^{M} w_m} \tag{2.219}$$

$$\sigma_E^2(\{\alpha^1\}) = \frac{\sum_{m=1}^{M} w_m \left(E_L(\mathbf{r}_m|\{\alpha^1\}) - E(\{\alpha^1\})\right)^2}{\sum_{m=1}^{M} w_m} \tag{2.220}$$

---

[14] The choice of the λ value is not unique. Since the variance goes to zero for any eigenstate, it is usually preferred to give more weight to the energy with respect to the variance and take $\lambda < 1$ (i.e. we use $\lambda = 0.5$).

where the weight factors w_m are given by the ratio between the new and the initial electronic distributions $w_m = \left|\psi_T(\{\alpha^1\})\right|^2 / \left|\psi_T(\{\alpha^0\})\right|^2$, to account the change of the distribution.

One must be careful, however, in maintaining fixed the electronic configurations, since if the values of the parameters become too far from the initial ones, the configurations $\mathbf{r}_m^0$ cease to be representative for the new distribution and the weights w_m in (2.219) and (2.220) can oscillate too much, leading to large error bars in the estimates. An indicator of the quality of the sampling can be the ratio

$$N_{\text{eff}} = \frac{\left(\sum_{m=1}^{M} w_i\right)^2}{\sum_{m=1}^{M} w_i^2} \tag{2.221}$$

Until N_{eff} remains comparable with the original number of configurations M, the initial set of electronic coordinates $\mathbf{r}_m^0$ can be used to compute the averages, otherwise the space sampling must be repeated.

Optimization Results

To illustrate the optimization procedure, we present here an example of our results. We have determined the best values of the wave functions parameters at different r_s in the range $r_s \in [1.07, 1.40]$, necessary for our calculations. For a number of densities in the selected range we performed preliminary CEIMC simulations, using the VMC to compute the electronic state and trial wave functions with only RPA terms. The temperature of the system in those simulations was chosen arbitrarily, but high enough for the disordered phase to be stable. We then selected $N = 16$ uncorrelated protonic configurations, on which to carry on the optimization of electron-proton and electron-electron Jastrow terms and electron-proton and electron-electron backflows, for a total of $N_p = 10$ variational parameters. To generate the sample configurations we used trial wave function containing only the RPA terms.

An example of the behavior of the function that we want to minimize, Equation (2.216), during the minimization is presented in Figure2.5. Each curve represents, for a different protonic configurations , the behavior of the functions $f(\alpha_{i_p}(j)|n_c)$ as a function of the minimization iteration j. Each curve is shifted with respect to the value assumed by the function at the beginning of the minimization, in order to visualize easily the overall gain due to the optimization. The values of the function decrease as the minimization proceeds, reaches a steady value at $j \gtrsim 5$ and then decreases again, when $j \gtrsim 15$ up to a lower minimum state at which the iterations stops. Correspondingly the parameters of the various configurations start spreading, from the initial values, remaining at the beginning quite close one to each other, as can be seen in Figures 2.8, 2.9 and 2.10. The jump to the second minimum in the $f(\alpha_{i_p}(j)|n_c)$ is accompanied by an increase of the fluctuation of the parameter values as well as of the dispersion of the values relative to different configurations. We are interested on values that can improve the wave function independently on the configuration, and then we averaged the values obtained for a given iteration j corresponding to first plateau in $f(\alpha_{i_p}(j)|n_c)$ to determine the $\alpha_{i_p}^{best}$. A numerical example of the averaging is presented in Table 2.1: we report the α_{i_p} best values for each configuration and their average.

We checked a posteriori the effective gain in energy, by comparing the energies of the N static configurations of protons, obtained with optimized and unoptimized wave functions, as showed in the left panel of Figure 2.6. The energy is lowered of about $1.2 mHa$ per particle in comparison with the results obtained with the wave function which contains only RPA terms.

The best values do not change significantly with the density, as can be seen from Table 2.2. Thanks to that, if a simulation must be carried on at an intermediate density in the range of $r_s \in [1.07, 1.40]$, we do not consider necessary to repeat the optimization but it is enough to use an interpolation or a fitting procedure to determine good values of the Jastrow and backflow parameters. To verify this assumption, on the right panel of Figure 2.7 we showed the energy difference obtained, for each protonic configuration, by using a wave function in which the variational parameters are optimized for another density ($r_s = 1.31$, red points) and the correctly optimized one (green points) the energy difference is quite negligible, of about $\approx 0.1 mHa$.

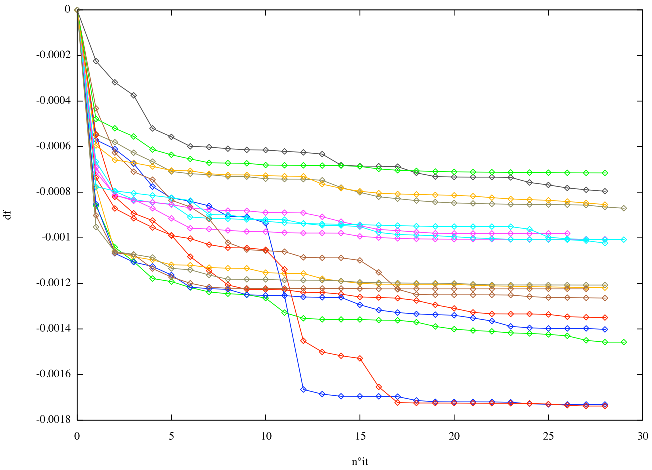

Figure 2.5. Behavior of the function $f(j) = f(\alpha_{i_p}(j)|n_c)$ during the optimization procedure. Plot shows the difference between the value in the current step and the initial value, as a function of the minimization iterations j and for each one of the N proton configurations considered. Example at $r_s = 1.07$.

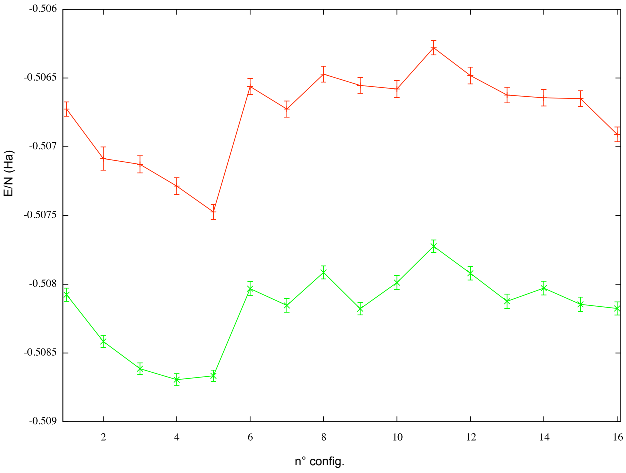

Figure 2.6. Energies per atom with and without optimized parameters. Results at $r_s = 1.31$, for the 16 configurations used in the optimization procedure. Green points represents optimized wave function data, red points the energies obtained with RPA Jastrow and backflows alone. The optimization gives a gain of about $1.2 mHa$ per particle in each protonic configuration.

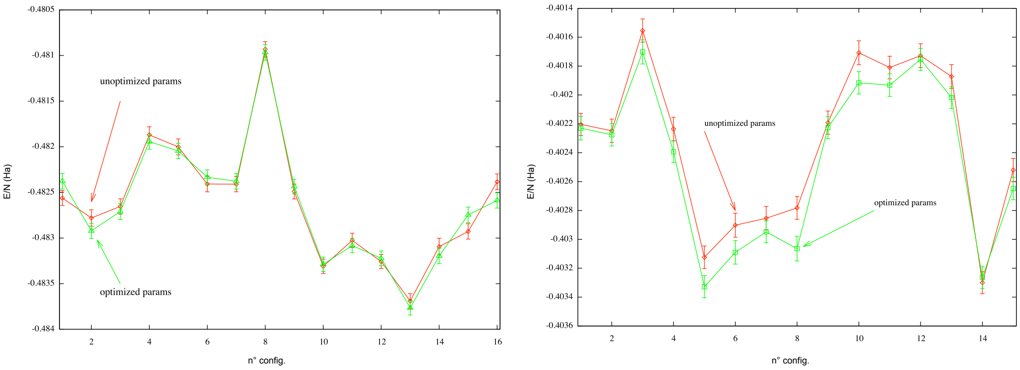

Figure 2.7. Energy comparison between unoptimized (red data points) and optimized (green points) wave functions. To test the density dependence of the parameters, we used as unoptimized wave function the one containing the best parameters determined for another density $r_s = 1.31$. Right panel: Energies per atom at $r_s = 1.25$. Left panel: Same at $r_s = 1.07$. At $r_s = 1.25$ the energies differences are negligible, at $r_s = 1.07$ distinguishable but still very small ($\approx 0.1 mHa$). A more detailed explanation is in the text.

Table 2.1. Electronic wave function parameters values after 17 iterations of the optimization procedure (values for each configuration. In the last line the average value). $r_s = 1.31$

n°conf.	$a_{\mathcal{J}}^{ep}$	$b_{\mathcal{J}}^{ep}$	γ_1^{ee}	γ_2^{ee}	γ_3^{ee}	γ_1^{ep}	γ_2^{ep}	γ_3^{ep}
1	-0.1043	0.6961	0.0292	0.0901	0.8818	-0.7937	-1.5433	1.3784
2	-0.1217	0.5906	0.0539	-0.5459	0.9297	-0.7134	-1.2173	1.1222
3	-0.0753	0.6336	0.0353	-0.4092	1.0539	-0.8799	-1.3918	1.2309
4	-0.1034	0.5492	0.0384	-0.4476	0.9484	-0.7457	-1.2491	1.1855
5	-0.0931	0.6391	0.0331	-0.2811	1.0096	-0.3116	-0.3949	0.7181
6	-0.0914	0.6558	0.0426	-0.5105	0.9793	-0.7612	-1.1309	1.0810
7	-0.0889	0.5782	0.1352	-0.8772	1.0405	-0.7571	-1.2806	1.1997
8	-0.1023	0.6131	0.1934	-0.9647	1.0560	-0.4536	-1.2908	1.2698
9	-0.1037	0.5767	0.0476	-0.3586	1.0239	-0.9155	-1.3939	1.1969
10	-0.1193	0.5912	0.0700	-0.7499	1.0626	-0.7729	-2.0343	1.5943
11	-0.0957	0.6582	0.0452	-0.5623	1.1056	-0.4086	-1.3110	1.2953
12	-0.0999	0.6211	0.0660	-0.7019	1.1713	-0.2900	-0.6007	0.9254
13	-0.0757	0.6932	0.0339	0.0817	0.9012	-0.4257	-0.9487	1.0891
14	-0.1418	0.6419	0.4997	-1.8878	1.3792	-0.6452	-2.0517	1.8428
15	-0.0777	0.6264	0.0326	-0.1599	0.9695	-0.9197	-1.1972	1.0379
16	-0.1014	0.5826	0.0599	-0.4817	0.9726	-0.7493	-1.0222	0.9830
	$a_{\mathcal{J}}^{ep}$	$b_{\mathcal{J}}^{ep}$	γ_1^{ee}	γ_2^{ee}	γ_3^{ee}	γ_1^{ep}	γ_2^{ep}	γ_3^{ep}
average	-0.098	0.62	0.07	-0.45	1.01	-0.81	-1.30	1.20

Table 2.2. Final values of the optimized parameters in the wave function, at different r_s. $a_{\mathcal{J}}^{ee} = -0.01$, $b_{\mathcal{J}}^{ee} = 0.7$

r_s	$a_{\mathcal{J}}^{ep}$	$b_{\mathcal{J}}^{ep}$	γ_1^{ee}	γ_2^{ee}	γ_3^{ee}	γ_1^{ep}	γ_2^{ep}	γ_3^{ep}
1.40	-0.0938	0.56	0.064	-0.54	1.10	-0.90	-1.65	1.19
1.31	-0.098	0.62	0.070	-0.45	1.01	-0.81	-1.30	1.20
1.25	-0.103	0.62	0.056	-0.47	1.07	-0.89	-1.46	1.27
1.19	-0.111	0.67	0.060	-0.575	1.07	-0.76	-1.51	1.37
1.07	-0.093	0.69	0.049	-0.477	1.00	-0.79	-1.46	1.33

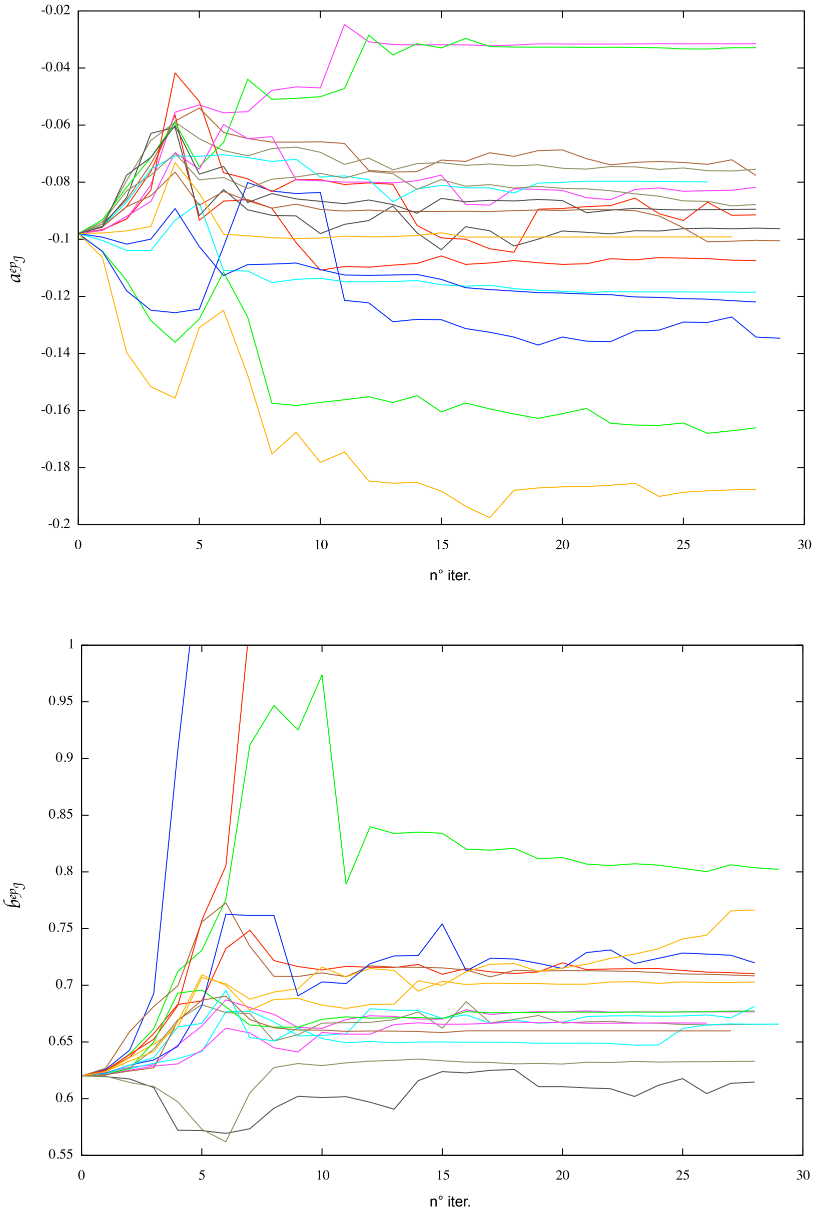

Figure 2.8. Electron-proton Jastrow parameters, $r_s = 1.07$

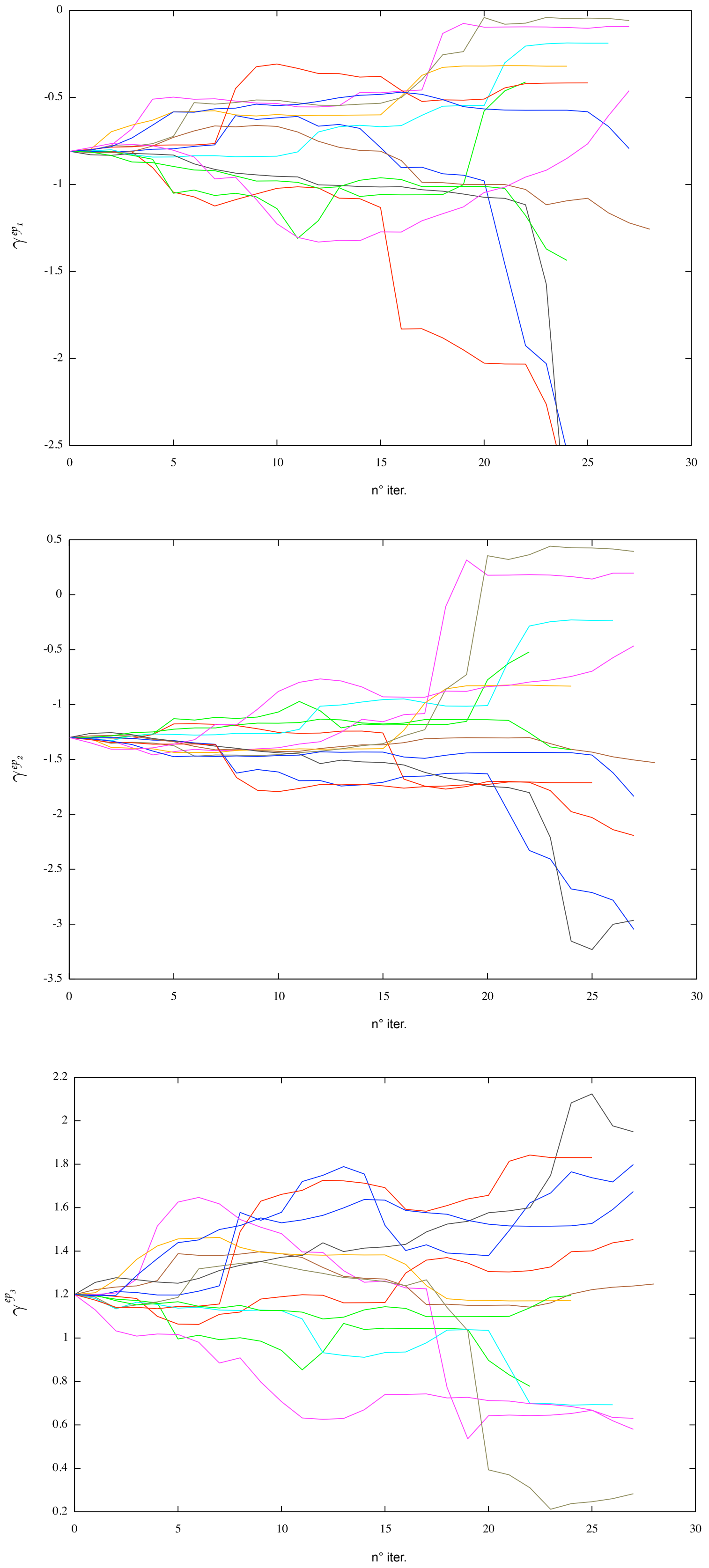

Figure 2.9. Electron-proton backflow parameters, $r_s = 1.07$

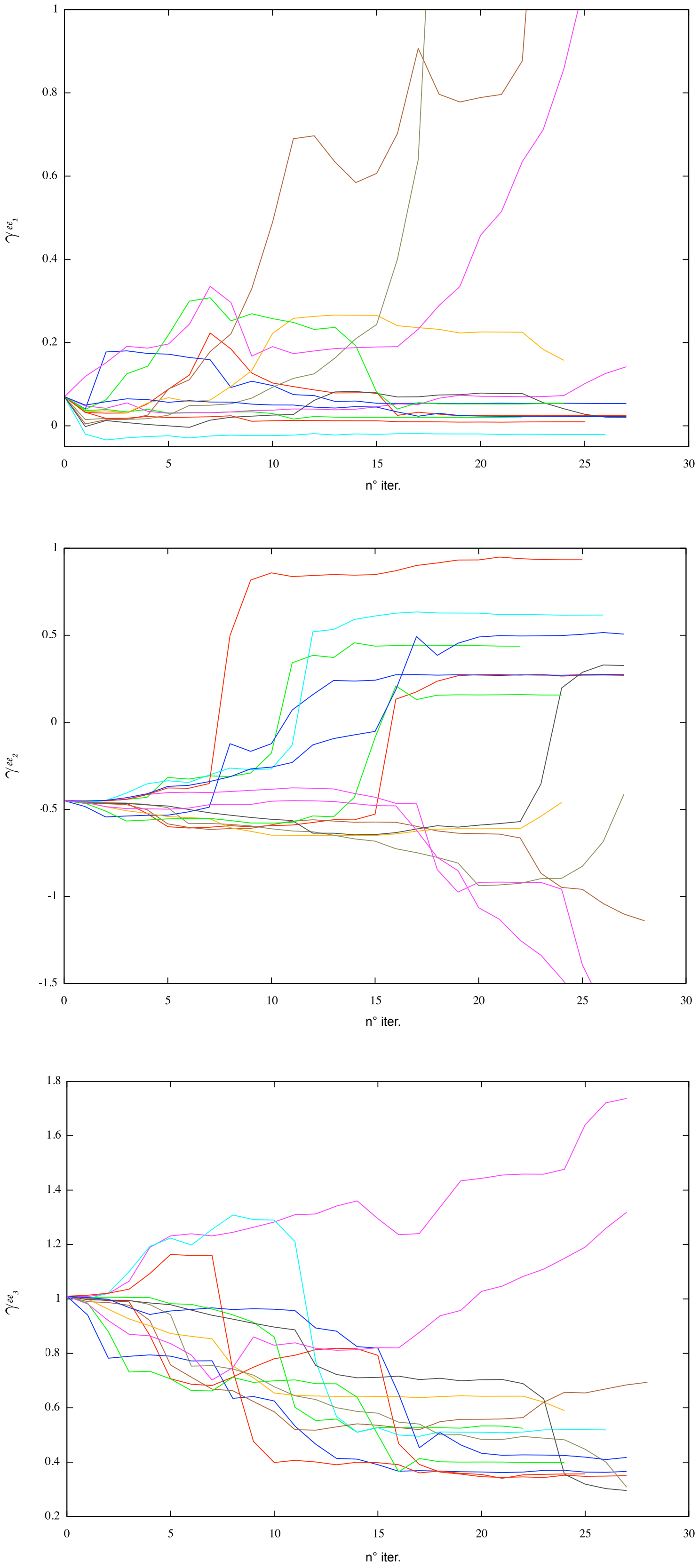

Figure 2.10. Electron-electron backflow parameters, $r_s = 1.07$

Chapter 3

Atomic melting at very high density

3.1 Introduction

The atomic region of the hydrogen phase diagram is still almost unexplored, due to the present experimental inability to reach pressures high enough. The knowledge of the atomic phases of hydrogen is then completely left to the *ab initio* numerical simulations. On the other hand, to add informations on the hydrogen behavior also in this part of the phase diagram is fundamental, especially in the field of Astrophysics [1, 2, 3].

At very high density, hydrogen behaves as a fully ionized plasma, in which protons and electrons are only loosely coupled. This system can be well described by an effective model of a single species of particles interacting through a suitable pair potential: the Screened Coulomb plasma model [100]. It has been found [54] that this simple model is able to reproduce the properties of hydrogen at densities above $\sim 10 g/cm^3$.

In this Chapter, we derive the Screened Coulomb pair potential and we present our results on the melting line for the Screened Coulomb Plasma model, obtained by means of free energy calculations, both for classical and for quantum protons, in the range of densities $\rho_m(g/cm^3) \in [12.475, 32.736]$.

3.2 The Screened Coulomb Plasma model

The effective Screened Coulomb Plasma (SCP) model has been introduced [100] to model fully ionized plasma at high density. Following Ref. [101] we want to derive the expression for the screened Coulomb potential in the case of hydrogen starting from the first principle Hamiltonian.

Let us consider a system of non relativistic N_p protons and N_e electrons in a volume Ω. The charge neutrality condition imposes $N_p = N_e = N$ and then the proton number density n_p is equal to the electron number density n_e: $n_p = n_e = n = N/\Omega$. Denoting the coordinates of protons by $\mathbf{R} \equiv \{\mathbf{R}_1, \ldots, \mathbf{R}_N\}$ and the coordinates of electrons by $\mathbf{r} \equiv \{\mathbf{r}_1, \ldots, \mathbf{r}_N\}$, the terms in the system Hamiltonian

(2.2) can be paired as

$$\hat{\mathcal{H}} = \left(\hat{\mathcal{K}}_p + \hat{\mathcal{V}}_{pp}\right) + \left(\hat{\mathcal{K}}_e + \hat{\mathcal{V}}_{ee}\right) + \hat{\mathcal{V}}_{ep} = \hat{\mathcal{H}}_{OCP} + \hat{\mathcal{H}}_{eg} + \hat{\mathcal{V}}_{int} \tag{3.1}$$

being

$$\hat{\mathcal{H}}_{\text{OCP}} = \hat{\mathcal{K}}_p + \hat{\mathcal{V}}_{pp} = \hat{\mathcal{K}}_p + \frac{1}{2\Omega}\sum_{\mathbf{k}\neq\mathbf{0}} \hat{v}(k)\left[\rho^p_{\mathbf{k}}\rho^p_{-\mathbf{k}} - N\right] \tag{3.2}$$

$$\hat{\mathcal{H}}_{\text{eg}} = \hat{\mathcal{K}}_e + \hat{\mathcal{V}}_{ee} = \hat{\mathcal{K}}_e + \frac{1}{2\Omega}\sum_{\mathbf{k}\neq\mathbf{0}} \hat{v}(k)\left[\rho^e_{\mathbf{k}}\rho^e_{-\mathbf{k}} - N\right] \tag{3.3}$$

$$\hat{\mathcal{V}}_{\text{int}} = \hat{\mathcal{V}}_{ep} = -\frac{1}{2\Omega}\sum_{\mathbf{k}\neq\mathbf{0}} \hat{v}(k)\left[\rho^p_{\mathbf{k}}\rho^e_{-\mathbf{k}} + \rho^p_{-\mathbf{k}}\rho^e_{\mathbf{k}}\right] \tag{3.4}$$

In the expressions above we have introduced the Fourier representation of the Coulomb potential $\hat{v}(k) = 4\pi/k^2$, being $k = |\mathbf{k}|$; $\rho^p_{\mathbf{k}} = e\sum_{i=1}^{N}\exp(i\mathbf{k}\cdot\mathbf{R}_i), \rho^e_{\mathbf{k}} = -e\sum_{i=1}^{N}\exp(i\mathbf{k}\cdot\mathbf{r}_i)$ are the Fourier component of the microscopic charge density of protons and electrons respectively.[1] $\hat{\mathcal{K}}_p$ and $\hat{\mathcal{K}}_e$ are as usual the protonic and electronic kinetic energy operators.

This rearrangement of the Hamiltonian contributions helps us to recognize the Hamiltonians of two well known systems: $\hat{\mathcal{H}}_{OCP}$ is the Hamiltonian of the One Component Plasma [102], a system of protons in a rigid background of negative neutralizing charge, and $\hat{\mathcal{H}}_{eg}$ is the Hamiltonian of the electron gas (jellium) [103], a system of electrons in a rigid background of positive neutralizing charge. $\hat{\mathcal{V}}_{int}$ is the coupling between the two species. In the limit of infinite density, the coupling term becomes negligible with respect to the other two terms and the system behaves as the superposition of the two independent models. For finite but large density $\hat{\mathcal{V}}_{int}$ can be treated as a perturbation.

Whithin the adiabatic approximation, to reduce the original two-component system to an effective one-component system of pseudo-ions [101] we need to trace the original Hamiltonian $\hat{\mathcal{H}}$ over the electronic degrees of freedom in their instantaneous ground state at fixed ionic positions, as showed in Section 2.2, obtaining

$$\hat{\mathcal{H}}^{\text{eff}} = \hat{\mathcal{H}}_{OCP} + \mathcal{E}^{\text{int}}_{eg}(\mathbf{R}) \tag{3.5}$$

where $\mathcal{E}^{\text{int}}_{eg}(\mathbf{R})$ is the ground state energy of the electron gas in presence of the interaction term $\hat{\mathcal{V}}_{\text{int}}$ for a given protonic configuration. $\mathcal{E}^{\text{int}}_{eg}(\mathbf{R})$ can be computed from the unperturbed ground state energy $\mathcal{E}^0_{eg}$ by coupling constant integration [104]. Let us first introduce the auxiliary Hamiltonian $\hat{\mathcal{H}}(\lambda) = \mathcal{H}_{eg} + \lambda\mathcal{V}_{\text{int}}$, which depends on the parameter $\lambda \in [0,1]$ used to switch off the interaction. We can then use the Hellman-Feynman theorem [104] to obtain the partial derivative of the ground state energy $\mathcal{E}_{eg}(\lambda)$ with respect to the parameter λ

$$\frac{\partial\mathcal{E}_{eg}(\lambda)}{\partial\lambda} = \frac{\partial\langle\hat{\mathcal{H}}\rangle_\lambda}{\partial\lambda} = \frac{\langle\partial\hat{\mathcal{H}}(\lambda)\rangle_\lambda}{\partial\lambda} \tag{3.6}$$

---

[1] The $k = 0$ term in the sums is not present as a consequence of the charge neutrality condition.

where the averages $\langle \cdots \rangle_\lambda$ are over the ground state wave function of the system with Hamiltonian $\mathcal{H}(\lambda)$. By integrating over λ from the unperturbed to the perturbed state we get

$$\mathcal{E}_{eg}^{\text{int}} = \mathcal{E}_{eg}^{0}(n) + \int_0^1 d\lambda' \, \langle \mathcal{V}_{\text{int}} \rangle_\lambda = \mathcal{E}_{eg}^{0}(n) - \int_0^1 \frac{d\lambda'}{2\Omega} \left\langle \sum_{\mathbf{k}\neq\mathbf{0}} \hat{v}(k) \left[\rho_{\mathbf{k}}^{p} \rho_{-\mathbf{k}}^{e} + \rho_{-\mathbf{k}}^{p} \rho_{\mathbf{k}}^{e} \right] \right\rangle_\lambda \tag{3.7}$$

where we have stressed the dependency of the ground state energy of the homogeneous electron gas on the electronic density n.

To compute $\mathcal{V}_{\text{int}}$ we can notice that, if this term of interaction is small, the linear response theory can be used to relate the average electronic charge density fluctuations to the instantaneous ionic charge density fluctuations, through the introduction of the response function of homogeneous electron gas $\chi(k)$

$$\langle \rho_{\mathbf{k}}^{\lambda} \rangle_e = -\lambda \hat{v}(k) \chi(k) \rho_{\mathbf{k}}^{p} = \left(\frac{1}{\varepsilon(k)} - 1 \right) \rho_{\mathbf{k}}^{p} \tag{3.8}$$

The average must be intended over the instantaneous electronic ground state corresponding to a given protonic configuration. To write the last equality we have used the relationship among the response function $\chi(k)$ and the dielectric function of the homogeneous electron gas $\varepsilon(k)$, $\varepsilon(k) = [1 - \hat{v}(k)\chi(k)]^{-1}$. By substituting (3.8) in (3.7), since the dependency on λ of the integrand is linear, the integral in (3.7) can be performed easily and gives a factor 1/2. Using this result, together with eq. (3.8), we finally obtain

$$\mathcal{E}_{eg}^{\text{int}} = \mathcal{E}_{eg}^{0}(n) + \frac{1}{2\Omega} \sum_{\mathbf{k}\neq\mathbf{0}} \hat{v}(k) \left(\frac{1}{\varepsilon(k)} - 1 \right) \left[\rho_{\mathbf{k}}^{p} \rho_{-\mathbf{k}}^{p} - N \right] \tag{3.9}$$

Substituting the last result in eq. (3.5) we arrive at the following effective Hamiltonian for the pseudo-ion system [101]

$$\begin{aligned}
\hat{\mathcal{H}}^{\text{eff}} &= \hat{\mathcal{H}}_{OCP} + \mathcal{E}_{eg}^{0}(n) + \frac{1}{2\Omega} \sum_{\mathbf{k}\neq\mathbf{0}} \hat{v}(k) \left(\frac{1}{\varepsilon(k)} - 1 \right) \left[\rho_{\mathbf{k}}^{p} \rho_{-\mathbf{k}}^{p} - N \right] \\
&= \hat{\mathcal{K}}_p + \mathcal{E}_{eg}^{0}(n) + \frac{1}{2\Omega} \sum_{\mathbf{k}\neq\mathbf{0}} \frac{\hat{v}(k)}{\varepsilon(k)} \left[\rho_{\mathbf{k}}^{p} \rho_{-\mathbf{k}}^{p} - N \right] \\
&= \hat{\mathcal{K}}_p + \mathcal{E}_{eg}^{0}(n) + \frac{1}{2} \sum_{i,j\neq i} v^{\text{eff}}(R_{ij}; n)
\end{aligned} \tag{3.10}$$

where $R_{ij} = |\mathbf{R}_{ij}|$, $v^{\text{eff}}(R; n)$ is the Fourier transform of $[v(k)/\varepsilon(k)]$ whose n dependence comes from the dielectric function. $\hat{\mathcal{H}}^{\text{eff}}$ is a state dependent Hamiltonian since it depends on the density of the system both through the volume term $E_{eg}(n)$ and the effective pair potential $v^{\text{eff}}(R; n)$.

The homogeneous electron gas has been largely studied and both its ground state energy and its dielectric function are well characterized [104]. The ground state energy of the homogeneous electron gas has been computed by Quantum Monte Carlo methods [103] and parametrized by several authors. We adopt the form of

Perdew and Zunger [104, 105] which at high density can be written as

$$\frac{\mathcal{E}_{eg}(r_s)}{N}[Hrt] \simeq \frac{1.105}{r_s^2} - \frac{0.468}{r_s} + A\ ln(r_s) + B + Cr_s ln(r_s) + Dr_s \tag{3.11}$$

where energy is in atomic units ($1Hrt = 27.2ev = 315.79 \times 10^3 K$) and r_s is the electron sphere radius (the radius of the sphere containing one electron, in units of the Bohr radius a_0) defined as $r_s = (3/4\pi n)^{(1/3)}$. The first two terms in (3.11) are the Hartree-Fock contributions to the energy while the remaining terms represent the correlation energy $\epsilon_c(r_s)$. The values of the parameters are [104, 105]: A=0.031, B=-0.048, C=0.002, D=-0.0116.

The dielectric function of the homogeneous electron gas is given by [104]

$$\varepsilon^{-1}(k) = 1 + \frac{\hat{v}(k)\mathcal{L}(k)}{1 - \hat{v}(k)\mathcal{L}(k)(1 - G(k))} \tag{3.12}$$

where $\mathcal{L}(k)$ is the static Lindhard function, i.e. the susceptibility of the ideal Fermi gas. In terms of the dimensionless wave number $q = k/2k_F$, where $k_F = (3\pi^2 n)^{1/3} = (9\pi/4)^{1/3}/(r_s\ a_0)$ is the Fermi wave vector, this quantity is

$$\mathcal{L}(q) = -\frac{k_F}{\pi^2 a_0}\left[\frac{1}{2} + \frac{1-q^2}{4q}\ln\left(\left|\frac{1+q}{1-q}\right|\right)\right] \tag{3.13}$$

The logaritmic singularity at $q = 1$ is at the origin of the Friedel oscillations observed in the tail of the effective potential, as shown in Fig. 3.1.

The factor $G(k)$, known as local field factor, has been introduced [106, 107] to give an improved representation of the exchange and correlation hole around an electron. This term is proportional, through the interaction potential $v(k)$, to the Fourier transform of the second functional derivative of the correlation energy functional with respect to the density [108]. Using Quantum Monte Carlo methods, it has been computed in a range of density corresponding to $2 \leq r_s \leq 10$ and parametrized in various analitical forms [104, 108, 109]. Since our system is at higher density, i.e. at lower correlation, we expect that the simpler Local Density Approximation form be accurate enough for our purpose [110]

$$\begin{aligned} G(q) &= q^2\left[1 - \frac{\pi}{3}\left(\frac{4}{9\pi}\right)^{1/3}\left(r_s^3\frac{d^2\epsilon_c}{dr_s^2} - 2r_s^2\frac{d\epsilon_c}{dr_s}\right)\right] \\ &= q^2\left[1 + \frac{\pi}{3}\left(\frac{4}{9\pi}\right)^{1/3} r_s\left(3A + Cr_s(1 + 2ln(r_s)) + 2Dr_s\right)\right] \end{aligned} \tag{3.14}$$

where $\epsilon_c = A\ ln(r_s) + B + Cr_s ln(r_s) + Dr_s$ is the correlation energy from eq. (3.11).

To assess the ability of the present model to describe the hydrogen at high density, we compared the electron-proton correlation function $h_{ep}(r)$ for our pseudo-ion model against the one obtained for the two component system by Variational Monte Carlo simulations. In both cases protons are kept fixed on the lattice sites of a Face Centered Cubic crystal.

The correlation function $h_{ep}(r)$ of the Screened Coulomb system can be computed from the proton-proton structure factor $S_{pp}(\mathbf{k}) = \langle \rho^p_{\mathbf{k}} \rho^p_{-\mathbf{k}} \rangle / N$ as

$$h_{ep}(r) = \frac{V}{N}\int \frac{d\mathbf{k}}{(2\pi)^3} S_{pp}(\mathbf{k})\left(\frac{1}{\varepsilon(k)} - 1\right) \tag{3.15}$$

The QMC data are obtained within Variational Monte Carlo using an optimized Slater-Jastrow trial wave function with DFT-LDA single electron orbitals plus a backflow transformation and two-body correlation factors in the Jastrow part as described in Section 2.5.1.

Results are shown in Fig. 3.2. The linear response theory is found to reproduce quite accurately the weak electron-proton correlation except close to the origin where the electron-proton cusp is rounded. The model becomes more accurate for increasing density and, as shown in the figure, for $r_s \leq 0.6$ it provides a very good approximation to real hydrogen.

3.3 Classical system study

We want to investigate the behavior of atomic hydrogen in the region of the phase diagram where it can be approximated by the pseudo-ion effective model. In this section we will describe our strategy for the classical system and present results for the melting line in this approximation. At this extreme pressures quantum effects on the protons are relevant: we will hence consider also quantum effects on the melting line. We have explored the interval of the coupling parameter $r_s \in [0.6, 0.435]$, corresponding for hydrogen to the mass density range $m[gr/cm^3] \in [12.475, 32.736]$[2].

Due to the density dependence of the effective Hamiltonian, additional terms must be added to the virial expression of the pressure [101, 111]. If $\mathcal{F}$ is the Helmholtz

---

[2] in the case of hydrogen, the mass density in gr/cm^3 is related to the parameter r_s by: $\rho_m(gr/cm^3) = 2.6946/r_s^3$.

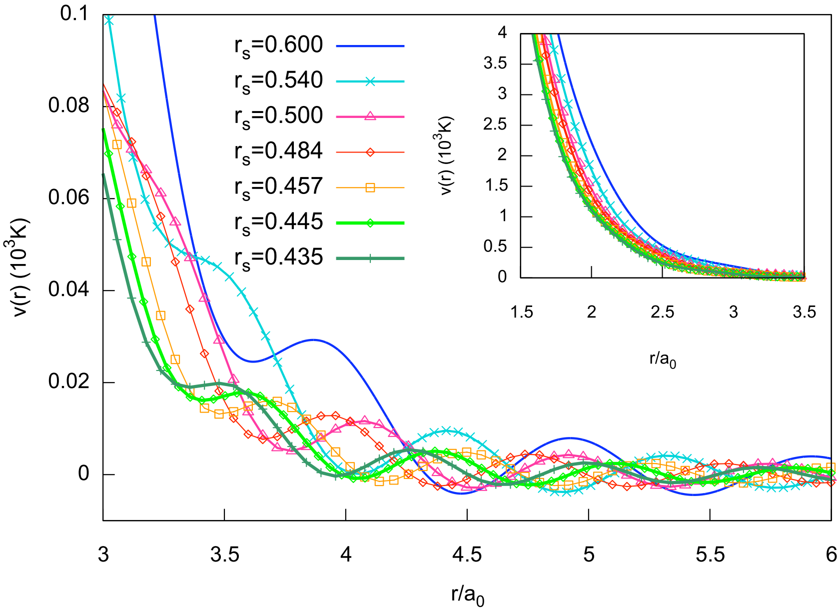

Figure 3.1. Friedel oscillations in the screened Coulomb pair potentials, for different densities corresponding to the range $r_s \in [0.435, 0.600]$. The inset shows a detail of the short-range repulsive part of the LRT potentials. Energy is expressed in kiloKelvin ($10^3 K$), distance in units of the Bohr radius a_0.

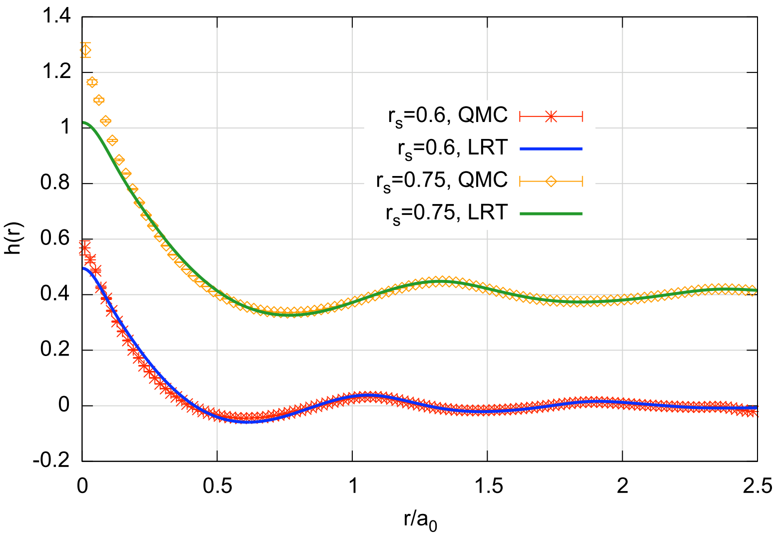

Figure 3.2. Electron-proton correlation function ($h_{ep}(r) = g_{ep}(r) - 1$) at $r_s = 0.75$ and $r_s = 0.6$. Comparison between QMC data and the linear response prediction. Data at $r_s = 0.75$ has been shifted upward by 0.4 for sake of clarity.

free energy of the pseudo-ions system, we have

$$\begin{aligned} p &= -\left(\frac{\partial \mathcal{F}}{\partial V}\right)_T = k_B T \frac{\partial}{\partial V} \log\left[Tr\left(e^{-\beta \mathcal{H}^{\text{eff}}}\right)\right] \\ &= \frac{2\langle \mathcal{K}_p \rangle}{3V} - \frac{1}{6V}\left\langle \sum_{i,j\neq}\left[R_{ij}\frac{\partial v^{\text{eff}}(R_{ij};r_s)}{\partial R_{ij}} - r_s f^{\text{eff}}(r_{ij};r_s)\right]\right\rangle + p_{eg}(r_s) \end{aligned} \tag{3.16}$$

where $\langle \ldots \rangle = Tr\left\{e^{-\beta\mathcal{H}^{\text{eff}}} \ldots\right\}$, $f^{\text{eff}} = \partial v^{\text{eff}}/\partial r_s$ is the density derivative of the potential and the last term is the electron gas contribution coming from the volume term

$$p_{eg}(r_s)\left[\frac{Hrt}{a_0^3}\right] = -\frac{r_s}{3V}\frac{\partial E_{eg}(r_s)}{\partial r_s} = \frac{1}{4\pi r_s^2}\left[\frac{2.210}{r_s^3} - \frac{0.468}{r_s^2} - \frac{A}{r_s} - Cln(r_s) - C - D\right] \tag{3.17}$$

For classical ions, $\langle \mathcal{K}_p \rangle$ is the average kinetic energy of the system $\langle \mathcal{K}_p \rangle = 3Nk_BT/2$. For quantum ions, we have already discussed in Section 2.4.4 various estimators for the kinetic energy and for the pressure.

3.3.1 Ground state structure

In order to study the melting transition we need to find good candidate crystal structures, i.e. structures with low ground state energy and enthalpy. To this aim we computed the energy as a function of density and the enthalpy as a function of the pressure for a number of different Bravais lattices with different symmetries, including

* 5 cubic structures: Simple Cubic (SC), Face Centered Cubic (FCC), Body Centered Cubic (BCC), the Diamond (DIAM) and A_{15}

- 2 tetragonal crystals: Simple Tetragonal (ST) and Body Centered Tetragonal (BCT)
- 2 hexagonal structures: Simple Hexagonal (SH) and Hexagonal Close Packed (HCP)

The choice of the selected structures was guided by previous works on hydrogen [47, 49, 112]. A sketch of the unit cell of those lattices is presented in Figures 3.3, 3.4 and 3.5.

Simple and Body Centered Tetragonal are originated respectively from Simple and Body Centered cubic by stretching the cells along the vertical direction (z). It follows that for those structures the cell geometry depends on the parameter $\gamma = c/a$, the ratio between the horizontal (a) and the vertical (c) cell sides, which need to be determined. Similarly, the Hexagonal structures depends on the parameter $\gamma = c/a$, which is the ratio between the side a of the basis hexagon and c the height of the cell. The best geometry of these non cubic structures, corresponding to the value of the parameter γ that minimize the energy (at fixed density) or the enthalpy (at fixed pressure) can be obtained by performing a series of zero temperature energy/enthalpy calculations at different values of the parameter γ. As a general result, we find that the minimum energy and enthalpy correspond to the cubic arrangement of the cells ($\gamma = 1$) for BCT and ST and to the value of $\gamma = 0.8$ in the SH structure. For the HCP, instead, we did not performed the geometry optimization and assumed the ideal value of the parameter $\gamma = 1.6333$.

As shown in Fig. 3.1, the effective pair potential is characterized by a repulsive behavior at short distance and by a small amplitude, slowly decaying and oscillating tail at larger distance ($\sim cos(k_f r)/r^3$). Because of such tail the Madelung energy is find to converge slowly to its bulk limit with the potential cut-off. In the upper panel of Fig. 3.6 for BCC and FCC lattices at one density, we show that full convergence for the Madelung energy requires very large cut-off of the order of 80-90 a.u.. However we are not interested in the absolute energy/enthalpy of the various structures, but on the energy/enthalpy differences among different candidates structures. This quantity converges more rapidly with the cut-off, as can be seen from the bottom panel of Fig. 3.6, showing that the BCC-FCC energy difference is already converged considering a cutoff of the order of $20a_0$.

In Fig. 3.7 we show the energy and enthalpy per particle, relative to the FCC quantites, of the various structures considered, and in Table 3.1 we report the numerical values of the absolute properties. FCC is the most favorable structure in the range of density considered except at the lowest density ($12.5g/cm^3$, corresponding to $r_s = 0.6$), followed by BCC, HCP and A15 structures. SH is considerably higher in energy and enthalpy while SC and the diamond structures are even higher and out of the scale of Fig. 3.7.

3.3.2 Temperature behavior

On the basis of the ground state analysis, we limited our investigation of the thermal behavior to the FCC and BCC structures. To determine their relative stability with temperature and their stability with respect to the liquid (disordered) phase, we want to compute the free energy of the various phases. To this aim we employed

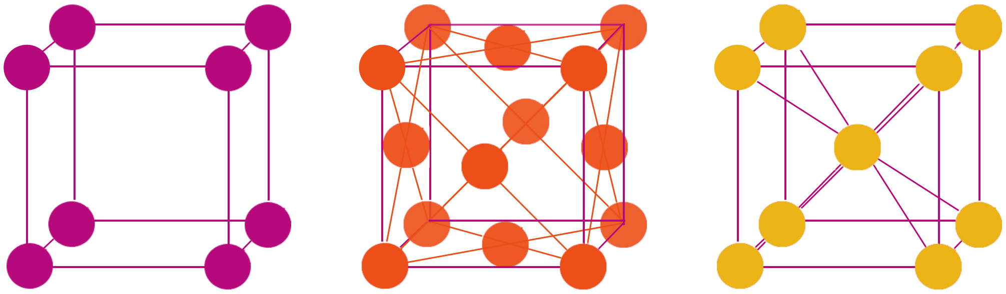

Figure 3.3. From left to right: Simple (SC), Face Centered (FCC) and Body Centered (BCC) structures. The tetragonal lattices Simple and Body Centered tetragonal can be derived respectively from SC and BCC by stretching the crystal along the vertical $\hat{z}$ direction.

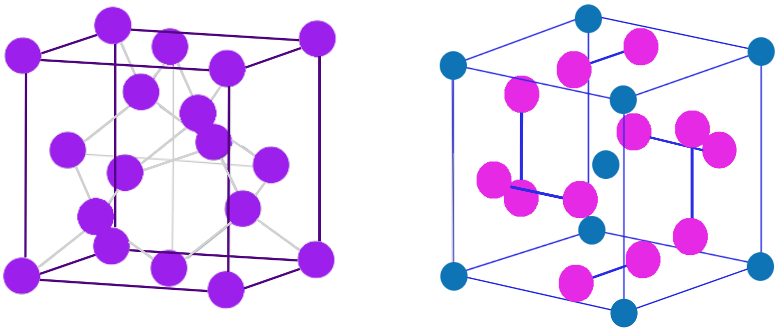

Figure 3.4. Left: Diamond structure (DIAM), given by two compenetrated FCC lattices: the second FCC cell is shifted along the diagonal of the first of 1/4 of the diagonal lenght. Right: A_{15} structure, obtained as a SC lattice with a basis of 8 atoms.

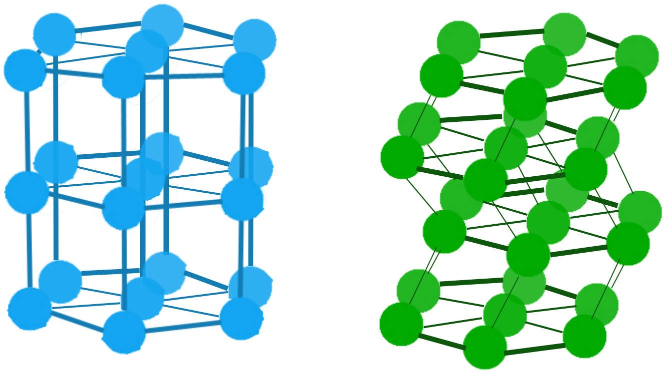

Figure 3.5. Hexagonal structures: on the left the Simple Hexagonal (SH) and on the right Hexagonal Close packed (HCP) structures.

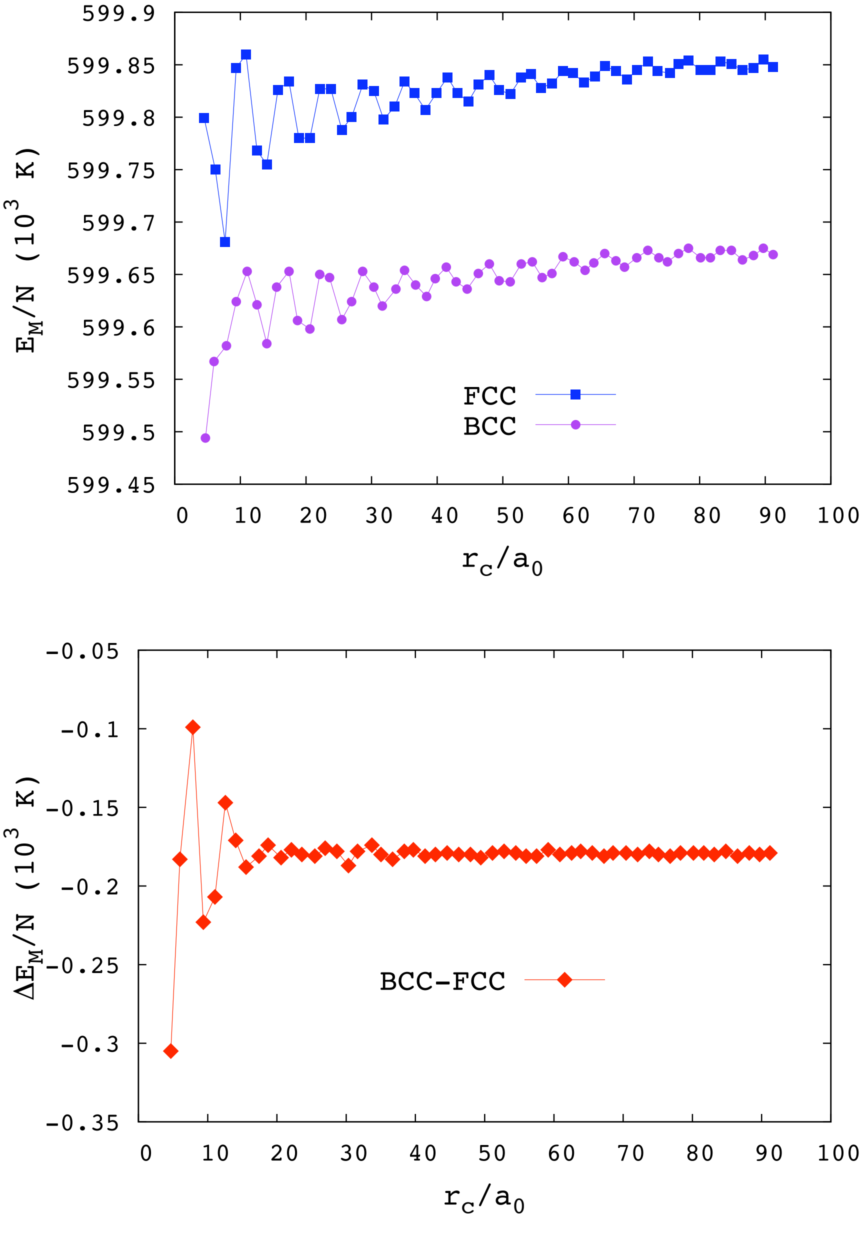

Figure 3.6. Top panel: Convergence with the potential cut-off r_c of the Madelung energy to its bulk value for the BCC and FCC structures at $r_s = 0.435$; bottom panel: convergence of the difference $E_{\rm BCC} - E_{\rm FCC}$ with the potential cut-off.

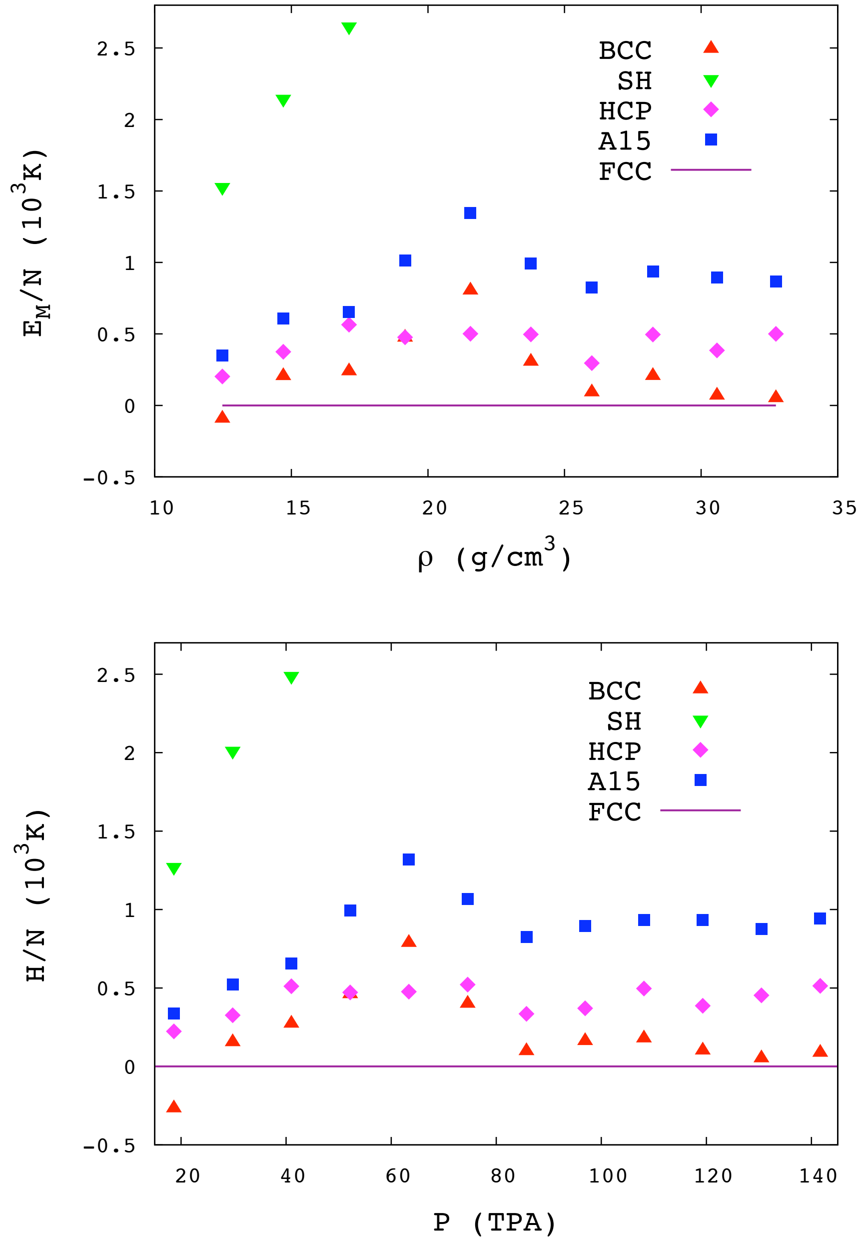

Figure 3.7. Madelung energies (upper panel) and zero temperature enthalpies (lower panel) comparison among different perfect lattices. Values are per particle and relative to the FCC phase. Data for less favorable structures (as β-Sn or Diamond) are out of scale.

Table 3.1. Converged Madelung energies for several crystalline structures as a function of density.

ρ_m (g/cm^3)	BCC (10^3K)	FCC (10^3K)	SC (10^3K)	A15 (10^3K)	DIAM (10^3K)	HCP (10^3K)	SH (10^3K)
12.4753	258.813	258.961	263.856	259.707	276.966	259.143	260.770
14.7049	303.489	303.364	307.130	303.919	322.686	303.649	305.662
17.1130	343.393	343.274	349.423	344.064	364.410	343.995	345.915
19.1645	381.034	380.319	387.246	381.576	403.618	381.019	384.271
21.5574	423.440	422.495	427.607	423.421	447.825	423.623	426.830
23.7668	455.850	455.917	463.008	456.628	481.713	456.471	459.890
25.9999	496.124	495.991	503.589	496.813	522.661	496.378	500.259
28.2330	530.119	529.977	536.258	530.720	557.527	530.513	533.665
30.5792	566.214	566.138	573.469	567.185	594.810	566.590	570.061
32.7369	599.669	599.848	608.699	600.416	628.853	600.248	604.070

Metropolis Monte Carlo in the NVT ensemble to explore the range of temperature $T \in [200, 5000]K$. In the range of densities considered this corresponds to a range of the Coulomb coupling parameter $\Gamma = 1/(r_s T(a.u.)) \in [105.2, 3630]$. Previous investigations of the same model [113, 114, 115] have been limited to values of $\Gamma \leq 150$, conditions relevant to high temperature plasmas found in the interior of Jovian planets and in white and brown dwarfs [113]. Properties were obtained by averaging over 40000 MC passes (global moves), after a sufficiently long equilibration period.

Because of the oscillating tail of the potential some care is needed in the energy calculation. Being our calculations at very high density, we cannot assume a cut-off of $\sim 20a_0$, necessary to achieve the convergence of the Madelung energy differences. The standard Ewald breakup turned out not to be efficient for our pair potential because it is not a very long range potential, as the pure Coulomb interaction, but have a middle ranged tail. We have then adopted another strategy in the present calculations, cutting the potential at a fixed distance ($r_c = 6.2a_0$), at which the amplitude of the potential at the cut-off is only a few degrees Kelvin at all densities investigated, much less then the minimum temperature considered in our calculations ($200K$). Despite, a small systematic error is introduced by this procedure: to partially remove the effect of a short cut-off on the energy, we corrected the MC estimates of the energy at finite temperature in the crystalline phases by adding the converged value of the Madelung energy and subtracting the Madelung energy obtained with this cut-off radius. In the liquid phase we added to the energy the standard tail correction [70], obtained assuming a unitary radial distribution function $g(r)$ beyond the cut-off radius.

In order to adopt this short cut-off radius and still use a limited number of particles in the simulation cell, we have considered, in addition to the interactions between particles in the primary simulation box, also the interactions with its 26 nearest images. With this strategy we are able to limit our system sizes to few hundreds particles (∼250) to be compared with several thousands of particles needed when fixing the box size at $L = 2r_c$. This procedure limits the maximum density

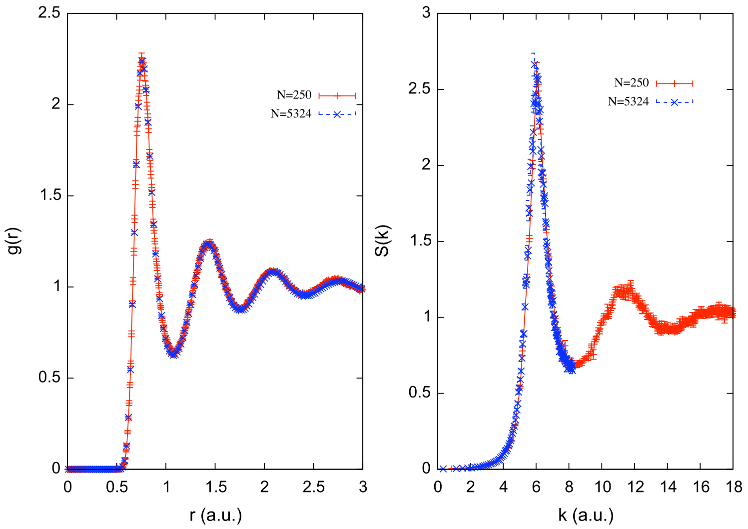

Figure 3.8. Comparison between structural properties of small (256) and large (5324) systems: radial distribution function $g(r)$ (left) and structure factor $S(k)$ (right) at $T = 4000K$ and $r_s = 0.445$.

that can be investigated to $\sim 40gr/cm^3$, corresponding to $r_s \sim 0.41$.

To check the residual effect of the artificial periodicity imposed by the summation on the nearest neighbors box images, we compared thermodynamic and structural properties computed with 256 particles in the liquid phase at $T = 4000K$ and different densities with those for a larger system ($N = 5324$) with box size $\gtrsim 2r_c$. Results are summarized in Table 3.2 and Figure 3.8. We found a very good agreement for the structural properties like the radial distribution function and the structure factor and for the energies, while a small residual error ($\sim 0.1\%$) remains on the pressure in particular for the higher densities.

In order to compute the free energy for the liquid and the two solid phases

Table 3.2. Comparison of energies per particle and pressures between data for a small system size ($N = 256$) summing over nearest box images, and data for a large system size ($N = 5324$) with minimum image convention. Liquid state at $T = 4000K$ and various densities.

r_s –	ρ_m (g/cm^3)	E_{256} (10^3K)	E_{5324} (10^3K)	$P_{256}V$ (10^3K)	$P_{5324}V$ (10^3K)
0.600	12.5	268.22(1)	268.237(2)	60.217(3)	60.210(1)
0.540	17.0	352.73(1)	352.730(2)	76.616(2)	76.614(1)
0.500	21.5	429.64(1)	429.647(2)	90.576(2)	90.6587(9)
0.484	23.7	466.40(1)	466.408(3)	98.969(2)	98.972(2)
0.468	26.3	503.42(1)	503.425(4)	107.225(2)	107.232(1)
0.457	28.2	539.02(2)	539.110(5)	112.818(1)	112.830(1)
0.445	30.5	575.84(2)	575.845(5)	118.392(3)	118.501(1)
0.435	32.7	609.09(1)	609.096(3)	126.032(2)	126.128(3)

we performed various simulations in the range of temperature $T \in [500, 4000]K$.

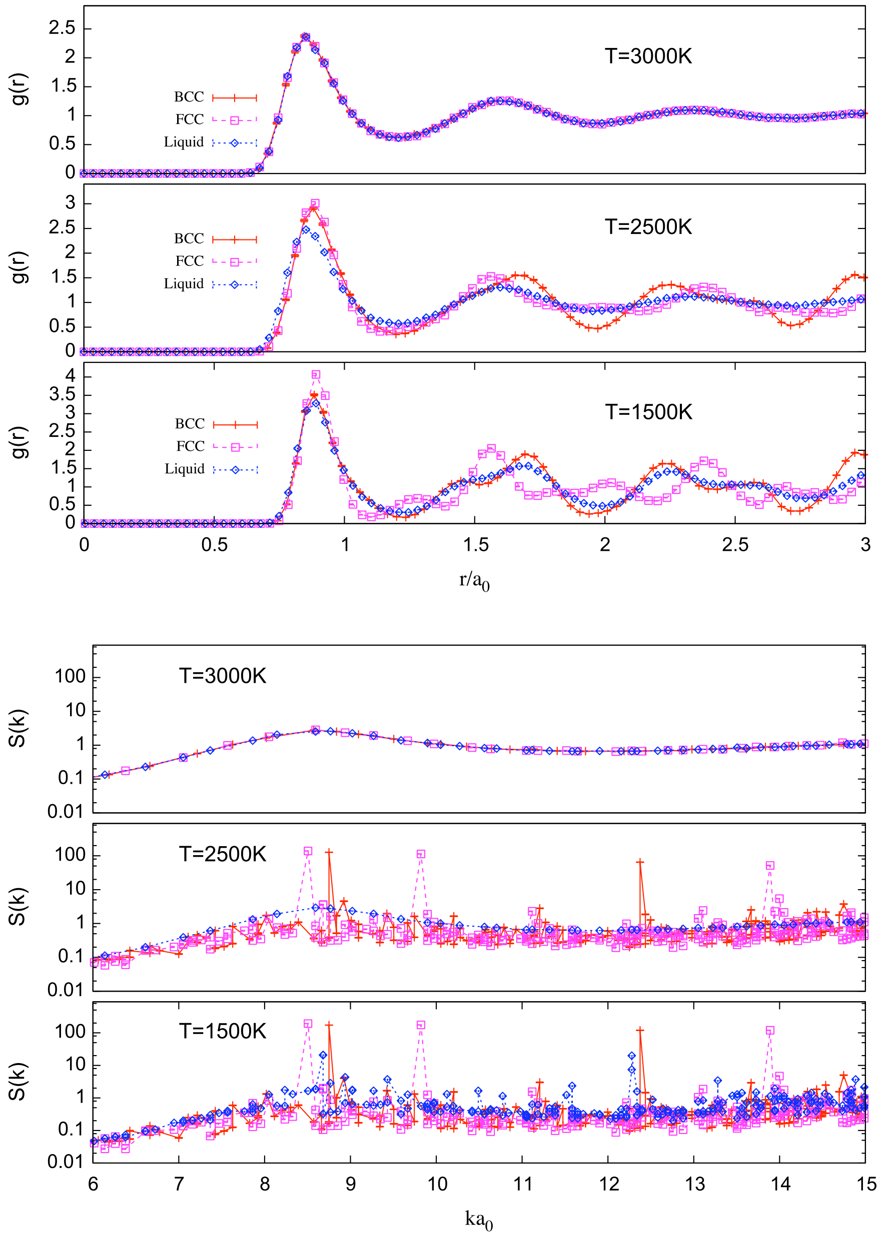

Figure 3.9. Pair distribution function and static structure factors of BCC, FCC and liquid at $r_s = 0.5$ and different temperatures: $T = 3000K$, $T = 2500K$ and $T = 1500K$ (from the upper panels to the lower).

Qualitative informations about the melting and freezing phenomena can be inferred looking at the structure functions. As an example, Fig. 3.9 compares the behavior of $g(r)$ and $S(k)$ for systems prepared in the liquid, FCC and BCC phases at $r_s = 0.5$ and different temperatures. The system sizes were $N = 250$ for BCC phase, and $N = 256$ for FCC and liquid phases. We can clearly recognize, in particular from the $S(k)$, the hysteresis indicating the presence of a first order phase transition between the solid and the liquid phase. At $T = 3000K$ the structure is unique and does not depend on the way the system has been prepared: this indicates that we are far enough from the transition. At $T = 1500K$ the system initially prepared in the liquid phase tends to freeze, as can be seen from the appearance of sharp peaks in its $S(k)$. Comparing the position of those peaks with the peaks of the BCC and of the FCC structures, it can be deduced that the disordered system is spontaneously rearranging into a BCC-like structure. However, since the number of particles of the system does not fit with the number necessary to form a perfect BCC structure, some defects are present. This is a first, qualitative indication that BCC is the stable crystal structure at melting. The FCC $S(k)$ instead, remains substantially unaltered, probably because the energy necessary to form a BCC structure with vacancies is higher than the free energy difference between BCC and FCC at this temperature. Finally, at the intermediate temperature among those shown (T=2500K) the system remains in the initial structure for a very long time; the large broadening of the $g(r)$ peaks in the solid phase probably indicates that the solids are overheated and metastable with respect to the liquid. To make these observations more quantitative and trace the melting line of the system, it is necessary to compute the free energy of the various phases, as described in the following section.

3.3.3 Free energy calculations

Quantitative information about the location of the melting line can be obtained by comparing the Helmholtz free energy of the three phases under consideration. To identify coexistence points from the analysis of Helmholtz free energy curves the common-tangent construction is necessary [116]: it consists in plotting the isothermal free energy of the two competing phases as a function of the specific volume, and then recognizing pairs of points belonging to different curves but lying on a common tangent. The abscissa of those points represents the specific volume of each phase at coexistence, while the opposite of the slope of the tangent is the coexistence pressure.

For each phase, the free energy can be obtained by thermodynamic integration

$$\mathcal{F}(\alpha_B) = \mathcal{F}(\alpha_A) + \int_{\alpha_A}^{\alpha_B} d\alpha \frac{\partial \mathcal{F}}{\partial \alpha} \tag{3.18}$$

where $\alpha = \rho$,$\partial_\rho \mathcal{F} = p/\rho^2$ along isotherms and $\alpha = T$,$\partial_T \mathcal{F} = -U/T^2$, with $U = \langle \mathcal{H} \rangle$, along isochores, once $\mathcal{F}(\alpha_A)$ is known [70]. The free energy of the reference state $\mathcal{F}(\alpha_A)$ can be computed by Coupling Constant Integration (CCI), i.e. by introducing a fictitious Hamiltonian dependent on a parameter $\lambda \in [0, 1]$ which couples the original system to a reference system of known (or easy-to-compute) free energy. If $\mathcal{H}_\lambda = \mathcal{H}_1 \lambda + \mathcal{H}_0(1 - \lambda)$, where $\mathcal{H}_1$ is the Hamiltonian of the reference system and

$\mathcal{H}_0$ the Hamiltonian of the original system, we have

$$\mathcal{F}(0) = \mathcal{F}(1) + \int_0^1 d\lambda \langle \mathcal{H}_0 - \mathcal{H}_1 \rangle_\lambda \tag{3.19}$$

where $\langle \dots \rangle_\lambda$ indicates a statistical average with weight $e^{-\beta \mathcal{H}_\lambda}$. In the solid phase the natural reference system is an "Einstein crystal" of same structure as the original solid, a system of independent oscillators of same elastic constant κ, each one with the equilibrium position on a lattice site [70, 117]. The λ integration performed with respect to this system is also known with the name of Frenkel-Ladd method [117]. For the liquid phase, we simply used the coupling parameter λ to switch off the interaction between the pseudo-ions $\mathcal{V}_\lambda = (1-\lambda)\mathcal{V}^{\text{eff}}$. This is equivalent of increasing the temperature up to the ideal gas limit. The integrals over λ are estimated with a Gauss-Legendre quadrature scheme with 12 points for the solid phases and 20 points for the liquid phase. In the latter case, since the integrand has a growth particularly steep as λ approaches 1, a correction accounting for the inability of the Gauss-Legendre interpolants to follow the behavior of the integrand has been added to the estimate of the integral, as described in Appendix .6.

Thermodynamic integrations along isochores are carried out for each density and for the three phases by: (1) computing the internal energies on a grid of temperatures, (2) fitting the energy data with a third order polynomial in T, $U(T,\rho) = \sum_{n=0}^{3} a_n(\rho) T^n$, and (3) performing explicitly the integration of the fitting function from a given reference temperature T_0 to the generic temperature T. This procedure leads to the following expression for the Helmholtz free energy

$$\begin{aligned} \mathcal{F}(T,\rho) &= \frac{T}{T_0}\mathcal{F}(T_0,\rho) + a_0(\rho)\left(1 - \frac{T}{T_0}\right) \\ &\quad - T\left[a_1(\rho)\ln\left(\frac{T}{T_0}\right) - a_2(\rho)\left(T - T_0\right) - a_3(\rho)\left(T^2 - T_0^2\right)\right] \end{aligned} \tag{3.20}$$

We set the reference temperature T_0 at $6000K$ for the liquid phase and at $500K$ for the solid phases. Numerical values of the fitting parameters a_n are given in Table 3.3. With this procedure we avoid to use the pressure data that, as already discussed, are affected by a residual finite size effect. Along isotherms, the density dependence of the excess Helmholtz free energy can be fitted with a second order polynomial in ρ_m. We can obtain an expression of the pressure with reduced systematic finite size errors by direct differentiation of this expression.

The inset (a) of Fig. 3.10 shows an example of the excess Helmholtz free energies, along the isotherm at $T = 2500K$, for the three competing phases: liquid, BCC and FCC. The three curves for the three phases are very close to each other and only slightly convex. In order to enhance their curvature, to help identify a common tangent, we have subtracted to all curves the same linear behavior κv: this operation will not affect the determination of the specific volumes of two competing phases. An example is given in the main panel of Fig. 3.10. Even with this subtraction the common tangent construction is particularly hard to apply: although our error bars on the free energy are very small (0.003%), the free energy curves are so close to each other that a quantitative estimate of the liquid and BCC specific volumes at coexistence with appropriate error bars turns out to be impossible.

Table 3.3. Values of the parameters used to fit the free energy of the BCC, the FCC and the liquid phase, according to Eq. (3.20). Densities are expressed in g/cm^3, f_0 and a_0 in units of 10^3K, a_1 is a dimensionless parameter, a_2 is in units of $(10^3K)^{-1}$ and a_3 in units of $(10^8K^2)^{-1}$.

ρ_m	12.5	17.0	21.5	23.7	26.3	28.2	30.5	32.7
f_0^L	283.963	369.807	447.776	484.973	522.443	558.328	595.599	629.097
a_0^L	261.106	344.778	421.768	458.798	494.198	536.023	567.483	599.164
a_1^L	2.59492	3.02028	2.66867	2.36179	3.71206	-1.15905	2.79676	3.95242
a_2^L	-0.28690	-0.36262	-0.22277	-0.13043	-0.49238	0.74571	-0.05808	0.07058
a_3^L	2.02837	2.62222	1.1955	0.40000	3.5556	-6.66667	2.26667	3.54815
f_0^F	265.192	349.350	425.924	462.543	499.655	535.112	571.897	604.990
a_0^F	261.155	345.007	421.300	457.972	495.242	530.686	567.417	600.403
a_1^F	1.35851	1.15098	2.11172	1.82019	1.45954	1.396	1.46372	1.44968
a_2^F	0.10355	0.32446	-0.40172	-0.18129	0.04134	0.08474	0.03438	0.14450
a_3^F	1.24273	-6.39716	10.4001	5.26667	0.58979	-0.39457	0.673656	-2.98644
f_0^B	265.042	349.214	425.941	462.584	499.650	535.153	571.938	605.039
a_0^B	261.032	345.108	421.513	457.977	495.277	530.863	567.907	600.478
a_1^B	1.42007	1.10833	1.72589	2.02952	1.50003	1.16169	1.5467	1.51647
a_2^B	-0.02345	0.34584	-0.13167	-0.33069	-0.02288	0.23754	-0.29343	-0.51038
a_3^B	5.87915	-6.67735	4.16266	8.05108	2.18527	-3.81446	2.49272	-1.24264

We interpreted this particular behavior as an indication that the change of specific volume at coexistence is negligibly small. First order phase transition with no specific volume change are known to occur in unscreened Coulomb systems (the One Component Plasma model and the Electron gas) because any specific volume discontinuity will cost an infinite energy due to the infinite range of the interaction potential and to the presence of the neutralizing rigid background. Our present model has a potential with finite range coming from a polarizing background and a volume discontinuity is in principle possible but probably very small. Neglecting any specific volume discontinuity at the coexistence between two phases α and β, the difference in Helmholtz free energy $\Delta\mathcal{F}_{\alpha,\beta}$ and the difference in Gibbs free energy $\Delta\mathcal{G}_{\alpha,\beta}$ both vanish

$$\Delta\mathcal{G}_{\alpha\beta}(T,P) = \mathcal{F}_\alpha(T,P(V_\alpha)) - \mathcal{F}_\beta(T,P(V_\beta)) + P(V_\alpha - V_\beta) = \Delta\mathcal{F}_{\alpha\beta}(T,P(V)) = 0 \tag{3.21}$$

As a consequence, a transition point between two phases can be detected as the intersection of the Helmholtz free energies curves relative to two competing phases, either along isotherms or isochores, having care to verify *a posteriori* that the pressure at coexistence is equal for the two phases. In panel (b) of Fig. 3.10 and in Fig. 3.11 we show an example of detecting a coexistence point along an isotherm and along an isochore, respectively. A BCC-liquid coexistence point is found as the point where $\Delta\mathcal{F}_{liq-BCC}(T,V) = 0$. On the left of this point (higher density or lower temperature) $\Delta\mathcal{F}_{liq-BCC}(T,V) > 0$ and the BCC phase is the stable one; on the other side (lower density or higher temperature) $\Delta\mathcal{F}_{liq-BCC}(T,V) < 0$ and the liquid is favored. To avoid using the pressure which is not directly obtained from the simulation data, we determine transition points along isochores. In Fig. 3.12 we report our data for the melting line, together with the melting line for the One Component Plasma, which corresponds to $\Gamma = 178$ [118]. As expected, we find that in the solid phase the BCC is more stable than the FCC at the coexistence with

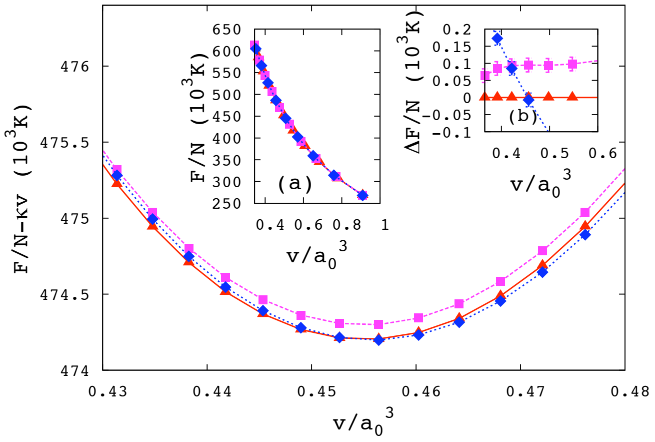

Figure 3.10. Comparison of the Helmholtz free energy curves, as a function of the specific volume v, for BCC (red triangles), FCC (magenta squares) and liquid (blue diamonds) phases, along the isotherm $T = 2500K$. In inset (a) the behavior of the isothermal free energies is showed. In the main figure, to enhance the curvature of the free energy lines, a linear term $l(v) = -\kappa v$, with $\kappa = 3.9\ 10^6 K/a_0^3$, has been subtracted to each curve. In inset (b) the FCC and the liquid phase free energy are plotted with respect to the BCC values, in order to highlight the intersections among the curves.

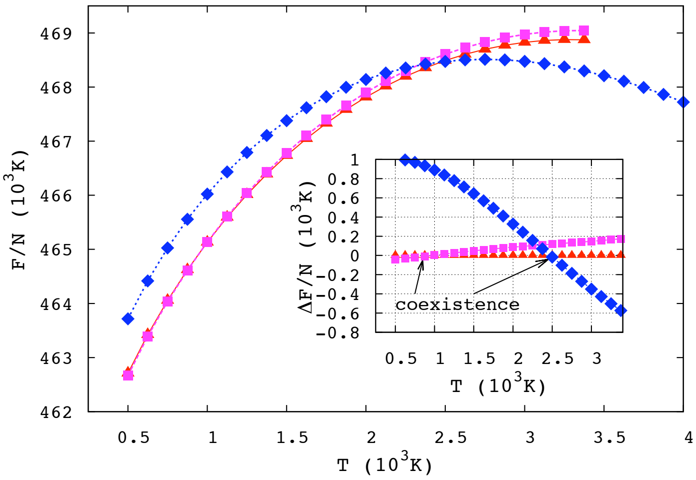

Figure 3.11. Free energies per particle of the liquid (blue diamonds), FCC (magenta squares) and BCC (red plus) phases, along the isotherm $T = 2500K$. Under the hypothesis of negligible volume discontinuities at the transition, the coexistence points can be easily recognized as the intersection between the curves. Inset: free energies relative to the BCC phase. Errors are smaller than the symbol size.

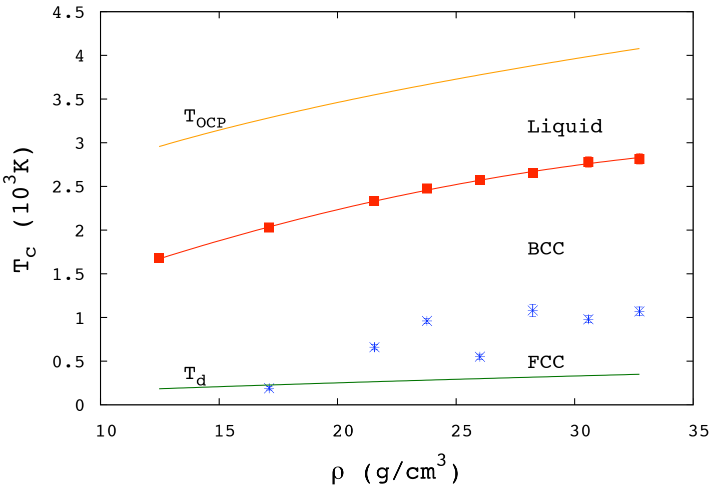

Figure 3.12. Coexistence points for the liquid-BCC phase transition (red squares) and for the BCC-FCC transition (blue stars), obtained assuming zero volume jump between the two phases at the transition. The One Component Plasma melting line ($\Gamma = 178$) (orange line) and the degeneracy temperature ($T_d[10^3 K] \approx 0.1597(\rho_m[g/cm^3])^{2/3}$, green line) for protons are also represented.

the liquid and that the melting line is slightly concave with a melting temperature between 1500K and 3000K in the explored density range. Numerical data for the melting line are summarized in the Table 3.4 together with the pressure for the solid and the liquid phases. At melting the pressure for the two coexisting phases, obtained from the density derivative of the free energy at constant temperature, are found to be in agreement within error bars, supporting the assumption that the transition occurs with a negligible specific volume discontinuity. Using the same procedure we can make predictions for the BCC-FCC transition line. Indeed from the Madelung energies in previous section we expect that FCC becomes more favorable than BCC at low enough temperature. This is confirmed by the free energy curves of the two solids along isochores, which mutually cross at some low

Table 3.4. Numerical data for the melting at different densities: melting temperature (T_m) and pressures of the liquid (P_l) and of the BCC phase (P_{BCC}) at coexistence are shown.

ρ_m (g/cm^3)	T_m $(10^3 K)$	P_l (TPa)	P_{BCC} (TPa)
12.5	1.68(4)	24.5(2)	24.7(2)
17.0	2.03(2)	42.1(2)	42.3(2)
21.5	2.33(3)	65.2(3)	65.5(3)
23.7	2.48(3)	81.0(4)	81.4(4)
26.3	2.57(3)	92.3(4)	92.8(4)
28.2	2.65(4)	103.3(4)	103.9(4)
30.5	2.78(6)	119.5(4)	120.1(4)
32.7	2.82(6)	136.3(4)	136.8(4)

T. The resulting transition points are depicted in Fig. 3.12. At variance with the BCC-liquid case, the free energy difference is now much smaller and statistical errors on the estimate are quite larger. Moreover the transition points are more scattered with density than observed for the liquid-BCC transition, most probably as an effect of the truncation of the potential adopted in our simulations which become more important at lower temperature, as discussed in the previous section. Nonetheless, our data indicates unequivocally the presence of a structural phase transition line with T between $250K$ and $1000K$ in the density range explored.

Finally we have investigated finite size effects on the transition points, by computing internal energies versus N for the three phases considered. For both crystalline phases we have found that the specific free energy rises by roughly $30K$, while for the liquid phase size effects are negligible. As a consequence our estimate of the FCC-BCC transition is unaffected by size effects while the BCC-liquid temperature is lowered by an amount which is however within the present statistical uncertainties.

3.4 Gibbs-Duhem integration in the (T, v) plane

The procedure described in the previous section to build the classical melting line is based on independent free energy calculations of the three phases (BCC, FCC and liquid) at different densities and in a large range of temperatures.

Another approach is the Kofke's technique [122] (also known as Gibbs-Duhem thermodynamic integration) that allows to move along a transition curve, once a single coexistence point is known. To move along the transition line the Clausius-Clapeyron equation [116]

$$\left.\frac{dP}{dT}\right|_{coex} = \frac{\Delta h}{T\Delta v} = \frac{Q_L}{T\Delta\Omega} \tag{3.22}$$

is exploited. This equation indeed relates the slope of the coexistence curve in the (P, T) plane to the ratio of the difference in enthalpy per particle, Δh (or latent heat Q_L) and the difference of specific volumes, Δv, between the two coexisting phases.

Despite that the standard Kofke's procedure is not applicable in our case because of the negligibly small volume jump at coexistence, it is however possible to derive a formula analogous to the Clausius-Clapeyron equation. We can imagine to advance along the coexistence line in the (T, v) plane by a two-steps process $(A \to C; C \to B$, being A and B coexistence points and C an intermediate point off of coexistence) overcoming in this way problems due to the small Δv. Let us then explicitly derive this equation. Being $A \equiv (T_A, v_A)$ a point on the coexistence line. We can reach the second point $B \equiv (T_B, v_B)$ on the coexistence curve by first going to the intermediate point $C \equiv (T_B, v_A)$ at the initial specific volume and at the final temperature, and than reaching the final point B by a volume change at constant temperature. For each phase $\alpha(= 1, 2)$ the free energy difference per particle between the points A and B along this path is

$$\begin{aligned} f_\alpha(T_B, v_B) &= f_\alpha(T_A, v_A) + \left.\frac{\partial f_\alpha}{\partial T}\right|_A \delta T + \left.\frac{\partial f_\alpha}{\partial v}\right|_C \delta v \\ &= f_\alpha(T_A, v_A) - s_\alpha(T_A, v_A)\delta T - P_\alpha(T_B, v_A)\delta v \end{aligned} \tag{3.23}$$

where $\delta T = T_B - T_A$, $\delta v = v_B - v_A$, s_α is the entropy per particle and P_α the pressure of phase α. By imposing the equality of the free energy at the coexistence we get

$$v_B = v_A - \frac{[s_1 - s_2]_A}{[P_1 - P_2]_C}\delta T = v_A - \frac{[e_1 - e_2]_A}{T_A[P_1 - P_2]_C}\delta T \tag{3.24}$$

where e_α is the specific internal energy of phase α. We have used $s = -f/T + e/T$ with the condition $f_1 = f_2$ at coexistence. If this condition is not satisfied at the initial point A we can still use the procedure but we need to retain the free energy difference

$$v_B = v_A - \frac{[e_1 - e_2]_A - [f_1 - f_2]_A}{T_A[P_1 - P_2]_C}\delta T \tag{3.25}$$

Note that the pressure difference at the denominator is computed off coexistence and therefore does not vanish. The same method can be developed in the (T, P) plane by using the Gibbs free energy rather than the Helmholtz free energy. In this case the volume difference will need to be computed off coexistence ensuring the non singular character of the integration scheme. We have tested the equations (3.24) and (3.25) on the BCC-liquid melting line. Results closely follow the melting line determined with the direct thermodynamic integration method, as summarized in Fig. 3.13.

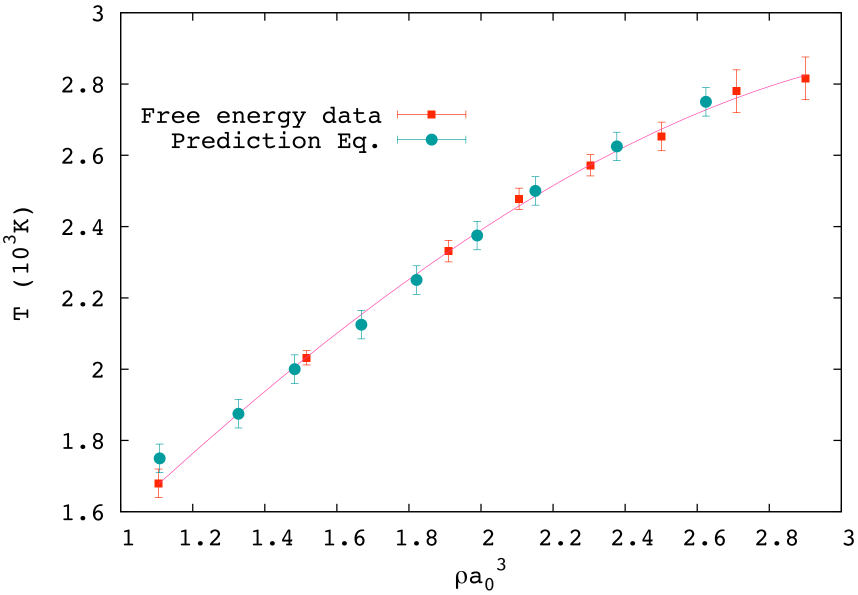

..

Figure 3.13. Classical melting curve. Squares are obtained through Helmholtz free energy comparison, diamonds by using Eq. (3.25) to follow the coexistence.

3.5 Nuclear quantum effects on the melting curve

Up to this moment we have considered the pseudo-ions in our system to be classical particles. However in the range of density and pressure considered quantum effects for protons might be relevant and affect the location of the transition lines. The relevance of quantum delocalization and statistics can be qualitatively understood by tracing with density the degeneracy temperature $T_D = \frac{\hbar^2}{m_p k_B} n^{2/3}$, defined as the temperature at which quantum delocalization equals interparticle distance; m_p is the proton mass. The Fermi temperature lies quite below the melting transition line and exchanges are negligible in the solid phase. Therefore in the range of densities investigated the effects of quantum statistics is negligible. Quantum effects are only due to delocalization and we expect to become large below the degeneracy temperature line. From Fig. 3.12 we see that T_D is mostly below the BCC-FCC line so that we expect quantum effects to be small on the transition lines.

Since our present estimate of the FCC-BCC line is only qualitative, we will compute the quantum correction for the melting line only.

To derive the quantum correction to the free energy curves, let us recall the equation (2.93), which relates the partial derivative of the free energy of a quantum system with respect to the parameter $\lambda = \hbar^2/2m$ to the average kinetic energy of the system

$$\frac{\partial \mathcal{F}}{\partial \lambda} = \frac{1}{\lambda} \left\langle \hat{\mathcal{K}} \right\rangle_\lambda \tag{3.26}$$

It follows that the free energy of a system characterized by $\lambda = \lambda_p$ and at a given thermodynamic condition (T, ρ) can be obtained from the free energy of another system at the same thermodynamic point, with same potential energy but different particle mass and then with a different $\lambda = \lambda_0$ through the formula

$$\mathcal{F}(\lambda_p) = \mathcal{F}(\lambda_0) + \int_{\lambda_0}^{\lambda_p} \frac{d\lambda'}{\lambda'} \left\langle \hat{\mathcal{K}} \right\rangle_\lambda \tag{3.27}$$

When λ_0 becomes sufficiently small, the reference system can be approximated with its classical limit, for which the free energy splits naturally into an ideal and an excess part. While the excess term is λ independent, the ideal free energy has a logarithmic dependency on λ

$$\mathcal{F}_{cl}^{\mathrm{id}}(\lambda) = -K_B T \ln \left[\frac{\Omega^N}{N!} \left(\frac{K_B T}{\lambda} \right)^{3N/2} \right] \tag{3.28}$$

Moreover, if we introduce the quantity $\Delta\mathcal{K}(\lambda)$, representing the deviation of the average quantum kinetic energy from the classical value

$$\Delta\mathcal{K}(\lambda) = \left\langle \hat{\mathcal{K}} \right\rangle_\lambda - \frac{3}{2} N K_B T \tag{3.29}$$

we can rewrite (3.27) as

$$\begin{aligned} \mathcal{F}(\lambda_p) &= \mathcal{F}_{cl}(\lambda_0) + \int_{\lambda_0}^{\lambda_p} \frac{d\lambda}{\lambda} \left[\left\langle \hat{\mathcal{K}} \right\rangle_\lambda - \frac{3}{2} N K_B T + \frac{3}{2} N K_B T \right] \\ &= \mathcal{F}_{cl}(\lambda_0) + \frac{3}{2} N K_B T \ln \left(\frac{\lambda_p}{\lambda_0} \right) + \int_{\lambda_0}^{\lambda_p} \frac{d\lambda}{\lambda} \Delta\mathcal{K}(\lambda) \end{aligned} \tag{3.30}$$

The second term on the right hand side summed to the ideal contribution of the classical free energy at $\lambda = \lambda_0$ reproduces the ideal free energy of a classical system at $\lambda = \lambda_p$. We than arrive at the final expression

$$\mathcal{F}(\lambda_p) = \mathcal{F}_{cl}(\lambda_p) + \int_0^{\lambda_p} \frac{d\lambda}{\lambda} \Delta\mathcal{K}(\lambda) \tag{3.31}$$

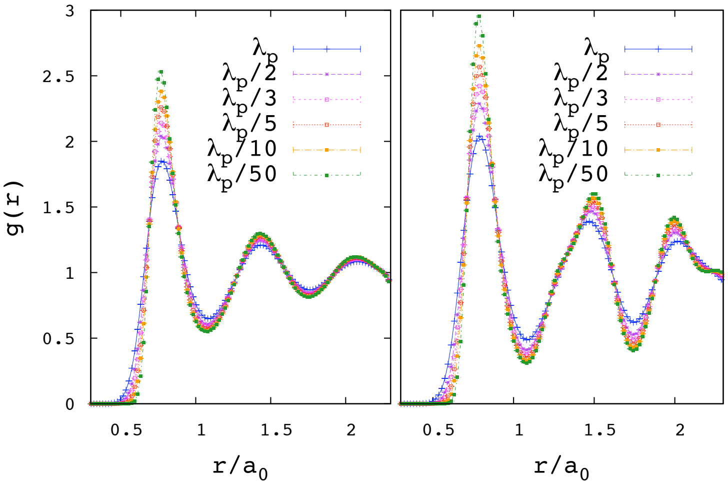

Figure 3.14. Behavior of the proton-proton radial distribution function with λ, for the liquid (left panel) and the BCC solid (right panel), near the classical melting temperature. $\rho_m = 30.5 g/cm^3$ (corresponding to $r_s = 0.445$), $T = 2780K$. At the smaller value of λ, $\lambda = \lambda_p/50$, the $g(r)$ of the system is identical within errorbars to the $g(r)$ of the classical system. The full quantum proton, instead, correspond to $\lambda = \lambda_p$. For quantum particles, the $g(r)$ becomes less structured and the height of the first peak is largely reduced with respect to the classical limit.

where $\mathcal{F}_{cl}(\lambda_p)$ is the free energy of the classical system with the actual value of λ_p. In the last equality the lower bound of the integral has been extended to 0 since $\Delta\mathcal{K}(\lambda)$ goes linearly with λ and cancels the divergence of the integrand at $\lambda = 0$. This formula allows to obtain the quantum free energy for all heavier isotopes at once.

To compute the quantum corrections (3.31) to the free energy curves of the BCC and the liquid phase and trace the quantum melting line, we carried out a series of Path Integral MC simulations in the NVT ensemble, at different densities in the range $\rho_m \in [12.5, 32.7] g/cm^3$, corresponding to $r_s \in [0.435, 0.600]$. Details on the PIMC technique can be found in Section 2.4 or in Ref.[64]. Since we expected the quantum effects on the melting temperature to be not too large, at each density ρ_m we calculated the corrections to the free energies only for three temperatures around the classical melting temperature $T_m^{cl}(\rho)$, for both the BCC and the liquid phases.

As for the classical simulations we have used systems of 250 protons and a cut-off radius for interaction of $r_c = 6.2a_0$. Both potential energy and pair actions have been obtained by considering each particle and its 26 nearest images. Since off-diagonal elements of the density matrix are short ranged, they were considered only for the nearest images.

In our calculations we used 32 protonic slices, which, according to preliminary tests, gives a satisfactory convergence ($\leq 3\%$) of the kinetic energy in the entire density range. Properties were averaged over 40000 MC steps, after equilibration.

Fig. 3.14 shows an example of the dependency of the radial distribution functions $g(r)$ on λ, for both the BCC solid and the liquid phase. In both phases, the $g(r)$

peaks broaden as λ is increased and for $\lambda = \lambda_p$ the height of the first peak is 60% smaller then the corresponding one observed for classical system. In addition, the rise of the $g(r)$ is less steep and begins at lower distances with respect to the classical limit.

To estimate the integral over λ in (3.31), we use a grid of six values from λ_p down to $\lambda_p/20$ below which the kinetic energy follows a linear behaviour compatible with the semiclassical prediction [119, 120]

$$\Delta\mathcal{K} \approx \lambda \frac{\pi}{3} \frac{\rho}{K_B T} \int_0^\infty r^2 g_{cl}(r) \left[\frac{d^2 V_{\text{eff}}(r)}{dr^2} + \frac{2}{r} \frac{dV_{\text{eff}}(r)}{dr} \right] dr + O(\lambda^2) \tag{3.32}$$

where the $g_{cl}(r)$ is the radial distribution function of the classical system.

The behaviour of the integrand with λ, illustrated in Fig. 3.15, can be accurately fitted with a third order polynomial in λ: $\Delta\mathcal{K} = \kappa_1\lambda + \kappa_2\lambda^2 + \kappa_3\lambda^3$. The fitting function can be integrated analytically to obtain the free energy of the quantum system as a function of λ

$$\mathcal{F}(\lambda_p|\rho, T) = \mathcal{F}_{cl}(\lambda_p|\rho, T) + \kappa_1(\rho, T)\lambda_p + \frac{\kappa_2(\rho, T)}{2}\lambda_p^2 + \frac{\kappa_3(\rho, T)}{3}\lambda_p^3 \tag{3.33}$$

As for the classical system, we assume that the volume discontinuities at coexistence are negligibly small, so that the melting temperature at fixed density can be obtained as the crossing points of the free energies of the competing phases along isochores. The numerical results for the melting temperature are summarized in Table 3.5 and illustrated in Fig. 3.16. Quantum effects on the melting are negligible ($\leq 2\%$) over the entire range of densities for the tritium isotope (T) and quite small ($\leq 4\%$) for deuterium (D), as shown in the inset of Fig. 3.16. In hydrogen, instead, the quantum melting curve results lowered and flattened at the highest densities considered, by as much as 10%.

Table 3.5. BCC-liquid transition temperature, as a function of the density, for classical protons ($T_m^{(cl)}$), tritium ($T_m^{(T)}$) , deuterium ($T_m^{(D)}$) and hydrogen ($T_m^{(H)}$).

r_s	ρ_m	$T_m^{(cl)}$	$T_m^{(T)}$	$T_m^{(D)}$	$T_m^{(H)}$
–	(g/cm^3)	$(10^3 K)$	$(10^3 K)$	$(10^3 K)$	$(10^3 K)$
0.600	12.5	1.68(4)	1.68(4)	1.68(4)	1.67(4)
0.540	17.0	2.03(2)	2.03(2)	2.03(2)	2.00(2)
0.500	21.5	2.33(3)	2.32(3)	2.32(3)	2.27(3)
0.484	23.7	2.48(3)	2.46(3)	2.45(3)	2.41(3)
0.457	28.2	2.65(4)	2.63(4)	2.60(4)	2.50(4)
0.445	30.5	2.78(6)	2.75(6)	2.70(6)	2.54(6)
0.435	32.7	2.82(6)	2.76(6)	2.71(6)	2.56(6)

3.6 Conclusions

We have traced the melting line of fully ionized hydrogen in a range of densities between $12.5 gr/cm^3$ and $32.7 gr/cm^3$ corresponding to the range of electronic

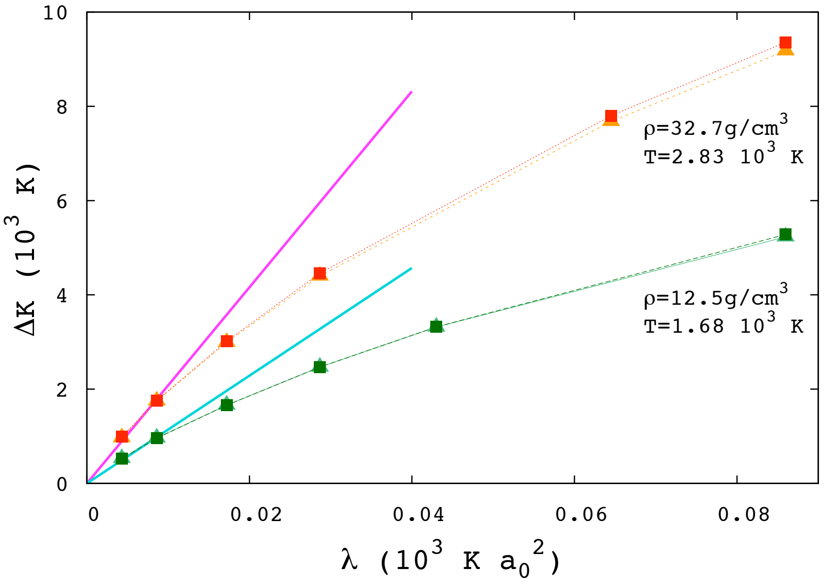

Figure 3.15. Kinetic energies per particle of the liquid (triangles) and the BCC phases (squares), as a function of λ, for the lowest ($\rho_m = 12.5g/cm^3$, green lines) and the highest ($\rho_m = 32.7g/cm^3$, red lines)densities we have considered, at the correspondent classical melting temperature ($T_m = 1.68\ 10^3K$ and $T_m = 2.82\ 10^3K$, respectively). Energies are scaled with respect to the classical contribution $3/2K_BT$. The straight lines represent the theoretical behavior at low λ from Eq. (3.32)

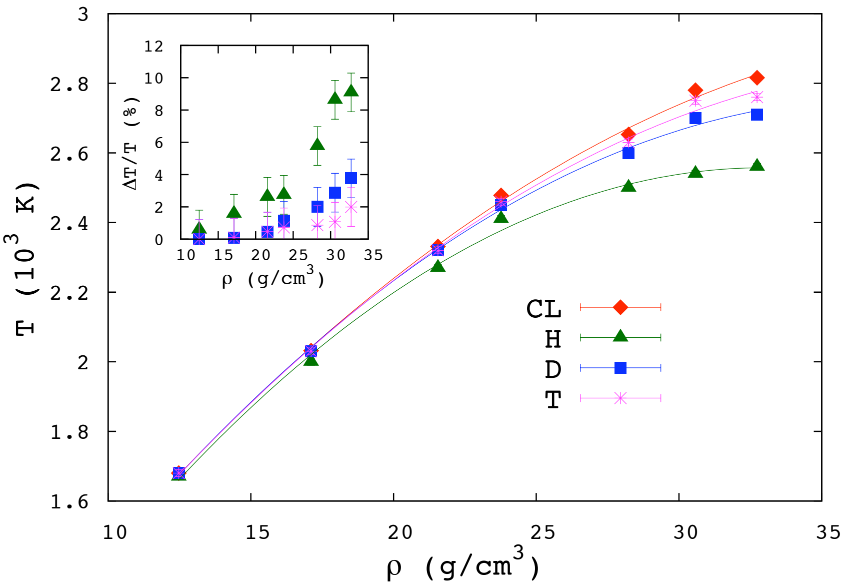

Figure 3.16. Melting lines for the Hydrogen (H, green triangles) and its isotopes deuterium (D, blue squares) and tritium (T, magenta squares), obtained by applying at the classical melting curve (CL, red diamonds) the quantum corrections (3.31). Dashed lines are polynomial fit of the data points. In the inset: differences in the melting temperatures between the classical and the quantum system.

Coulomb coupling parameter $r_s \in [0.430, 0.600]$ and to the range of pressure $24TPa \leq P \leq 140TPa$, well beyond the experimental reach. At these extreme conditions the fully degenerate electrons are weakly coupled to the proton charges and their interactions can be accurately described by linear response theory: the system is then equivalent to a system of pseudo-ions interacting with a screened Coulomb pair potential.

Due to the middle-ranged, oscillating tail of the effective pair potential the standard Ewald breakup revealed inefficient: it was not possible to find a good compromise between the cut-off length of the real space potential and that of the potential in the reciprocal space. It was then needed to assume a fixed cut-off for the potential: this approach is the main source of systematic errors in our simulations, that however has been checked to be quite small and to have negligible effect on the final results about the melting transition. Moreover, to limit the number of particles in our system to a reasonably small value, we considered not only interactions among particles inside the simulation box, but also the interactions with the 26 nearest neighbor boxes. This procedure, however, fix a limit for the upper densities that we can achieve considering only systems of a thousand particles. For those reasons we are developing an alternative Ewald breakup, capable to handle the screened Coulomb potential, that we will adopt in future calculations.

We have found that the FCC crystal is more favorable at $T = 0K$ among several cubic and non cubic structures. BCC structure is only slightly above in energy (or enthalpy) but gain stability in temperature, becoming the stable crystal structure near melting. The melting and the FCC-BCC lines have been computed by free energy methods and located between 1500K - 2500K and 200K-1000K respectively. Our estimate of melting is in rough agreement with previous predictions based on Lindemann criterium and *ab initio* Molecular Dynamics simulation of the electron-proton system [123]. Quantum correction to the melting transition has been computed by thermodynamic integration in the inverse mass from the classical to the quantum system, using PIMC. The melting line of hydrogen is barely affected by proton quantum effects at low density while it is lowered by as much as 10% in temperature at the highest density considered. Quantum effects on the FCC-BCC transition line has not been considered because of the qualitative character of our prediction for this line.

Our present results are relevant to the determination of the phase diagram of high pressure hydrogen, a system still largely unknown. In particular it is not known what is the state of hydrogen in a region of phase diagram between $200GPa \leq P \leq 25TPa$ and $T \leq 2000K$. In this regions several interesting physical phenomena occur (melting, molecular dissociation, metallization) and their quantitative location and interplay is far from clear. Even the ground state structure and its evolution with density from molecular to atomic hydrogen and beyond, are unknown. Our study of the effective model at ultrahigh pressures is preliminary to the study of hydrogen at lower pressures ($\sim 300GPa$) by *ab initio* simulations (with the Coupled Electron-Ion Monte Carlo Method) and represents a starting point to trace the melting line and the solid-solid phase transition lines of atomic hydrogen from the high density side of the interesting physical region.

Chapter 4

Monoatomic hydrogen melting

4.1 Introduction

The detailed study of the monoatomic and metallic pressure range of the hydrogen phase diagram is presently limited to the numerical simulations alone, being the maximum pressure that can be experimentally achieved of $\sim 350GPa$ [7, 8], still in the molecular region. Zero temperature studies predict that the transition from a molecular to a monoatomic solid occurs at pressures of $\sim 300GPa$ corresponding to $r_s = 1.31$, while the location of the same transition at finite temperature is still undetermined.

Another point to address is the determination of the solid-liquid transition in atomic hydrogen. In the first chapter of this thesis we presented three possible scenarios for the undetermined part of the hydrogen phase diagram, schematized in Figure 4.1. Besides the possibility of a dissociation and metallization transition occurring at low temperature in the solid phase (middle and right panels of Figure 4.1), the presence of a reentrant melting line in the molecular region and the slope and the position of the metallization line in the fluid phase, make possible the existence of a low temperature liquid monoatomic phase, which separates the molecular solid from the atomic solid phases of the diagram (left panel of Figure 4.1). To discriminate among the different possibilities it is then necessary to draw at pressure higher than $\sim 300GPa$ transition lines of the molecular system and to trace the melting line of the monoatomic phase.

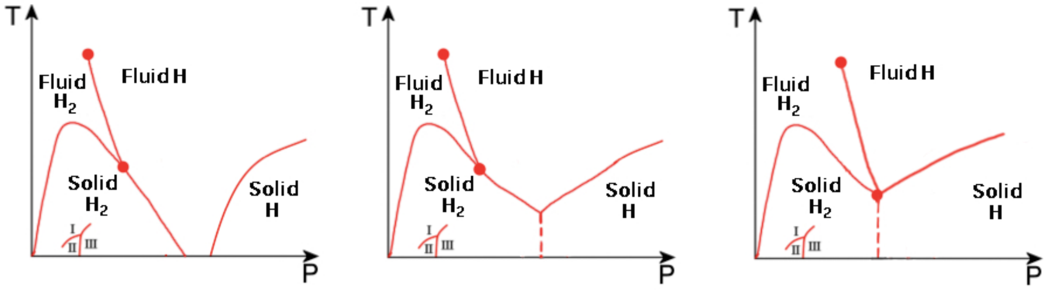

Figure 4.1.

The main difficulty in tracing the melting line in this part of the thermodynamic plane is due to the fact that, for loss of experimental data, the crystalline structure of the atomic hydrogen is unknown. Several theoretical studies [47, 48, 49] have proposed a list of possible candidate solids, but there is no conclusive evidence that the ground state structure of atomic hydrogen is among them. Indeed, those studies have considered only a limited set of crystals of simple symmetry, but it cannot be excluded that also a simple system as hydrogen could have a more complex crystallization lattice. Alternative approaches to determine the ground state crystal structures have been developed, such as the Ab Initio Random Structure Search method [28, 29] applied by Pickard and Needs to determine the ground state structure of the phase III of molecular hydrogen [28] and adopted very recently for the atomic hydrogen [52].

In line with earlier works, we have performed ground state energy/enthalpy calculations for several monoatomic lattices in the range of densities $\rho_m \in [1.20, 1.60] g/cm^3$, corresponding to $r_s \in [1.19, 1.31]$, using the RQMC simulations. Our results are presented in the first part of this chapter. At the lowest density, the temperature stability of a restricted set of structures has been investigated; we also computed the free energy of the most stable, the diamond structure, and compared it with the free energy of the liquid phase, obtaining a first estimate of the melting temperature. These results are described in the second part of the chapter.

4.2 Zero temperature study

In absence of experimental indications, to determine the crystallization structure of the monoatomic hydrogen at pressures higher than $\sim 350 GPa$, a systematic investigation extended to a large number of possible candidate lattices is needed. To this aim we compared energies and enthalpies of several perfect lattices, obtained from QMC simulations at zero temperature, at different densities in the range corresponding to $r_s \in [1.31, 1.19]$. In this analysis we assumed classical protons.

The set of Bravais lattices we considered includes

* 6 cubic crystals: Simple Cubic (SC), Face Centered Cubic (FCC), Body Centered Cubic (BCC), Diamond (DIAM), A_{15}, Fluorite (FL)

* 4 tetragonal crystals: Simple Tetragonal (ST), Body Centered Tetragonal (BCT), βSn (or CsIV), βNp

* 1 rhombohedral crystals: SmI

* 2 hexagonal crystals: Simple Hexagonal (SH), Hexagonal Close Packed (HCP)

The proton arrangement in those lattices is shown in Figures from 3.3 to 3.5 and from 4.2 to 4.4.

ST, BCT, SH, DIAM and CsIV, have been already considered as possible crystallization structures for the atomic hydrogen [49]. To these solids, we added the βNp, rather similar to the CsIV, as can be seen from Figure 4.3. The remaining structures in the set above have been suggested as good structures for alkali metals, as sodium or lithium, at high pressure [124].

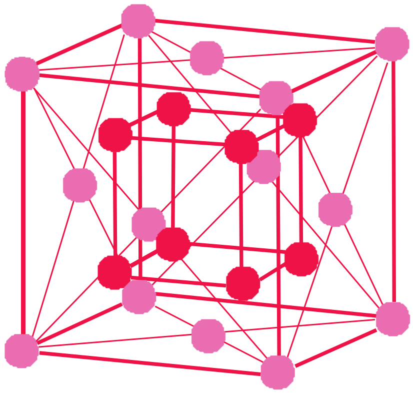

Figure 4.2. The fluorite (FL) crystal structure, belonging to the space group Fm$\bar{3}$m. Pink atoms lies on a face centered cubic lattice of side a. To complete the structure, one must add to this lattice the basis: $v_1 = (0,0,0)$, $v_2 = (1/4,1/4,1/4)a$, $v_3 = (-1/4,-1/4,-1/4)a$. The resulting structure has 12 atoms per unit cell.

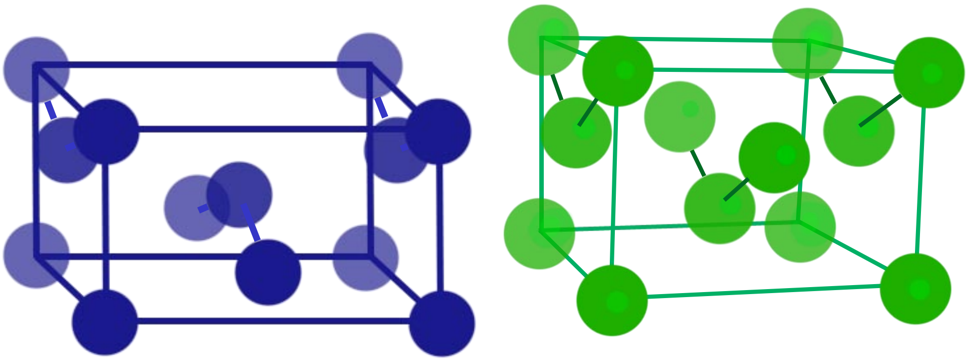

Figure 4.3. Left: The βSn (or CsIV) crystal structure, belonging to the space group I4$_1$/amd. This structure can be obtained from a Body Centered Tetragonal lattice by attaching to each lattice site the basis: $v_1 = (0,0,0)$, $v_2 = (0,-a/4,-c/8c)$, where a is the side of the horizontal cubic face and c the vertical side of the cell. Right: The βNp crystal structure, belonging to the space group P4/nmm. This structure has a cubic primitive cell of sides, defined by the vectors $p_1 = (a,0,0)$, $p_2 = (0,a,0)$ and $p_3 = (0,0,c)$, with the 4 atoms basis: $v_1 = (3a/4,a/4,0)$, $v_2 = (a/4,3a/4,0)$, $v_3 = (a/4,a/4,\alpha c)$, $v_4 = (3a/4,3a/4,\alpha c)$. The geometry of this structure depends on the ratio c/a and on the basis parameter α.

Figure 4.4. The SmI crystal structure, belonging to the space group R$\bar{3}$m. The primitive cell vectors are $p_1 = (1/2,-2\sqrt{3},\sqrt{6})a$, $p_2 = (0,\sqrt{3},\sqrt{6})a$, $p_3 = (-1/2,-2\sqrt{3},\sqrt{6})a$. To each lattice site corresponds three basis vectors: $v_1 = (0,0,0)a$, $v_2 = (0,0,3\sqrt{6})a$, $v_3 = (0,0,3\sqrt{6})a$.

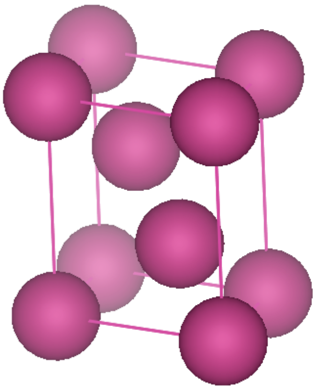

4.2.1 Simulation details

To determine the ground state energies and enthalpies of the various solids we performed RQMC electronic simulations with static protons fixed at the lattice positions, at different densities in the range corresponding to $r_s \in [1.19, 1.31]$. We used electronic trial wave functions of the Slater-Jastrow form, described in Section 2.5.1, using backflow transformations to improve the nodal surface. At each density the wave functions were preliminarily optimized following the procedure described in Section 2.6.4. For any given structure, at least 500 simulation RQMC blocks of 1000 electronic steps were carried out to compute the averages of energy and pressure with sufficiently small error bars.

In each RQMC calculation we adopted a total projection time $\beta = 2.00 Ha^{-1}$ and a timestep $\tau = 0.02 Ha^{-1}$, corresponding to the use of $N_s = 100$ slices per electron. According to a preliminary convergence study, these values of β and τ ensures the convergence of the energies within the error bars. Pressures, instead, must be corrected for the finite τ.

The number of protons (and, consequently, of electrons) was chosen to match the one required to form perfect, vacancy-free lattices, and as a consequence varies in the different structures, as summarized in the table below

ST	BCT	FCC	DIAM	FL	A15	HCP	CsIV	βNp	SH	SmI
64	54	108	64	96	64	64	108	108	64	64

To limit the finite size effects we followed the approaches described in 2.6.3. In our calculations we adopted Twist Averaged Boundary Conditions, employing a fixed grid of 64 twist angles; in addition finite size corrections were applied to pressures and energies.

4.2.2 Static geometry optimization

For most of the non-cubic structures among the lattices under analysis we performed a preliminary geometry optimization. In BCT, ST and CsIV solids the cell geometry depends in fact on a single dimensionless parameter h, equal to the ratio between the height of the cell and the length of the square basis side. To determine the best value of the parameter h, corresponding to the geometry of minimum energy/enthalpy, a number of fixed proton simulations at different values of h were hence carried out. Then, the energy E and the enthalpy H are plotted against h to localize the minimum. The same procedure was applied also to the SH structure, in which the parameter h represents the ratio between the distance of two adjacent hexagon planes and the side length of an hexagon.

The behavior of the energy/enthalpy curves around their minimum is different for the various structures.

In the SH solid (Figure 4.5) the curves have a fairly parabolic shape around the minimum and it is then possible to fit them with a second order polynomial and extract from the fits the position of the minima.

In the other structures energies and enthalpies behave more irregularly as the cell parameter h varies. In BCT and CsIV solids the energy and enthalpy curves

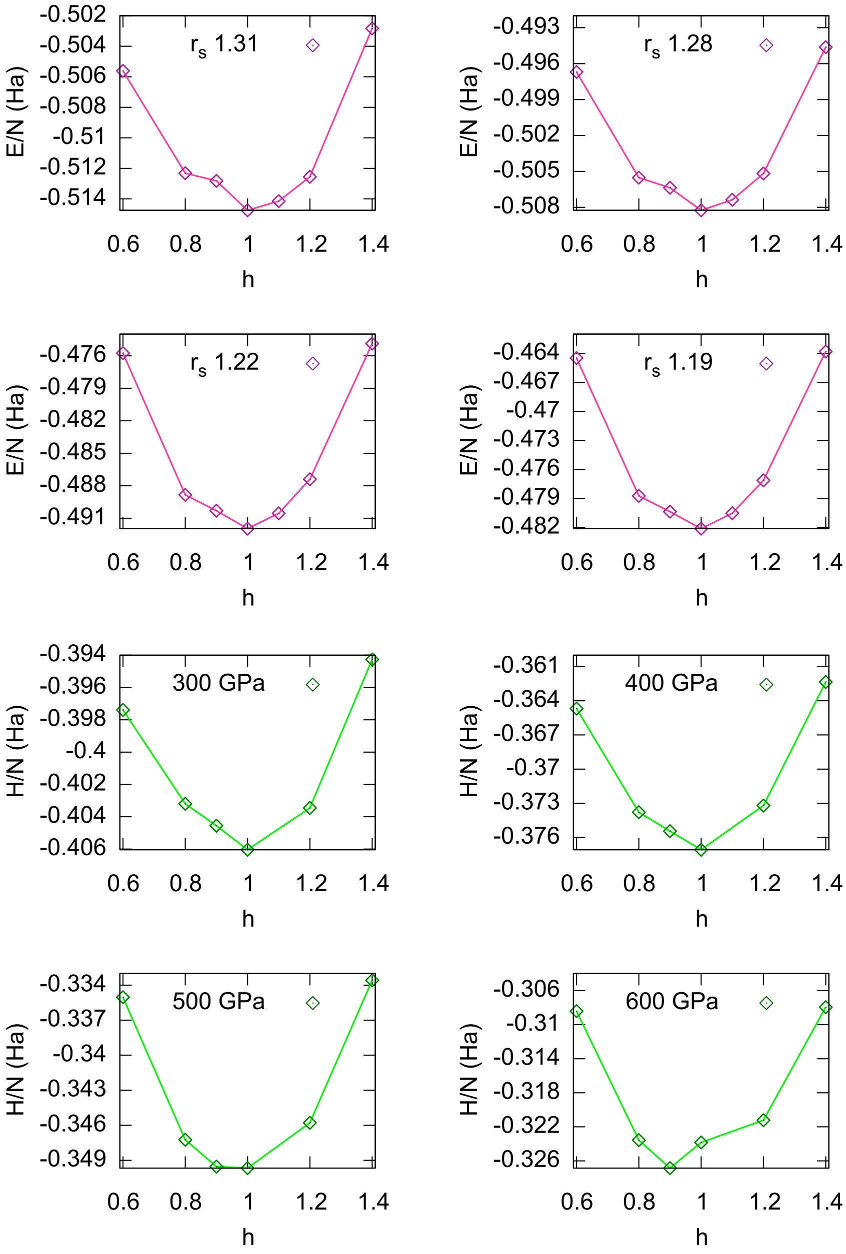

Figure 4.5. Curves for the structural optimization of the Simple Hexagonal structure. Upper panels: Energy per particle (magenta curves) as a function of the dimensionless parameter h at different values of the density. Lower panels: Enthalpy per particle (green curves) as a function of h at different pressures.

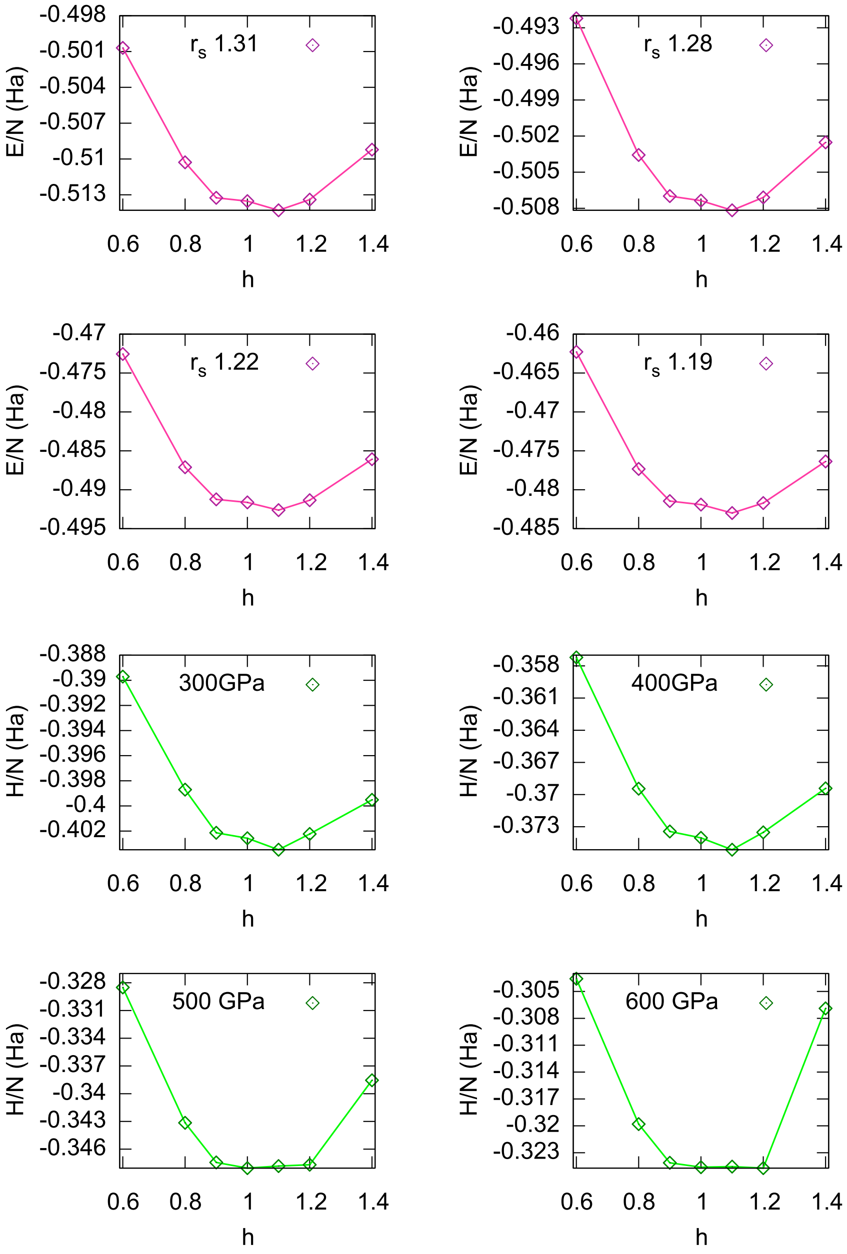

Figure 4.6. Curves for the structural optimization of the Body Centered Tetragonal structure. Upper panels: Energy per particle (magenta curves) as a function of the dimensionless parameter h at different values of the density. Lower panels: Enthalpy per particle (green curves) as a function of h at different pressures.

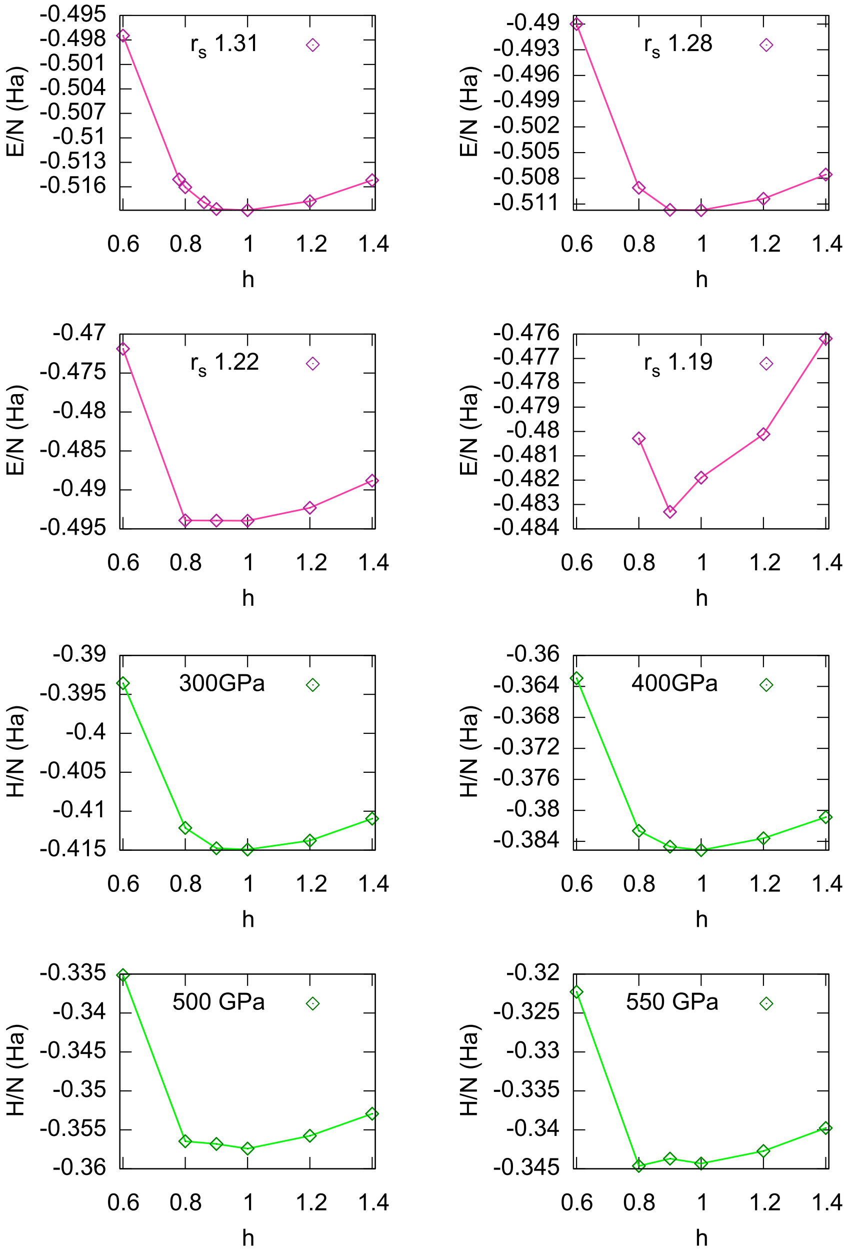

Figure 4.7. Curves for the structural optimization of the CsIV structure. Upper panels: Energy per particle (magenta curves) as a function of the dimensionless parameter h at different values of the density. Lower panels: Enthalpy per particle (green curves) as a function of h at different pressures.

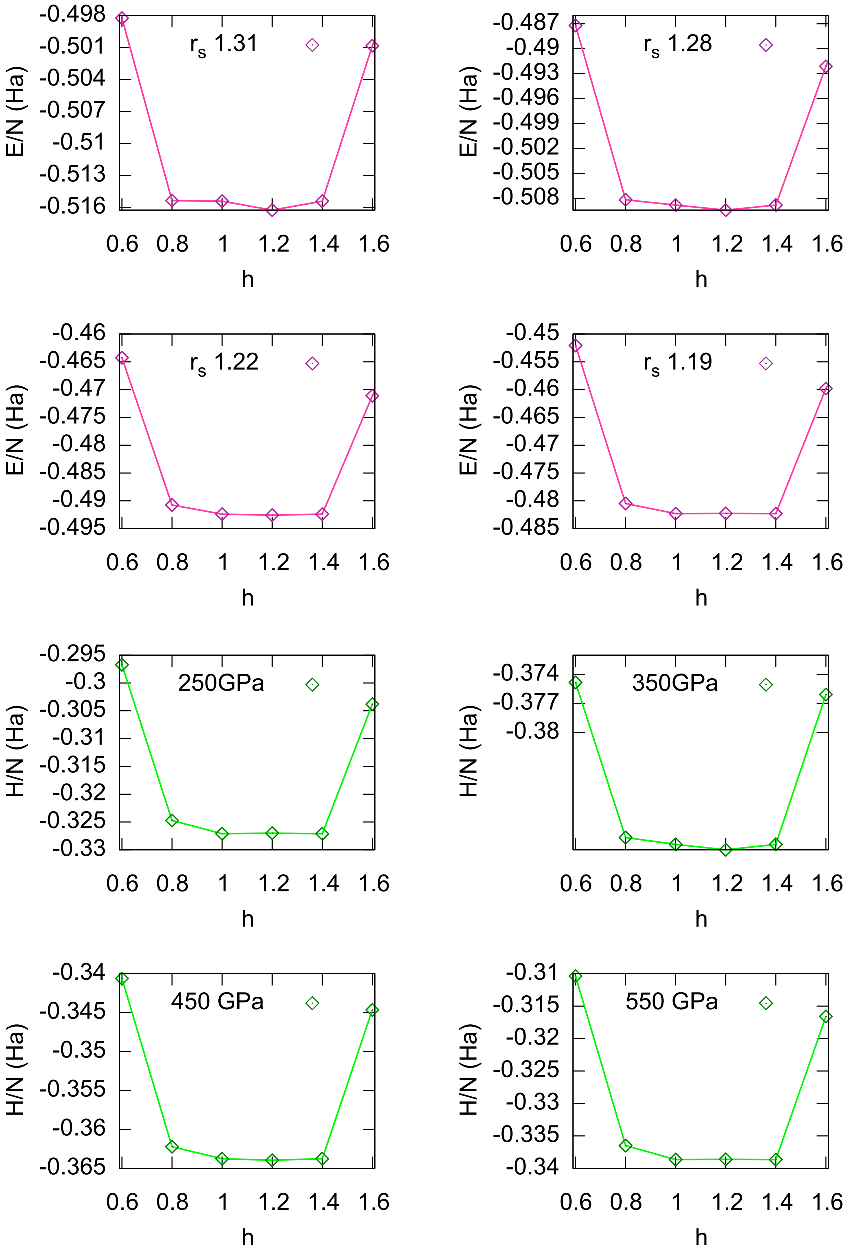

Figure 4.8. Curves for the structural optimization of the Simple Tetragonal structure. Upper panels: Energy per particle (magenta curves) as a function of the dimensionless parameter h at different values of the density. Lower panels: Enthalpy per particle (green curves) as a function of h at different pressures.

look quite similar, being the curves not symmetric with respect to the position of their minimum (h_{best}), as can be seen in Figures 4.6 and 4.7.

Finally, in the ST lattices (Fig. 4.8), the energy and enthalpy remain quite constant over a wide region of h values ($h \in [0.8, 1.4]$); in this interval two small and quite equivalent minima can be distinguished in the enthalpy curve, while outside this interval energy and enthalpy increases rapidly also for a small change of h. A similar behavior was already noticed by Natoli [125], that performed LDA ground state calculations for the same lattice structures and static protons.

Our optimization results for the single parameter structures are summarized in Table 4.1. Because of the curves irregularities discussed above, the values presented are estimates of the best h values for each lattice, with only two significant digits. To improve these estimates, the calculation of energies and enthalpies on a finer h grid would be required. However this improvement is not necessary for our purposes for every structure. Indeed, we are not interested in the geometry optimization of any structure, but in recognizing, among our set of structures, those having the lower energy/enthalpy. Since these quantities do not change significantly around the values of h_{best} showed in Table 4.1 a more accurate optimization of every lattice is superfluous.

Table 4.1. Best values of the cell parameter h for the non-cubic solids considered (CsIV, BCT, SH, ST): $h_{\text{best}(H)}$ correspond to the minimum enthalpy, $h_{\text{best}(E)}$ to the minimum energy.

	$h_{\text{best}(E)}$					$h_{\text{best}(H)}$			
r_s	CsIV	BCT	SH	ST	P(GPa)	CsIV	BCT	SH	ST
1.31	0.95	1.1	1.0	1.4	600	0.80	1.0	1.0	1.4
1.28	0.95	1.1	1.0	1.2	550	0.80	1.0	1.0	1.2
1.25	0.95	1.1	1.0	1.2	500	1.0	1.1	1.0	1.2
1.22	0.90	1.1	1.0	1.2	400	0.95	1.1	1.0	1.2
1.19	0.90	1.1	1.0	1.2	300	0.90	1.1	1.0	1.2

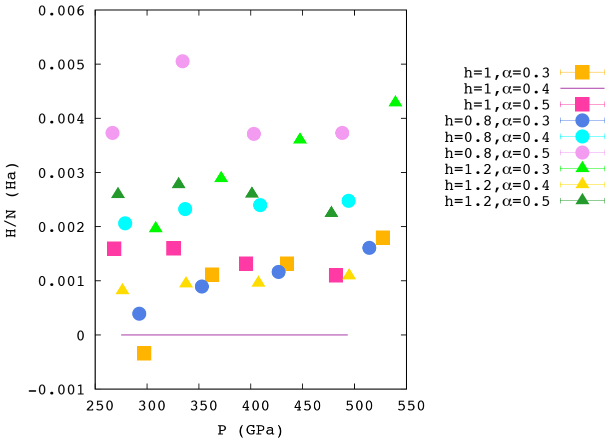

Figure 4.9. Enthalpy of the βNp structure as a function of the pressure for different values of the parameters $h = c/a$ and α. Values are relative to the geometry with $h = 1$ and $\alpha = 0.4$.

The last structure in our set that must be optimized is the βNp. In this case the cell geometry depends on two parameters: the cell parameter h which represents, as in the other tetragonal structures, the ratio among the vertical and the horizontal cell sides, and an internal coordinate α that defines the lattice basis, as described in the caption of Figure 4.3. With two parameters to take into account the static geometry optimization is a bit more demanding, since we need to determine the minimum of a 2-dimensional surface and a fine 2-dimensional grid may be required to obtain accurate estimates of the best parameter values. To begin we considered a coarse grid of h and α values, and we found that the pair of parameters giving the minimum energy and enthalpy corresponds to $h = 1$ and $\alpha \sim 0.4$, at least in the range of pressures $P \in [300, 550] GPa$, as showed in Figure 4.9.

4.2.3 Static calculations results

Figures 4.10 and 4.11 show, respectively, the behavior of the energy as a function of the density and of the enthalpy as a function of the pressure for the crystalline lattices examined. In the case of non-cubic structures the values showed are relative to the otpimal geometry, determined as described above. Numerical values are in Tables 4.3 and 4.4.

The solids with lower energy are the HCP and the CsIV, followed by the diamond structure. If we look instead at the enthalpy curves as a function of the pressure, we notice that the ordering of the three lattices changes: the CsIV curve becomes the lower among the three, followed by the diamond curve at low pressure and HCP at high.

We want now investigate the stability of the solid phase in temperature.

4.3 Finite temperature analysis and free energy calculations.

As discussed in the previous chapter, working at constant volume the coexistence points among different phases can be determined by building the Helmoltz free energy curves of the competing phases, let us say s and l, as a function of the specific volume v and applying the Maxwell construction [116].

In this section we present our finite temperature results. For the moment, we limited our investigation to the density $\rho = 1.197 g/cm^3$, corresponding to $r_s = 1.31$.

4.3.1 Liquid phase free energy

The free energy curve in temperature for the liquid phase was built in three steps: first, at a given temperature T_0, that we set to be $T_0 = 2000K$, we determined through λ integration the liquid free energy with respect to a suitable reference system. Then the free energy of the reference system in the same thermodynamic point was computed through density integration[1], to obtain the absolute free energy of liquid hydrogen. Finally the free energy curve for our *ab initio* model of hydrogen in temperature is determined through thermodynamic integration.

The reference system used to compute the first point on the free energy curve is

---

[1] We cannot use the density integration to determine directly the free energy of the liquid since at low density the fluid monoatomic hydrogen will transform into a molecular fluid and the thermodynamic integration is no longer applicable if a phase coexistence region is encountered.

Table 4.2. Madelung energies of different perfect lattices ($T = 0k$), for $r_s \in [1.31, 1.19]$

	r_s 1.19	r_s 1.22	r_s 1.25	r_s 1.28	r_s 1.31
ST	-0.470298(1)	-0.480126(1)	-0.488535(1)	-0.495815(1)	-0.502194(1)
BCT	-0.465655(1)	-0.477944(1)	-0.485918(1)	-0.492849(1)	-0.498609(1)
FCC	-0.471825(1)	-0.481549(1)	-0.491417(1)	-0.497990(1)	-0.504637(1)
DIAM	-0.473239(1)	-0.483147(1)	-0.493056(1)	-0.501210(1)	-0.508471(1)
FL	-0.467481(1)	-0.480450(1)	-0.489214(1)	-0.496827(1)	-0.503456(1)
A_{15}	-0.466540(1)	-0.478429(1)	-0.486603(1)	-0.493589(1)	-0.499715(1)
SmI	-0.465135(1)	-0.477103(1)	-0.485297(1)	-0.492449(1)	-0.498585(1)
CsIV	-0.474784(1)	-0.486260(1)	-0.495325(1)	-0.503545(1)	-0.511007(1)
SH	-0.467565(1)	-0.479594(1)	-0.488027(1)	-0.495461(1)	-0.501632(1)
HCP	-0.477535(1)	-0.487538(1)	-0.497070(1)	-0.504460(1)	-0.511993(1)

Table 4.3. Pressures of different perfect lattices ($T = 0k$), for $r_s \in [1.31, 1.19]$

	r_s 1.19	r_s 1.22	r_s 1.25	r_s 1.28	r_s 1.31
ST	574.849(1)	500.751(1)	414.153(1)	341.384(1)	281.737(1)
BCT	575.248(1)	472.025(1)	388.284(1)	318.429(1)	260.967(1)
FCC	573.15(1)	481.989(1)	390.893(1)	326.743(1)	263.737(1)
DIAM	636.501(1)	548.177(1)	459.864(1)	382.476(1)	318.4(1)
FL	616.224(1)	510.117(1)	421.48(1)	351.456(1)	289.156(1)
A_{15}	589.455(1)	486.089(1)	400.627(1)	329.733(1)	271.044(1)
SmI	583.91(1)	482.27(1)	395.646(1)	325.712(1)	267.822(1)
CsIV	639.016(1)	526.845(1)	443.792(1)	368.429(1)	305.25(1)
SH	596.508(1)	491.739(1)	406.621(1)	335.016(1)	274.887(1)
HCP	564.059(1)	466.283(1)	385.614(1)	316.461(1)	260.289(1)

Table 4.4. Enthalpies of different perfect lattices ($T = 0k$), for $r_s \in [1.31, 1.19]$

	r_s 1.19	r_s 1.22	r_s 1.25	r_s 1.28	r_s 1.31
ST	-0.33228(1)	-0.35057(1)	-0.37329(1)	-0.39381(1)	-0.41195(1)
BCT	-0.32754(1)	-0.35582(1)	-0.37787(1)	-0.39770(1)	-0.41502(1)
FCC	-0.33422(1)	-0.35685(1)	-0.38264(1)	-0.40036(1)	-0.42016(1)
DIAM	-0.32042(1)	-0.34133(1)	-0.36509(1)	-0.38693(1)	-0.40649(1)
FL	-0.31953(1)	-0.34848(1)	-0.37193(1)	-0.39181(1)	-0.41084(1)
A_{15}	-0.32502(1)	-0.35267(1)	-0.37512(1)	-0.39507(1)	-0.41290(1)
SmI	-0.32494(1)	-0.35233(1)	-0.37520(1)	-0.39513(1)	-0.41280(1)
CsIV	-0.32136(1)	-0.34996(1)	-0.37183(1)	-0.39346(1)	-0.41324(1)
SH	-0.32435(1)	-0.35237(1)	-0.37488(1)	-0.39536(1)	-0.41359(1)
HCP	-0.34211(1)	-0.36690(1)	-0.38976(1)	-0.40990(1)	-0.42862(1)

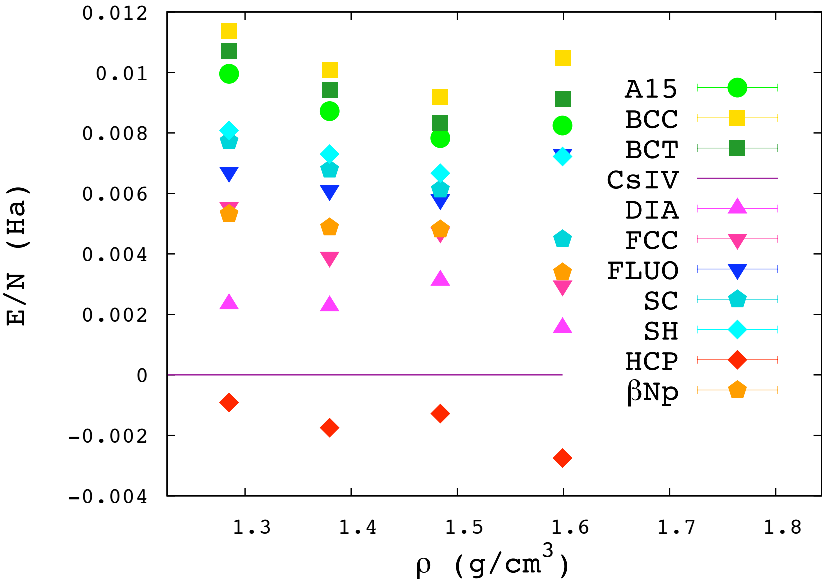

Figure 4.10. Energies per particle of the (optimized) structures as a function of ρ. Values are relative to the CsIV phase.

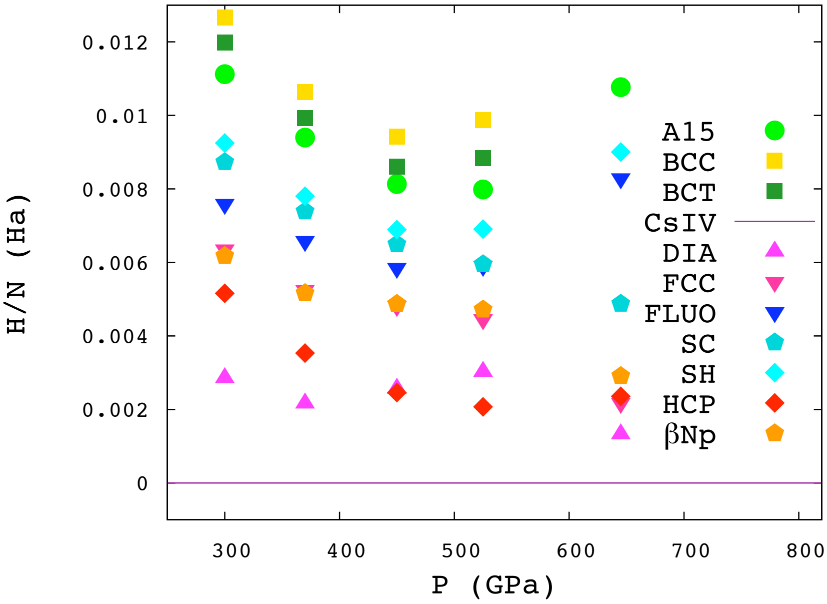

Figure 4.11. Enthalpies per particle of the (optimized) structures as a function of the pressure. Values are relative to the CsIV phase.

a classical one-component system in which particles interactions are described by a pair potential $v(r)$. We obtained this potential by inverting the proton-proton radial distribution function of the *ab initio* system, $g_{pp}(r)$, to obtain a pair potential capable to reproduce the proton-proton correlations in the CEIMC system at the reference thermodynamic point. In this way we expect the difference $\langle \mathcal{V}_{\text{ref}} - \mathcal{V}_0 \rangle_\lambda$ to be a smooth function of λ over the entire integration interval $\lambda \in [0, 1]$. This allows to evaluate the integral in λ using a small number of integration points.

The inversion procedure we applied to obtain the effective pair potential $v(r)$ is based on the Hypernetted-chain equation (HNC) [101], holding for a system in the liquid phase

$$g(r) = e^{-\beta v(r) + g(r) - c(r) - 1}, \ \forall r \text{ such that } g(r) > 0 \tag{4.1}$$

in which $c(r)$ is the direct correlation function, representing the part of correlation arising from the direct interactions between pair of particles; the $c(r)$ is related to the $g(r)$ by the Ornstein-Zernicke (OZ) equation [101]

$$g(\mathbf{r}) - 1 = c(\mathbf{r}) + \rho \int d\mathbf{r}' c(\mathbf{r} - \mathbf{r}')(g(\mathbf{r}) - 1) \tag{4.2}$$

In homogeneous systems the OZ equation can be solved for $c(r)$, once the $g(r)$ of the system is known, using the Fourier space representation.

The obtained effective potential is shown in Figure 4.12: since no information on the potential can be extracted from regions where the $g_{pp}(r)$ is zero, we extrapolated the potential at the origin with a gaussian. We cut the potential at $r_c = 3.99 a_0$, corresponding to half the length of the simulation box side at $r_s = 1.31$ and for a system of 54 protons.

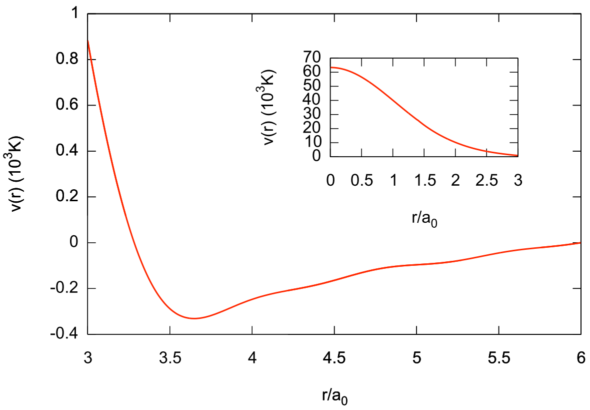

Figure 4.12. Pair potential of the reference system used in the λ integration. The potential has been derived by inverting the proton-proton radial distribution function $g_{pp}(r)$ of hydrogen at the same density and temperature, using the HNC equation 4.1. The behavior at the origin, where $g_{pp}(r) = 0$, has been extrapolated with a gaussian.

Since the free energy of this reference system is not computable analytically, it is necessary to determine it from simulations. To obtain the free energy of the classical reference system we applied the thermodynamic integration in density

$$\frac{\mathcal{F}(\rho, T)}{N} = \frac{\mathcal{F}(\rho_0, T)}{N} + \int_{\rho_0}^{\rho} \frac{P}{\bar{\rho}^2} d\bar{\rho} \tag{4.3}$$

We choose the lowest density in the integration range, ρ_0, to be such that at this density the pressure of the reference system is well described by the virial expansion truncated at the second order in ρ

$$P(\rho,T) = \frac{\rho}{\beta} + B_2\frac{\rho^2}{\beta} + \mathcal{O}(\rho^3) \tag{4.4}$$

were B_2 is the second virial coefficient, that can be determined by fitting the pressure at low density.

Indeed, using the relationship (4.4) between the pressure and the density, the free energy of the classical system at ρ_0 can be computed analytically with respect to the noninteracting particle limit

$$\begin{aligned}\frac{\mathcal{F}(\rho_0,T)}{N} &= \frac{\mathcal{F}^{ex}(\rho_0,T)}{N} + \frac{\mathcal{F}^{id}(\rho_0,T)}{N} = \frac{\mathcal{F}^{id}(\rho=0,T)}{N} + \int_0^{\rho_0}\frac{d\bar{\rho}}{\bar{\rho}}\left[1+\frac{B_2}{\beta}\bar{\rho}\right] \\ &= \frac{\mathcal{F}^{id}(\rho_0,T)}{N} + B_2\rho_0 \end{aligned} \tag{4.5}$$

where we have separated the ideal and the excess free energy contributions in order to arrive at the final result.

Moreover, in a system of pair potential $v(r)$ and in the fluid phase, the value of B_2 at a given density ρ and temperature T can be evaluated independently as [101]

$$\begin{aligned} B_2 &= -\frac{2}{3}\pi\beta\int_0^\infty r^3\frac{\partial v(r)}{\partial r}g(r)dr \approx \frac{2}{3}\pi\int_0^\infty r^3\frac{\partial}{\partial r}\left[e^{-\beta v(r)}-1\right]dr \\ &= -2\pi\rho\int_0^\infty r^2\left[e^{-\beta v(r)}-1\right]dr \end{aligned} \tag{4.6}$$

where to simplify the integral we have used the low density approximation of the $g(r)$, $g(r) \approx e^{-\beta v(r)}$, and performed the integral by parts. Estimated B_2 from formula (4.6), we can compare the pressure obtained from the Monte Carlo simulations with its truncated virial expansion estimate and check if a sufficiently low density is reached.

The final expression of the excess free energy of the classical reference system is hence

$$\frac{\mathcal{F}^{ex}(\rho,T)}{N} = \frac{B_2\rho_0}{\beta} + \int_{\rho_0}^{\rho}\frac{d\bar{\rho}}{\bar{\rho}}\frac{P^{ex}(\bar{\rho},T)}{\bar{\rho}} \tag{4.7}$$

where P^{ex} is the excess contribution to the pressure.

The integral that appears in (4.7) must be performed numerically. We then carried on 13 classical MC simulations at different densities in the range $\rho \in [0.0012, 1.1968] g/cm^3$ and at $T = 2000K$, on a system of $N = 250$ particles. Quantities are obtained by averaging over 20000 Monte Carlo steps, after a sufficiently high number of equilibration steps. Figure 4.13 shows the behavior of the reduced excess pressure $\beta P^{ex}/\rho$ as a function of the density. Numerical values can be found in Table 4.5. At the lowest pressure, the data are well fitted by the linear behavior predicted from (4.4). From the numerical evaluation of the integral in density we obtain the excess free energy of the classical system is $\mathcal{F}^{ex}_{\text{ref}} = 0.10023 \pm 0.00008$ Ha.

Finally, we estimated the magnitude of finite size effects on the free energy of the reference point. We repeated the free energy calculation for a smaller system of 54 particles and for a larger system of 500 particles. The size effects on pressure and energy are negligible, in both cases around the 0.1% and comparable with the

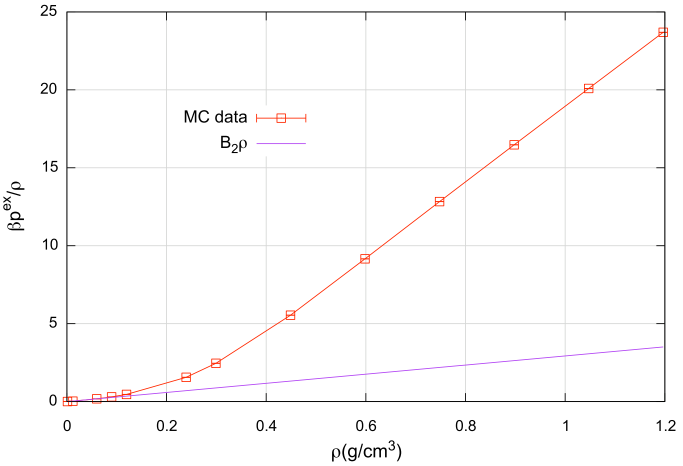

Figure 4.13. Reduced excess pressure $\beta P^{ex}/\rho$ as a function of the density (red squares), for the classical reference system. The purple line shows the linear behavior at small densities, given by the second order virial expansion $\beta P^{ex}/\rho \approx B_2\rho$.

$\rho(g/cm^3)$	$\beta_0 P^{ex}/\rho$
0.001195	0.0035(8)
0.011968	0.0283(7)
0.059842	0.1773(8)
0.089752	0.302(1)
0.119673	0.460(2)
0.239358	1.557(4)
0.299189	2.456(3)
0.448783	5.542(2)
0.598389	9.158(2)
0.747983	12.830(2)
0.897578	16.474(2)
1.047172	20.086(3)
1.196767	23.689(2)
$\mathcal{F}_0^{ex}/N$ (Ha)	0.1002(1)

Table 4.5. Reduced excess pressure values for different densities and at T=2000K, for the classical system used as reference in the λ integration (liquid phase). In the last line, the value $\mathcal{F}_0^{ex}$ of the excess free energy per particle of the reference system.

statistical error bars. This reflects in a systematic finite size error on the free energy which is itself within the error bars.

We then completed the calculation of the first point on the isochore free energy of the CEIMC system by coupling constant integration. To evaluate the λ integral we carried on 5 CEIMC simulations with the mixed potential $\mathcal{V}_\lambda = \lambda\mathcal{V}_{\text{ref}} + (1-\lambda)\mathcal{E}_{BO}$, at $\lambda = 0.0, 0.25, 0.5, 0.75, 1.0$. We considered systems of 54 classical protons and 54 electrons. We used optimized Slater-Jastrow wave functions with backflows transformations to describe the electronic state and the RQMC to compute the Born-Oppenheimer energy. We adopted a time step $\tau = 0.02Ha^{-1}$ and $\beta = 1.00Ha^{-1}$, corresponding to consider 50 electronic slices. With these values energies are converged within the error bars while pressures must be corrected for finite τ and β. A grid of 64 fixed twist angles is used to reduce the finite size errors; moreover finite size corrections to the values of energy and pressure are added. Protons are considered as classical particles and put on a disordered initial configuration, chosen among the equilibrium configuration of the reference system at the same temperature

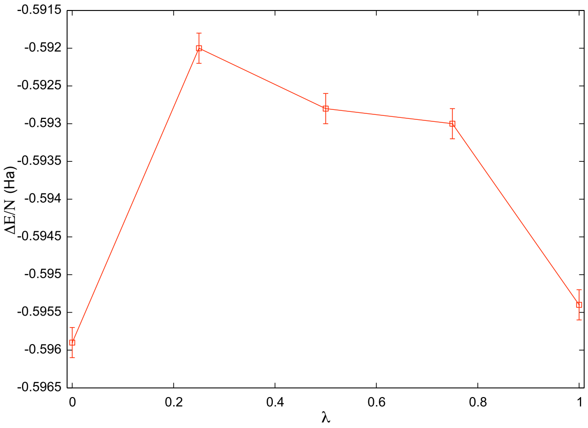

Figure 4.14. Energy differences for the λ integration method, in the liquid phase at $T = 2000K$ and $r_s = 1.31$

and density. The final values of the quantities of interest are obtained averaging over 25000 protonic steps, after an initial equilibration of other 8000 protonic steps.

Table 4.6 and Figure 4.14 present the final values of $\langle \mathcal{V}_{\text{ref}} - \mathcal{E}_{BO} \rangle_\lambda$ obtained in the simulations with the mixed hamiltonian at the various λ.

Table 4.6. Energy differences $\Delta E = \langle \mathcal{V}_{\text{ref}} - \mathcal{E}_{BO} \rangle_\lambda$ for the λ integration in the liquid phase. $T = 2000K$, $r_s = 1.31$. In the last two lines the result of the integral $\Delta\mathcal{F}/N$ and the obtained free energy (excess + ideal part).

λ	$\Delta E/N$(Ha)
0.00	-0.5959(2)
0.25	-0.5920(2)
0.50	-0.5928(2)
0.75	-0.5930(2)
1.00	-0.5954(2)
$\Delta\mathcal{F}/N$ (Ha)	-0.5934(2)
$\mathcal{F}/N$ (Ha)	-0.5186(3)

Table 4.7. Energies and Helmoltz free energies (excess + ideal) per particle as a function of the temperature, for the liquid phase at $r_s = 1.31$.

T(K)	E/N (Ha)	$\mathcal{F}/N$(Ha)
350	-0.5021(1)	-0.5030(3)
500	-0.5011(1)	-0.5035(3)
750	-0.4997(1)	-0.5050(3)
1000	-0.4981(1)	-0.5070(3)
1250	-0.4965(1)	-0.5094(3)
1500	-0.4949(1)	-0.5121(3)
1750	-0.4934(1)	-0.5151(3)
2000	-0.4916(1)	-0.5186(3)

The free energy curve in temperature can be built, starting from the reference point at $T_0 = 2000K$ by thermodynamic integration in T. We performed a total of 7 CEIMC simulations at different temperatures in the range $T \in [350, 2000]K$, starting from a disordered protonic configuration. The characteristics of the electronic runs are the same of the mixed Hamiltonian simulations (optimized Slater-Jastrow wave function plus backflows, RQMC, $\tau = 0.02Ha^{-1}$ and $\beta = 1.00Ha^{-1}$, 64 twist angles on a fixed grid). The final energies, obtained by averaging over 25000 protonic steps, after 8000 equilibrating steps, were corrected for residual finite size error as described in Section 2.6.3. The energies were then fitted with a second order polynomial, to perform analytically the integral in temperature and obtain an analytic form for $\mathcal{F}(T)$. The resulting free energy curve is showed in Figure 4.19. The energy curve in temperature is shown in Figure 4.15, and the numerical data are presented in Table 4.7.

4.3.2 Solid phase free energy

From the comparison of the zero temperature enthalpies of various lattices, described in Section 4.2, we concluded that at $T = 0K$ and for pressures $P \in [\sim 300, 650]GPa$ the most stable structures among those considered are the CsIV and the Diamond lattices. Still, temperature effects and zero point effects can be important and change the energy ordering of the structures, then we extended our finite temperature calculations also to the BCC and the FCC solids, which are good candidate structures of hydrogen at very high pressure.

To determine the free energy of a given solid at fixed density and as a function of the temperature, we first computed the free energy at a reference temperature T_0 by applying the Frenkel-Ladd technique, then we completed the curve using thermodynamic integration in temperature.

Diamond structure

To investigate the stability at finite temperature of the diamond structure we considered systems of 64 classical protons and 64 electrons. The electronic wave function we used is a Slater-Jastrow function, with backflow transformations, optimized as described in Section 2.6.4. To compute the electronic energies, we adopted the RQMC scheme, employing a time step $\tau = 0.02Ha^{-1}$ and a total projection time $\beta = 0.80Ha^{-1}$, corresponding to a number of electronic slices $N_s = 40$, values that ensures the convergence of the energies within the error bars. We adopted the Twist Averaged Boundary conditions (see Section 2.6.3 or Ref. [96]), using a fixed grid of 64 twist angles, to reduce finite size errors, and we added to energies and pressures the finite size corrections [97] derived in Section 2.6.3.

We choose a reference temperature of $T_0 = 500K$ to compute the first point of the free energy curve. The radial distribution function and the static structure factor of the system at this temperature are shown in Figures 4.16 and 4.17.

To apply the Frenkel-Ladd method (see Section 3.3.3) we first need to determine the optimal value of the harmonic spring α that couples the Einstein oscillators with the lattice points. We then performed a preliminary simulation, in order to determine the mean square displacement of the protons from which compute α

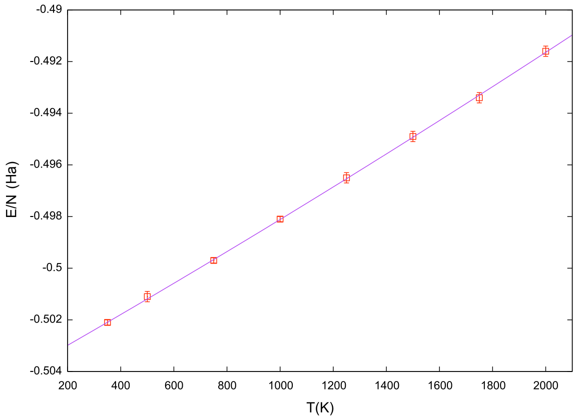

Figure 4.15. Energies per particle as a function of the temperature for the CEIMC liquid phase at $r_s = 1.31$. Data (red squares) can be fitted with a second order polynomial $E(T)/N = a + bT + cT^2$, with $a \approx -0.50416$ (Ha), $b \approx 5.8\ 10^{-6}$ (Ha/K), $c \approx 2.1\ 10^{-10}$(Ha/K^2), represented by the purple curve.

as $\alpha = 3/(2\beta\langle|\Delta\mathbf{r}|^2\rangle)$, being $\langle|\Delta\mathbf{r}|^2\rangle$ the root mean square displacement from the lattice positions in the system with the original potential. We get $\alpha = 0.0792 Ha/a_0^2$. With this value of α we performed 5 different CEIMC runs with the mixed potential and at fixed center of mass to compute the free energy at the reference point. The difference $\langle E_{\mathrm{BO}} - E_{\mathrm{Ein}}\rangle_\lambda$ with the parameter λ is a smooth curve and can be easily fitted with a second order polynomial, as can be seen from Figure 4.18.

We found that the free energy at the reference point is various mHa higher than the one of the liquid phase at the same thermodynamic point, so we are observing a metastable state. Indeed, at higher temperature ($T = 750K$) the diamond structure becomes unstable and melts after a while. We added another point to the free energy curve by computing the internal energy of the diamond structure at $T = 350K$ and applying the thermodynamic integration. Also this point has a free energy quite higher than the one of the liquid phase. These data are summarized in Table 4.9.

By extrapolating at lower temperature the diamond free energy curve (see Figure 4.19), we found that it intersects the extrapolation of curve for the liquid phase at $T \approx 200K$: under the hypothesis of negligibl volume change at the coexistence, this temperature would represent the diamond-liquid coexistence point at $r_s = 1.31$. The hypothesis of a small volume differences at coexistence must be however checked

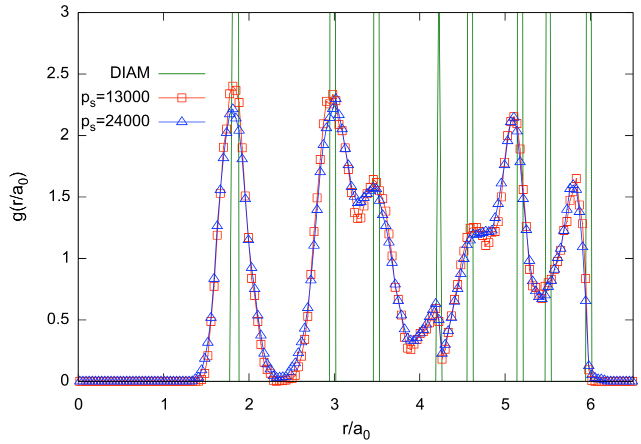

Figure 4.16. Radial distribution function $g(r)$ of the system initially forming a perfect diamond lattice, after 13000 (red squares) and 24000 (blue triangles), compared with the perfect diamond $g(r)$ (dark green). $T = 500K$ and $r_{s=1.31}$.

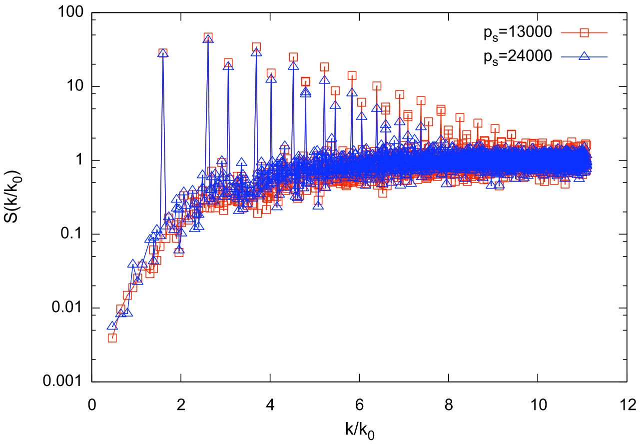

Figure 4.17. Static structure factor $S(k)$ of the system initially forming a perfect diamond lattice, after 13000 (red squares) and 24000 (blue triangles). $T = 500K$ and $r_{s=1.31}$.

by building the isothermal free energy curves of the two phases and applying the Maxwell construction to determine the coexistence point. However, it is reasonable to think that the difference of volume at coexistence will be small also for this system, as for the model system described in the previous chapter, and than that the liquid-diamond solid coexistence temperature is not too far from the present estimate.

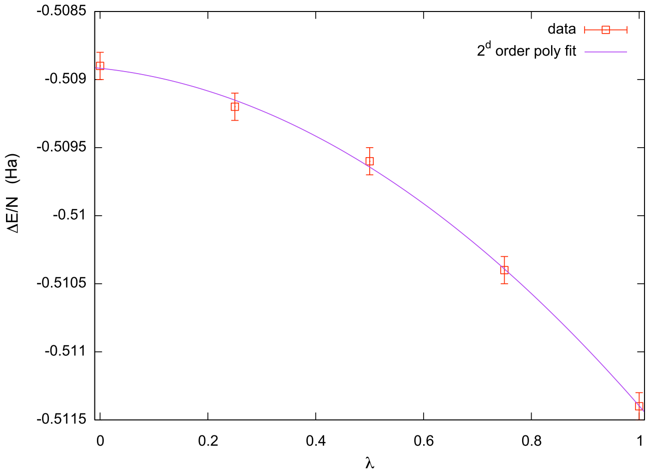

Figure 4.18. Energy differences for the Frenkel-Ladd integration for the diamond structure at $T = 500K$ and $r_s = 1.31$. Data (red squares) are well fitted with a 2^{nd} order polynomial (purple line).

Table 4.8. Energy differences $E = \langle \mathcal{E}_{BO} - \mathcal{V}_{Ein} \rangle_\lambda$ for the λ integration in the diamond phase. In the last line, the free energy of the solid with respect to the one of the Einstein crystal.

λ	$\Delta E/N$(Ha)
0.00	-0.5089(1)
0.25	-0.5092(1)
0.50	-0.5096(1)
0.75	-0.5104(1)
1.00	-0.5114(1)
$\Delta\mathcal{F}$(Ha)	-0.5098(1)

Table 4.9. Energies and Helmoltz free energies (excess + ideal part) per particle, at $r_s = 1.31$ and two temperatures, for the diamond phase.

$T(K)$	E/N(Ha)	$\mathcal{F}/N(Ha)$
350	-0.5051(2)	-0.4993(2)
500	-0.5042(1)	-0.4962(1)

FCC results

We considered also a system of 32 classical protons and 32 electrons initially placed on the sites of an FCC lattice. However it was not possible to compute the free energy of this structure since during a preliminary simulation at $T = 500K$ we observed spontaneous destruction of the FCC solid, as it is evident from the Figure 4.20. An analysis of the evolution during the simulation of the peaks of the static structure factor $S(k)$ reveals the tendency of the system to rearrange in another crystalline structure, as can be seen in Figure 4.21, showing the $S(k)$ at three different simulation times. After $p_{steps} \approx 2700$ proton steps the peak positions of the $S(k)$

Figure 4.19. Free energies at $r_s = 1.31$ and at different temperatures for the liquid phase (dark pink triangles) and the diamond solid (blue squares). The dotted magenta curve is an interpolation of the diamond points.

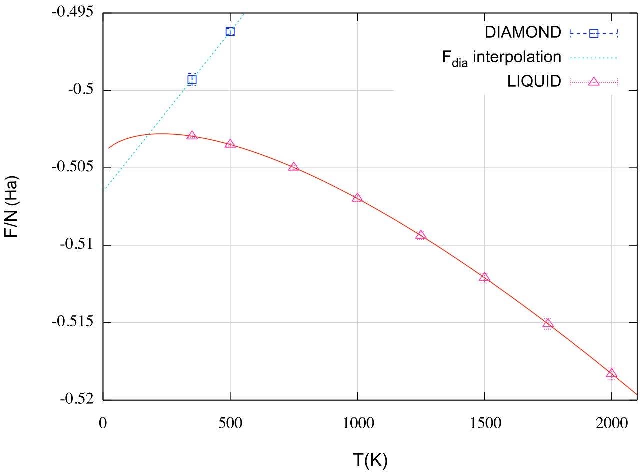

correspond to those of an FCC structure, as expected. However, at $p_{steps} \approx 14000$ those peaks disappear, substituted by another peak at lower k. This may indicate an attempt of the protons to form a different solid structure. After $p_{steps} \approx 27000$ the height of the primary peak is grown and probably a secondary one is appearing. Despite the informations from the $S(k)$ are not sufficient to recognize the new lattice, we can make some comments, having in mind the results of our preliminary study on the static lattices. Being the new peak position k_p lower than the first peak of the FCC structure, in the new solid the length of at least one cell side must be greater than the value for an FCC. At constant density this implies either that the number of particles per cell of the new solid is higher than the one (4) in the FCC, or that the new structure is not cubic. The first hypothesis is consistent with the crystallization in the diamond structure, which has 8 atoms per cell; the second is compatible with a crystallization structure like the CsIV. Obviously other possibilities cannot be discarded.

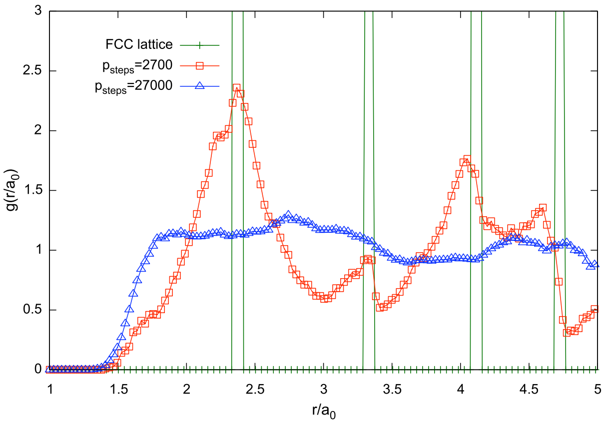

Figure 4.20. Radial distribution function $g(r)$ of the system initially forming a perfect FCC lattice, after 2700 (red squares) and 27000 (blue triangles), compared with the perfect FCC $g(r)$ (dark green). $T = 500K$ and $r_s = 1.31$.

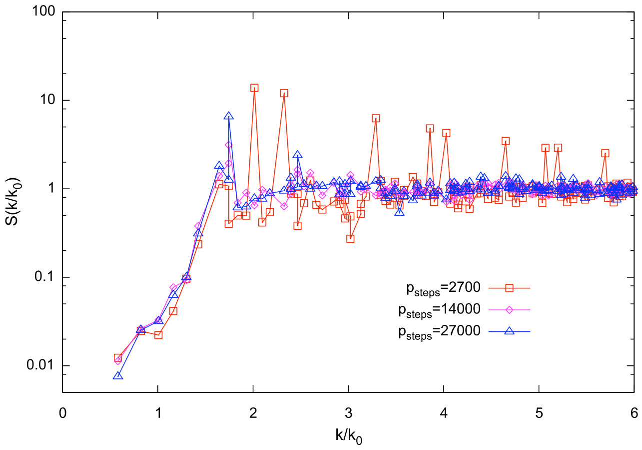

Figure 4.21. Static structure factor $S(k)$ of the CEIMC system of 32 protons initially placed on a FCC lattice, at three different simulation times (expressed in terms of the number p_{steps} of protonic steps from the beginning of the simulation). $T = 500K$, $r_s = 1.31$. The peak positions of the perfect FCC corresponds to the peak positions in the red curve.

BCC results

Finally we considered a BCC solid formed by 54 protons and electrons, still at $T = 500K$. Also this structure appears to be unstable: after a very long CEIMC simulation (35000 protonic steps) the system is not fully equilibrated and the root mean square displacement continues to increase. Moreover, as can be seen in Figure 4.22, the first two peaks in the $g(r)$ merged into a broad peak, as well as other peak as higher distances. We interpreted those qualitative results as the indication of the melting and decided to stop the simulations.

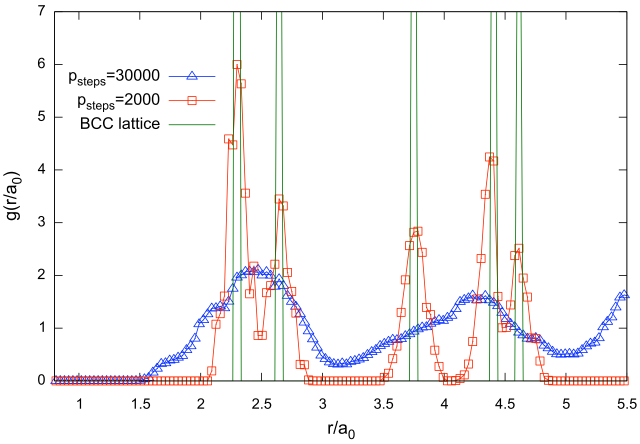

Figure 4.22. Radial distribution function $g(r)$ of the system initially forming a perfect BCC lattice, after 2700 (red squares) and 30000 (blue triangles), compared with the perfect BCC $g(r)$ (dark green). $T = 500K$ and $r_{s=1.31}$.

4.4 Conclusions and future work

The main source of difficulties we encountered in the determination of the melting transition in the atomic hydrogen by CEIMC simulations relies on the impossibility to know the hydrogen crystallization structure at a given pressure, due to the absence of experimental indications. In this situation it was necessary to choose *a priori* a limited set of structures to take into account in the calculations, on the base of previous simulation results found in literature [47, 48, 49].

We performed $T = 0K$ investigations on a set of 12 structures with different symmetry, but obviously our collection does not cover all the possibilities. E.g., we have not considered complex lattices, whose cell geometry depends on more than one parameter (except the βNp structure, that has 2 free parameters). Indeed, the static geometry optimization we described in Section 4.2.2 cannot be efficiently applied when we are dealing with many parameters: a grid in the parameter space has a number of points which scales exponentially with the number of parameters; moreover with the number of parameters the complexity of the energy/enthalpy surface may increase, with the appearance of several local minima. As a consequence, the determination of the set of parameters giving the minimum energy/enthalpy would become prohibitively expensive. Other approaches, as the Ab Initio Random Structure Search (AIRSS) of Pickard and Needs [29], are more suitable to a systematic exploration of the possible crystalline structures. Those schemes however, needing the knowledge of the forces on ions, use DFT electronic calculations: a geometry optimization of this kind that uses QMC would require indeed larger amounts of computer time.

Very recently the AIRSS technique was applied by McMahon and Ceperley [52] to the atomic hydrogen at pressures in the range $[500, 5000]GPa$, using DFT electronic energies. Zero point effects on protons were also included, at a self-consistent harmonic level. As can be seen in the the left panel of Figure 4.23, they found that without considering the protonic zero point motion the lowest enthalpy lattice up to $\sim 500GPa$ is a molecular structure belonging to the Cmca symmetry group, while above $500GPa$ and up to $\sim 2.5TPa$ the most stable lattice is the (atomic) CsIV (indicated in the article by the name of its symmetry group, $I4_1/amd$). Although two different structures of this symmetry were generated, one with a value of the ratio c/a less than unit ($h \sim 0.85$) and the other with $h \sim 2.59$, with similar enthalpies below $500GPa$, is the latter structure which gains stability at increasing pressure. Moreover, this is the lattice which remains with the lowest enthalpy after the addition of the protonic zero point energy. From our static calculations, with RQMC electronic energies and classical protons we have also found that the CsIV lattice is the atomic structure with the lowest enthalpy, in the range of pressures $p \in [300, 650]GPa$. We have also noticed the presence of a two minima in the energy/enthalpy versus h, one at $h \sim 0.9$ and the other at $h \sim 2.5$; however from our calculations it seems that the energetically favored structure among the two is the one with $h \sim 0.9$. Our future objective is to repeat the static calculations for quantum protons, going beyond the harmonic approximation, to check the effect of the anharmonicity of the protonic zero point motion.

We also performed finite temperature simulations, for classical protons, in order to compute the free energy of the solid and of the liquid phase and determine the

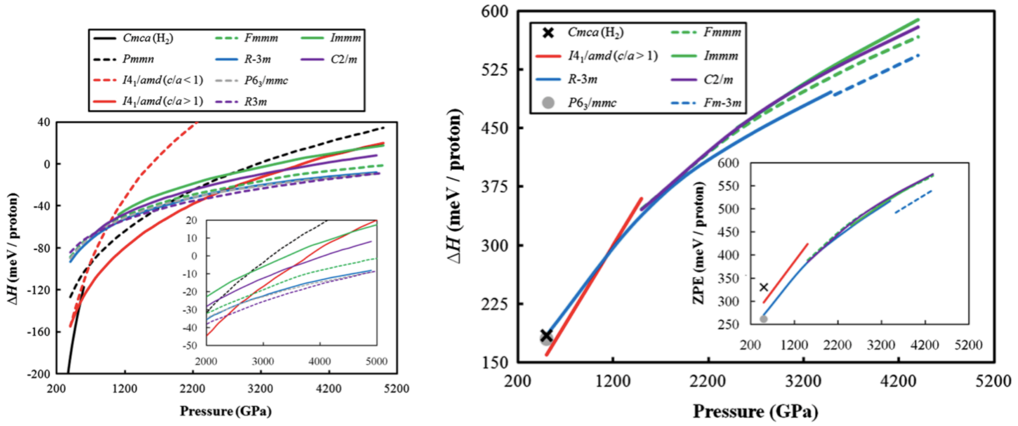

Figure 4.23. Ground state enthalpies, relative to the fcc structure, of several perfect hydrogen lattices, without (left panel) and with (right panel) including the protonic zero point energy (ZPE). Figures from [52].

melting transition. Assuming that the crystal structure at melting is the diamond structure and under the hypothesis of zero volume difference at transition, we obtained a first point on the melting in the atomic hydrogen, at $r_s = 1.31$ and at $T \sim 200K$.

To complete the melting curve, the free energy calculations must be extended to higher densities. The zero volume assumption must also be verified, by applying the Maxwell construction to the isothermal free energy curves. Moreover, in addition to the diamond lattice other structures (such as the CsIV) must be included in future calculations. Once determined the first point on the melting curve, the Gibbs-Duhem procedure [122] (in the original version or in the modified version for transitions with zero volume discontinuity, described in Section 3.4) can be also applied to complete the curve.

Chapter 5

Liquid-Liquid Transition at Megabar pressures

5.1 Introduction

The understanding of the hydrogen behavior at pressures of the order of $1Mbar = 100GPa$ and for temperatures of thousands K, is crucial for the description of astrophysical objects such as gaseous planets [126, 127, 128], brown dwarfs [1] or stars [2], as well as to the modeling of ignition targets used in inertial confinement fusion experiments [129]. Under these extreme conditions, hydrogen undergoes a transition from the molecular insulating phase to a dissociated and ionized, conducting state, and finally, at very high pressures, to a fully ionized plasma. The reconstruction of the hydrogen phase diagram in this very interesting region of the (P,T) plane and the investigation of the nature of the insulator to metallic transition are then object of intense studies, from both theoretical [18, 19, 37] and experimental [10, 11, 46, 130] point of wievs.

The metallic transition in the solid phase has not been observed up to the highest pressure that can be presently achieved by static compression experiments ($\approx 350GPa$) [7, 8]. In the liquid phase, however, the metallization occurs at lower pressures and has already been observed. The first evidence of a non-zero conductivity state has been found by W. J. Nellis et al. [130] in compressed hydrogen at a pressure of $140GPa$ and a temperature of about $2600K$ and by G. W. Collins at al. [10] in laser shocked deuterium at $P \approx 55GPa$ and $T \approx 8000K$. Despite the numerous experiments carried out in the fluid phase metallization region and the number of different approaches, many open issues still remains, concerning the nature of the transition. The main questions are if it is a continuos or first-order process, and if the metallization is a consequence of the dissociation or, at the opposite, if it is the change of the electronic state that leads to the breaking of the molecular bonds. Only recently, in the 2007, V. E. Fortov et al. experiments [11] noticed a sharp jump of 4 orders of magnitude in the electrical conductibility corresponding to a region of quite constant pressure, evidence of a first-order transition. However, it is not easy in experimental observations to obtain a continuous set of data around the transition, as would be necessary to answer the questions on the nature of the transition, mainly because in the dynamic compression techniques, employed to reach high pressures at high temperature, it is difficult to fine tuning both P and T. Numerical calculations are for that reason fundamental for a better understanding of the matter.

5.2 Previous ab-initio results on the liquid-liquid transition

Despite the large computational efforts spent to clarify the nature of the metallization transition, the situation remained for long time far from clear, because of the differences - both quantitative and qualitative - in the predictions obtained with different ab-initio techniques. The first ab-initio study on the metallization in the liquid phase, was carried out by S. Scandolo [18] with Car-Parrinello Molecular Dynamics (CPMD) in the NPT ensemble. In this work, a jump on the isotermal ($T = 1500K$) specific volume curve, at a pressure of about $125GPa$, was interpreted as the fingerprint of a first order transition; this transition was identified as passage from an insulating to a conducting fluid phase by analyzing the electronic density of states. The indication of a first order insulating-to-metallic transition was also obtained (at $P = 200GPa$ and $T \sim 950K$) by Bonev et al. [12], still with CPMD. On the contrary, the first Born-Oppenheimer Molecular Dynamics (BOMD) works on the fluid hydrogen metallization [42, 43] as well as an early Coupled Electron-Ion Monte Carlo work [44], finding a continuous transition instead of a first-order transition, seemed to disprove the CPMD results.

However it was later found that the BOMD results were biased by finite size effects and the CEIMC results by the use of trial wave functions not accurate enough. The recent work of Morales et al. [19] compares CEIMC and Born-Oppenheimer MD simulation results on the liquid metallization and finds a good agreement, at least qualitative, between the two methods. In both cases, analyzing the pressure behavior as a function of the density along different isotherms, a plateau which indicates a first order transition has been detected. Correspondently, a sharp increase of the static electrical conductivity has been noticed, sign of an insulator to metal transition. However, the two methods are comparable only qualitatively, as can be seen from Figure 5.1, in which the blue curves represents the insulator-to-metal transition lines obtained from BOMD simulations (triangles) and from CEIMC simulations (squares). The two curves are fairly parallel and both terminates in a critical point at $T \approx 2000K$, but, probably because of the DFT gap underestimation, the metallic state is predicted to appear at lower pressures by BOMC than by CEIMC. Indeed, far enough from the metallization transition the BOMD and CEIMC techniques have already been proven to be in quantitative agreement [131].

5.3 Present results

With the CEIMC method, Morales et al. [19] computed the liquid-liquid transition curve in the interval of pressures $P \in [120, 220]GPa$, corresponding to a range of temperatures $T \in [2000, 1000]K$. We want to extend the CEIMC simulations to higher pressures/lower temperatures. Since by extrapolating the Morales data it is expected that the liquid-liquid transition line and the molecular melting curve

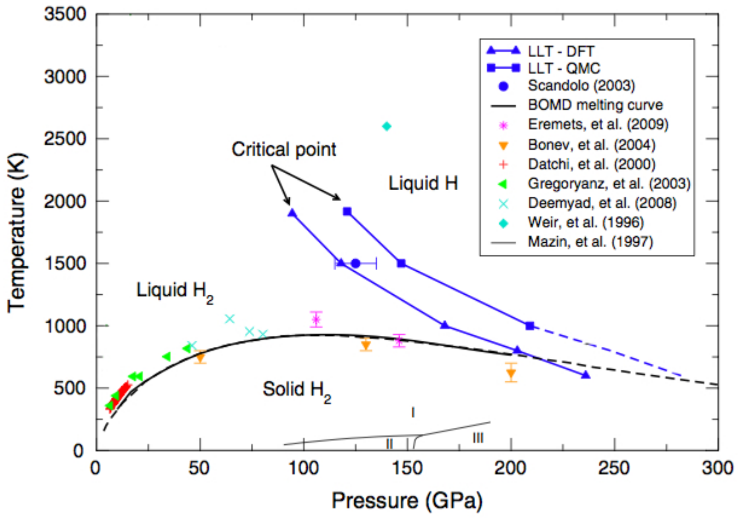

Figure 5.1. High pressure hydrogen phase diagram, that illustrates the different prediction of the PPT transition obtained from BOMC (blue triangles)and CEIMC (blue squares) simulations. Experimental and simulation results for the metallization and the melting are also shown. Figure from [19].

will met in a triple point at $T \sim 600K$ and $P \sim 290GPa$, we decided to perform our CEIMC calculation at this temperature, to look also at the stability of the fluid phase at low T.

The work of Morales et al. [19] also pointed out a substantial qualitative agreement between BOMD and CEIMC methods in the prediction of the metallization transition in the liquid phase, altough quantitatively the two methods gives different results, being the transition line obtained with the BOMD simulations shifted at pressures between $\sim 50GPa$ and $\sim 75GPa$ lower. We are now interested on investigating the effect of the electronic method used in the CEIMC simulations (either RQMC or VMC) on the prediction about the transition curve. Indeed, since the VMC calculation are faster than the RQMC, an eventual equivalence of results obtained with the two tecniques would be advantageous in view of future systematic calculation in this region of the phase diagram.

5.3.1 Simulation details

In order to locate the liquid-liquid transition pressure, we analyzed the behavior of the pressure versus density along the isotherm at $T = 600K$. At this temperature we performed CEIMC simulations with classical protons for 11 different densities in the range corresponding to $r_s \in [1.31, 1.40]$. To investigate the relevance of the electronic ground state method, we repeated the simulations at the same thermodynamic points using the VMC and the RQMC methods.

In both cases the electronic trial wave function is of the Slater-Jastrow type (2.107), with backflow transformation, as described in Section 2.5.1. At any density the Jastrow and the backflow terms are optimized in advance, according to the following procedure (described in detail in Section 2.6.4). For a given density, 16 uncorrelated proton configurations are chosen among the equilibrium proton configurations obtained in a preliminary CEIMC simulation in the fluid phase. These preliminary simulations are performed with the VMC electronic energies and the electronic trial wave function contains only RPA terms. For each one of these configurations the optimal set of values of the variational parameters is determined by requiring the minimization of a combination of the energy and of its variance, using a standard minimization algorithm and correlated sampling. The final values of the parameters are obtained by averaging over the 16 optimal sets. The optimization was carried out only at few densities in the interval under analysis: at the remaining densities the best values of the parameters are obtained through a interpolation procedure.

Since our systems are made by 54 protons and 54 electrons, in order to reduce the finite size errors we adopted Twist Averaged Boundary Conditions (see Section 2.6.3), with a fixed grid of 64 twist angles [96]. In addition, pressures and energies are corrected for finite size applying the formulas presented in Section 2.6.3.

For the RQMC data set, the values of the time step τ ($0.02 Ha^{-1}$) and of the total projection time β ($1.00 Ha^{-1}$) were chosen to obtain converged energies. With those values of τ and β the convergence of the pressures is still not achieved; it was then necessary to add a correction to account for the finite β and the nonzero τ to the raw pressure data. In order to determine the correction, a convergence study with τ and β was performed on 10 different protonic configurations uncorrelated and of equilibrium.

Each simulation starts from a disordered configuration of 27 molecules: with the word molecule we mean here two protons at a distance $r_M \sim 1.4$. To obtain the initial protonic configuration, we build a perfect BCC lattice of 27 lattice points to which the molecules are attached. Then the system is disordered through a classical MC simulation (without electrons) that uses effective potentials to represent the inter and intra molecular interactions. The Silvera-Goldman potential [132] is used to describe the intermolecular interactions, while two protons inside a molecule are bounded by the Kolos-Wolniewicz interactions [133]. The classical simulation is performed for a long enough sampling to reach a fluid of randomly oriented molecules. Once this disordered initial state is achieved, the bonding and the intermolecular effective potentials are removed and the molecules are left free to dissociate, by performing standard ab-initio CEIMC simulations. At least the first 8000-10000 proton steps - depending on the density - are discarded before starting to accumulate averages. To reduce the error bars in the thermodynamic quantities to values small enough to appreciate small variations of the pressure, at least 30.000-35.000 protonic steps must be used at densities near the transition.

5.3.2 Discussion of the results

To recognize the first order liquid-liquid transition we look at the pressure of the system as a function of the density along the isotherm at $T = 600K$. In both data sets (VMC and RQMC) we found a plateau of constant pressure. In the interval of densities corresponding to the pressure plateau the compressibility of the system $\kappa = V^{-1}(\partial P/\partial V)$ diverges: this indicate the occurrence of a first order transition.

As can be seen from Figure 5.2 and from Table 5.1, the agreement among the results obtained with VMC and RQMC is rather good. The RQMC and the VMC curves relatives to the behavior of the pressure with the density are very close, especially at densities below the transition, where the pressures from different electronic methods are within the errorbars. Above the transition the pressure differences are a bit larger, although still below $\sim 1\%$. Despite the interval of densities corresponding to the plateaux is not coincident in the RQMC and the VMC curves, the transition pressures are very similar: $P_T^{\mathrm{RQMC}} \approx 277GPa$ and $P_T^{\mathrm{VMC}} \approx 275GPa$.

As expected, those values of P_T are also in agreement with the extrapolation at $T = 600K$ of the liquid-liquid transition curve from CEIMC simulations of Morales et al. [19], showed in Figure 5.1.

Let us look now at the energy curves in Figure 5.3: in this case in correspondence of the edges of pressure plateau, mark of the first order transition, it can be noticed a small discontinuity in the energy. The behavior of the VMC and of the RQMC curves is similar, despite the numerical agreement of data is not as good as for pressures.

The phase transition is accompanied by a the partial dissociation of the H_2 molecules, as can be observed from the behavior of the proton-proton radial distribution function $g_{pp}(r)$ with the density, illustrated in Figure 5.4 for 10 different values of r_s across the transition. On the left panel we present the $g_{pp}(r)$ obtained for the VMC set of simulations, on the right those for RQMC. The sharp peak at about $r_M = 1.4a_0$ is due to the H_2 molecular bond and disappears gradually going from the lowest to the highest density, indicating the progressive breaking of molecules and the resulting appearance of unpaired protons. However, as can be better seen from the inset in Figure 5.2, the molecular peak in the radial distribution functions is still evident after the transition has occurred. This seems to indicate that the first order transition is not due to the complete dissociation of the molecules, that occur with continuity and not abruptly.

Figure 5.5 shows the proton-electron (left panel) and the electron-proton (right panel) radial distribution function at different densities across the transition. The differences here are less pronounced that in the case of the $g_{pp}(r)$, and we can only observe that for increasing densities the correlations become slightly lower. In fact the value at zero of the $g_{ep}(r)$ passes from ~ 5.3 to $\sim 4.$ going from $r_s = 1.40$ (lower density) to $r_s = 1.31$ (higher density). Similar behavior can be found in the $g_{ee}(r)$: the first correlation peak is slightly shifted at lower distances and becomes less pronounced as we go from the higher r_s to the lower.

The comparison of VMC and RQMC simulation results seems to suggest the equivalence of the two electronic methods, at least for what is concerning the position of the liquid-liquid phase transition.

5.4 Conclusions

We have determined a point on the liquid-liquid coexistence line by CEIMC simulations, observing the position of the plateau in the pressure curve in density along the isotherm $T = 600K$. We compared the results obtained with the two different QMC methods implemented in our code, the VMC and the RQMC, and we found a substantial agreement. This result is very promising, especially in view of the future addition of quantum effects on the transition line: indeed a VMC simulation is several times faster than a RQMC, in the same conditions, an essential aspect

Table 5.1. Energies and pressures along the $600K$ isotherm, for the VMC and RQMC data.

r_s	$\rho(g/cm^3)$	$E_{RQMC}(Ha)$	$P_{RQMC}(GPa)$	$E_{VMC}(Ha)$	$P_{VMC}(GPa)$
1.310	1.197	-0.50082(8)	331.6(6)	-0.49915(6)	327.2(6)
1.320	1.170	-0.50259(8)	311.4(4)	-0.50229(6)	305.2(6)
1.330	1.144	-0.50493(8)	293.9(6)	-0.50429(6)	284.0(6)
1.340	1.119	-0.50798(8)	283.8(7)	-0.50729(6)	275.9(6)
1.350	1.094	-0.51111(8)	277.2(7)	-0.51096(6)	275.0(6)
1.355	1.082	-0.51190(9)	277.8(8)	-	-
1.360	1.070	-0.51438(8)	271.5(6)	-0.51256(6)	262.8(6)
1.370	1.047	-0.51611(8)	253.1(6)	-0.51526(6)	252.6(6)
1.380	1.024	-0.51809(8)	240.7(6)	-0.51691(6)	239.2(5)
1.390	1.002	-0.52078(8)	231.0(6)	-0.51937(6)	229.6(6)
1.400	0.981	-0.52247(8)	220.4(6)	-0.52062(6)	217.8(6)

which would allow to reduce the global computational time of our simulations.

To conclude, let us make a further comment. As can be seen from Figure 5.1, the region of pressure we explored here is expected to be near to a triple point, crossing of the metallization line and of the molecular melting line. Estimating the slope of the liquid-liquid transition line around $T = 600K$ from the Clausius-Clapeyron equation, $TdP/dT = \Delta H/\Delta V$, it is possible to predict the intersection of this line with the molecular melting line. Calculating the enthalpy and the volume differences at transition from data, as summarized in Table 5.2, we obtain that the position of the triple point is $T \sim 535K$ and $P \sim 297GPa$ for the VMC data and $T \sim 507K$ and $P \sim 309GPa$ for the RQMC data, in rough agreement with the estimate of Morales et al. ($T \sim 550K$ and $P \sim 290GPa$) (see Figures 5.6 and 5.7)

Table 5.2. Enthalpy (first column) and volume differences (second) at the liquid-liquid transition, for the VMC and the RQMC data. In the third column the value of the pressure at transition is showed.

	$\Delta H/N(Ha)$	$\Delta V/N(a_0^3)$	$P_{PPT}(Ha/a_0^3)$
VMC	0.001547(12)	-0.227398(8)	0.00934(3)
RQMC	0.0014566(18)	-0.114984(10)	0.00941(3)

However, at none of the densities in the range explored by our present simulations an indication of freezing of the molecular liquid has been found.

The absence of an indication of transition from the molecular fluid to the molecular solid phase is not necessarily incompatible with our prediction about the triple point. First, it is possible that the stability of the liquid phase at low temperatures is due to a finite size effect. The number of protons in our systems is indeed quite small ($N = 54$) and as a consequence it may be impossible for the protons to rearrange themselves and form a lattice with a small number of vacancies. The energetic cost of a vacancy can then make unstable an eventual molecular crystal.

Another possibility is that the system at these pressures evolves very slowly and then it is not easy to recognize an eventual metastability of the liquid phase and observe spontaneous freezing.

On the other hand, it can be possible that the extrapolation of molecular melting line, done according to the empirical Kechin form [30], does not remain accurate enough up to the pressure of metallization ($P \sim 280GPa$). Further investigations are hence required to identify the triple point. Among the others, we report two possible approaches that may be attempted to this aim: (1) the use of a number of particles compatible with a vacancy-free molecular crystal[1] and collocate the protons on or near the lattice sites of this crystal to observe qualitatively the stability of the molecular solid phase with respect to the liquid (and eventually compute their free energies to have quantitative informations on the relative stability of the phases) and (2) the extension of the melting line up to the dissociation pressures, to check its high P behavior.

---

[1] for example one can choose a number of protons to form a perfect HCP molecular structure. This is possibly the crystallization structure characteristic of the molecular hydrogen phase I, as already seen in the first Chapter of this thesis

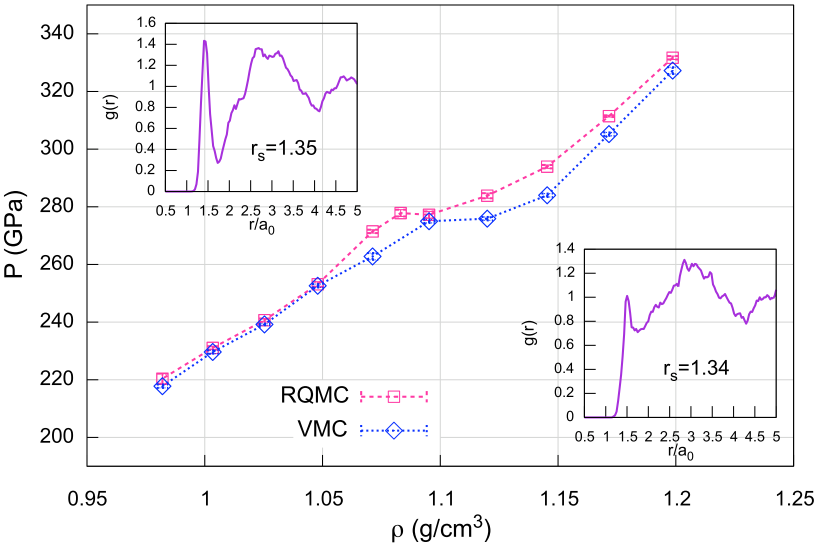

Figure 5.2. Pressure as a function of the density, along the isotherm $T = 600K$; VMC (blue diamonds) and RQMC (pink squares) data are compared. The metallization transition corresponds to the well visible plateau at about $280GPa$. Lines are just guides to the eye. The insets display the radial distribution functions for the two densities at the edges of the plateau (RQMC data), and show a marked reduction of the molecular peak, that is still present, also in the metallic side.

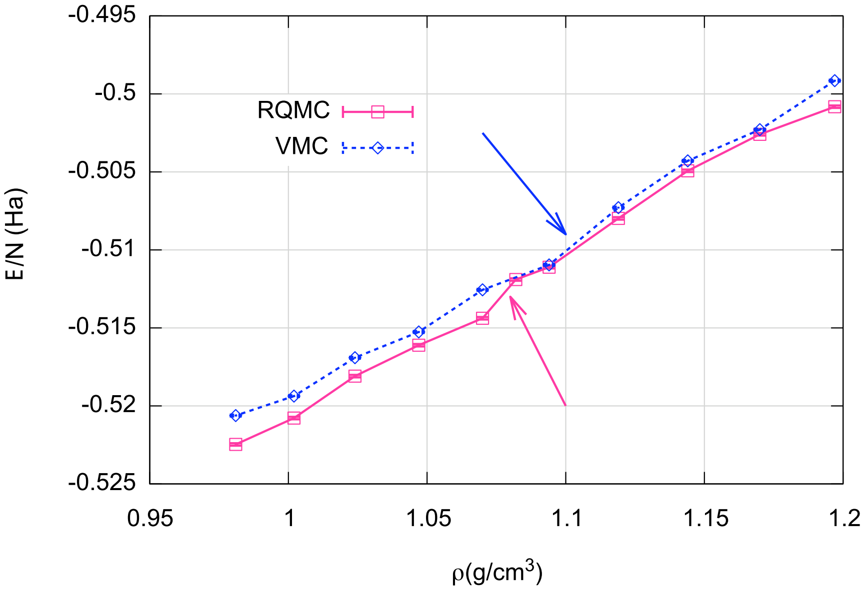

Figure 5.3. Energy as a function of the density, along the isotherm $T = 600K$; VMC (blue diamonds) and RQMC (pink squares) data are compared. Errors are within the symbol size. The range of the pressure plateau for each method is indicated by the arrows.

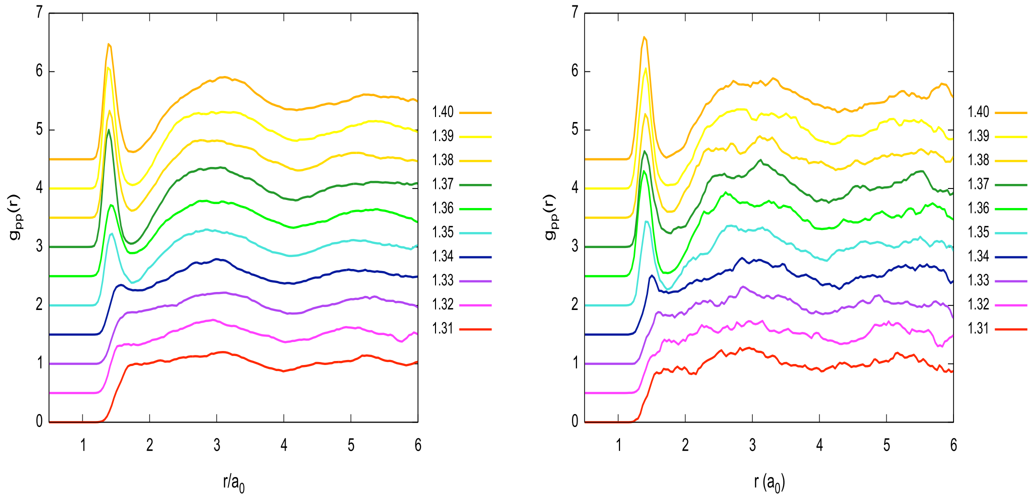

Figure 5.4. Proton-proton radial distribution functions at different densities for the $T = 600K$ isotherm. VMC data on the left and RQMC data on the right. In both cases it is evident the gradual disappearance of the molecular peak, as the density is increases. To avoid superpositions of the curves at different r_s, each curve is shifted from the previous of $+0.5$ along the vertical axis.

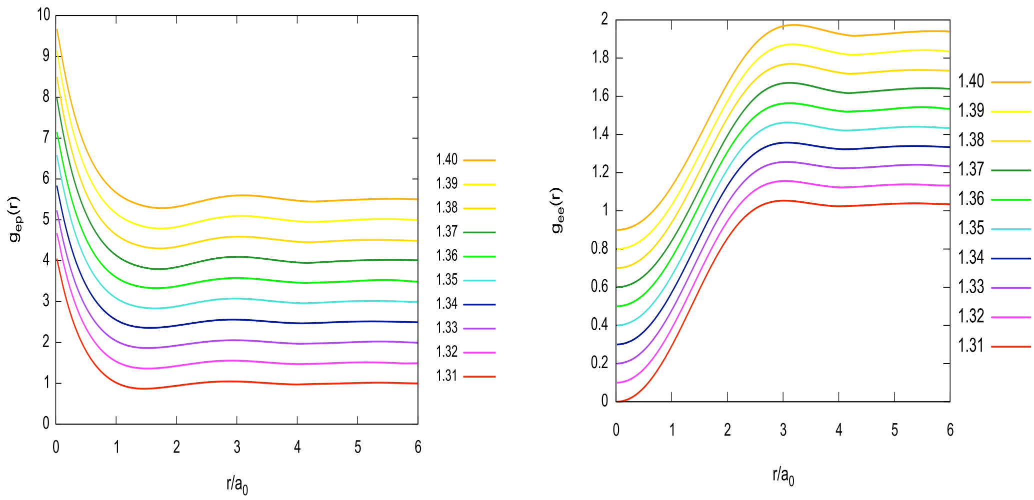

Figure 5.5. Proton-electron and electron-electron radial distribution functions at different densities for the $T = 600K$ isotherm, from the VMC data sets. Similar behavior is found for the RQMC data. To avoid superpositions of the curves at different r_s, each curve is shifted from the previous of $+0.1$ along the vertical axis.

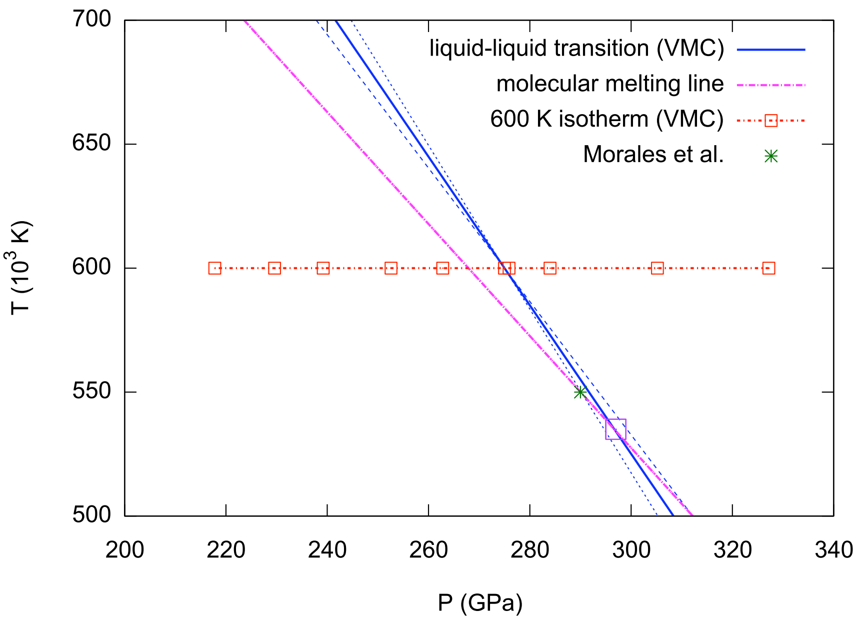

Figure 5.6. Estimate of the position of the triple point (coexistence among liquid H_2, solid H_2 and liquid H) obtained from VMC data. The slope of the liquid-liquid transition (continuous blue line) around the transition point at $T = 600K$ has been derived from the Clausius-Clapeyron equation. The dashed blue lines are representative of the confidence level of the estimated liquid-liquid transition. The extrapolation of the molecular melting line computed by BOMD simulations (Ref. [19]) is represented by the magenta dash-dotted line. The two transition lines crosses at $T \sim 535K$ and $P \sim 297GPa$ (purple point). The green star represents the previous estimate of the triple point by Morales et al. [19]. The isotherm at $T = 600K$ is also presented (red squares).

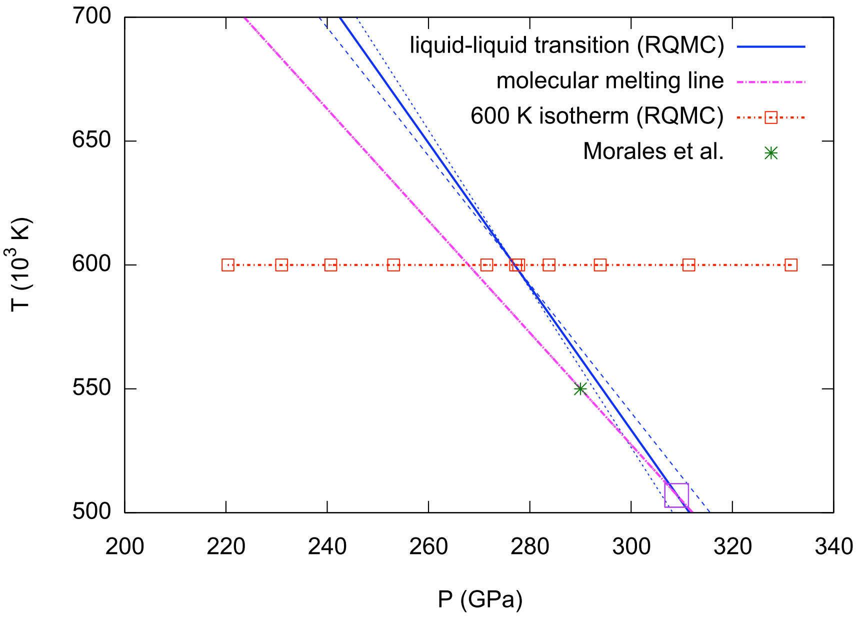

Figure 5.7. Same of Fig. for the RQMC data. The estimated triple point is at $T = 507(\pm 10)K$ and $P = 309(\pm 10)GPa$ (purple point).

Conclusions

The aim of this thesis was the investigation of the phases of high pressure hydrogen, by means of Monte Carlo techniques. In the most of our calculations we adopted a novel *ab initio* approach, the Coupled Electron-Ion Monte Carlo method, which relies on the Born-Oppenheimer approximation to treat separately the protonic and the electronic degrees of freedom and which is based on Monte Carlo techniques both for determining the electronic ground state relative to a fixed protonic configuration and for sampling the protonic configurational space.

We have focused our interest mainly to the monoatomic region of the hydrogen phase diagram, a region which is not experimentally accessible.

A first part of this work was devoted to the study of an effective model which is able to represent satisfactorily the hydrogen in the very high pressure regime, above several TPa. At these pressures hydrogen is fully ionized and behaves as a two component plasma made by protons and electrons. The two component system can be reduced to an effective single component system of pseudo ions interacting via a screened Coulomb pair potential, derived from static linear response theory applied to electrons. The resulting pair potential is equivalent to a Yukawa potential at short distances and is characterized by an oscillating, slowly decaying tail at large distances. The use of a standard Ewald breakup to treat this middle ranged potential has revealed inefficient, since it was not possible to obtain a good compromise between the length of the real space cut-off, allowing to consider systems with a small number of particles, and the number of k-vector shells to be considered in the reciprocal space in order to achieve convergence. It was then necessary to cut the potential at short distance and, in order to handle systems with a reasonably small number of particles, we considered not only interactions among particles inside the simulation box, but also the interactions with the 26 nearest neighbor boxes. This procedure is source of systematic errors, that however have been checked to be quite small and to have negligible effect on the final results. For this model system we first determined the most stable solid structures at $T = 0K$ by comparing energies and enthalpies of several perfect lattices of classical particles and in a range of densities $\rho_m \in [12.5, 32.7] g/cm^3$. We found that the FCC solid is the most stable, followed by the BCC solid, in the entire range, except at the lower density, at which the energetically favored structure becomes the BCC. We then considered the temperature behavior of the two solids, preforming Metropolis Monte Carlo simulations in the NVT ensemble. We computed by thermodynamic integration the free energy curves of BCC, FCC and of the liquid phase, in the same range of densities and in a range of temperatures $T \in [200, 5000]K$, in order to locate phase transitions. Our data indicates the presence of a BCC-FCC structural transition for temperatures between $250K$ and $1000K$, whose precise determination is, however, beyond the precision of the method applied. The most stable structure at melting is then BCC. Applying the Maxwell construction to determine the coexistence points we found that the volume difference between the BCC and the liquid at coexistence is practically negligible. Under the assumption of zero volume discontinuities at transition, we then determined the classical melting curve for the system. Our estimate of melting temperature is in agreement with previous predictions based on Lindemann criterium and *ab initio* Molecular Dynamics simulations of the two component system. We then determined the quantum corrections to the free energy curves of the classical system by thermodynamic integration in the inverse mass and using the Path Integral Monte Carlo technique. This procedure allows to obtain quantum corrections for all the hydrogen isotopes (hydrogen, deuterium and tritium) at once. We found that the quantum effects on the melting curve are practically negligible for the heavier isotope (tritium) while become more significant for hydrogen, lowering by as much as 10% the melting temperature at the higher density considered. Although on a model system, the present results can be relevant for the reconstruction of the phase diagram of high pressure hydrogen since the melting curve of the screened Coulomb system can be used as a starting point to determine the melting transition of the atomic hydrogen at lower densities by *ab initio* simulations. To this aim we have derived a predictor-corrector procedure which, under the assumption of zero volume differences between the phases at transition, allows to move along the coexistence line once a first coexistence point is known. This equation is the analogous of the Kofke scheme, based on the Clausius-Clapeyron equation and valid for finite volume differences. In the determination of the phase transitions small systematic errors can lead to inaccurate predictions. To remove the approximation of the finite size potential cut-off and of the sum of interactions in the nearest simulation box images, we are presently investigating a modified Ewald breakup, able to handle the screened Coulomb potential, which we will use in future calculations.

At lower densities and pressures the description of the hydrogen through the effective screened Coulomb system cease to be valid and the use of *ab initio* simulations becomes necessary to determine phase transitions. The prior source of difficulty encountered in the study of the melting of the monoatomic hydrogen is the absence of experimental indications about the crystal structure. We then performed a systematic study at $T = 0K$ to determine the most favorable solid structures among a wide set of lattices of different symmetries. We computed energies and enthalpies of several lattices by Reptation Quantum Monte Carlo simulations with fixed (classical) protons, in a range of densities $\rho_m \in [1.2, 1.6] g/cm^3$ and pressures $P \in [300, 650] GPa$. We found that in the entire range under analysis the most stable structure is a structure belonging to the symmetry group $I4_1/amd$, or $CsIV$. However, this approach has a fundamental limitation: only a finite number of structures can be considered and it is not guaranteed that the set chosen contains the actual ground state structure. A recent work using a dynamic method to search structures, the Ab Initio Random Structure Search (AIRSS) based on DFT electronic calculations, has found that, at $T = 0K$ and for classical protons, the $I4_1/amd$ structure is the most stable crystal structure for the monoatomic hydrogen in a wide range of pressures, up to $2500GPa$, a result in agreement with ours. Moreover, in the same work the contribution of protonic zero point motion on the enthalpies was also included at an harmonic level. This contribution has a non negligible effect on the enthalpic ordering of the structures, reducing the stability of the $I4_1/amd$ structure to a smaller interval of pressures, up to $1200Gpa$, in favor of a structure of different symmetry (belonging to the space group $R3m$). Quantum effect on protons are then relevant: for that reason in the next future we want to repeat the static calculations including the contributions of the protonic zero point motion, beyond the harmonic approximation.

We also performed finite temperature CEIMC simulations, for classical protons, in order to determine the melting transition, by means of free energy calculations. This part of the work was in fact started before the analysis of the zero temperature enthalpies of the various crystals. We then considered only BCC, FCC and the diamond structure. Both BCC and FCC structure turned out to be dynamically unstable also at low temperature (down to $350K$) and melted during the CEIMC simulations. Only for the diamond structure it was then possible to compute the free energy. Assuming that the crystal structure at melting is the diamond structure and neglecting the volume difference between diamond and liquid at transition, we identified a first point on the transition curve, at $\rho = 1.197 g/cm^3$ and at $T \sim 200K$. The pressure is around $300GPa$. The free energy calculations must be extended to higher densities. The zero volume assumption must also be verified, by applying the Maxwell construction to the isothermal free energy curves. Moreover, in addition to the diamond lattice other structures must be included in future calculations, in particular the $CsIV$ which at zero temperature has an enthalpy of several mHa lower than the diamond structure. Once determined the first solid-liquid coexistence curve, the melting curve can be extended by applying a predictor corrector scheme (in the original version or in the modified version we developed for transitions with zero volume discontinuity at transition).

Finally we applied the CEIMC technique to study the liquid-liquid dissociation transition at low temperature, to extend at lower temperature the transition curve obtained by CEIMC simulations in a previous work of Morales et al. (*PNAS* **107**, 12799 (2010)). The occurrence of a first order transition can be evinced from the presence of a plateau of constant pressure in the pressure curve along an isotherm. To build this curve we then performed 10 constant volume CEIMC simulations at different densities in the range $\rho_m \in [0.981, 1.197] g/cm^3$ along the isotherm $T = 600K$, assuming classical protons. We compared the results obtained with two different Quantum Monte Carlo methods for the electronic energy: the Variational and the Reptation Monte Carlo. We found a substantial agreement in the two predictions. Since the VMC simulations are several times faster than the RQMC, in the same conditions, this is a promising result in view of future calculations with quantum protons. At these low temperatures, indeed, the quantum effects can modify significantly the location of this transition and must be taken into account in future calculations. A further comment can be done. We used the Clausius-Clapeyron equation to compute the slope of the liquid-liquid transition curve at temperatures around the coexistence point at $T = 600K$. In this way we are able to extrapolate the transition curve and to give a prediction of the intersection of this curve with a recent prediction - via Ab Initio Molecular Dynamics (AIMD) - of the molecular melting curve. In this way we can estimate the position of the triple point (solid H_2, liquid H_2, liquid H). The triple point is located at $T \sim 500K$ and $P \sim 300GPa$, quite close to the points of our simulations. Indeed, the lower pressure points we simulated on the isotherm $T = 600K$ lies in a region of the thermodynamic plane below the molecular melting curve. However, we did not observe during our simulation any indication of spontaneous freezing of the molecular liquid. This region of the phase diagram, being at the boundaries between the molecular insulating and the atomic metallic phases, is probably one of the most interesting. Accurate and systematic simulations are then needed to trace different lines on the phase diagram. The molecular melting line can be recomputed by using the CEIMC technique to verify the validity of AIMD near the metallization transition. Free energy calculations of the molecular solid (phase I or phase III) and the molecular liquid phase may be performed to this aim. The liquid-liquid transition curve can be extended itself to lower temperatures. Moreover, at low temperature quantum effects on both curves can be relevant and as already anticipated must be added.

Acknowledgements

I thank my advisors, Prof. Carlo Pierleoni and Prof. Giovanni Ciccotti, for their guidance, their support, their suggestions, their patience and their encouragement.

I thank the GCI group members, former and newer, for their scientific support, their friendship and for the nice time spent together.

I want also to thank Prof. David Ceperley for having invited me at University of Illinois at Urbana-Champaign at the beginning of my PhD and for useful suggestions about my work, and Dr. Miguel Morales for having shared with me part of its experience with the Coupled Electron-Ion Monte Carlo technique.

La formula “Un grazie a..” non si adatta molto al significato che vorrei dare a questa pagina. In questa tesi non c’è solo il mio lavoro. Ci sono le giornate passate qui a Roma, le esperienze vissute, i luoghi visitati, gli istanti condivisi che trascorsi in solitudine avrebbero perso gran parte del loro valore. Tutto questo (e quel che non riesco a dire) vorrei includere nei miei “grazie”.

Un grazie collettivo a tutte le persone che sono entrate piacevolmente nella mia vita in questi anni di PhD e a quelle che, facendone già parte, non si sono allontanate. In particolare:

Un grazie a Chiara per il suo primo invito, che mi ha fatto sentire un po’ più a casa, e per la sua amicizia in questi miei anni romani. E a Chiara (di nuovo), Odeta e Gihan, un grazie per ognuno dei nostri psicoaperitivi, ottima conclusione di giornate spese nei rispettivi lab.

Uno ad Emanuele, mia guida esclusiva alla Roma magica e nascosta e procacciatore di libri.

Uno a Giuseppe (tontuss!), insieme ad un grande in bocca al lupo per la conclusione del suo dottorato.

[2].

Uno ai miei genitori, per l’appoggio dato alle mie scelte, anche a quelle che mi allontanano da loro.

E infine, naturalmente, un grande ringraziamento ad Ale, per tante ragioni, difficili da sintetizzare in poche - pubbliche - righe. Soprattutto, ti ringrazio di essermi ancora accanto, oggi come ieri, e per la promessa di esserci sempre (paura, eh?).

---

[2] Anche per Michele Montefer ci sarebbe un grazie a parte, ma.. “mo non me ne tiene” :).

Appendices

.1 Experimental high pressure setups for hydrogen

Several methods has been conceived to compress liquid, solid or gaseous samples up to pressures hundreds times higher than the atmospheric. Among those we can distinguish into static methodologies, as mechanical presses, allowing to maintain a constant compression for large amount of time, and dynamic techniques, used to reach very high pressure and temperatures. The main techniques belonging to those two categories are the Diamond Anvil Cells (static compression) and the Shock Wave method (dynamic). In this appendix we want to give to the reader an overview on those methods.

.1.1 Diamond Anvil Cells

Diamond Anvils Cells (DAC) are very powerful instruments to study the properties of matter under high pressure. DACs allow to compress hydrogen up to $\approx 350GPa$, in a range of temperatures up to $6000K$. Work conditions can be maintained stable for long time, allowing to perform accurate measurements of the high pressure properties of the samples. Both pressure and temperature can be easily tuned to the desired value, providing a number of data across the T-P range with the same setup. Moreover the transparency of diamonds over a wide range of wavelengths (from InfraRed to X-ray) makes the DAC an ideal technique to couple with spectroscopic experiments.

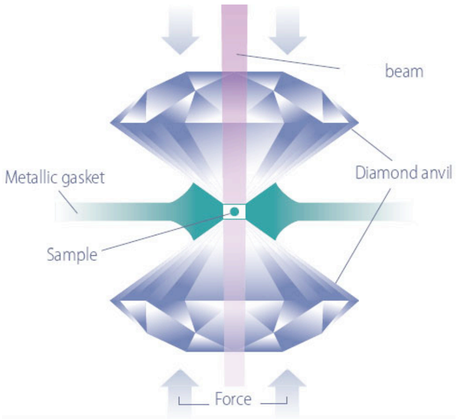

Figure .8. Schematic representation of Diamond Anvils for DAC experiments. An external force is applied on the outer plane faces (tables) and compress the sample contained in the metallic gasket hole. Thanks to the diamond transparency, DAC compression is suitable for spectroscopy analysis: a beam light can be focused on the sample through the diamond anvil.

A schematic representation of a DAC is showed in Figure .8. A metallic thin plate, acting both as a gasket and as a sample holder, is placed between two diamond anvils in opposite configuration and with parallel plane faces. The correct alignment of anvils is necessary to a more efficient compression and to avoid premature diamond breaking. Diamonds are conveniently shaped to amplify the external applied pressure of the desired amount, determined by the ratio between the external flat face (table) and the internal one (culet). For $100 - 200GPa$ compression, typical values of table and culet diameters are $\approx 1 - 2mm$ and $\approx 100\mu$, respectively.

The sample is contained into a small hole on the gasket; if the sample is in the solid phase the hole is filled with an hydrostatic medium that ensures the isotropic transmission of the pressure. In order to resist at pressures of hundreds of GPa, gaskets are made of hard metals as rhenium. The gasket is obtained pre-indenting a $200\mu m$ thick metallic sheet with the diamond tips, up to the desired thickness ($\approx 20 - 50\mu m$). This procedure gives to the gasket a cratere-shape (see Figure .9): the material accumulated at the boundary of the intended area strengthen the gasket in the proximity of the diamond tips and improve its performances. Finally, the sample holder is obtained by drilling a small hole at the center of the culet imprint.

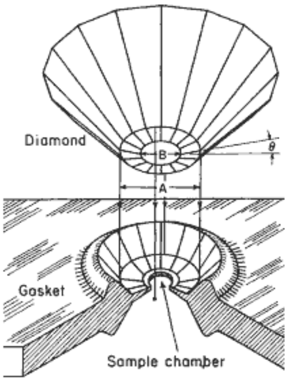

Figure .9. Schematic representation of a DAC gasket. The diamond anvil is used to indent the metallic foil of original thickness of about $200\mu m$ up to final height of about $20 - 50\mu m$. The smashed material accumulates at the edges of the central area, enhancing the stress resistance of the gasket. The drilled hole, constituting the sample chamber, has a diameter less than $1/3^d$ of the thin area. Image from Ref. [21]

The external pressure to squash the diamond anvils is provided by a suitable designed press, that completes the DAC apparatus. If it is necessary to maintain a constant pressure on the sample for long time, a fixed-pressure cell is needed: this apparatus is realized by clamping a piston to an hanging support which avoid that a gradual relaxation may reduce the load. In some situations, instead, such as the study of a phase transition, it may be necessary to change the pressure during the experiment. In these cases a membrane cell with pneumatic loading, which allows the fine control of the pressure during the experiment, is used.

To measure the pressure on the sample, a small ruby is inserted into the sample holder. The ruby fluorescence spectrum is in fact characterized by a bright and intense doublet of peaks, usually denominated R_1 and R_2 lines, whose wavelengths are strongly dependent on the interatomic distances in the ruby and consequently on the pressure. The dependence of the R_1 line wavelength on the pressure has been

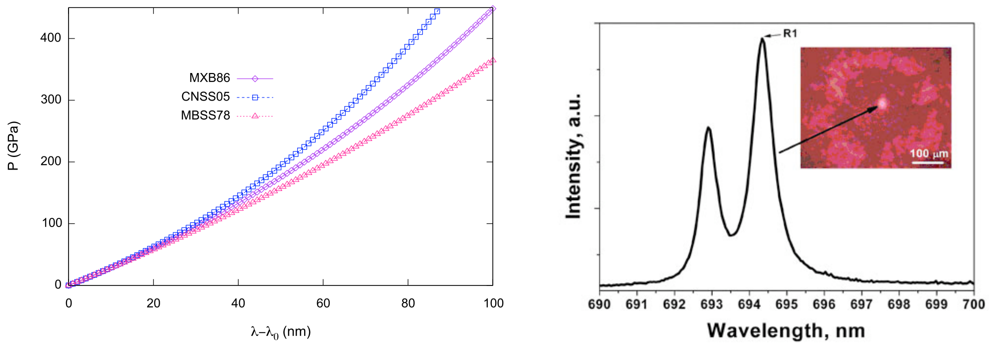

Figure .10. Left: Ruby calibration curves examples. Early measurements by Mao et al. (purple diamonds and magenta triangles) and last calibration data (2007) by I. Silvera et al (blue squares). Right: Ruby fluorescent spectrum. In the inset image of fluorescent ruby in a DAC.

widely studied and is well described by

$$P(GPa) = \frac{A}{B}\left[\left(\frac{\lambda}{\lambda_0}\right)^B - 1\right] \qquad (.1)$$

where λ is the wavelength of the R_1 peak at the pressure P and λ_0 is the wavelength of the same line as measured at $P_0 = 1GPa$, $\lambda_0 = 694.24nm$; the values of the parameters A and B are obtained by preliminary ruby calibration studies: the more recent literature values are $A = 1876 \pm 6.7$ and $B = 10.71 \pm 0.14$. This formula can accurately reproduce the behavior of the ruby fluorescence peak R_1 up to $300GPa$.

During a DAC experiment it is then possible to determine the pressure inside the sample chamber by irradiating the ruby with a green light laser and by measuring the redshift of the R_1 fluorescence line. Moreover, by monitoring the behavior of the ruby fluorescence peaks it is possible to control that an hydrostatic compression is realized: indeed, the less the compression is isotropic the more the ruby fluorescence peaks tend to broaden.

Not only the pressure, but also the temperature of the sample can be changed during a DAC experiment. The main methods employed to heat the samples are Ohmic and laser heating. In the first case an external resistance placed near the sample chamber is used to convert electric current into heat; in the second case, an heat absorber is placed into the sample holder and irradiated with a laser. The temperature is then measured by observing the black body emission spectra of the absorber. To avoid that high thermal gradients may establish into the sample chamber and that the diamond anvils may heat excessively, the absorber is not irradiated continuously but by an high power pulse of a duration of the order $\approx 100ns$. Temperature equilibrium is reached after short time, and without heating too much the anvils and the gasket. This technique allow to reach temperature of few thousands Kelvin.

The maximum pressure that can be reached in a DAC depends on several factors, such as the shape and the purity of the diamonds, the gasket material and the material of the sample. The primary limitation to the pressure arises from embrittlement and crack formations in the diamonds, favored by the presence of impurities. In the case of liquid hydrogen, the permeation of part of the sample into the diamonds is the major cause of the anvils weakening and breaking. This effect is enhanced by the temperature, limiting the accessibility of DAC experiments to the lower region of the thermodynamic (P, T) plane.

.1.2 Dynamic compression: Shock waves

The shock wave technique allows the dynamic compression of materials at very high pressures ($P \geq 100GPa$) and temperatures ($T \geq 1000K$). It can be considered a methodology complementary to the DACs as it allows to achieve a range of temperature and pressure well above the maximum reached by static compression. Conversely, due to the noticeable temperature rise accompanying the pressure increment, it is impossible to employ shock waves to investigate low temperature states. At variance with the DAC technique, which allows a compression stable in time, in a shock wave experiment the sample conditions can be maintained for a time of the order of nanoseconds; to measure the quantities of interest (reflectivity, conductivity..) specific fast techniques are hence needed.

A shock wave is a traveling sharp discontinuity in the characteristics of the propagating medium (pressure, temperature and density) caused by the impulsive release of large amount of energy in a localized region. In laboratory, a shock wave can be produced for example through some plate that hits at high speed the sample holder, leading to the formation of a compression wave that propagates at supersonic speed through the material. The final state reached in the shocked media is self-determined and depends only on the initial conditions of sample and impactor and on the compressibility characteristics of the material.

A simple unidimensional model helps in visualizing the quantities that characterize the wave propagation: suppose to have a long chain of beads connected by springs, as in Figure .11. One of the edges of the chain is in contact with a piston, used to compress the chain. If the piston is moved at constant velocity w, greater than the sound speed u_s in the chain, only a limited region near to the piston is initially compressed and passes from the initial density ρ_0 to an higher density ρ_c; the farthest zones remain unperturbed. The regions at different densities are separated by a thin region called the shock front, in which particles are not in equilibrium. Since we are interested on the equilibrium properties in the compressed and the uncompressed regions and not on the behavior at their boundary, our simple model will assume that the thickness of the shock front is zero. The shock front moves

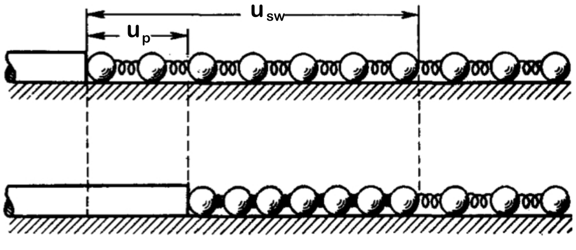

Figure .11. Unidimensional model useful to visualize the difference between the particle velocity (u_p) and the shock wave velocity (u_{sw}).

with velocity $u_{sw} > u_p$. Figure .12 presents a schematic representation of the density and the velocity profiles in our unidimensional model. Before the shock generation the system has neat velocity along the horizontal axis x equal to zero and a density $\rho = \rho_0$. A time Δt after the shock, the piston has travelled along x of an amount $l_p = w\Delta t$, while the shock front has advanced up to $l_{sf} = u_{sw}\Delta t$ with respect to the original position of the piston. In the portion of the chain between l_{sf} and l_c the chain is compressed and the particle density is some $\rho_c > \rho_0$ and in which the particles are pushed forward with a velocity $u_p = w$. Ahead of the shock front (at distances $x > l_{sw}$) the system is unperturbed and remains in the initial condition.

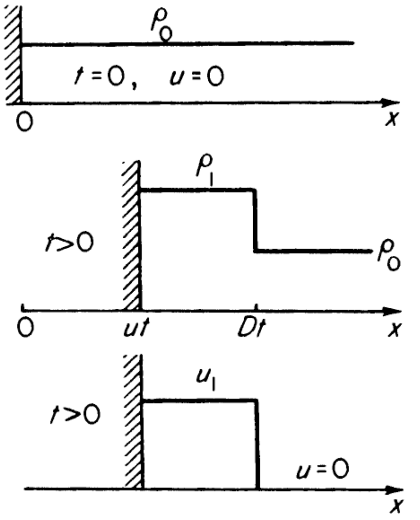

Figure .12. Illustration of the density and velocity profiles in the unidimensional model described in the text and represented in Figure .11. The chain is initially at density ρ_0 and has a pressure P_0. The initial particle velocity u along x is zero. A time t after the shock generation two regions can be distinguished: a compressed region at density $\rho_c > \rho_0$ and in which the particles move along x with velocity u_p and an unperturbed region of particles at rest and still at density ρ_0.

Under the hypothesis of stationarity of the wave, imposing the conservation of mass, momentum and energy it is possible to derive three conservation equation, known as the Rankine-Hugoniot equations, which relate the characteristics of the wave and the thermodynamic properties of the propagating medium in the two regions (compressed and unperturbed)

$$\frac{\rho_c}{\rho_0} = \frac{u_{sw}}{u_{sw} - u_p} \qquad \text{(mass conservation)} \qquad (.2a)$$

$$P_c - P_0 = u_{sw} u_p \rho_0 \qquad \text{(momentum conservation)} \qquad (.2b)$$

$$E_c - E_0 = \frac{P_c + P_0}{2}\left(\frac{1}{\rho_0} - \frac{1}{\rho_c}\right) \qquad \text{(energy conservation)} \qquad (.2c)$$

where $P_{c/0}$, $\rho_{c/0}$ and $E_{c/0}$ are the pressure, density and internal energy in the compressed/uncompressed region.

Let us then derive the Rankine-Hugoniot equations considering our unidimensional model.

- Mass conservation

  Let us indicate with S the section of the piston and with L the initial length of the chain. At the beginning the whole system fills the volume $V = LS$ with a density ρ_0. The average particle velocity is zero. At t=0, the piston starts to move and the shock wave is originated. After a time lapse Δt has passed, the length of the compressed region, delimited by the shock front and the piston surface, is equal to $l_c = (u_{sw} - u_p)\Delta t$. In this region the particle density is equal to ρ_c. The uncompressed part of the chain, still at the initial density ρ_0, is contained on a region of lenght $l_0 = L - u_{sw}\Delta t$. Imposing the mass conservation we can then write

$$\rho_0 LS = \rho_0 l_0 S + \rho_c l_c S = \rho_0(L - u_{sw}\Delta t)S + \rho_c(u_{sw} - u_p)\Delta t S \qquad (.3)$$

This expression can be simplified and becomes

$$\begin{aligned} 0 &= -\rho_0 u_s + \rho_c(u_{sw} - u_p) \\ \Rightarrow & \frac{\rho_c}{\rho_0} = \frac{u_{sw}}{(u_{sw} - u_p)} \end{aligned} \qquad (.4)$$

which corresponds to Equation (.2a)

- Momentum conservation

  The system is initially at rest. After the shock, the particles in the compressed region acquire a velocity u_p. After a time Δt the volume of the compressed region is $Sl_c = S(u_{sw} - u_p)\Delta t$ and then the total momentum of the system is then $S(u_{sw} - u_p)\rho_c u_p$. Since the total momentum change is equal to the impulse of the pressure forces we can write

  $$S(u_{sw} - u_p)\Delta t \rho_c u_p = (P_c - P_0)S\Delta t$$

  Simplifying the previous expression and using the mass conservation relationship (.2a) to express the difference $u_{sw} - u_p$, we finally obtain

  $$P_c - P_0 = \rho_0 u_p u_{sw} \qquad (.5)$$

  i.e. Equation (.2b).

- Energy conservation

  Finally, we want to impose the energy conservation to obtain the equation (.2c). The total energy is the sum of the internal particle energy (due to particle interactions) and of the kinetic energy. Denoting with E_c and E_0 the internal energy per unit mass of the system in the compressed and the uncompressed regions, respectively, we can write the energy difference between the initial state, immediately before the shock and a final state a time Δt after as

  $$\begin{aligned} \Delta E &= \rho_c(E_c + u_p^2/2)S(u_{sw} - u_p)\Delta t + \rho_0 E_0 S(L - u_{sw}\Delta t) - \rho_0 E_0 SL \\ &= \rho_c(E_c + u_p^2/2)S(u_{sw} - u_p)\Delta t - \rho_0 E_0 S u_{sw}\Delta t \end{aligned} \qquad (.6)$$

  We can now sum the two terms in the last equality by using (.2a) to rewrite $(u_{sw} - u_p)\rho_c = u_{sw}\rho_0$ and we get

  $$\Delta E = \rho_0(E_c + u_p^2/2)S u_{sw}\Delta t - \rho_0 E_0 S u_{sw}\Delta t = \rho_0(E_c - E_0 + u_p^2/2)S u_{sw}\Delta t \qquad (.7)$$

  The energy difference must be equal to the work of the piston on the system, $W = P_c S u_p \Delta t$, then we have

  $$P_c u_p = \rho_0(E_c - E_0 + u_p^2/2)u_{sw} \qquad (.8)$$

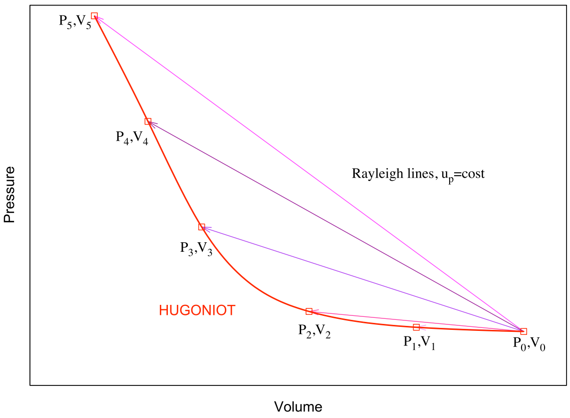

Figure .13. Example of Hugoniot curve for a single steady shock wave. Pressure and volume are in arbitrary units. Different points on the curve can be achieved for different particle velocity u_p. For each point the relative Rayleigh curve, representing the actual succession of intermediate equilibrium, is represented drawn as an arrow.

Rearranging the terms in the previous equation we obtain

$$E_c - E_0 = -\frac{u_p^2}{2} + \frac{P_c u_p}{\rho_0 u_{sw}} = u_p \left(\frac{-u_p u_{sw} \rho_0 + 2P_c}{2\rho_0 u_{sw}} \right) = \left(\frac{P_c + P_0}{2} \right) \frac{u_p}{\rho_0 u_{sw}}$$

where we have used (.2b) to rewrite $u_p u_{sw} \rho_0 = P_c - P_0$. From (.2a) we obtain that the ratio u_p / u_{sw} is equal to $1/\rho_0 - 1/\rho_c$. By substituting this into the previous equation, we obtain (.2c).

An alternative derivation of the Rankine-Hugoniot, based on the microscopic equations expressing the conservation laws is presented in the book of Zel'dovich [134].

Since the internal energies are functions of the state of the system, defined by its pressure and density, the (.2c) relates the final pressure of the shocked system to its density and the initial conditions $P_c = P_H(\rho_c, \rho_0, P_0)$. To this equation, representing the locus of possible final states (P, ρ) accessible with a single shock compression for given initial sample state (P_0, ρ_0) one often refers as Hugoniot curve. The Hugoniot can also be represented in a (P, u_p) diagram, by using the (.2).

The Rankine-Hugoniot relations are hence a system of 3 equations in 6 variables. The points lying on the same Hugoniot cannot be joined during a single shock: the actual path of intermediate states from P_0, V_0 to P_1, V_1 of a steady shock wave propagating with velocity u_{sw} is in fact a straight line joining the initial and the final state on the Hugoniot, and is called Rayleigh line.

Several methods have been developed to measure the velocities of the shock

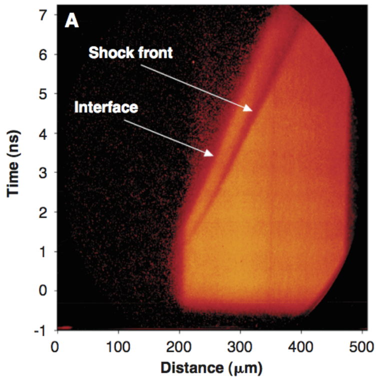

Figure .14. Example of radiographic image of a shock wave in a D_2 target. The red area represents the sample, the linear shadows the evolution of the edges of the compressed region evolved in time. The slopes of the interface and the shock front lines gives a measure of the velocities u_p and u_{sw}. Image from Ref. science front u_{sw} and of the particles u_p, necessary to identify the Hugoniot. The shock front velocity u_{sw} can be determined in a relatively easy way, by recognizing the passage of the wave in two points at known distance through electronic sensors and measuring the transit time from one to the other. Otherwise, time-resolved X-ray radiography allows to visualize the evolution of the shock wave into the media and to estimate the velocities from the slope of the lines representing the evolution of the front and of the back of the wave (see Fig. .14). Another possibility is the interferometric approach, using a VISAR (Velocity Interferometer System for Any Reflector) to monitor the medium. This apparatus consist in a probe laser, whose light is reflected by the shock front, and cameras to record the reflected signals. From the Doppler-shifts of the outcoming light frequencies, due to the motion of the reflecting surface, it is possible to deduce the shock velocity. Finally, the impedance matching is a graphical technique adopted to measure u_p once u_{sw} is known. Consider the passage of a shock from the material A (impactor) of known equation of state, to the medium B (sample). Two waves are produced: one moving forward into B and the other reflected backward into A. We can represent this process in a pressure-velocity diagram as shown in Figure .15, drawing the Rayleigh lines for A and B: $P_R^\alpha(u) = u_{sw}^\alpha \rho^\alpha u, \alpha = A, B$. The state of A immediately before the shock, (u_1^A, P_1^A), can be identified as the crossing between the Hugoniot for A and the curve $P_R^A(u)$. After the shock wave is reflected in A a new state is established, represented by a relaxation curve $P_{rel}^A(u)$ passing in (u_1^A, P_1^A). Noticing on the contact surface the two media must have same pressure and velocity, these quantities can be found as the intersection of $P^A(u)$ the Rayleigh curve of B.

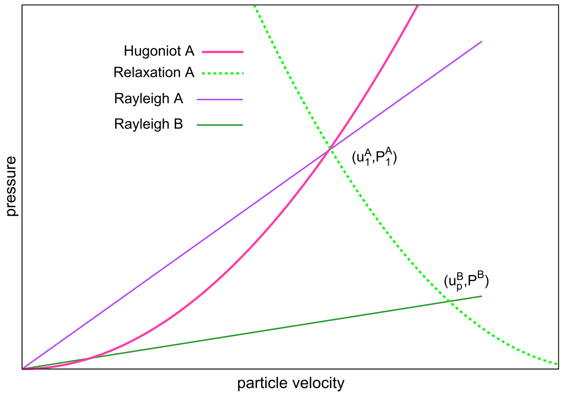

Figure .15. Example of impedance matching technique, to find the particle velocity u_p after a shock wave. The magenta continuous and the green dotted curves represents, respectively, the Hugoniot and the relaxation curves of the impactor material “A”. The straight lines are the Rayleigh lines for the impactor “A” (purple) and the shocked media “B” (dark green). The particle velocity and the pressure of the sample are represented by the point (u_p^b, P^b). Pressure and velocities are in arbitrary units.

Different techniques can be applied to obtain shock waves in media, the most common are gas gun experiments, flyer plates, laser driven acceleration.

Gas gun

A schematic representation of a two stages gas gun is presented in Figure .16. The first stage is a cylinder filled with a light gas. Inside the cylinder can slide a piston to allow the compression of the gas. The piston is set in motion at the desired initial velocity by burning a suitable amount of gunpowder. The second stage, is a cylinder with smaller section than the first, from which is separated by a thin membrane, that breaks when the pressure in the first stage reaches a determined value. At this point the hydrogen flows into the narrow second stage, pushing forward, with increased pressure, the impactor, placed in origin immediately behind the valve. This device allows to achieve impactor velocity from 1 to 8 kilometers per second, depending on the amount of gunpowder fired, on the driving gas (lighter gases for higher velocities), on the maximum pressure sustained from the valve, on the impactor mass and on the geometry of the stages.

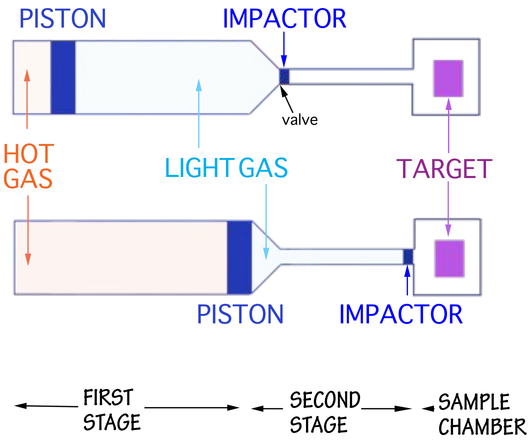

Figure .16. Scheme of a two stages gas gun. Three parts can be distinguished: the first stage in which the light gas is initially compressed up to the desired maximum pressure by pushing the piston; the second narrow stage, in which the gas reaches higher pressures and speed up the impactor; the sample chamber, where occurs the impactor-target hit, originating the shock waves.

Lasers

Lasers can be used to produce shock waves essentially in two ways: by speeding up impactors (flyer plates), as in the gas gun experiment, or directly by inducing onto the sample the production of an inertially confined high pressure plasmas that generates stress waves (direct driving). Inertially confined plasmas are produced by focusing a pulsed laser on a narrow spot on the surface of the material. The energy release will cause locally a rapid increase of the pressure and the subsequent expansion will induce the shock wave. Similarly the laser focusing can be used also to launch a flyer plate, that is attached on a multilayer substrate in which a shock wave is induced by the pulsed laser.

.2 Crystallographic nomenclature

.2.1 Symmetry operations

In order to understand the crystallographic nomenclature adopted somewhere in this thesis and largely in literature to describe the less common crystal structure, it is necessary to recall first some basic notions on the symmetry operation in a crystal.

The principal symmetry operations that can be recognized in an infinite system are

- *Rotation*, of an angle $\theta = 2\pi/n$, where n is an integer number, around an axis Z: a system has rotational symmetry if it is invariant under a coordinate transformation as: $x \rightarrow xcos\theta - ysin\theta$; $y \rightarrow ysin\theta + ycos\theta$; $z \rightarrow z$. According to the value of the integer n, the order of the rotation, the rotation axis is usually defined an $n-$fold axis.

- *Translation*, of a vector $\mathbf{v} \equiv (v_x, v_y, v_z)$: a system possess translational symmetry if it is invariant under a coordinate transformation as: $x \rightarrow x + v_x$, $y \rightarrow y + v_y$, $z \rightarrow z + v_z$.

- *Mirror reflection*, with respect to a plane $\Pi = XY$: a system possess a mirror symmetry if it is invariant under a coordinate transformation as: $x \rightarrow x$; $y \rightarrow y$; $z \rightarrow -z$.

- *Inversion*, with respect to a point P: a system has inversion symmetry if it is invariant under a coordinate transformation $x \rightarrow -x$; $y \rightarrow -y$; $z \rightarrow -z$ assuming P is the origin of the reference cartesian system. The point P is called center of inversion.

The combination of pairs of the previous symmetry operations can to additional symmetry operation, that are

- *Roto-inversion*, obtained from a rotation of order n followed by an inversion of coordinates. This symmetry is due to the presence of an $n-$fold axis of rotation that has a center of symmetry lying on it.

- *Mirror-rotation*, arising from a mirror reflection followed by a rotation of order n. This symmetry is due to the presence of a mirror plane with an $n-$fold axis of rotation lying on it. For odd n this operation correspond to a $2n$ roto-inversion.

- *Roto-translation*, that comes from the combination of a rotation of order n with a translation of a vector $\mathbf{v}$, parallel to the rotation axis, called screw axis. The length of the vector $\mathbf{v}$ is not arbitrary, but must be such that the symmetry operation can fit with the lattice. Let us consider a crystal structure and suppose to apply a roto-translation around the screw axis n times: since after n pure rotations the system returns to its original position, the final result of these operations is a translation of $n\mathbf{v}$. In order for the crystal points to lie on the lattice it is then necessary that $n\mathbf{v} = p\mathbf{t}$, being m an integer and $\mathbf{t}$ the shortest lattice vector along the screw axis. It follows that $\mathbf{v} = p\mathbf{t}/n$.

- *Mirror-translation*, that comes from the combination of a mirror reflection with a translation of a vector **v**, parallel to the plane. Planes of mirror-translation are called glide planes. As for the roto-translations, the vector cannot be arbitrary: in this case **v** must be equal to a fraction of the shortest lattice vector parallel to the plane.

.2.2 The Hermann-Mauguin notation

The crystal structures can be classified on the base of the symmetries they possess. The collection of all the symmetry operation of a crystal is called "space group". Since some symmetry operations can be mutually exclusive and since the simultaneous existence of two or more simmetries can imply the presence of other operations, it has been showed that only a finite number (230) of space groups exists. In the international notation (or Hermann-Mauguin notation) crystal lattices are classified on the base of the space group they belong to. The rules to assign the names to the space groups can be summarized as follows

- A mirror plane is denoted by a lowercase m
- An $n-fold$ rotational axis is denoted by the integer n representing the angle of rotation as $\theta = 2\pi/n$. If several rotational axis are present, they are listed in decreasing order of n. To indicate a rotational axis orthogonal to a mirror plane the notation n/m is used.
- An $n-fold$ roto-inversion axis is denoted as $\bar{n}$, where the integer n representing the angle of rotation as $\theta = 2\pi/n$.
- A screw axis is indicated by two integer numbers as n_p. The number n represents the order of rotation, the subscript p denotes the amount of the translation along a lattice vector parallel to the screw axis. As an example: the symbol 2_1 indicates the presence of a rotational symmetry of an angle $\theta = \pi$ followed by a translation of 1/2 of the lattice vector.
- A glide plane is indicated by one of the following lowercase letters: a, b or c, to represent a glide translation of 1/2 of the lattice vector along the x, the y or the z lattice vector, respectively; n to represent a glide translation of 1/4 along a

.2.3 Pearson notation

Another crystal designation that can be encountered in literature is the Pearson notation. At a variance with the Hermann-Maguin notation, the Pearson symbols that identify the crystal only describes the main features of the structure and do not take into account all the simmetries it possess. In other words, Pearson symbols do not indicate space groups. It follows that the correspondence of the Pearson notation and of the international notation is not biunivocal, since the informations on the lattice symmetries contained in the former are minor.

A lattice is identified through a pair of letters followed by an integer number. The first letter, lowercase, identifies the crystal class, the second, capital, the face centering, according to the definitions in Table .3. Finally the integer represents the number of atoms in the unit cell.

c	cubic
h	hexagonal
t	tetragonal
o	orthorhombic
m	monoclinic
a	triclinic

C	side face centered
F	face centered
I	body centered
R	rhombohedral
P	primitve

Table .3. Meaning of the lowercase and capital letters forming a Pearson symbol.

.2.4 Crystal designation correspondance

The table below (.4) summarizes the correspondence among the different designations of some common lattices appearing throughout this thesis. The common name, the space group and the Pears symbol are shown.

Name	Space Group	Pearson symbol
SC	$mPm\bar{3}m$	cP1
BCC	$Im\bar{3}m$	cI2
FCC	$Fm\bar{3}m$	cF4
Diamond	$Fd\bar{3}m$	cF8
A_{15}	$Pm\bar{3}n$	cP8
Fluorite	$Fm\bar{3}m$	cF12
CsIV	$I4_1/amd$	tI4
SH	$P6/mmc$	hP1
HCP	$P6_3/mmc$	hP2

Table .4. Correspondence among the name of some common crystal lattices (first column), the space group of belonging (second column) and the Pearson designation (third column).

.3 Derivative of exponential of operators

We want to proof that, given an operator $\hat{X}(\lambda)$ that depends on the parameter λ and an operator $\hat{E}(\lambda,\beta) = e^{\beta\hat{X}(\lambda)}$, depending also on the parameter β, the following equality holds

$$\frac{\partial \hat{E}(\lambda,\beta)}{\partial\lambda} = \int_0^\beta e^{\tau\hat{X}(\lambda)} \frac{\partial \hat{X}(\lambda)}{\partial\lambda} e^{(\beta-\tau)\hat{X}(\lambda)} d\tau \tag{.9}$$

where $\tau = \beta/M$ and M a positive integer.

Let us first rewrite the operator $\hat{E}(\lambda,\beta)$ as

$$\hat{E}(\lambda,\beta) = \left[e^{\tau\hat{X}(\lambda)}\right]^M = \left[\hat{E}(\lambda,\tau)\right]^M \tag{.10}$$

For $\tau \to 0$ (and $M \to \infty$), we can use the Taylor expansion up to the first order in τ to rewrite

$$\frac{\partial \hat{E}(\lambda,\tau)}{\partial\lambda} \approx \frac{\partial}{\partial\lambda}[1+\tau\hat{X}(\lambda)] = \tau\frac{\partial \hat{X}(\lambda)}{\partial\lambda} \tag{.11}$$

From this expression we get, applying the rule of the derivative of products

$$\begin{aligned}\frac{\partial \hat{E}(\lambda,\beta)}{\partial\lambda} &= \lim_{\substack{\tau\to 0\\ M\to\infty}} \sum_{k=1}^{M} \left[\hat{E}(\lambda,\tau)\right]^k \tau\frac{\partial \hat{X}(\lambda)}{\partial\lambda} \left[\hat{E}(\lambda,\tau)\right]^{M-k-1} \\ &= \int_0^\beta e^{\tau\hat{X}(\lambda)} \frac{\partial \hat{X}(\lambda)}{\partial\lambda} e^{(\beta-\tau)\hat{X}(\lambda)} d\tau \end{aligned} \tag{.12}$$

the last equality obtained going to the continuous limit.

.4 Derivation of the virial estimator for the energy

In this appendix we want to derive the general expression for the energy virial estimator

$$E_V = \left\langle \frac{3N}{2M\tau} - \frac{1}{4M\tau^2\lambda}(\mathbf{R}_{M+i} - \mathbf{R}_i)\cdot(\mathbf{R}_{i+1} - \mathbf{R}_i) - \frac{1}{2}F_i\Delta_i + \frac{d\mathcal{U}_i}{d\tau}\right\rangle \qquad (.13)$$

where $F_i = -(\nabla_i\mathcal{U}_{i-1} + \nabla_i\mathcal{U}_i)/\tau$ and $\Delta_i = \sum_{j=-M+1}^{M-1}(\mathbf{R}_i - \mathbf{R}_{i+j})/2M$; $\mathcal{U}_i = \mathcal{U}(\mathbf{R}_i, \mathbf{R}_{i+1}; \tau, \lambda)$ (in the primitive approximation $\mathcal{U}_i = -\tau[\mathcal{V}(\mathbf{R}_i) + \mathcal{V}(\mathbf{R}_{i+1})]/2$); $\lambda = \hbar^2/2m$; M is the number of slices, τ the time slice, so that $\beta = M\tau$. A slightly different derivation can be found in in Appendix A of Ref. [64].

Let us first introduce the quantity

$$G = \left\langle \sum_{i=1}^{L-1}(\mathbf{R}_i - \mathbf{R}_0)\cdot\nabla_i \right\rangle = \mathcal{Z}^{-1}\int\prod_{j=1}^{M-1}d\mathbf{R}_j\left(\sum_{i=1}^{L-1}(\mathbf{R}_i - \mathbf{R}_0)\cdot\nabla_i\right)e^{-\sum_{i=1}^{M}\mathcal{S}_i} \qquad (.14)$$

where L is an arbitrary number of slices $L \in [1, M]$. The functions $\mathcal{S}_i$ are defined in (2.85), which we copy here for ease of reading

$$\mathcal{S}_i = \mathcal{S}(\mathbf{R}_i, \mathbf{R}_{i+1}; \tau) = \frac{3N}{2}\ln(4\pi\lambda\tau) + \frac{(\mathbf{R}_i - \mathbf{R}_{i+1})^2}{4\lambda\tau} + \mathcal{U}(\mathbf{R}_i, \mathbf{R}_{i+1}; \tau, \lambda) \qquad (.15)$$

Solving by parts and noticing that the surface term goes to zero for small τ, since $\exp[-\mathcal{S}_i] \sim \tau \to 0$ as $\tau \to 0$, we get

$$G = -\mathcal{Z}^{-1}\int\prod_{j=1}^{M-1}d\mathbf{R}_j\left(\sum_{i=1}^{L-1}\nabla_i(\mathbf{R}_i - \mathbf{R}_0)\right)e^{-\sum_{i=1}^{M}\mathcal{S}_i} = -3N(L-1) \qquad (.16)$$

If, instead, we explicitly perform the derivative we obtain

$$\begin{aligned} G &= -\left\langle \sum_{i=1}^{L-1}(\mathbf{R}_i - \mathbf{R}_0)\cdot\left(\sum_{j=1}^{M}\nabla_i\mathcal{S}_j\right)\right\rangle \\ &= -\left\langle \sum_{i=1}^{L-1}(\mathbf{R}_i - \mathbf{R}_0)\cdot\left(\frac{2\mathbf{R}_i - \mathbf{R}_{i-1} - \mathbf{R}_{i+1}}{2\lambda\tau} + \nabla_i(\mathcal{U}_i + \mathcal{U}_{i+1})\right)\right\rangle \end{aligned} \qquad (.17)$$

We hence get

$$\frac{3N(L-1)}{2\tau} = \left\langle \sum_{i=1}^{L-1}(\mathbf{R}_i - \mathbf{R}_0)\cdot\left(\frac{2\mathbf{R}_i - \mathbf{R}_{i-1} - \mathbf{R}_{i+1}}{4\lambda\tau^2} + \frac{\nabla_i\mathcal{U}_i + \nabla_i\mathcal{U}_{i+1}}{2\tau}\right)\right\rangle \qquad (.18)$$

In order to rewrite the previous expression in a more suitable form, we can express the path coordinates $\mathbf{R}_i$ in terms of the variables $\delta_j = \mathbf{R}_j - \mathbf{R}_{j-1}$ such that

$$\mathbf{R}_i = \mathbf{R}_0 + \sum_{j=1}^{i}\delta_j \qquad (.19)$$

With this substitution

$$\begin{aligned}
\sum_{i=1}^{L-1}(\mathbf{R}_i-\mathbf{R}_0)\cdot(2\mathbf{R}_i-\mathbf{R}_{i-1}-\mathbf{R}_{i+1}) &= \sum_{i=1}^{L-1}\left(\sum_{j=1}^{i}\delta_j\right)\cdot(\delta_i-\delta_{i+1}) = \\
= & \sum_{i=1}^{L-1}\sum_{j=1}^{i}\delta_j\cdot\delta_i-\sum_{i=1}^{L-1}\sum_{j=1}^{i}\delta_j\cdot\delta_{i+1} \\
= & \sum_{i=1}^{L-1}\delta_i^2+\sum_{i=2}^{L-1}\sum_{j=1}^{i-1}\delta_j\cdot\delta_i-\sum_{k=2}^{L}\sum_{j=1}^{k-1}\delta_j\cdot\delta_k
\end{aligned} \tag{.20}$$

where in the last line we have separated the δ_i^2 terms in the first sum and we have substituted $i+1=k$ in the last sum. Since the k is a dumb index, we can put together the last two sums in (.20), then we get

$$\begin{aligned}
= & \sum_{i=1}^{L-1}\delta_i^2-\sum_{j=1}^{L-1}\delta_j\cdot\delta_L=\sum_{i=1}^{L}\delta_i^2-\sum_{j=1}^{L}\delta_j\cdot\delta_L \\
= & \sum_{i=1}^{L}(\mathbf{R}_i-\mathbf{R}_{i-1})^2-(\mathbf{R}_L-\mathbf{R}_0)\cdot(\mathbf{R}_L-\mathbf{R}_{L-1})
\end{aligned} \tag{.21}$$

The first term reconstruct the kinetic contribution in the expression for the $\mathcal{S}_i$, (.15). Substituting (.21) into (.18) we obtain

$$\begin{aligned}
\frac{3N(L-1)}{2\tau} = & \left\langle \frac{\sum_{i=1}^{L}(\mathbf{R}_i-\mathbf{R}_{i-1})^2}{4\lambda\tau^2}-\frac{(\mathbf{R}_L-\mathbf{R}_0)\cdot(\mathbf{R}_L-\mathbf{R}_{L-1})}{4\lambda\tau^2}\right. \\
+ & \left.\sum_{i=1}^{L-1}(\mathbf{R}_i-\mathbf{R}_0)\cdot\frac{\nabla_i\mathcal{U}_i+\nabla_i\mathcal{U}_{i+1}}{2\tau}\right\rangle
\end{aligned} \tag{.22}$$

from which we get

$$\begin{aligned}
& \left\langle-\sum_{i=1}^{L}\frac{(\mathbf{R}_i-\mathbf{R}_{i-1})^2}{4\lambda L\tau^2}\right\rangle=\left\langle-\frac{(\mathbf{R}_i-\mathbf{R}_{i-1})^2}{4\lambda\tau^2}\right\rangle=\left\langle\frac{3N(1-L)}{2L\tau}\right. \\
- & \left.\frac{(\mathbf{R}_L-\mathbf{R}_0)\cdot(\mathbf{R}_L-\mathbf{R}_{L-1})}{4\lambda L\tau^2}+(\mathbf{R}_i-\mathbf{R}_0)\cdot\frac{\nabla_i\mathcal{U}_i+\nabla_i\mathcal{U}_{i+1}}{2\tau}\right\rangle
\end{aligned} \tag{.23}$$

where we have interpreted the sums over L appearing in (.22) as averages over the selected subset of L slices. Since the average contribution of each slice can be considered equal, we substituted to the sums the value on a single slice i.

We can use this expression to substitute the kinetic term into the thermodynamic estimator of the energy (2.88), that becomes

$$E_V=\left\langle\frac{3N}{2L\tau}+\frac{\partial U_i}{\partial\tau}-\frac{(\mathbf{R}_L-\mathbf{R}_0)\cdot(\mathbf{R}_L-\mathbf{R}_{L-1})}{4\lambda L\tau^2}+(\mathbf{R}_i-\mathbf{R}_0)\cdot\frac{\nabla_i\mathcal{U}_i+\nabla_i\mathcal{U}_{i+1}}{2\tau}\right\rangle \tag{.24}$$

Usually, L is chosen to be equal to the total number of slices M. In this case, averaging the previous expression over the end points we recover the (2.100).

.5 Ewald decomposition

In section 2.6.3 we introduced the Ewald decomposition for the Coulomb potential in order to derive the finite size corrections to the potential energy. We want to derive here the Ewald expression of the Coulomb potential.

.5.1 The Ewald breakup

Let us consider a system of charged particles, enclosed in a cubic box of side lenght L, which interact via a pair potential $v(|\mathbf{r}|)$. If the potential decays slowly, i.e. its range, defined by the radius r_c, is much larger than one half of the simulation box side, $r_c >> L/2$ it is necessary to define a method to compute correctly the interaction energy of the system. This energy, using periodic boundary conditions, can be written as

$$\mathcal{V}(\Omega) = \frac{1}{2} \sum_{\mathbf{n},\mathbf{n}'} {}^{\prime} \sum_{i,j} z_i z_j v(|\mathbf{r}_i + \mathbf{n}'L - \mathbf{r}_j - \mathbf{n}L|) \tag{.25}$$

where $\Omega = L^3$ is the volume of the simulation box, z_i is the charge of the i^{th} particle, $\mathbf{r}_i$ its position and $\mathbf{n}$ and $\mathbf{n}'$ are $3-$dimensional vectors of integer numbers, introduced to describe the periodic images of the particles. In the primed sums the term $\mathbf{n} = 0$ is present only if $i \neq j$.

For the Coulomb potential and other not integrable potentials, the sum is infinite if the system is not electrically neutral, while if the system is neutral, the sum is only conditionally convergent, the result depending on the order of the terms in the sum. The Ewald strategy to compute the interaction energy for long range potentials consists in splitting the original sum in two parts, both rapidly convergent.

In order to derive the Ewald formulas, let us first associate to each particle in the simulation box a rigid background of opposite charge. The charge density $n(\mathbf{r})$ of the particles plus their periodic images plus the background can be written as

$$n(\mathbf{r}) = \sum_j n_j(\mathbf{r}) = \sum_j z_j \left[\sum_{\mathbf{n}} \delta(\mathbf{r} - \mathbf{r}_j - \mathbf{n}L) - \frac{1}{\Omega} \right] \tag{.26}$$

If the original system is not neutral the addition of the background serves to guarantee that the total potential energy is finite. If, on the contrary, the original system is neutral, the addition of an equal number of positive and negative backgrounds z_i/Ω has a zero net effect.

We can then compute the interaction energy of the particle i with the charge distribution described by the charge density $n_j(\mathbf{r})$ as

$$\begin{aligned} w_{PBC}(\mathbf{r}_{ij}) &= z_i \int d\mathbf{r} v(|\mathbf{r}_i - \mathbf{r}|) n_j(\mathbf{r}) = z_i z_j \left[\sum_{\mathbf{n}} v(|\mathbf{r}_i - \mathbf{r}_j - \mathbf{n}L|) - \frac{1}{\Omega} \int d\mathbf{r} v(\mathbf{r}) \right] \\ &= z_i z_j \left[\sum_{\mathbf{n}} v(|\mathbf{r}_i - \mathbf{r}_j - \mathbf{n}L|) - \frac{\hat{v}_0}{\Omega} \right] \end{aligned} \tag{.27}$$

where, in the last equality we have introduced the Fourier transform of the potential

$$\begin{aligned} \hat{v}_{\mathbf{k}} &= \int d\mathbf{r} e^{i\mathbf{kr}} v(\mathbf{r}) && (.28) \\ v(\mathbf{r}) &= \int \frac{d\mathbf{k}}{(2\pi)^3} e^{-i\mathbf{kr}} \hat{v}_{\mathbf{k}} && (.29) \end{aligned}$$

In a completely equivalent way, it is also possible to express the periodic interaction energy w_{PBC} in the reciprocal space. The Poisson formula, that holds for a Fourier transform pair $f(\mathbf{r})$ and $\hat{f}(\mathbf{k})$

$$\frac{1}{\Omega} \sum_{\mathbf{k}} \hat{f}(\mathbf{k}) = \sum_{\mathbf{n}} f(\mathbf{n}L) \tag{.30}$$

allows to rewrite the charge density associated to the particle j as

$$n_j(\mathbf{r}) = z_j \left[\sum_{\mathbf{n}} \delta(\mathbf{r} - \mathbf{r}_j - \mathbf{n}L) - \frac{1}{\Omega} \right] = \frac{z_j}{\Omega} \left[\sum_{\mathbf{k}} e^{i\mathbf{k}(\mathbf{r}-\mathbf{r}_j)} - 1 \right] = \frac{z_j}{\Omega} \sum_{\mathbf{k}\neq 0} e^{i\mathbf{k}(\mathbf{r}-\mathbf{r}_j)} \tag{.31}$$

where the vectors $\mathbf{k}$ are given by $\mathbf{k} = 2\pi\mathbf{m}/L$ and $\mathbf{m}$ is a vector of integers. With this form for n_j the periodic interaction energy w_{PBC} becomes

$$\begin{aligned} w_{PBC}(\mathbf{r}_{ij}) &= \frac{z_i z_j}{\Omega} \sum_{\mathbf{k}\neq 0} \int d\mathbf{r} v(\mathbf{r}_i - \mathbf{r}) e^{i\mathbf{k}(\mathbf{r}-\mathbf{r}_j)} \\ &= \frac{z_i z_j}{\Omega} \sum_{\mathbf{k}\neq 0} \int d\mathbf{s} v(\mathbf{s}) e^{i\mathbf{k}(\mathbf{s}+\mathbf{r}_i-\mathbf{r}_j)} = \frac{z_i z_j}{\Omega} \sum_{\mathbf{k}\neq 0} e^{i\mathbf{k}(\mathbf{r}_i-\mathbf{r}_j)} \hat{v}_k && (.32) \end{aligned}$$

In the case of the Coulomb interactions $v(r) = r^{-1}$, or generally speaking, of a slowly decaying potential, both sums are slowly convergent. However, the equivalence of the two expressions for the periodic interactions w_{PBC} can be exploited to recast in a more convenient form the electrostatic energy. In fact, we can rewrite the original potential $v(\mathbf{r})$ as the sum of a short range and a long range potentials $v(\mathbf{r}) = v^s(\mathbf{r}) + v^l(\mathbf{r})$. The contribution to the total energy arising from the short range interactions is limited now to a finite number of pairs and can be computed in the real space. On the other hand, the Fourier transform of the long range potential decays rapidly with $\mathbf{k}$ and then this contribution can be computed in the reciprocal space.

In order to decompose the original potential into a short range and a long range part, let us introduce a function $\eta(\mathbf{r}|\alpha)$ to rewrite

$$v(\mathbf{r}) = \eta(\mathbf{r}|\alpha) v(\mathbf{r}) + (1 - \eta(\mathbf{r}|\alpha)) v(\mathbf{r}) = v^s(\mathbf{r}) + v^l(\mathbf{r}) \tag{.33}$$

where α is some parameter used to adjust properly the range of the potential $v_s(\mathbf{r})$. The function $\eta(\mathbf{r}|\alpha)$ must: (a) be finite in $\mathbf{r} = 0$, (b) go exponentially to zero as $r \to \infty$ and (c) ensure that $v^l(\mathbf{r})$ is regular at small $\mathbf{r}$, so that the Fourier transform of the short range potential converges rapidly to zero as k increases. Mixing the real space and the reciprocal space representations of the periodic interaction energy w_{PBC} we get

$$w_{PBC}(\mathbf{r}_{ij}) = z_i z_j \left[\sum_{\mathbf{n}} v^s(\mathbf{r}_i - \mathbf{r}_j - \mathbf{n}L) - \frac{\hat{v}_0^s}{\Omega} \right] + \frac{z_i z_j}{\Omega} \sum_{\mathbf{k}\neq 0} e^{i\mathbf{k}(\mathbf{r}_i-\mathbf{r}_j)} \hat{v}_k^l \tag{.34}$$

We can now compute the total energy of the system, given by

$$\mathcal{V}(\Omega) = \frac{1}{2}\sum_{i,j\neq i}^{N} w_{PBC}(\mathbf{r}_{ij}) + \sum_{i=1}^{N} z_i^2 e_M = \mathcal{V}^s(\Omega) + \mathcal{V}^l(\Omega) + E^{\mathrm{self}} \qquad (.35)$$

where e_M, the Madelung energy, represents the interaction of a particle i with all its periodic images and the background, E^{self} is the sum over all the particles of these contributions, $\mathcal{V}^s(\Omega)$ and $\mathcal{V}^l(\Omega)$ are, respectively, the sums of the short and the long range contributions of the periodic energy.

E^{self} is given by

$$\begin{aligned} E^{\mathrm{self}} = \sum_{i=1}^{N} z_i^2 e_M &= \frac{1}{2}\sum_{i=1}^{N} z_i^2 \lim_{\mathbf{r}\to 0}\left[w_{PBC}(\mathbf{r}) - v(\mathbf{r})\right] \\ &= \frac{1}{2}\sum_{i=1}^{N} z_i^2 \lim_{\mathbf{r}\to 0}\left[\sum_{\mathbf{n}} v^s(\mathbf{r}+\mathbf{n}L) - v(\mathbf{r})\right] + \frac{1}{2\Omega}\sum_{i=1}^{N} z_i^2 \left[\sum_{\mathbf{k}\neq 0} \hat{v}^l_{\mathbf{k}} - \hat{v}^s_0\right] \\ &= \frac{1}{2}\sum_{i=1}^{N} z_i^2 \lim_{\mathbf{r}\to 0}\left[v^s(\mathbf{r}) - v(\mathbf{r})\right] + \frac{1}{2\Omega}\sum_{i=1}^{N} z_i^2 \left[\sum_{\mathbf{k}\neq 0} \hat{v}^l_{\mathbf{k}} - \hat{v}^s_0\right] \qquad (.36) \end{aligned}$$

where to write the last equality we assumed that the range of $v^s(r)$ is small enough that the energy contribution from the terms $\mathbf{n}\neq 0$ of the sum over the particle images is zero.

The short range contribution $\mathcal{V}^s(\Omega)$ to the total electrostatic energy is

$$\begin{aligned} \mathcal{V}^s(\Omega) &= \frac{1}{2}\sum_{i,j\neq i}^{N} z_i z_j \sum_{\mathbf{n}} v^s(\mathbf{r}_{ij} - \mathbf{n}L) + \left[\sum_{i,j\neq i}^{N} z_i z_j\right]\frac{\hat{v}^s_0}{2\Omega} \\ &= \frac{1}{2}\sum_{i,j\neq i}^{N} z_i z_j v^s(\mathbf{r}_{ij}) + \left[\sum_{i}^{N} z_i^2 - \left(\sum_{i}^{N} z_i\right)^2\right]\frac{\hat{v}^s_0}{2\Omega} \qquad (.37) \end{aligned}$$

again assuming that the terms $\mathbf{n}\neq 0$ of the sum over the particle images are zero.

The long range energy contribution $\mathcal{V}^l(\Omega)$ is

$$\mathcal{V}^l(\Omega) = \frac{1}{2}\sum_{i,j\neq i}\frac{z_i z_j}{\Omega}\sum_{\mathbf{k}\neq 0} e^{i\mathbf{k}(\mathbf{r}_i - \mathbf{r}_j)}\hat{v}^l_k = \frac{1}{2\Omega}\sum_{\mathbf{k}\neq 0}\rho_{\mathbf{k}}\rho_{-\mathbf{k}}\hat{v}^l_k - \frac{1}{2\Omega}\sum_i z_i^2 \sum_{\mathbf{k}\neq 0}\hat{v}^l_k \qquad (.38)$$

having defined $\rho_{\mathbf{k}} = \sum_i z_i \mathrm{exp}[i\mathbf{k}\mathbf{r}]$ and used the fact that

$$\sum_{i,j\neq i} z_i z_j e^{i\mathbf{k}(\mathbf{r}_i - \mathbf{r}_j)} = \sum_{i,j} z_i z_j e^{i\mathbf{k}(\mathbf{r}_i - \mathbf{r}_j)} - \sum_i z_i^2 = \rho_{\mathbf{k}}\rho_{-\mathbf{k}} - \sum_i z_i^2 \qquad (.39)$$

Summing up the three contributions and simplifying the terms where possible we get

$$\mathcal{V}(\Omega) = \frac{1}{2}\sum_{i,j\neq i}^{N} z_i z_j v^s(\mathbf{r}_{ij}) + \frac{1}{2\Omega}\sum_{\mathbf{k}\neq 0}\rho_{\mathbf{k}}\rho_{-\mathbf{k}}\hat{v}^l_k + E_0 \qquad (.40)$$

being

$$E_0 = \frac{1}{2}\sum_{i=1}^{N} z_i^2 \lim_{\mathbf{r}\to 0}\left[v^s(\mathbf{r}) - v(\mathbf{r})\right] - \left(\sum_{i}^{N} z_i\right)^2 \frac{\hat{v}_0^s}{2\Omega} \tag{.41}$$

.5.2 The Ewald expression for the Coulomb potential

In a 3−dimensional system and for the Coulomb pair potential, $v(r) = r^{-1}$, the conventional choice for the auxiliary function $\eta(r|\alpha)$ used to separate the long range and the short range contributions of the pair potential is

$$\eta(r|\alpha) = \mathrm{erfc}(\alpha r) = \frac{2}{\sqrt{\pi}}\int_{\alpha r}^{x} e^{x^2} dx \tag{.42}$$

Indeed, this form of the function $\eta(r|\alpha)$ satisfies all the requirement listed in the previous section (i.e. it is finite in $r = 0$, goes exponentially to 0 as $r \to \infty$ and allow a rapid convergence of the Fourier transform of the long range part.) With this choice of the function $\eta(r|\alpha)$. Moreover, with this choice for $\eta(r|\alpha)$ and for $v(r) = r^{-1}$ it is possible to compute analytically the Fourier transform of the long range potential, as well as the constant terms appearing in the expression of the electrostatic energy.

In fact we have

$$v^l(r) = \frac{\mathrm{erf}(\alpha r)}{r} \quad \Rightarrow \quad \hat{v}_k^l = \frac{4\pi}{k^2} e^{-k^2/4\alpha} \tag{.43}$$

$$v^s(r) = \frac{\mathrm{erfc}(\alpha r)}{r} \quad \Rightarrow \quad \hat{v}_k^s = \frac{4\pi}{k^2}(1 - e^{-k^2/4\alpha^2}) \tag{.44}$$

from which we obtain the constant expressions

$$\hat{v}_0^s = \frac{\pi}{\alpha^2} \tag{.45}$$

$$\lim_{r\to 0}[v^s(r) - v(r)] = -\frac{2\alpha}{\sqrt{\pi}} \tag{.46}$$

Putting together Eqn. from (.43) to (.46) we finally arrive at

$$\mathcal{V}(\Omega) = \frac{1}{2}\sum_{i,j\neq i}^{N} z_i z_j \frac{\mathrm{erfc}(\alpha r_{ij})}{r_{ij}} + \frac{1}{2\Omega}\sum_{\mathbf{k}\neq 0} \rho_{\mathbf{k}}\rho_{-\mathbf{k}} \frac{4\pi}{k^2} e^{-k^2/4\alpha} + E_0 \tag{.47}$$

being

$$E_0 = -\sum_{i=1}^{N} z_i^2 \frac{\alpha}{\sqrt{\pi}} - \left(\sum_{i}^{N} z_i\right)^2 \frac{\pi}{2\Omega\alpha^2} \tag{.48}$$

.6 Corrections to the Gauss integration

Derivation of the correction formula

In the Gauss-Legendre integration scheme a definite integral of the kind

$$I = \int_a^b f(x)dx \tag{.49}$$

is approximated by summing the values of the function $f(x)$ calculated in N points $\{x_n\}$, weighting each term in a suitable way

$$I \approx \sum_{n=1}^{N} f(x_n)w_n \tag{.50}$$

Where the points $\{x_n\}$ corresponds to the N roots of a Legendre polynomial of order N defined in the interval $x \in [a, b]$. This correspond to interpolate the N reference points of the integrand with the Legendre polynomial and lead to a more accurate estimate of I with respect to other algorithms such as the trapezoidal rule. However, in such schemes the values of $f(x)$ at the boundary of the integration interval $[a, b]$ are never taken into account: this may cause wrong estimations of I, whenever $f(x)$ increases or decreases steeply as $x \to a$ or $x \to b$, because the interpolating polynomial is not able to reproduce the true behavior of the function. This may occur for example while applying the Frenkel-Ladd method [117] to evaluate the free energy of a solid, or, more generally whenever the coupling constant integration described in Section 3.3.3 is applied.

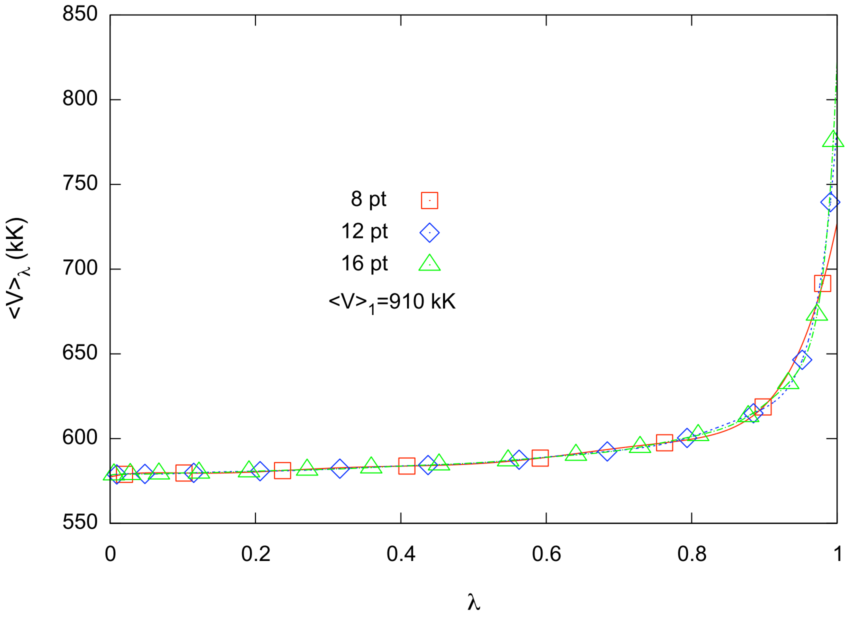

Figure .17. Gauss integration data: values of $\langle \mathcal{V} \rangle_\lambda$ and Legendre interpolating polynomial, for 8, 12 and 16 Gauss points. The estimated value at $\lambda = 1$ is of about $910kK$.

To overcome this problem the number N of integration points x_n may be increased until the desired accuracy level is reached. This approach can reveal prohibitively expensive in terms of computing time, especially in our CEIMC simulations, since the required number of Gauss points can be quite high. As an example, Figure .17 shows the values of the average of the potential energy $\left\langle V^{\text{eff}}\right\rangle_\lambda$ (per particle) as a function of the parameter $\lambda \in [0,1]$ for a liquid system of total potential $\mathcal{V}_\lambda = (1-\lambda)V^{\text{eff}}$. As $\lambda \to 1$ the interactions are switched off and the particles fill homogeneously the simulation box. As a consequence, the average of the potential energy $\left\langle V^{\text{eff}}\right\rangle_\lambda$ rises steeply. The exact value of $\left\langle V^{\text{eff}}\right\rangle_\lambda$ for $\lambda = 1$ can be estimated as the integral $\rho \int d\mathbf{r} v^{\text{eff}}(r) g(r)$ by assuming that the radial distribution function $g(r)$ in absence of interactions is equal to 1 everywhere. This estimate can be used to check the accuracy of the Legendre interpolation at $\lambda = 1$. The figure compares the behavior of the interpolating Legendre polynomial corresponding to the choice of $N = 8$, $N = 12$ and $N = 16$ Gauss integration points: the interpolation of the data is quite good in the interval $\lambda \in [0, \lambda_N]$, but the extrapolation at $\lambda \to 1$ is noticeably underestimated with respect to the exact value (about $910kK$, in this case). For that reason in our free energy calculations we decided to apply to the Gauss integration results a correction that can account of the wrong behavior of the interpolating polynomial as $\lambda = 1$.

Let us suppose that we need to apply the Gauss-Legendre integration scheme to the function $f(\lambda)$ defined in the interval $\lambda \in [0,1]$. Let us also assume that the value of $f(\lambda)$ at $\lambda = 1$ is known. If the N^{th} point λ_N of the Gauss integration is enough close to $\lambda = 1$, we can approximate the function in this sub interval $\lambda \in [\lambda_N, 1]$ with a third order polynomial $\Gamma(\lambda) = a + b(1-\lambda) + c(1-\lambda)^2 + d(1-\lambda)^3$. The polynomial $\Gamma(\lambda)$ has the correct value at $\lambda = 1$ and can represent better than the Legendre interpolating polynomial $G_N(\lambda)$ the function $f(\lambda)$ in the interval $\lambda \in [\lambda_N, 1]$ $f(\lambda)$. A more accurate estimate of the integral I is then

$$I \approx \sum_{n=1}^{N} f(\lambda_n) w_n - \int_{\lambda_N}^{1} G_N(\lambda) d\lambda + \int_{\lambda_N}^{1} \Gamma(\lambda) d\lambda \qquad (.51)$$

where we have subtracted the Legendre contribution to the integral I between λ_N and 1 and added of the contribution arising from the more correct interpolation with $\Gamma(\lambda)$.

It just remains to determine the value of the coefficient of the new polynomial. In order to do that, we must impose four conditions

- Value in $\lambda = 1$: $P_3(\lambda = 1) = f(\lambda = 1)$
  $\Rightarrow a = f(\lambda = 1)$

- First derivative in $\lambda = 1$: $P_3'(\lambda = 1) = f'(\lambda = 1)$
  $\Rightarrow -b = f'(\lambda = 1)$

- Value in $\lambda = \lambda_N$: $P_3(\lambda = \lambda_N) = f(\lambda = \lambda_N)$
  $\Rightarrow a + b(1-\lambda_N) + c(1-\lambda_N)^2 + d(1-\lambda_N)^3 = f(\lambda = \lambda_N) = \gamma_N$

- First derivative in $\lambda = \lambda_N$: $P_3'(\lambda = \lambda_N) = f'(\lambda = \lambda_N) = \gamma_N'$
  $\Rightarrow -b - 2c(1-\lambda_N) - 3d(1-\lambda_N)^2 = f'(\lambda = \lambda_N)$

By combining the four equations, we get $c = (-2b+\gamma'_N)/(1-\lambda_N)+3(\gamma_N-a)/(1-\lambda_N)^2$ and $d = (b-\gamma'_N)/(1-\lambda_N)^2 - 2(\gamma_N - a)/(1-\lambda_N)^3$.

The correction term due to the new interpolant can be computed analitically as

$$\int_{\lambda_N}^{1} d\lambda\Gamma(\lambda) = a(1-\lambda_N) + \frac{b}{2}(1-\lambda_N)^2 + \frac{c}{3}(1-\lambda_N)^3 + \frac{d}{4}(1-\lambda_N)^4 \tag{.52}$$

The contribution of the Legendre interpolant, on the contrary, must be evaluated numerically, as well as the values of the derivatives $f'(1)$ and $f'(\lambda_N)$ and of the value $f(1)$.

A correction example

To illustrate the effect of this correction to the Gauss-Legendre integration, we show the results obtained in the case just mentioned, namely the evaluation through λ integration with respect to the non interacting system of the free energy of a classical liquid. Tables below show the values estimated of the parameters of the interpolating curve Γ between λ_N and 1, for a number of Gauss points $N = 8$, $N = 12$, $N = 16$ and $N = 20$. For each N, the values of the integral obtained by direct Gauss integration (I_{old}), the correction computed following our scheme (ΔI), the new value of the integral (I_{new})are also showed. On the right of each table the Legendre interpolant (green curves) and the third order polynomial $\Gamma(\lambda)$ (red curves) are compared. The amount of the correction becomes smaller as the number of integration points is increased.

8 points

λ_N	0.98014492824876809
a	906.197
b	-24648.67
γ_i	691.546
γ'_i	1557.264
I_{old}	14.068
ΔI	1.035
I_{new}	15.103

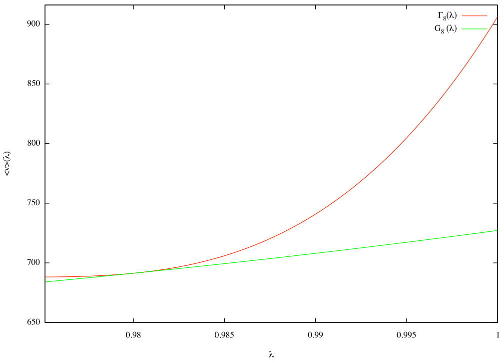

12 points

λ_N	0.99078031712335957
a	906.197
b	-24648.67
γ_i	739.538
γ'_i	4214.061
I_{old}	7.0152
ΔI	0.4732
I_{new}	7.4884

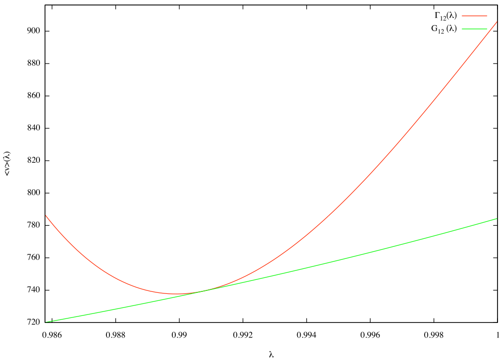

16 points

λ_N	0.99470046749582497
a	906.197
b	-24648.67
γ_i	775.57
γ_i'	7838.28
I_{old}	4.2313
ΔI	0.1856
I_{new}	4.4169

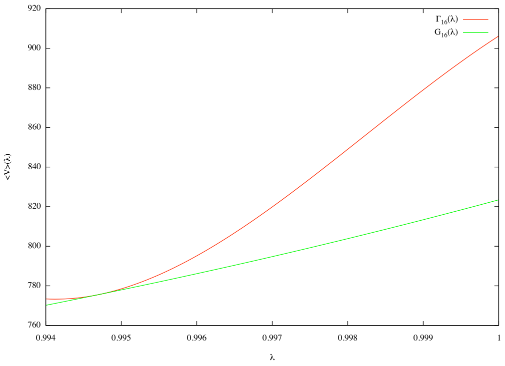

20 points

λ_N	0.996564299592547
a	906.197
b	-30122.824
γ_i	802.704
γ_i'	11721.9836
I_{old}	2.9175
ΔI	0.0813
I_{new}	2.8362

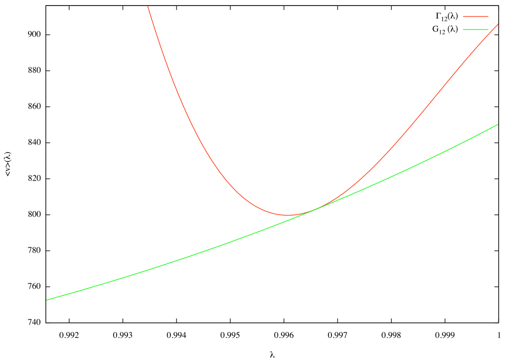

Bibliography

[1] W. B. Hubbard, T. Guillot, J. I. Lunine, A. Burrows, D. Saumon, M. S. Marley, and R. S. Freedman, Phys. Plasmas **4**, 2011 (1997)

[2] G. Chabrier and I. Baraffe, *Astron. Astrophys.* **327**, 1039 (1997).

[3] T. Guillot, *Annu. Rev. Earth Planet Sci.* **33**, 493 (2005).

[4] W. B. Hubbard, A. Burrows and J. I. Lunine, *Annu. Rev. Astron. Astrophys.* **40**, 103 (2002).

[5] D. J. Stevenson, *Rep. Prog. Phys.* **46**, 555 (1983)

[6] E. Wigner and H. B. Hungtington, *J. Chem. Phys.* **3**, 764 (1935)

[7] C. Narayana, H. Luo, J.Orloff and A. L. Luoff, *Nature* **393**, 46(1998)

[8] P. Loubeyre, F. Occelli and R. LeToullec, *Nature* **416**, 613 (2002)

[9] S. T. Weir, A. C. Mitchell and W. J. Nellis, *Phys. Rev. Lett.* **76**, 1860 (1996)

[10] G. W. Collins, L. B. Da Silva, P. Celliers, D. M. Gold, M. E. Foordr, R. J. Wallace, A. Ng, S. V. Weber, K. S. Budil and R. Cauble, *Science* **281**, 1178 (1998)

[11] V. E. Fortov, R. I. Ilḱaev, V. A. Arinin, V. V. Burtzev, V. A. Golubev, I. L. Iosilevskiy, V. V. Khrustalev, A. L. Mikhailov, M. A. Mochalov, V. Ya. Ternovoi and M. V. Zhernokletov, *Phys. Rev. Lett.* **99**, 185001 (2007)

[12] S. A. Bonev, E. Schwegler, T. Ogitsu and G. Galli, *Nature* **431**, 669 (2004)

[13] M. I. Eremets and I. A. Trojan, *JETP letters* **89**, 174 (2009)

[14] F. Datchi, P. Loubeyre and R. LeToullec, *Phys. Rev. B* **61**, 6535 (2000)

[15] S. Deemyad and I. F. Silvera, *Phys. Rev. Lett.* **100**, 155701 (2008)

[16] E. Gregoryantz, A. F. Goncharov, K. Matsuishi, H. K. Mao and R. J. Hemley, *Phys. Rev. Lett.* **90**, 175701 (2003)

[17] I. I. Mazin, R. J. Hemley, A. F. Goncharov, M. Hanfland, and H. K. Mao, *Phys. Rev. Lett.* **78**, 1066 (1997).

[18] S. Scandolo, *PNAS* **100**, 3051 (2003)

[19] M. Morales, C. Pierleoni, E. Schweglerd and D. M. Ceperley, *PNAS* **107**, 12799 (2010)

[20] M. Li, M. Hanfland, R. J. Hemley and H. K. Mao *Bull. Am. Phys. Soc.* **39**, 336 (1994).

[21] H. K. Mao and R. J. Hemley, *Rev. Mod. Phys.* **66**, 671 (1994)

[22] A. F. Goncharov, R. J. Hemley, and H. K. Mao, *J. Chem. Phys.* **134**, 174501 (2011)

[23] I. F. Silvera, *Rev. Mod. Phys.* **52**, 393 (1980)

[24] J. Kohanoff, S. Scandolo, G. L. Chiarotti, and E. Tosatti, *Phys. Rev. Lett.* **78**, 2783 (1997)

[25] P. Tolédano, H. Katzke, A. F. Goncharov and R. J. Hemley, *Phys. Rev. Lett.* **103**, 105301 (2009)

[26] I. Goncharenko and P. Loubeyre, *Nature* **435**, 1206 (2005)

[27] M. Hanfland, R. J. Hemley, and H. K. Mao, *Phys. Rev. Lett.* **70**, 3760 (1993)

[28] C. J. Pickard and R. J. Needs, *Nature* **3**, 473 (2007)

[29] C. J. Pickard and R. J. Needs, *Phys. Rev. Lett.* **97**, 045504 (2006)

[30] V. V. Kechin, *JETP letters* **79**, 40 (2004)

[31] C. Attaccalite and S. Sorella, *Phys. Rev. Lett.* **100**, 114501 (2008)

[32] W. J. Nellis, A. C. Mitchell, M. van Thiel, G. J. Devine, R. J. Trainor, and N. Brown, *J. Chem. Phys.* **79**, 1480 (1983)

[33] G. W. Collins, P. Celliers, L. B. Da Silva, R. Cauble, D. Gold, M. Foord, K. S. Budil, R. Stewart, N. C. Holmes, M. Ross, B. A. Hammel, J. D. Kilkenny, R. J. Wallace, and A. Ng, *Phys. Plasmas* **5**, 1864 (1998)

[34] D. G. Hicks, T. R. Boehly, P. M. Celliers, J. H. Eggert, S. J. Moon, D. D. Meyerhofer and G. W. Collins, *Phys. Rev. B* **79**, 014112 (2009)

[35] M.D. Knudson, D. L. Hanson, J. E. Bailey, C. A. Hall, J. R. Asay and C. Deeney, *Phys. Rev. B* **69**, 144209 (2004)

[36] G.V. Boriskov, A. I. Bykov, R. I. Ilḱaev, V. D. Selemir, G. V. Simakov, R. F. Trunin, V. D. Urlin, A. N. Shuikin, and W. J. Nellis, *Phys. Rev. B* **71**, 092104 (2005)

[37] S.A. Bonev, B. Militzer and G. Galli *Phys. Rev. B* **69**, 014101 (2004)

[38] D. Saumon and G. Chabrier, *Phys. Rev. A* **44**, 5122 (1991)

[39] M. Ross, *Phys. Rev. B* **58**, 669 (1998)

[40] $http://t1web.lanl.gov/doc/SESAME\_3Ddatabase\_1992.html$

[41] H. Juranek, R. Redmer, and Y. Rosenfeld, *J. Chem. Phys.* **117**, 1768 (2002)

[42] J. Vorberger, I. Tamblyn, B. Militzer, and S.A. Bonev, *Phys. Rev. B* **75**, 024206 (2007)

[43] B. Holst, R. Redmer and M. Desjarlais, *Phys. Rev. B* **77**, 184201 (2008)

[44] K. T. Delaney, C. Pierleoni and D. M. Ceperley *Phys. Rev. Lett.* **97**, 235702 (2006)

[45] I. Tamblyn and S. A. Bonev, *Phys. Rev. Lett.* **104**, 065702 (2010)

[46] W. J. Nellis, S. T. Weir and A. C. Mitchell *Phys. Rev. B* **59**, 3434 (1999)

[47] D. M. Ceperley and B. J. Alder, *Phys. Rev. B* **36**, 2092 (1987)

[48] T. W. Barbee III, A. García, M. L. Cohen, and J. L. Martins, *Phys. Rev. Lett.* **62**, 1150 (1989)

[49] V. Natoli, R. M. Martin and D. M. Ceperley, *Phys. Rev. Lett.* **70**, 1952 (1993)

[50] M. Städele and R. M. Martin, *Phys. Rev. Lett.* **84**, 6070 (2000)

[51] M. Städele, J. A. Majewski, P. Vogl, and A. Görling, *Phys. Rev. Lett.* **79**, 2089 (1997)

[52] J. M. McMahon and D. M. Ceperley, *Phys. Rev. Lett.* **106**, 165302 (2011).

[53] J. Kohanoff and J. P. Hansen, *Phys. Rev. E.* **54**, 768 (1996).

[54] J. Kohanoff and J. P. Hansen, *Phys. Rev. Lett.* **74**, 626 (1995)

[55] C. Pierleoni, D. M. Ceperley and M. Holtzmann, *Phys. Rev. Lett.* **93**, 146402 (2004).

[56] W. J. Nellis, A. A. Louis and N. W. Ashcroft, *Phil. Trans. R. Soc. Lond. A* **356**, 119 (1998)

[57] N. W. Aschroft, *J. Phys. Cond. Matt.* **12**, A129 (2000)

[58] N. W. Ashcroft, *J. Phys. A: Math. Gen.* **36**, 6137 (2003)

[59] N. W. Ashcroft, *Phys. Rev. Lett.* **21**, 1748 (1968)

[60] E. Babaev, A. Sudbø and N. W. Ashcroft, *Nature* **431**, 666 (2004)

[61] M. Born and R. Oppenheimer, *Annalen der Physik* **84**, 457 (1927).

[62] C. Pierleoni and D. M. Ceperley, *Lect. Notes Phys.* **703**, 641 (2007).

[63] N. Metropolis, A. N. Rosenbluth, M. N. Rosenbluth, A. H. Teller, and E. Teller. *Journal of Chemical Physics* **21**, 1097 (1953).

[64] D. M. Ceperley, *Rev. Mod. Phys.* **67**, 279 (1995).

[65] B. L. Hammond, W. A. Lester Jr. and P. J. Reynolds, "*Monte Carlo Methods in ab-initio quantum chemistry*", World Scientific (Singapore, 1994).

[66] S. Baroni and S. Moroni, *Phys. Rev. Lett.* **82**, 4757 (1999).

[67] C. Pierleoni, K. T. Delaney, M. A. Morales, D.M. Ceperley, and M. Holzmann, *Comp. Phys. Comm.* **179**, 89 (2008).

[68] D. M. Ceperley "*Path integral Monte Carlo methods for fermions.*" In K. Binder and G. Ciccotti, editors, Monte Carlo and Molecular Dynamics of Condensed Matter Systems. Editrice Compositori, Bologna, 1996.

[69] J. M. Thjiessen, *Computational Physics*, Cambridge University press, (1999).

[70] D. Frenkel and B. Smit, "*Understanding molecular simulation, from algorithms to applications*", 2nd ed., Academic Press (San Diego, 2002)

[71] L. E. Reichl. "*A Modern Course in Statistical Physics*". Wiley-Interscience Publication, (1998)

[72] R. P. Feynman, *Statistical Mechanics*, Addison-Wesley, Reading, MS, (1972).

[73] R. M. Wilcox, *J. Math. Phys.* **8**, 962 (1967).

[74] H. F. Trotter, *Proc. Am. Math Soc.* **10**, 545 (1959).

[75] E.L. Pollock and D.M. Ceperley, *Phys. Rev. B* **30**, 2555 (1984).

[76] R. G. Storer, *J. Math. Phys.* **9**, 964 (1968).

[77] P. Lévy, *Compositio Math.* **7**, 283 (1939).

[78] D. M. Ceperley and E.L. Pollock, in "*Monte Carlo methods in theoretical physics*" edited by S. Caracciolo and A. Faborcini, ETS Editrice (Pisa 1992)

[79] M. F. Herman, E. J. Bruskin, and B. J. Berne, *J. Chem. Phys.* **76**, 5150 (1982)

[80] W. M. C. Foulkes, L. Mitas, R. J. Needs and G. Rajagopal, *Rev. Mod. Phys.* **73**, 33 (2001)

[81] R. Jastrow, *Phys. Rev. Lett.* **98**, 1497 (1955)

[82] T. Kato, *Commun. Pure Appl. Math.* **10**, 151 (1957); R. T. Pack and W. B. Brown, *J. Chem. Phys.* **45**, 556 (1966).

[83] N. D. Drummond, M. D. Towler and R. J. Needs, *Phys. Rev. B* **70**, 235119 (2004).

[84] D. Bohm and D. Pines, *Phys. Rev.* **92**, 609 (1953)

[85] T. Gaskell, *Proc. Phys. Soc. London* **77**, 1182 (1961)

[86] M. Holzmann, D. M. Ceperley, C. Pierleoni, and K. Esler, *Phys. Rev. E* **68**, 046707 (2003)

[87] Y. Kwon, D. M. Ceperley, and R. M. Martin, *Phys. Rev. B* **58**, 6800 (1998)

[88] R. P. Feynman and M. Cohen, *Phys. Rev.* **102**, 1189 (1956).

[89] L. M. Fraser, W. M. C. Foulkes, G. Rajagopal, R. J. Needs, S. D. Kenny, and A. J. Williamson, *Phys. Rev. B* **53**, 1814 (1996)

[90] M. Dewing and D. M. Ceperley *Methods in Coupled Electron-Ion Monte Carlo*, World Scientific (2002).

[91] C. Pierleoni and D. M. Ceperley, *Chem. Phys. Chem.* **6**, 1 (2005)

[92] K. Huang, "Statistical Mechanics", 2ed. (Wiley, 1987)

[93] G. Ortiz, D. M. Ceperley, and R. M. Martin, *Phys. Rev. Lett.* **71**, 2777 (1993)

[94] G. Ortiz and D. M. Ceperley, *Phys. Rev. Lett.* **75**, 4642 (1995)

[95] D. M. Ceperley and M. Dewing, *J. Chem. Phys.* **110**, 9812 (1999)

[96] C. Lin, F. H. Zong, and D. M. Ceperley, *Phys. Rev. E* **64**, 016702 (2001)

[97] S. Chiesa, D. M. Ceperley, R. M. Martin, and M. Holzmann,*Phys. Rev. Lett.* **97** 076404 (2006)

[98] N. D. Drummond, R. J. Needs, A. Sorouri and W. M. C. Foulkes, *Phys. Rev. B* **78**, 125106 (2008)

[99] W. L. McMillan, *Phys. Rev.* **138**, A442 (1965)

[100] J. Hammerberg and N. W. Ashcroft, *Phys. Rev. B* **9**, 409 (1974).; Errata, *Phys. Rev. B* **3**, 1511 (1974).

[101] J. P. Hansen and I. R. McDonald, *Theory of simple liquids*, Academic Press (London, 1986)

[102] S. Ichimaru, H. Iyetomi and S. Tanaka, *Phys. Rep.* **59**, 1 (1980).

[103] D. M. Ceperley and B. J. Alder, *Phys. Rev. Lett.* **45**, 566 (1980).

[104] G. Giuliani and G. Vignale, *Quantum theory of electron liquids*, Cambridge University Press, Cambridge (2005).

[105] J. Perdew and A. Zunger, *Phys. Rev. B* **23**, 5048 (1981).

[106] J. Hubbard, *Proc. R. Soc. London Ser. A* **243**, 336 (1957).

[107] G. D. Mahan, *Many-particle physics*, 2^{nd}ed., Plenum Press, New York (1993)

[108] S. Moroni, D. M. Ceperley and G. Senatore, *Phys. Rev. Lett.* **69**, 1837 (1992).

[109] M. Corradini, R. Del Sole, G. Onida, and M. Palummo, *Phys. Rev. B* **57**, 14569 (1998).

[110] K.S. Singwi and M.P. Tosi, *Solid State Physics* **36** 177 (1981).

[111] P. Ascarelli and R. Harrison, *Phys. Rev. Lett.* **22**, 285 (1969).

[112] V. Natoli, R. M. Martin and D. M. Ceperley, *Phys. Rev. Lett.* **74**, 601 (1995).

[113] W. B. Hubbard and W. L. Slattery, *Astroph. J.* **168**, 131 (1971).

[114] M. Ross, H. E. DeWitt and W. B. Hubbard, *Phys. Rev. A* **24**, 1016 (1981).

[115] G. Chabrier, *J. Phys. (France)* **51**, 1607 (1990).

[116] M. Baus and C. F. Tejero, *Equilibrium Statistical Physics: Phases of Matter and Phase Transitions*, Springer (2008).

[117] D. Frenkel and A. J. C. Ladd, *J. Chem. Phys.* **81**, 3188 (1984).

[118] G. S. Stringfellow, H. E. DeWitt and W. L. Slattery, *Phys. Rev. A* **41**, 1105 (1990).

[119] E. Wigner, *Phys. Rev.* **40**, 749 (1932); J. G. Kirkwood, ibid. **44**, 31 1933.27

[120] C. Filippi and D. M. Ceperley, *Phys. Rev. B* **57**, 252 (1997)

[121] E. Liberatore, M. A. Morales, C. Pierleoni and D. M. Ceperley, in preparation.

[122] D. A. Kofke, *J. Chem. Phys.* **98**, 4149 (1993).

[123] J. Kohanoff, *J. Low. Temp. Phys.* **122**, 297 (2001).

[124] N. E. Christensen and D. L. Novikov, *Solid State Communications* **119**, 477 (2001)

[125] V. D. Natoli, *"A Quantum Monte Carlo study of high pressure phases of hydrogen"*, Ph.D. thesis, University of Illinois (1994).

[126] G. Chabrier, D. Saumon, W. B. Hubbard, and J. I. Lunine, *Astrophys. J.* **391**, 817 (1992)

[127] W. J. Nellis, *Planetary and Space Science* **48**, 671 (2000)

[128] E. E. Salpeter, *Astrophys J.* **181**, L83 (1973).

[129] S. W. Haan, S. M. Pollaine, J. D. Lindl, L. J. Suter, R. L. Berger, L. V. Powers, W. E. Alley, P. A. Amendt, J. A. Futterman, W. K. Levedahl, M. D. Rosen, D. P. Rowley, R. A. Sacks, A. I. Shestakov, G. L. Strobel, M. Tabak, S. V. Weber, and G. B. Zimmerman *Phys. Plasmas* **2**, 2480 (1995)

[130] W. J. Nellis, *Phys. Rev. B* **54**, 3434 (1999)

[131] M. A. Morales, C. Pierleoni, and D. M. Ceperley, *Phys. Rev. E* **81**, 021202 (2010)

[132] I. Silvera and V. V. Goldman, *J. Chem. Phys.* **69**, 4209 (1978)

[133] W. Kolos W and I. Wolniewicz, *J. Chem. Phys.* **49**, 404 (1968)

[134] Ya. B. Zel'dovich and Yu. P. Razier. "*Physics of Shock Waves and Hydrodynamic Phenomena*", Academic Press, London, 1967